Ruprecht-Karls-Universität

Analysis of High-Precision Spectroscopic Data in Search of Exoplanet Signals Close to the Stellar Noise Limit

Stephan Amir Stock

A thesis submitted in fulfillment of the requirements
for the degree of Doctor of Natural Sciences

to the

Combined Faculty of Natural Sciences and Mathematics

Oral examination: April 28, 2021

Dissertation

submitted to the
Combined Faculty of Natural Sciences and Mathematics
of Heidelberg University, Germany
for the degree of

Doctor of Natural Sciences

Put forward by

Stephan Amir Stock
born in Heidelberg, Germany

Oral examination: April 28, 2021

Analysis of High-Precision Spectroscopic Data in Search of Exoplanet Signals Close to the Stellar Noise Limit

Referees: PD Dr. Sabine Reffert
Prof. Dr. Joachim Wambsganß

Stephan Amir Stock

Analysis of High-Precision Spectroscopic Data in Search of Exoplanet Signals Close to the Stellar Noise Limit

Ruprecht-Karls-Universität, April 28, 2021
Reviewers: PD Dr. Sabine Reffert and Prof. Dr. Joachim Wambsganß
Supervisors: PD Dr. Sabine Reffert and Prof. Dr. Andreas Quirrenbach

Ruprecht-Karls-Universität
Extrasolar Planet Research Group
Landessternwarte Königstuhl
Zentrum für Astronomie
Königstuhl 12
69117 Heidelberg

Abstract

Due to their low mass and low temperature, M-dwarf stars are promising targets for the detection of planets in the host star's temperate zone with the radial velocity (RV) method. However, M dwarfs typically exhibit stellar activity, producing noise in the RV data which can mask the signals from existing planets or, as well as aliasing caused by data sampling, can lead to false candidates or to wrongly determined planetary parameters. I present RV analyses for four M dwarfs with the aim of detecting and characterizing potential planetary signals. To overcome the aliasing problems, I developed the public tool `AliasFinder`, which is an improvement of an already known method for distinguishing aliases from actual signals. For the disentanglement of stellar activity and planetary signals, and for their modeling, I used current state-of-the-art analysis techniques, e.g., Bayesian statistics and Gaussian process (GP) regression. The properties and the performance of GP models have been investigated and tested on simulated RV data of active M dwarfs. These GP models, along with additional data taken by CARMENES, have resulted in improved planetary parameters for four previously known planets (the multiplanetary system YZ Ceti and the single-planet system of Lalande 21185) and two new planet discoveries (the temperate super-Earth GJ 251 b and the warm super-Earth HD 238090 b). The analyses, results, and partially unique approaches in this thesis demonstrate that it is possible to detect and model planetary RV signals at the limit of the stellar astrophysical noise by applying rigorous statistical models, along with prior information from auxiliary data and further simulations.

Zusammenfassung

Aufgrund ihrer geringen Masse und niedrigen Temperatur sind M-Zwergsterne aussichtsreiche Ziele, um mit der Radialgeschwindigkeitsmethode (RV-Methode) Planeten in der gemäßigten Zone ihres Zentralsterns zu entdecken. Allerdings zeigen M-Zwerge sehr oft stellare Aktivität, was Störungen in den RV-Daten erzeugt. Dieses stellare Rauschen kann die Signale von existierenden Planeten überdecken oder, ebenso wie Alias-Effekte (die durch zeitliche Muster in der Datenerfassung entstehen), zu falschen Kandidaten oder falsch bestimmten Planetenparametern führen. Ich stelle die RV-Analysen für vier M-Zwerge vor, mit dem Ziel, potenziell vorhandene Planeten-Signale zu entdecken und zu charakterisieren. Um die Alias-Probleme zu lösen, entwickelte ich das frei verfügbare Programm `AliasFinder`, das eine Verbesserung einer bereits bekannten Methode zur Unterscheidung von Alias- und tatsächlichen Signalen darstellt. Zur Unterscheidung von stellarer Aktivität und Planetensignalen sowie deren Modellierung nutzte ich moderne Analyseverfahren, wie z.B. bayessche Statistik und Gaußprozess-Regression. Die Eigenschaften und das Verhalten der Gaußprozessmodelle habe ich untersucht und an simulierten RV-Daten aktiver M-Zwerge getestet. Diese Gaußprozessmodelle haben zusammen mit zusätzlichen Daten, die von CARMENES aufgenommen wurden, zu verbesserten Planetenparametern für vier bisher bekannte Planeten (das Mehrfach-Planetensystem YZ Ceti und das Einfach-Planetensystem von Lalande 21185) und zu zwei neuen Planetenentdeckungen (der gemäßigten Super-Erde GJ 251 b und der warmen Super-Erde HD 238090 b) geführt. Die Analysen und Ergebnisse dieser Arbeit sowie die darin verwendeten teilweise einzigartigen Ansätze zeigen, dass es möglich ist, planetare RV-Signale an der Grenze zum stellaren astrophysikalischen Rauschen zu entdecken und zu modellieren, indem man präzise statistische Modelle, Erkenntnisse aus zusätzlich verfügbaren Daten und weiterführende Simulationen miteinander kombiniert.

Acknowledgements

Countless people have supported me during the last three and a half years of my PhD, and I would like to thank all of them herewith, even though I cannot list them all individually.

The first person I would like to thank is my supervisor, PD Dr. Sabine Reffert, who supported me not only during the doctoral period but also already during my master thesis. The scientific discussions I had with her were always constructive and helpful, in particular they led me to further develop some scientific ideas and approaches that played a major role in solving numerous problems. I would like to thank her for the opportunity to come to her office and ask questions at any time! I am also grateful to her for allowing me to pursue my scientific interests as much as possible during my time at the Landessternwarte and for never pressuring me.

Furthermore, I would like to thank my second supervisor, Prof. Dr. Andreas Quirrenbach, Director of the Landessternwarte Königstuhl (LSW). Through his expertise, discussions with him were always a good source of inspiration for solving any kind of problems that arose during my research. I am also grateful to him for agreeing to be one of the four examiners for my disputation.

A big thank you also goes to my third supervisor, Dr. Martin Kürster from the Max Planck Institute for Astronomy (MPIA), for the discussions we had on various occasions. I would also like to thank Prof. Dr. Joachim Wambsganß, who agreed to be the second examiner for this work, and Prof. Dr. Björn Malte Schäfer for his willingness to be the fourth examiner.

Many thanks also to my great and always helpful colleague Dr. Trifon Trifonov from MPIA, who was an unofficial fourth supervisor for me, for all the discussions I could have with him about science in general and about dynamics in particular! I was able to learn a lot from his expertise in dynamics and radial velocity modeling, and his software, `EXOSTRIKER`, made my work much easier in some areas. Not only have we collaborated on many publications, I also have to thank him for the fact that I was able to observe twice with the HARPS spectrograph at La Silla Observatory in Chile. I will never forget this great opportunity, which actually every PhD student should get! Thank you for these unforgettable experiences and for your support during this time!

I would like to thank all my colleagues and the staff at LSW and MPIA. A special thanks also goes to my colleague (and former fellow student) Jonas Kemmer, with whom I was able to spend countless hours discussing science, either in his office or mine (or via Zoom and Slack during the Covid 19 pandemic)! These discussions were extremely helpful for a deeper understanding of many things. Most of the time, his office mate, Dr. Adrian Kaminski, whom I would also like to thank in this way, also participated in these discussions. I would also like to thank the following people for the scientific discussions I had with them and for their support: Dr. Stefan Brems, Dr. Marcelo Tala Pinto, Dr. Steffi Yen, Sepideh Sadegi, Vera Wolthoff, Paul Heeren, Phillip Hottinger, Diana Kossakowski, Dr. Nestor Espinoza, Dr. Man Hoi Lee, Dr. Rob Harris and many more.

The fact that this work is readable is also a credit to my proofreaders. I would especially like to thank my wife and colleague Katja Stock, as she read my work twice from cover to cover. I would also like to thank Dr. Uwe Reichert, Jonas Kemmer, Jan Kohlmüller and Diana Kossakowski, who also read large parts of my work and had many helpful suggestions at hand. Finally, I would also like to thank Dr. Trifon Trifonov and Dr. Adrian Kaminski for reading the dynamics part, and the instrument part of the paper, respectively.

Many thanks also to all my friends who have accompanied me on my life's journey, especially Jan Kohlmüller, who always stood by my side and was always there for me! Furthermore, I would like to thank my former physics and math teacher, Mrs. Hassenpflug, who fueled my scientific enthusiasm, especially for astronomy, with her commitment, e.g. in "Schüler experimentieren" and "Jugend forscht".

Apart from my friends and colleagues, I would also like to thank my family, e.g. my late great uncle Dr. Mansour, who always supported my education. I also thank my grandparents and uncles and aunts for their support, as well as my parents-in-law.

But in particular, the support from my wife, Katja Stock, has been huge, especially in the last few months. She has supported me emotionally throughout the PhD, which was not always easy, especially since large parts of this thesis had to be written at home during the nationwide lockdown due to the Covid 19 pandemic. She had to do almost all of the housekeeping during that time. Thank you for all your support! I love you!

I would also like to thank my mother, who has always encouraged me. Her support and love have brought me to where I am now. I know that she will be very proud once I have handed in this thesis and passed the defense, just as my father would have been, but unfortunately he passed away far too early and will not be able to witness this day.

Danksagung

Unzählige Leute haben mich während der letzten dreieinhalb Jahre meiner Doktorarbeit unterstützt, denen ich hiermit allen danken möchte, auch wenn ich nicht alle einzeln aufzählen kann.

Die erste Person, der ich ganz besonders danken möchte, ist meine Betreuerin, PD Dr. Sabine Reffert, die mich nicht nur während der Doktorzeit, sondern auch bereits in meiner Masterarbeit unterstützt hat. Die wissenschaftlichen Diskussionen, die ich mit ihr geführt habe, waren stets konstruktiv und hilfreich, insbesondere haben sie dazu geführt, dass ich einige wissenschaftlichen Ideen und Ansätze weiterentwickeln konnte, die bei der Lösung zahlreicher Probleme eine große Rolle spielten. Ich möchte ihr für die Möglichkeit danken, jederzeit zu ihr ins Büro kommen und Fragen stellen zu können! Außerdem bin ich ihr dafür dankbar, dass ich während meiner Zeit an der Landessternwarte meine wissenschaftlichen Interessen so weit wie möglich ausleben konnte und nie unter Druck gesetzt wurde.

Des Weiteren möchte ich meinem zweiten Betreuer, Prof. Dr. Andreas Quirrenbach, Direktor der Landessternwarte Königstuhl (LSW), danken. Durch seine Fachkenntnisse waren Diskussionen mit ihm immer eine gute Inspirationsquelle für die Lösung jeglicher Art von Problemen, die während meiner Forschung aufgetreten sind. Ich bin ihm außerdem dankbar dafür, dass er sich bereit erklärt hat, einer der vier Prüfer für meine Disputation zu sein.

Ein großes Dankeschön geht auch an meinen Drittbetreuer, Dr. Martin Kürster vom Max-Planck-Institut für Astronomie (MPIA), für die Diskussionen, die wir bei verschiedenen Gelegenheiten geführt haben. Außerdem möchte ich Prof. Dr. Joachim Wambsganß danken, der sich bereit erklärt hat, der Zweitprüfer für diese Arbeit zu sein, sowie Prof. Dr. Björn Malte Schäfer für seine Bereitschaft, der vierte Prüfer zu sein.

Herzlichen Dank auch an meinen großartigen und stets hilfsbereiten Kollegen Dr. Trifon Trifonov vom MPIA, der für mich ein inoffizieller vierter Betreuer war, für all die Diskussionen, die ich mit ihm über Wissenschaft im Allgemeinen und über Dynamik im Speziellen führen konnte! Von seinem Fachwissen über Dynamik und Radialgeschwindigkeits-Modellierung konnte ich viel lernen, und seine Software, der `EXOSTRIKER`, hat meine Arbeit in manchen Bereichen deutlich vereinfacht. Wir haben nicht nur in vielen Veröffentlichungen zusammengearbeitet,

ich habe ihm auch zu verdanken, dass ich zweimal mit dem HARPS Spektrografen am La Silla-Observatorium in Chile beobachten konnte. Ich werde diese großartige Möglichkeit, die eigentlich jeder Doktorand bekommen sollte, nie vergessen! Danke für diese unvergesslichen Erfahrungen und für deine Unterstützung in dieser Zeit!

Ich möchte all meinen Kollegen und den Mitarbeitern an der LSW und dem MPIA danken. Ein besonderes Dankeschön auch an meinen Kollegen (und ehemaligen Kommilitonen) Jonas Kemmer, mit dem ich unzählige Stunden über Wissenschaft diskutieren konnte, entweder in seinem oder meinem Büro (oder über Zoom und Slack während der Covid-19-Pandemie)! Diese Diskussionen waren extrem hilfreich für ein tiefergehendes Verständnis vieler Dinge. Meistens nahm auch sein Bürokollege, Dr. Adrian Kaminski, dem ich ebenfalls auf diesem Weg danken möchte, an diesen Diskussionen teil. Außerdem möchte ich bei folgenden Personen für die wissenschaftlichen Diskussionen, die ich mit ihnen geführt habe, und für ihre Unterstützung bedanken: Dr. Stefan Brems, Dr. Marcelo Tala Pinto, Dr. Steffi Yen, Sepideh Sadegi, Vera Wolthoff, Paul Heeren, Phillip Hottinger, Diana Kossakowski, Dr. Nestor Espinoza, Dr. Man Hoi Lee, Dr. Rob Harris und viele mehr.

Dass diese Arbeit lesbar ist, ist auch ein Verdienst meiner Korrektoren. Ganz besonders danken möchte ich meiner Frau und Kollegin Katja Stock, da sie meine Arbeit zweimal von vorne bis hinten gelesen hat. Außerdem möchte ich Dr. Uwe Reichert, Jonas Kemmer, Jan Kohlmüller und Diana Kossakowski danken, die ebenfalls große Teile meiner Arbeit gelesen haben und viele hilfreiche Vorschläge parat hatten. Letztlich möchte ich auch Dr. Trifon Trifonov und Dr. Adrian Kaminski dafür danken, dass sie den Dynamik-, bzw. den Instrumenten-Teil der Arbeit gelesen haben.

Herzlichen Dank auch an alle meine Freunde, die mich auf meinem Lebensweg begleitet haben, besonders Jan Kohlmüller, der mir stets zur Seite stand und immer für mich da war! Weiterhin danke ich meiner ehemaligen Physik- und Mathelehrerin, Frau Hassenpflug, welche mit ihrem Engagement, z.B. bei „Schüler experimentieren“ und „Jugend forscht“ meine wissenschaftliche Begeisterung, insbesondere auch für die Astronomie, befeuert hat.

Abgesehen von meinen Freunden und Kollegen möchte ich natürlich auch meiner Familie danken, z.b. meinem verstorbenen Großonkel Dr. Mansour, der meine Bildung stets gefördert hat. Auch danke ich meinen Großeltern sowie Onkeln und Tanten für ihre Unterstützung, ebenso wie meinen Schwiegereltern.

Insbesondere aber die Unterstützung durch meine Frau, Katja Stock, war, vor allem in den letzten Monaten, riesig. Sie hat mich während der gesamten Doktorzeit emotional unterstützt, was nicht immer einfach war, besonders da große Teile dieser Arbeit während des landesweiten Lockdowns

infolge der Covid-19-Pandemie zuhause geschrieben werden mussten. Sie hat mir in dieser Zeit im Haushalt immer den Rücken freigehalten. Danke für all deine Unterstützung! Ich liebe dich!

Ich möchte auch meiner Mutter danken, die mich immer gefördert hat. Ihre Unterstützung und Liebe haben mich dahin gebracht, wo ich jetzt bin. Ich weiß, dass sie sehr stolz sein wird, sobald ich diese Arbeit abgegeben und die Disputation bestanden habe, genauso wie mein Vater es gewesen wäre, der aber leider viel zu früh verstorben ist und diesen Tag leider nicht mehr miterleben kann.

Contents

1 Introduction **1**

1.1 Exoplanets . . . 1

1.1.1 The long way . . . 1

1.1.2 Outline and purpose of this thesis . . . 4

1.1.3 Definition of (exo)planets . . . 6

1.1.4 Exoplanet detection methods . . . 8

1.1.5 Exoplanet distribution and properties . . . 23

1.1.6 Multiplanetary systems . . . 28

1.2 Host stars . . . 34

1.2.1 The radial velocity method for different types of host stars . . . 35

1.2.2 Stellar activity . . . 37

2 The radial velocity method **45**

2.1 Radial velocity techniques . . . 45

2.1.1 Radial velocity precision . . . 45

2.1.2 Gas cell techniques . . . 46

2.1.3 CARMENES as an example for the simultanous reference technique . . . 47

2.1.4 Difficulties and limitations . . . 52

2.2 Statistics and modeling of radial velocity data . . . 53

2.2.1 Modeling of orbital parameters . . . 53

2.2.2 Bayesian methods for the radial velocity analysis . . . 56

2.2.3 Posterior sampling . . . 64

2.2.4 Radial velocity modeling within this thesis . . . 68

3 Gaussian processes for radial velocity modeling **73**

3.1 Motivation . . . 73

3.2 Basics for Gaussian Processes . . . 74

3.2.1 The univariate Gaussian distribution . . . 74

3.2.2 The multivariate Gaussian distribution . . . 76

3.2.3 Marginalization and conditioning . . . 76
3.3 Gaussian processes . . . 78
3.3.1 Definition . . . 78
3.3.2 Kernels, hyperparameters, and predictions . . . 80
3.3.3 Controversial aspects of GPs . . . 82
3.4 The quasi-periodic kernel for radial velocity data . . . 85
3.4.1 GP kernel and hyperparameters . . . 85
3.4.2 Physical motivation . . . 85
3.4.3 Physically motivated hyperparameter priors . . . 87
3.5 Investigations on quasi-periodic Gaussian processes . . . 88
3.5.1 Goals and assumptions of this analysis . . . 88
3.5.2 Derivation of stellar activity properties by the QP-GP . . . 92
3.5.3 Absorption of planetary signals by quasi-periodic Gaussian processes . 103
3.5.4 Model comparison in a Bayesian framework: Keplerian model vs. QP-GP model . . . 108
3.5.5 Investigations on planetary parameters . . . 114

4 `AliasFinder`: A tool to de-alias radial velocity data 121
4.1 Introduction . . . 121
4.1.1 Motivation . . . 121
4.1.2 Fourier transform . . . 122
4.1.3 Evenly sampled data and the spectral window function . . . 123
4.1.4 Periodograms and unevenly sampled data . . . 125
4.1.5 Aliasing in the case of irregularly sampled data . . . 126
4.2 `AliasFinder` . . . 128
4.2.1 The conceptual basis of `AliasFinder` . . . 128
4.2.2 `AliasFinder` as a tool . . . 129

5 Characterization of the nearby ultra-compact multi-planetary system YZ Ceti 131
5.1 Motivation . . . 131
5.2 Data . . . 133
5.2.1 CARMENES . . . 133
5.2.2 HARPS . . . 133
5.2.3 Photometry . . . 134
5.3 Properties of YZ Ceti . . . 137
5.3.1 Basic physical parameters . . . 137
5.3.2 Photometric analysis . . . 137

5.3.3 Spectroscopic activity indicators . . . 141
5.4 YZ Ceti planetary system . . . 143
5.4.1 Search for planetary signals . . . 143
5.4.2 Configuration of the system . . . 147
5.5 Simultaneous fitting of stellar activity and Keplerians . . . 152
5.5.1 Transit search with *TESS* . . . 158
5.5.2 *N*-body integrations . . . 159
5.6 Discussion and conclusions . . . 163

6 Three temperate to warm super-Earths 167
6.1 Motivation . . . 167
6.2 Data . . . 169
6.2.1 High-resolution spectroscopy . . . 169
6.2.2 Photometry . . . 171
6.3 Methods . . . 173
6.3.1 Periodograms . . . 173
6.3.2 Modeling of RV and photometric data . . . 173
6.3.3 De-aliasing . . . 176
6.4 Stellar properties . . . 177
6.5 GJ 251 . . . 178
6.5.1 Photometric monitoring . . . 178
6.5.2 Spectroscopic activity indicators . . . 180
6.5.3 Periodogram analysis and RV modeling . . . 182
6.5.4 A second planet in the system? . . . 185
6.5.5 Simultaneous Keplerian and GP modeling . . . 187
6.5.6 Transit search and analysis with *TESS* . . . 193
6.6 HD 238090 . . . 195
6.6.1 Photometric monitoring . . . 195
6.6.2 Spectroscopic activity indicators . . . 196
6.6.3 Periodogram analysis . . . 199
6.6.4 RV modeling . . . 199
6.6.5 Transit search with TESS . . . 204
6.7 Lalande 21185 . . . 205
6.7.1 Photometry and spectroscopic activity indicators. . . . 205
6.7.2 Periodogram analysis . . . 207
6.7.3 RV modeling with CARMENES and SOPHIE . . . 212

6.7.4 HIRES RV data . . . 215
6.7.5 Transit search with TESS . . . 215
6.8 Discussion . . . 216
6.8.1 GJ 251 . . . 216
6.8.2 HD 238090 . . . 217
6.8.3 Lalande 21185 . . . 218
6.8.4 Formation scenario . . . 218
6.9 Summary . . . 219

7 Discussion and Conclusion **221**

Bibliography of own publications **235**

Bibliography **237**

List of Abbreviations **253**

A Appendix for Chapter 5 **257**
A.1 RV data . . . 257
A.2 Cornerplot of stable solutions . . . 257
A.3 Additional table . . . 259
A.4 α_{GP}-vs.-P_{GP} diagram of the photometry . . . 261

B Appendix for Chapter 6 **263**
B.1 Priors for `juliet` . . . 263
B.2 Corner plots . . . 266
B.3 `AliasFinder` plot of HD 238090 . . . 272

Declaration **277**

1 Introduction

> *In some worlds there is no Sun and Moon, in others they are larger than in our world, and in others more numerous. In some parts there are more worlds, in others fewer (...); in some parts they are arising, in others failing. There are some worlds devoid of living creatures or plants or any moisture.*
>
> — **Democritus**
> (460-370 B.C.)

> *There are infinite worlds both like and unlike this world of ours. For the atoms being infinite in number, as was already proven, (...) there nowhere exists an obstacle to the infinite number of worlds.*
>
> — **Epicurus**
> (341-270 B.C.)

> *This space we declare to be infinite... In it are an infinity of worlds of the same kind as our own.*
>
> — **Giordano Bruno**
> (1548-1600)

1.1 Exoplanets

1.1.1 The long way

The three quotes mentioned on this page date back up to 2400 years and show how humanity has speculated since ancient times that other worlds like our own might exist. Although there

has been a widespread belief in modern-times society that planets are probably not limited to our Solar System, there has been no scientific evidence to support this assumption because until a few years ago, the necessary detection techniques were not sufficiently developed. During the 19th and 20th centuries, some detections of planets orbiting stars other than our Sun were claimed. These putative discoveries of extrasolar planets, or abbreviated exoplanets, included, for example, 70 Ophiuchi (Jacob 1855; See 1896) and Barnard's star (van de Kamp 1963), as well as Lalande 21185 (van de Kamp & Lippincott 1951), a star which I also address in this thesis. However, none of these claims could be confirmed; some of them were even refuted.

Nevertheless, these claims resulted from a rapidly evolving scientific community searching for such potential planets and the growing technical capabilities of astronomical instruments in the 19th and 20th centuries finally led to the detection of exoplanets. It was not until the end of the 20th century that the first two extrasolar planets were finally discovered around the pulsar PSR 1257+12 (Wolszczan & Frail 1992). After this first unusual discovery of a multi-planetary system around a pulsar (a neutron star, a possible remnant of a supernova explosion of a star more massive than 8 $M_\odot$), many more followed. By January 2021, more than 4,300 exoplanets have been confirmed[1], and each one has provided us with new insights into planetary science.

Figure 1.1 shows a histogram of confirmed planet discoveries, binned to their year of discovery. A fit of a simple exponential model is overplotted and extrapolated to the year 2030 to make an order of magnitude estimation of future detections. With the model, about 90,000 detected exoplanets can be expected by the end of the year 2030, more than twenty times the current number of confirmed planets. Even though such a large number of detections seem very optimistic, surveys like *Gaia* (Gaia Collaboration et al. 2018) and *PLATO* (Rauer et al. 2014), as well as new data reduction techniques based on machine learning and neural networks, will help to reach such a high number of detections. For example, the highly awaited second part of *Gaia* DR3 and following *Gaia* data releases will potentially allow the detection of several tens of thousands of exoplanets based on precise astrometric measurements (Perryman et al. 2014). All these current and future exoplanet detections will help understand planet formation and exoplanet properties.

Some of the exoplanet discoveries already forced astronomers and physicists to reconsider previous ideas about possible occurrences and architectures of planets around stars. In this line of unusual detections falls the first detected exoplanet around a main-sequence star, which was discovered in 1995 by Mayor & Queloz (1995) around the Sun-like star 51 Pegasi. This giant planet, called 51 Pegasi b, orbits its host star at only ~ 0.05 au with a period of ~ 4.2 d, a configuration quite different compared to giant planets in our Solar System and not expected at

[1] https://exoplanetarchive.ipac.caltech.edu/index.html

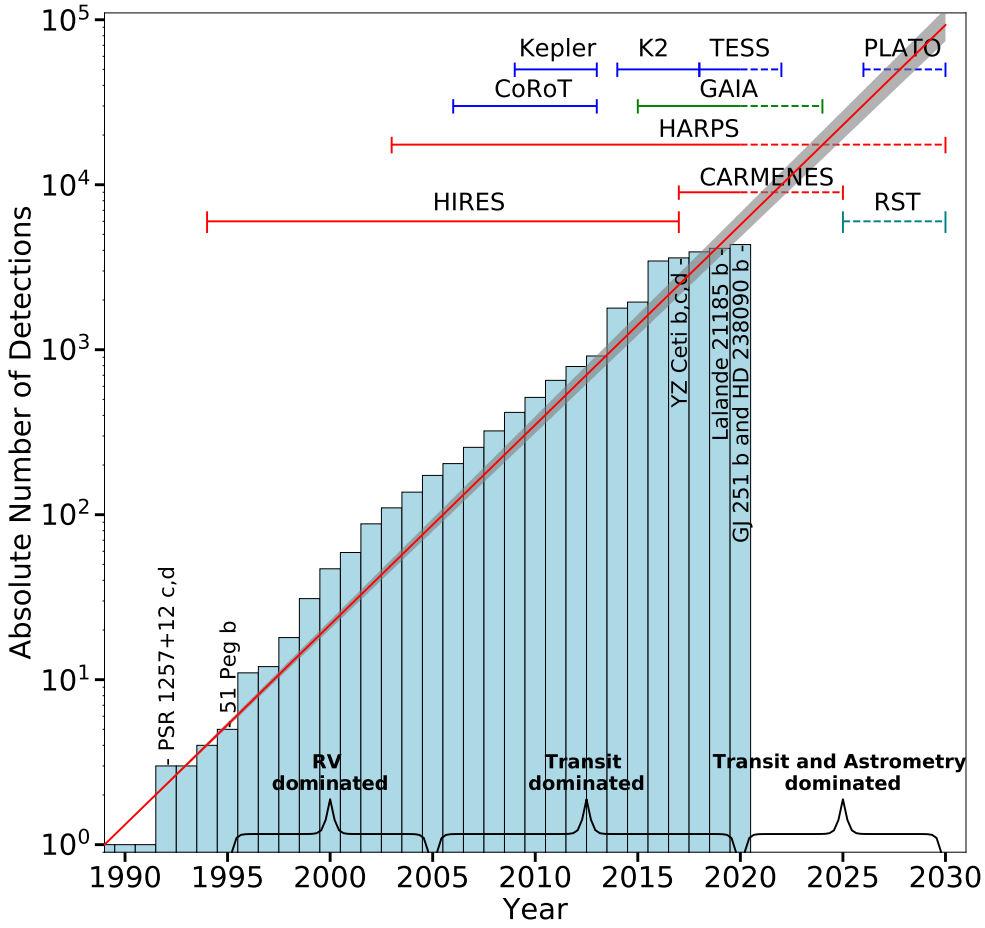


Fig. 1.1.: Cumulative histogram of exoplanet detections binned to the discovery year. An approximated exponential model and its 3σ uncertainties are plotted as the red line and its surrounding gray area. The model is extrapolated to the next decade. A subjective number of different exoplanet detection instruments and their lifetime is provided as the line plots in the upper part of the diagram, color-coded with the detection method, where red is radial velocity, blue is transit photometry, green astrometry, and teal microlensing. Interesting exoplanets in the author's eye or exoplanets used in this thesis are named in their discovery year's histogram bin. *Credit:* The data for this plot have been obtained from the NASA Exoplanet Archive in February 2021.

the time of its detection. 51 Pegasi b was detected by the radial velocity (RV) method, which is by now the second most successful method in terms of numbers of detections and the primary detection method used within this thesis. Many more planetary companions similar to 51 Pegasi b

were found afterward. These objects form the class of hot Jupiters. Results show that, on average, 1% of nearby solar-like stars (spectral types F, G, and K) are orbited by such hot Jovian-mass planets (Wright et al. 2012).

The attentive reader might have noticed the discrepancy between the year of the first planet discovery listed in Fig. 1.1 and the planets discussed so far within the text as the first exoplanet detections. The NASA Exoplanet Archive includes a substellar companion around HD 114762 discovered by Latham et al. (1989) using the RV method. This companion has an estimated minimum mass of $11.5 \pm 1\,M_J$ (Jovian masses), which is inside the regime of giant planets, but since the inclination of the system was unknown, the mass could not be estimated by the RV method. Later analyses based on *Gaia* data showed that the companion mass is well above that of a giant planet and lies inside the regime of a brown dwarf or even red dwarf (Kiefer 2019). This example shows that it is not straightforward to classify a detection as a planet or as a more massive substellar companion. Besides, the host stars' stellar activity can also mimic a planetary signal in the case of the RV and transit detection methods.

Techniques for exoplanet discovery and analysis have evolved in recent decades. Hence, a reanalysis of some of the confirmed planets listed in the NASA Exoplanet Archive, e.g., by applying some of the tools used within this thesis, might lead to the conclusion that the putative planet signal was not caused by a planet but by another source or effect. Two examples of heavily discussed or rejected RV planet detections are GJ 581 b and g (see, for example, Vogt et al. 2010; Andrae et al. 2010; Robertson et al. 2014; Anglada-Escudé & Tuomi 2015) or Aldebaran b (Hatzes et al. 2015, 2018; Reichert et al. 2019). Therefore, reanalyses and further characterizations of known systems are essential.

Additionally, some of the confirmed planets might orbit their host star with a different orbital period than the published one, e.g., 55 Cnc e (Fischer et al. 2008; Dawson & Fabrycky 2010) or YZ Ceti b (Astudillo-Defru et al. 2017; Stock et al. 2020b); the latter one being the least massive planet found with the RV method thus far and also discussed within this thesis. While it can be expected to have some erroneous or doubtful detections within the exoplanet sample, the largest fraction of the sample should not be significantly affected.

1.1.2 Outline and purpose of this thesis

The purpose of this thesis is to show that with good statistical models, prior information from auxiliary data and additional simulations, one can recover and model planetary signals that are on the order of the noise or even slightly weaker.

In the following section in this introduction, I will define (exo)planets using physical conditions. I will then outline the different methods to detect exoplanets and give a small overview of the statistical distribution of the currently detected sample of exoplanets and some implications that arise as a result. The multiplicity of planets is a special aspect, which is discussed after that in Sec. 1.1.6. To detect and refine exoplanets, it is beneficial to have a good understanding of the exoplanets host star whose basic properties and influence on the detections, in particular regarding RV and transit surveys, I discuss in Sec. 1.2. In that section I will mostly focus on M-dwarf stars, which are the prime targets of this work.

All the detections and most investigations in this thesis rely on the precise RV method and its modeling. I will therefore elaborate on the RV technique in much more detail in Sec. 2. In the first part of that section, different techniques used to measure RVs are outlined with a particular focus on the CARMENES instrument, the simultaneous calibration technique, and the extraction of the RVs. The RV method's difficulties and limitations are discussed after that, and a large part of the section is then about applying meaningful physical models to measured RV variations, which includes variations due to instrumental and astrophysical noise.

A recent and promising approach within the RV community to account for such astrophysical noise contributions within RV data are Gaussian Process (GP) regression models, which I discuss in Chapter 3. I will illustrate what GPs are and how they behave by using an easy to understand semi-mathematical approach before I focus on the practical applications of such models on RV and photometric data. I then simulate some RV systems and try to recover the properties of simulated planetary companions and stellar activity by simultaneously fitting these signals with Keplerian and GP models. These results are of particular interest regarding the refinement of the planetary parameters when a GP is used in the chapters following this one.

As mentioned, some planets detected by the RV method might orbit at periods different from those published in the discovery paper due to the detected planetary signals' sampling pattern. Aliasing of sampled signals is a problem which has already led to incorrectly published planetary periods (see, for example, Dawson & Fabrycky 2010). Chapter 4 introduces `AliasFinder`, a self-developed software that uses periodogram simulations to distinguish between the true underlying signal and its aliases. In Chapter 5, GPs and `AliasFinder` were applied to the real ultra-compact multi-planetary system YZ Ceti in order to derive the precise orbital properties of the planets within that system. YZ Ceti consists of three detected terrestrial planets for which strong aliasing and stellar noise were major problems that needed to be overcome. Additionally, a dynamical N-body analysis of that system has been performed and dynamical constraints have been set to its orbital parameters. Chapter 6 will then focus on the detection of three super-Earth planets in three systems, GJ 251 b, HD 238090 b, and Lalande 21185 b, whose radial velocity

signals are close to the stellar noise of their host star. For HD 238090 b and Lalande 21185 b, aliasing was a problem, as well. Chapter 7 then discusses additional and future prospects and serves as a conclusion of this thesis.

1.1.3 Definition of (exo)planets

As mentioned in the former section, the classification of an object as exoplanet is sometimes not straightforward. Such ambiguities in classification exist even among objects in our Solar System. For 76 years the Solar-System object Pluto had been classified as a planet, until the IAU (International Astronomical Union) downgraded the object to a dwarf planet in August 2006[2]. This decision was based on resolution B5 which defines a planet of our Solar System to follow three criteria (excerpt from the resolution):

"*A Planet is a celestial body which*

- *is in orbit around the Sun,*
- *has sufficient mass for its self-gravity to overcome rigid body forces so that it assumes a hydrostatic equilibrium (nearly round) shape, and*
- *has cleared the neighborhood around its orbit.*"

As there are many other objects with sizes and orbits similar to Pluto around our Sun (Kuiper belt objects, and so-called "Trans-Neptunian Objects"), the third point was not fulfilled by Pluto, which is the reason it was downgraded to a dwarf planet.

"*A dwarf planet is a celestial body that*

- *is in orbit around the Sun,*
- *has sufficient mass for its self-gravity to overcome rigid body forces so that it assumes a hydrostatic equilibrium (nearly round) shape,*
- *has not cleared the neighborhood around its orbit, and*
- *is not a satellite.*"

[2] https://www.iau.org/static/resolutions/Resolution_GA26-5-6.pdf

The above definitions are used for our Solar System but can also be applied to exoplanets, although with current techniques, it can be difficult to determine if an exoplanet has cleared its orbit of other objects. As written in 2006, the IAU definition provides a rule for the lower mass limit of exoplanets.

In 2003 the IAU recommended a working definition (which could be subject to change in the future) for the upper mass limit of exoplanets (Boss et al. 2007). The rules can be summarized as follows:

- Objects below the limit of thermonuclear fusion of deuterium (calculated to be at $\sim 13\,M_J$ for solar metallicity) and which orbit stars or stellar remnants are planets.
- Objects with masses that allow thermonuclear fusion of deuterium but whose masses are below the mass required for thermonuclear fusion of hydrogen are defined as brown dwarfs.
- Objects below the limit of thermonuclear fusion of deuterium which do not orbit stars are so-called sub-brown dwarfs.

Within the exoplanet community, several additional sub-classifications have been proposed and established. These are based on specific properties, e.g., mass, period, composition. Within this thesis, I use the following definitions, which are by far not exhaustive but represent a widely accepted classification scheme of non-stellar companions used within the (RV) exoplanet community. However, I note that there is no strict definition, and depending on the author or study there might be differences to the classifications shown below.

Terrestrial Planets This definition is based on composition. Terrestrial planets are planets with rocky composition, e.g., silicate rocks or metals. Earth and Mars are prototypes in our Solar System. Masses of terrestrial planets are generally believed to be below a few Earth masses.

Super-Earths/mini-Neptunes This definition is based on mass and composition. Super-Earth planets are planets with a density consistent with a rocky composition and with masses from $2\,M_\oplus$ to $10\,M_\oplus$. Mini-Neptunes are gaseous planets with masses from $2\,M_\oplus$ to $10\,M_\oplus$. By measuring the mass and radius of a planet by complementing observations of radial velocity and transit photometry it is possible to derive an estimate of the density. Our Solar System does not host any super-Earth or mini-Neptune.

Neptunes This definition is based on mass and composition. Neptunes are planets with masses and composition similar to that of Neptune ($17\,M_\oplus$) and Uranus ($14.5\,M_\oplus$) in our Solar System.

Giant planets This definition is based on mass. Giant planets are massive planets with masses similar to Saturn ($95\,M_\oplus$), Jupiter ($318\,M_\oplus = 1\,M_J$) or higher, up to the deuterium burning limit of $13\,M_J$. Thus far, most planet formation models and all currently detected planets indicate that all giant planets are gas giants.

Hot Jupiters This definition is based on the mass and the orbital regime. Hot Jupiters are giant planets with short orbital periods, typically less than ten days, resulting in a very high stellar insolation and hot surface temperatures. The first-ever detected exoplanet around a main-sequence star is classified as a hot Jupiter. Many hot Jupiters show signs of atmospheric loss due to the high insolation.

Cold Jupiters This definition is based on the mass and the orbital regime. Cold Jupiters are giant planets in wide orbits around their host stars, often residing beyond the snow line where they initially are thought to form. Saturn and Jupiter are Solar System examples.

1.1.4 Exoplanet detection methods

The detection of exoplanets is a scientific achievement of humanity which has only recently become possible. The small angular separation and the contrast ratio between the exoplanet and its host star make it difficult to detect planets directly. Most exoplanet detection methods are indirect techniques. This section provides a fundamental and short overview of some successful techniques that resulted in most current exoplanet detections, with particular focus on Doppler spectroscopy.

Doppler spectroscopy

Doppler spectroscopy, also known as the RV method, is an indirect method for detecting exoplanets. If the observed star has a companion, then both objects orbit their common center of mass, which from the terrestrial observer's point of view leads to a periodic change in the position and radial velocity of the star in the line of sight. This line-of-sight movement of the star results in a Doppler shift of the emitted stellar light which then allows to derive the RV of the object.

Doppler spectroscopy in general has a history dating back more than 100 years (Huggins 1868), and binary stars were regularly detected and characterized using this method in the 20th-century (Christie & Wilson 1938). Technical and scientific achievements in the last decade of the 20th-century allowed the technique to become sensitive enough to detect exoplanets — a prediction that was already made in 1952 by Struve (1952). In this subsection, I will elaborate on the basic physical principles of the RV method and discuss some vital scientific results obtained with it. As the RV method is the method mainly used within this work, I will provide further details and discussion in Sec. 2.

The measurement of the RV with Doppler spectroscopy is based on the principle of the Doppler shift of electromagnetic waves. The Doppler shift of an emitted frequency f to the received frequency f' can be calculated by

$$f' = f\frac{\sqrt{1-\beta^2}}{1-\beta\cos\Theta}, \tag{1.1}$$

which includes the Lorentz factor $\beta = v/c$ and an angle Θ between the velocity vector of the source and the receiver. For the RV method, this angle is either zero or π resulting to $\cos\Theta = \pm 1$. In most cases (and in all cases within this work), the relativistic effects can be neglected, since the velocity of the host star's motion or any other effects are non-relativistic ($v << c$). Therefore, one can also write

$$\frac{\Delta f}{f} = \frac{\Delta\lambda}{\lambda} = \pm\frac{v_\mathrm{r}}{c}, \tag{1.2}$$

where λ is the wavelength of the emitted light. From Eq.1.2, one can calculate the RV v_r based on the measured wavelength shift of spectral features in the stellar light. These spectral features are generally caused by the absorption and emission of atoms and molecules in the stellar atmosphere, and one can derive the wavelength shift by comparing the measured stellar features to the equivalent features of a synthetic spectrum based on values measured at a rest frame, e.g., a laboratory. Such RVs, with respect to a synthetic spectrum at rest wavelength, are called "absolute radial velocities" and their accuracies are limited by the quality of the wavelength calibration. RV values are typically of the order of a few $100\,\mathrm{m\,s^{-1}}$ (Chubak et al. 2012; Wright 2018; Lafarga et al. 2020). The RV precision needed for the detection of terrestrial planets must be several orders of magnitude smaller. Such precision can be achieved by using differential RVs, as for the differential values, many systematic uncertainties cancel out. Specific details will be revisited in Sec. 2.

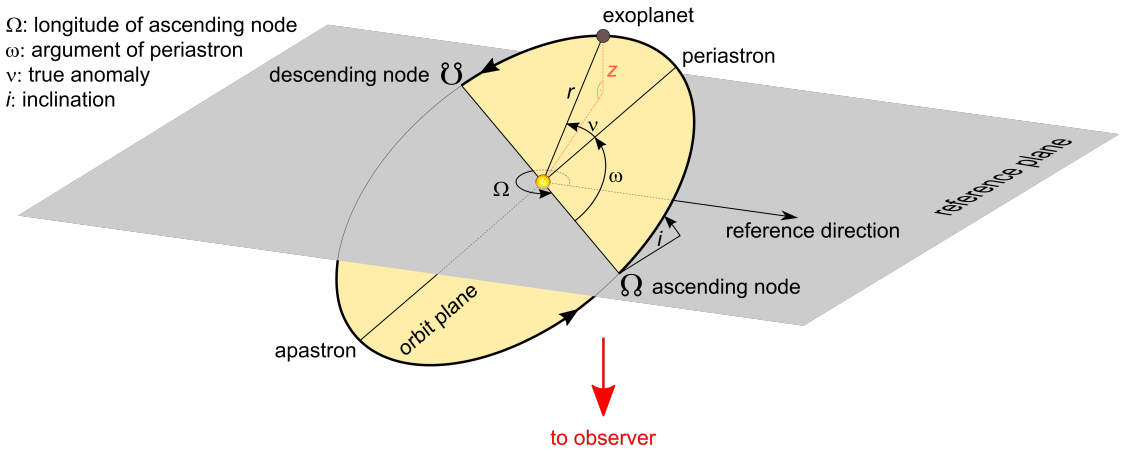


Fig. 1.2.: This figure shows the parameters of an elliptical orbit of an object around the barycenter. *Credit:* Uwe Reichert.

As a large part of this thesis is about modeling RV, it is essential to outline how the RV caused by two masses orbiting each other can be measured. In the following, the RV semi-amplitude is derived using polar coordinates, which simplifies the problem, and the derivation follows the notation of Perryman (2011). Figure 1.2 shows the orbital parameters of an object orbiting the system's center of mass (barycenter), which is located in one of the two foci of the ellipse, according to Kepler's first law. A Keplerian orbit in three dimensions can be described by seven parameters[3]: the semi-major axis a, the eccentricity of the ellipse e, the orbital period P, the time of periastron passage t_p, the inclination i, the longitude of ascending node Ω and the argument of periastron ω. The semi-major axis a and the eccentricity of the ellipse e define the shape of the ellipse. The RV is the line-of-sight movement towards the observer, and it is common to define this direction as the z-axis. From Fig. 1.2 it is straightforward to obtain that

$$z(t) = r(t) \sin i \sin(\omega + \nu), \tag{1.3}$$

with $r = r(t)$ being the distance to the barycenter. In the following, it will be shown how to get from Eq. 1.3 to the solution for the RV towards an observer (Perryman 2011):

$$v_r = K[\cos(\omega + \nu) + e\cos(\omega)], \tag{1.4}$$

[3]Since P and a are connected by Kepler's third law, P is sometimes omitted, since six parameters are sufficient to unambiguously determine a Kepler orbit.

where ν is the true anomaly and K is the RV semi-amplitude of the host star. The absolute orbits of star and planet as well as the relative orbit are in proportion, so that $a_* : a_{\rm pl} : a_{\rm rel} = M_* : m_{\rm pl} : (M_* + m_{\rm pl})$, and the eccentricity and period are the same for the scaled planetary orbit (Perryman 2011). The Keplerian orbital parameter Ω cannot be determined by the RV method and is assumed to be zero, from which it follows that the longitude of periastron ϖ equals the argument of periastron ω, since $\varpi = \omega + \Omega$. This assumption is in particular important for any dynamical RV analysis.

The derivation of Eq. 1.4 from Eq. 1.3 is not trivial, which is why I show a few interim solutions that are not provided by Perryman (2011). Since we are interested in the line-of-sight movement, we need to derive the time derivative of Eq. 1.3 and by using the product rule one derives

$$v_r \equiv \dot{z} = \sin i \Big(\dot{r} \sin(\omega + \nu) + r\dot{\nu} \cos(\omega + \nu) \Big). \tag{1.5}$$

This equation can now be brought into the form given in Eq. 1.4 by substituting r, $\dot{r}$ and $r\dot{\nu}$. It is important to recall that the distance r to one of the foci of an ellipse is given by

$$r = \frac{a(1 - e^2)}{1 + e \cos \nu}. \tag{1.6}$$

Calculating the time derivative of this equation allows to obtain $\dot{r}$, and one can solve for $r\dot{\nu}$ by integrating Kepler's second law $d\mathrm{A}/d\mathrm{t} = A/P = 1/2r^2\dot{\nu}$, where A is the area of an ellipse $A = \pi ab = \pi a^2 \sqrt{1 - e^2}$. With the help of these substitution terms and further trigonometric identities, one can therefore bring Eq. 1.5 into the form:

$$v_r = \frac{2\pi a \sin i}{P \sqrt{1 - e^2}} \Big[\cos(\omega + \nu) + e \cos(\omega) \Big], \tag{1.7}$$

where $\frac{2\pi a \sin i}{P \sqrt{1-e^2}} \equiv K$ is defined as the RV semi-amplitude of the host star.

From Eq. 1.4 and Fig. 1.2 it follows that the RV can have values between $v_{\rm r,max} = K(1 + e \cos(\omega))$ and $v_{\rm r,min} = K(-1 + e \cos(\omega))$, from which it follows that the RV semi-amplitude is $K = (v_{\rm r,max} - v_{\rm r,min})/2$ (Lovis & Fischer 2010; Perryman 2011). Equation 1.7 does not provide a lot of information to an observer, but with substitution of variables, it can be brought into various other

forms, e.g., the RV semi-amplitude in dependence of the host star mass M_* and planet mass $m_{\rm pl}$ is given by

$$K = \frac{(2\pi G/P)^{1/3}}{\sqrt{1-e^2}} \left(\frac{m_{\rm pl}^3 \sin^3 i}{(M_* + m_{\rm pl})^2} \right)^{1/3}, \tag{1.8}$$

where G is the gravitational constant and

$$f(m) = \frac{m_{\rm pl}^3 \sin^3 i}{(M_* + m_{\rm pl})^2} = \frac{K^3 P (1-e^2)^{3/2}}{2\pi G} \tag{1.9}$$

is called the mass function (Wright 2018).

Including Kepler's third law ($P^2 = 4\pi^2 a^3/(GM)$) and transforming to a different set of units, one can also rewrite K to

$$K = \frac{28.433\ \mathrm{m\,s^{-1}}}{\sqrt{1-e^2}} \frac{m_{\rm pl} \sin i}{M_{\rm J}} \left(\frac{m_{\rm pl} + M_*}{M_\odot} \right)^{-2/3} \left(\frac{P}{\rm yr} \right)^{-1/3} \tag{1.10}$$

(Lovis & Fischer 2010).

From the mass function it becomes clear that the planetary mass and the inclination of the system towards the observer are degenerate quantities, and, therefore, the RV method can only provide a lower mass limit of the planetary companion with the assumption that the orbit is viewed face-on ($i = 90°$). However, under the assumption of randomly orientated orbits, one can derive that $\cos i$ is uniformly distributed, from which it follows that 87% of the systems should have an inclination larger than 30°, which implies that, statistically, the planetary mass of 87% of all planets is within a factor of two or smaller regarding the derived minimum mass limit $m_{\rm min} \equiv m \sin i$. Based on a large number of detections, this fact allows to deduce the properties of planets and to classify them. The distribution and some rough classification of confirmed exoplanets (by any method) with known masses or minimum masses are shown in Fig. 1.7.

As already mentioned in Sec. 1.1.1, the RV method was the first method that succeeded in finding an exoplanet around a Sun-like main-sequence star (Mayor & Queloz 1995). After this first detection, a "golden decade" of the RV technique followed. Although the RV method is now superseded by the transit method in terms of the absolute number of planet detections, it remains a valuable method for deriving lower mass limits on planets, and several significant results regarding our understanding of extrasolar planetary systems are due to this method.

υ Andromeda is one of such major discoveries, as it marks the first multiplanetary system detected. υ Andromeda b is a hot Jupiter with a 4.62 d orbital period that was discovered by Butler et al. (1997). Further observations with the spectrograph at Lick observatory and with the Advanced Fiber-Optic Echelle spectrometer (AFOE) at Smithsonian's Whipple Observatory, showed that there are two more planets in the system (Butler et al. 1999). The masses of the planets suggest that they could be dynamically interacting. For some multiplanetary systems as υ Andromeda, or the GJ 876 system (Delfosse et al. 1998), which is another other example, it is warranted to fit the signals with more sophisticated models that take this dynamical interaction into account (see Sec. 1.1.6 and Sec. 2.2.1).

The detection of planets around solar-like stars of spectral class FGK was the main focus in the beginning of the "RV decade", but soon astronomers started to look for planets around other types of stars to better understand planet formation as a function of stellar mass. Some types of stars, like M dwarfs, have other advantages (and disadvantages) when surveyed with the RV method, which will be discussed in Sec. 1.2.1. Here, I name two first-time discoveries regarding such non-solar-like stars: the first planet discovered orbiting a giant star, ι Draconis b, in 2002 by Frink et al. (2002) and the first planet orbiting an M dwarf, GJ 876 b, in 1999 by Delfosse et al. (1998). Soon thereafter, the GJ 876 system was found to be a multiplanetary system (Marcy et al. 1999) and this system is further discussed in Sec. 1.1.6 and Sec. 2.2.1 that goes into the topic of multiplanetary systems and dynamical modeling.

More recent significant RV discoveries around M dwarfs comprise of close-by systems around famous stars: Teegarden's star, the 24th nearest star to the Sun, is hosting two temperate Earth-mass planets with high Earth Similarity Index (ESI, see Schulze-Makuch et al. 2011) reaching 0.94 and 0.8 for Teegarden b and c, respectively (Zechmeister et al. 2019). With this values, Teegarden b is the planet with the highest ESI so far. As an additional fact, Earth can currently be observed as a transiting planet from the Teegarden's system (Zechmeister et al. 2019). Proxima Centauri, the closest star to our own Solar System is orbited by one planet (Anglada-Escudé et al. 2016; Suárez Mascareño et al. 2020). Barnard's star, the second closest system, is orbited by one planet (Ribas et al. 2018). Lalande 21185, famous for a spurious astrometric detection of a planetary companion (as is Barnard's star, both companions are refuted by now, see, for example, van de Kamp & Lippincott 1951), is orbited by one planet (Díaz et al. 2019), and the system is further discussed in this thesis, as the planet detected by Díaz et al. (2019) could be confirmed using CARMENES data (Stock et al. 2020c). YZ Ceti, the 21st nearest star to the Sun, is orbited by three close-in Earth-mass planets and represents a very compact multiplanetary system (Astudillo-Defru et al. 2017; Stock et al. 2020b). As such it was further observed with the CARMENES instrument and is discussed in this thesis. An additional rare type of system is

GJ 3512 which hosts a $\sim 0.5\,M_J$ planet around a $\sim 0.1\,M_\odot$ host star, challenging current planet formation models (Morales et al. 2019).

Transit photometry

In the early days of the RV method, when there were only a handful of detected planets, some astronomers were questioning the reliability and origin of the measured Doppler signals, as these could have also been objects of stellar mass with inclination angles close to zero or a signal caused by stellar activity (Lovis & Fischer 2010). Such doubts were discarded when one of the planets detected with the RV method, HD 209458 b, was also found to transit its host star (Charbonneau et al. 2000; Henry et al. 2000).

The transit photometry method to detect exoplanets uses the circumstance that a potential planet can move in front of the host star's stellar disk as viewed by an observer. Under the assumption of randomly distributed circular orbits, the probability for such a transit is usually rather small and can be calculated as

$$p = \frac{R_*}{a_{\rm pl}} \tag{1.11}$$

and it depends on the stellar radius R_* and the semi-major axis $a_{\rm pl}$ of the planet (Borucki & Summers 1984). From Eq. 1.11, one can also easily derive the maximum inclination under which a planet fully transits. In the case of a transit event, the flux of the host star is reduced, leading to a dip in the light curve that depends on the stellar radius R_* and the planet radius $R_{\rm pl}$. The so-called transit depth ΔF can be approximated as

$$\Delta F = \left(\frac{R_{\rm pl}}{R_*}\right)^2. \tag{1.12}$$

Figure 1.3 shows examples of transit lightcurves obtained by the Kepler space mission (Borucki et al. 2010). The Kepler space mission, which was launched in 2009, led to the discovery of thousands of exoplanets. Because of this extraordinary success, the number of exoplanets detected with the transit method has surpassed the number of detections with the RV method. This large number of detections was possible by continually observing a large fraction of the sky, which is the preferred observing strategy for photometric transit observations. The precise RV method is currently not applicable to such large areas of the sky. Nevertheless, both methods, RV and transit

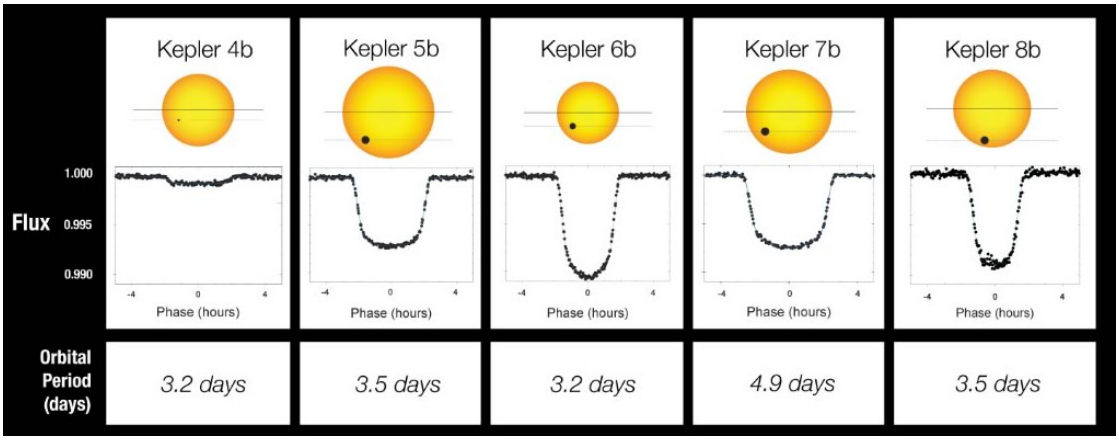


Fig. 1.3.: Transit light curves of the first five discoveries of the Kepler mission (Borucki et al. 2010) and a sketch of the possible star-to-planet ratio with the distance of the planet passing from the centerline of the disk. Image Credit: NASA/Kepler Mission, slightly modified.

photometry, complement one another. The transit method is unable to derive planetary-mass estimates, but the planetary radius can be determined if the stellar radius (or density) is known.

Additionally, both methods have a preferred sensitivity for large (massive) short-period planets so that RV observations can follow up observations of many transiting planets. The RV observations confirm the planetary nature — as the stellar activity, binarity, or background contamination can mimic transit candidates — and derive exoplanet densities by combining mass and radius estimates thereby allowing to learn more about exoplanet properties. Additionally, in some cases, it is possible to probe planetary atmospheres by using transit spectroscopy, which opens a new window to exoplanet chemistry (see, for example, Lovis & Fischer 2010; Charbonneau et al. 2002; Sánchez-López et al. 2019; Yan et al. 2019; Lampón et al. 2020; Palle et al. 2020).

While the Kepler mission has successfully detected and characterized thousands of exoplanets, new transit photometry instruments and surveys are already running or planned. One of them is the Transiting Exoplanet Survey Satellite (*TESS*, Ricker et al. 2015). *TESS* is a space satellite that searches for transiting planets around nearby stars. The primary mission goal consisted of photometric observations of 26 sectors with 24×96 $\deg^2$ in the northern and southern hemispheres and has already finished. An extended *TESS* mission is currently running. *TESS* has already allowed the discovery of many transiting planets, some of them around nearby M dwarfs. The CARMENES spectrograph followed up some detections, and a few publications have been co-authored by the author of this thesis (Kemmer et al. 2020; Luque et al. 2019). In this thesis, *TESS* data have been used to search for potential transits of the exoplanets detected by the RV method.

Other Methods

There are many other methods to detect exoplanets, but they were not used in this work and therefore, they will not be discussed in detail. Nevertheless, I shortly outline three other primary techniques below. An introduction of other detection methods or a more in-depth discussion of the techniques given below can be found in a textbook, e.g., Perryman (2011).

Direct imaging The direct imaging technique is based on the simple idea to photograph the exoplanet. The planet is either detected by the host star's reflected light or by its thermal emission measured in the infrared. But the flux ratios, which can be as small as about 10^{-10}, and the minute angular separation between an exoplanet and his host star present tremendous challenges. The flux ratio of planet and host star depends on several factors which are: the semi-major axis of the planet's orbit around the host star, the host star's spectral type, the mass of the planet, the radius of the planet, the composition of the planet, the age of the planet, the atmosphere of the planet, and the observed wavelength range. The angular separation Θ (in arcsec) on the other side depends on fewer parameters, the semi-major axis a (in au), eccentricity e of the orbit, and the distance d (in parsec) to the star. The angular separation is given by

$$\Theta = a(1 + e)/d, \tag{1.13}$$

(Traub & Oppenheimer 2010). Typical angular separations of exoplanets can be between 0.1" to 0.5" (Perryman 2011).

The most promising targets for direct imaging are young, nearby planets that orbit their host star, at wide separations because the planet then still emits some of the energy from its formation period and has a larger angular separation. The first exoplanets detected by direct imaging, Formalhaut b[4] ($a \approx 115$ au, age $\sim 100 - 300$ Myr, d≈ 7.6 pc; Kalas et al. 2008) and three planets around HR 8799 ($a_b \approx 68$ au, $a_c \approx 38$ au, $a_d \approx 24$ au, age ~ 30 Myr, d≈ 39 pc; Marois et al. 2008), are perfect examples of exoplanets with such properties. As of August 18th, 2020, the NASA Exoplanet Archive lists 50 directly imaged planets; however, according to the IAU's recommended upper mass limit, a significant fraction (about half of the sample) should be classified as brown-dwarfs rather than exoplanets. A famous recent discovery by direct imaging was PDS 70 b, a young protoplanet that still accretes material (Keppler et al. 2018). The same system hosts the least-massive exoplanet imaged so far, PDS 70 c (Haffert et al. 2019), and has

[4]The existence of this planet is currently debated in the literature (Gaspar & Rieke 2020).

an estimated mass of $2 \pm 1\,M_J$ (Wang et al. 2020). The object imaged closest to its host star is the brown-dwarf CFBDSIR J145829+101343 b with a semi-major axis of 2.6 au (Liu et al. 2011).

Gravitational microlensing Gravitational microlensing uses a phenomenon first described by Albert Einstein (Einstein 1911): light of a distant source is being bent by the gravitational field of a massive body. This effect later turned out to be an important consequence of Einstein's general theory of relativity (Einstein 1916), but which was found by Einstein even before his theory was formulated. Again, it was Einstein who showed several years later that the deviation of light in the gravitational field of a star can act like an optical lens, but he saw no hope of ever observing this phenomenon directly (Einstein 1936). Whereas gravitational microlensing has a broad range of applications, from stars to distant quasars, only the photometric aspect for exoplanet detection using stellar microlensing will be described in this section.

On rare occasions, an object (or multiple objects), hereafter referred to as a "lens", cross the line-of-sight between an observer on Earth and a distant background star, causing a microlensing event. The basic geometric properties of such an event are illustrated in Fig. 1.4. The received light from the background source is deflected by the gravitational potential of the foreground lens. This deflection can be approximated by two unperturbed rays of light that intersect with an angle $\hat{\alpha}$ at the lens plane. By assuming small angles[5], it follows that $\tan(\Theta) \approx \Theta$, therefore, $\overline{L'S} = \overline{L'I_1} - \overline{SI_1}$ can be written as $\beta D_S \approx \Theta D_S - \hat{\alpha} D_L$. Additionally, from the small-angle approximation it follows that $\hat{\alpha} D_L \approx \alpha D_S$. Inserting the latter equation into the previous equation and dividing by D_S gives the so-called lens equation

$$\beta = \Theta - \alpha \tag{1.14}$$

(Gaudi 2010). For a point lens, the lens equation can be written as

$$\beta = \Theta - \frac{4GM}{c^2\Theta}\frac{D_{LS}}{D_L D_S}, \tag{1.15}$$

[5]This approximation is applicable at the corresponding distances.

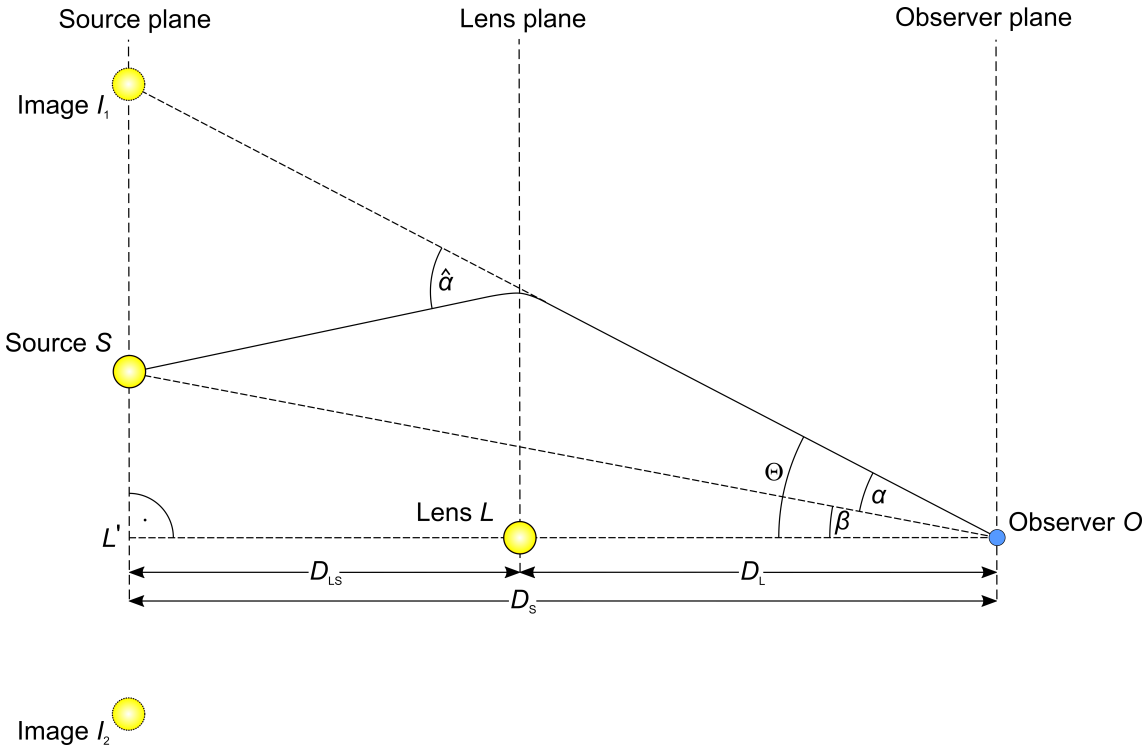


Fig. 1.4.: This plot shows the geometry that causes a gravitational lensing event. The lens L at a distance D_L from the observer O is deflecting the light of a background source at a distance D_S by an angle $\hat{\alpha}$. The apparent angular position of the distorted image I_1 is indicated by the angle Θ, while β is the angular position of the source S in the absence of any perturbations by the lens. D_{LS} is the distance from the source to the lens. *Credit:* Uwe Reichert.

where M is the mass of the lens, c the speed of light, and G the gravitational constant (see Gaudi 2010). A perfect alignment ($\beta = 0$) of the lens and the source results in a ring-like structure, a so-called Einstein ring, which has an angular radius of

$$\Theta_E = \sqrt{\frac{4GM}{c^2}\frac{D_{LS}}{D_L D_S}} \tag{1.16}$$

(Batista 2018). It is common to normalize all length scales and time scales with respect to the Einstein radius. Therefore, the lens equation can also be written as

$$\beta = \Theta - \frac{\Theta_E^2}{\Theta} \tag{1.17}$$

(Batista 2018). Multiplying this equation by Θ yields a quadratic equation, and its solution is

$$\Theta_{1,2} = \frac{\beta}{2} \pm \sqrt{\frac{\beta^2}{4} + \Theta_{\mathrm{E}}^2}. \tag{1.18}$$

Hence, in the case of an imperfect alignment of the source and the lens ($\beta > 0$), two images exist on opposite sides of the source — the major image outside the Einstein ring and the minor image inside the Einstein ring. The angular distance of these images is approximately $2\Theta_{\mathrm{E}}$.

The surface brightness of the distorted images is conserved, resulting in a magnification of the signal depending on the exact geometry. This magnification can be photometrically detected by measuring the flux. The magnification's strength is given by the ratio of the distorted image areas to the source area. The characteristic time scale for the flux change is given by the Einstein crossing time t_{E}, the time to cross the Einstein radius in the reference frame of the lens, which is given by

$$t_{\mathrm{E}} = \frac{\Theta_{\mathrm{E}}}{\mu_{\mathrm{rel}}}, \tag{1.19}$$

where μ_{rel} is the relative proper motion between source and lens, as seen by the observer (Gaudi 2010).

When a planet is orbiting the star that acts as a primary lens, the companion will further distort the lensed image, leading to a secondary signal. Lens configurations which consist of two lenses are called binary lenses (Gaudi 2010). The secondary signal can be explained by the lens equation's solutions of a two-point mass lens resulting in regions around a closed curve for which the magnification tends towards infinity (Batista 2018). These closed curves are so-called caustics, and their properties play an essential role in planetary microlensing, particularly regarding the shape of the secondary signal (Han 2006; Batista 2018). Figure 1.5 shows the imperfect alignment of a source with a lens that hosts an exoplanet, along with the corresponding measurable photometric signal.

The probability of a microlensing event is small, which is why most surveys observe regions of increased stellar density, for example, the crowded galactic bulge. The observing strategy for detecting exoplanets with gravitational microlensing is similar to the search of transiting planets: photometric surveys simultaneously monitor large fractions of the sky. If a lensing event is detected, a worldwide network of additional telescopes is alerted that follows up the microlensing event in real-time, ideally without any observational gaps. Therefore, the observations are

typically not carried out by a single telescope but by a global telescope network instead. In contrast to transit photometry or many other exoplanet detection methods, gravitational microlensing is a one-time event, and the timescale for an event is on the order of days at maximum. Due to its uniqueness, it is not possible to independently confirm the event using a second measurement at a later time. However, this is not needed because of the unambiguous character of the event and because other telescopes are usually able to measure the same event shortly after the alerting by the first telescope. The latter one reduces the possibility of false positives or missed observations caused by an instrumental malfunction.

The main property of exoplanets detected by gravitational microlensing that can be extracted from the data is the planet-to-star mass ratio. In many cases, it is possible to derive an estimate of the stellar mass, e.g., by using high-resolution imaging, which then gives a reasonable estimate of the planetary mass (Gaudi 2010). The main advantage of detecting exoplanets with the microlensing technique is that the method is sensitive to a region in the parameter space that is difficult to observe with other techniques (see, for example, Fig. 1.7). However, the exoplanet can only be detected for particular geometric configurations relative to the primary lens. The sensitivity is high close to the Einstein ring, which, in general, corresponds to a distance of the exoplanet that lies beyond the snow line[6]. As a consequence of this bias, microlensing is less sensitive to habitable planets (Gaudi 2010).

Additionally, the microlensing method can detect free-floating terrestrial planets that are not gravitationally bound to a host star. The first terrestrial-mass planet of this kind has been detected in September 2020 (Mróz et al. 2020). Such detections are extremely challenging due to the small lens masses, resulting in short Einstein crossing times and low lens magnifications. The microlensing method's other advantages are a weak dependence on the host star mass and an insensitivity to the exoplanet's distance from Earth. Therefore, in principle, the microlensing method has the potential to detect exoplanets outside of the Milky Way (Gaudi 2010).

The first exoplanet detection using the gravitational microlensing technique has been announced in 2003 (Bond et al. 2004), and, as of January 2021[7], 106 planets have been detected by this method in total. Based on microlensing, a key result has been the estimation of the occurrence rate of planets with masses of $5\,M_\oplus$ to $10\,M_J$, and semi-major axes of 0.5 to 10 au. For these objects, the occurrence rate has been determined to be $1.6^{+0.72}_{-0.89}$ (Cassan et al. 2012). Based on this result, each star in the Galaxy hosts on average at least one planet. This occurrence rate was much higher and covered a larger parameter space in mass and semi-major axis than any previous estimate based on transit or RV data.

[6]The region in the protoplanetary disk where water ice can exist (Kennedy & Kenyon 2008).
[7]https://exoplanetarchive.ipac.caltech.edu/docs/counts_detail.html

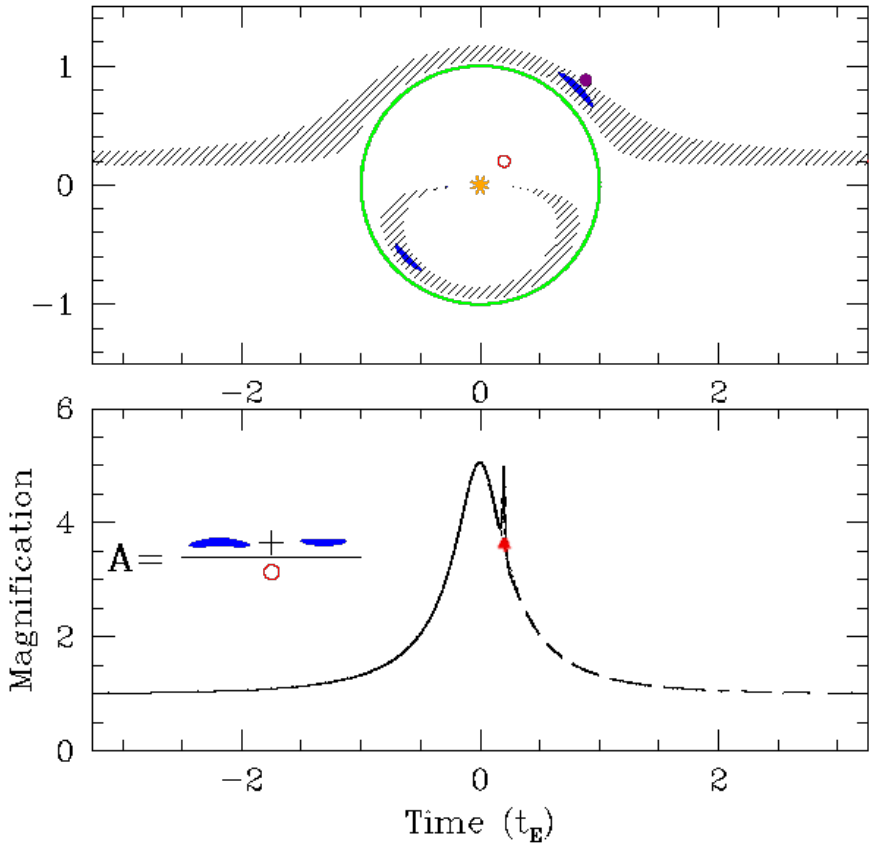


Fig. 1.5.: *Top:* This plot shows a time segment of a binary lensing event. The resulting major and minor images (blue ellipses) are caused by the current relative positions between the lensing foreground objects (red circle) and the background source (yellow point). The shaded area marks the major and minor image positions over the entire lensing event, the purple circle marks the position on the sky of an exoplanet orbiting the lens, and the Einstein radius is indicated as the green circle. *Bottom:* Magnification of the light curve as a function of time. The red arrow indicates the time shown in the top plot. After that, the light curve is shown as a dashed line. A second magnification event is observed and caused by the fact that the major image is further distorted as it traverses, by chance, the position of the exoplanet on the sky, which then acts as a secondary lens. The lens's current magnification is semi-mathematically indicated as the area ratio of the lensed images to the source. *Credit:* Based on a GIF animation by B. Scott Gaudi (http://www.astronomy.ohio-state.edu/~gaudi/movies.html), free for public use if acknowledged, slightly modified.

Astrometry Astrometry was the first method used to find planet candidates around stars other than our Sun. During the 1960s, about eight planet candidates were known (O'Leary 1966). However, these candidates proved to be spurious signals, and have all been refuted. Mainly because of insufficient precision and numerous sources of error, astrometry has not been able to

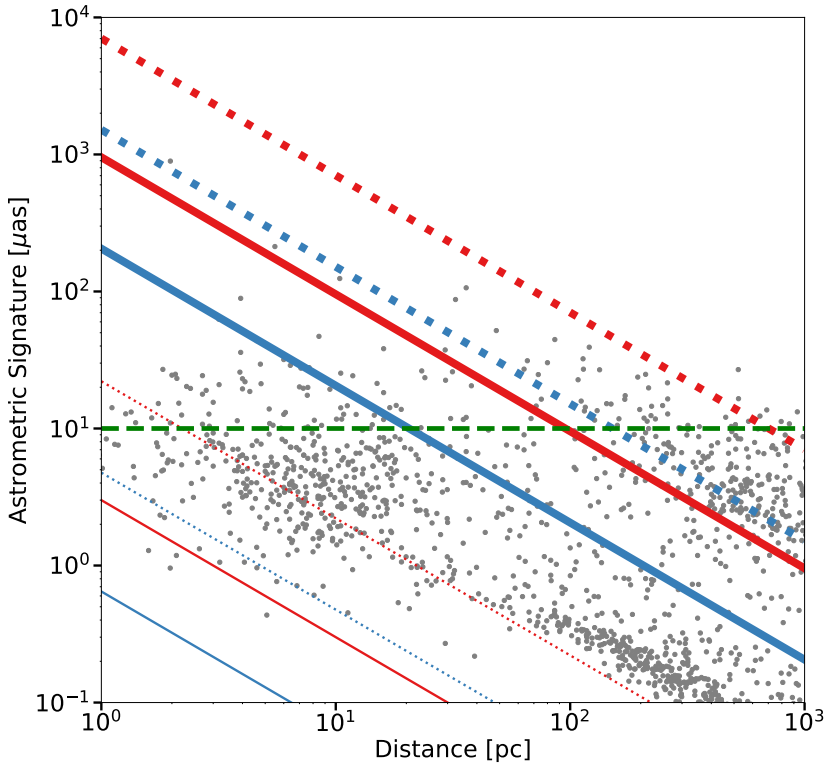


Fig. 1.6.: This plot shows the functional dependence of the astrometric signature on different parameters. The width of the diagonal lines represent the mass of the exoplanet, 1 $M_\oplus$ (thin), 1 M_J (thick), the color represents the mass of the host star where blue is 1 $M_\odot$ and red 0.1 $M_\odot$ and the linestyle represents the period of the exoplanet where the solid line represents a 0.1 yr orbit and dotted line a 2 yr orbit. The horizontal green dashed line represents the detection limit of *Gaia* for bright objects (V<10 mag). The gray dots represent the currently known exoplanets' astrometric signals with available masses, host star masses, orbital periods, and distances if viewed face-on and under the assumption of circular orbits. *Credit:* The data for this plot have been obtained from the NASA Exoplanet Archive in February 2021.

fulfill the expectations placed in it in the past and contributed very few detections of exoplanets or substellar companions (see, for example Sahlmann et al. 2013; Curiel et al. 2020).

Astrometry can be regarded as the complement to the RV method. The underlying physical process responsible for the detection is the same as for the RV method, namely the measurement of the host star's gravitational perturbation due to an orbiting object's mass. In contrast to the RV method, astrometry does not measure the line-of-sight movement but the displacement of the

star in the plane of the sky (perpendicular to the line-of-sight movement). By simple geometric reasoning and the assumption that $m_{\rm pl} << M_*$ one can deduce that the astrometric signature $\Theta_{\rm A}$ is given by

$$\Theta_{\rm A} = \frac{m_{\rm pl}}{M_*}\frac{a}{d} = 3\mu{\rm as} \cdot \frac{m_{\rm pl}}{{\rm M}_\oplus}\left(\frac{M_*}{{\rm M}_\odot}\right)^{-2/3}\left(\frac{P}{\rm yr}\right)^{2/3}\left(\frac{d}{\rm pc}\right)^{-1} \tag{1.20}$$

(Quirrenbach 2010). Figure 1.6 shows the astrometric signature as a function of distance for two different exoplanet masses, two different host star masses, as well as two different orbital periods of the exoplanet. The figure shows that astrometric exoplanet searches are best suited for close systems with long-period planets, as the astrometric signal is linearly dependent on the distance and measured the change in position of the planet, in contrast to the RV method. However, similar to the RV method, the signal strength increases for lower stellar masses and higher planetary masses. One can also see that the astrometric signal varies greatly over several orders of magnitude, depending on the type of object. Given the expected precision of *Gaia* for bright targets (V<10 mag), which is $\sim$ 10 μas[8] (Malbet & Sozzetti 2018), one can see the difficulty to measure these signals. As an exemplary distribution, the astrometric exoplanet signatures of all currently confirmed exoplanets with available masses, host star masses, periods, and distances, and under the assumption of circular orbits viewed face-on is overplotted in Fig. 1.6. There is no reason to believe that the distribution will significantly be different for systems when viewed face-on, as to when they are viewed close to edge-on (as for the RV or transit method). While many individual planet signatures are below the detection limit of *Gaia*, it has to be taken into account that *Gaia* will have observed more than 1 billion stars at the end of its mission. Based on knowledge and assumptions of planet occurrence rates, Perryman et al. (2014) estimated to find about $70,000 \pm 20,000$ substellar objects with masses of 1 M_J to 15 M_J up to a distance of 500 pc for a full 10-yr mission of *Gaia*.

1.1.5 Exoplanet distribution and properties

The distribution of exoplanets can be analyzed and visualized in various planes of parameters, allowing us to draw additional conclusions about physical properties and possible formation scenarios of planets and whole systems. An important question — because it is also connected to the humanity's instinctive curiosity whether we are unique in the Universe — is the habitability of exoplanets. Even such fundamental but complicated questions can be investigated by using

[8] https://www.cosmos.esa.int/web/gaia/science-performance

exoplanet demographics. The NASA Exoplanet Archive provides a good overview of different two-dimensional distributions of planet parameters to which I refer for a basic overview[9].

The discussion of all these properties and parameters is informative but would go beyond the scope of this thesis. I limit myself to showing the distributions of parameters that can be derived from the RV method and that fit into the context of this thesis. In Fig 1.7, the distribution of the current sample of exoplanets in the mass (or minimum mass in case of most RV observations) versus semi-major axis plane is shown. Note that planets without mass measurement, e.g., most transiting planets, are not included in the plot. From this plot, one can clearly see that the different exoplanet detection techniques are sensitive to different regions in this two-dimensional parameter space of mass versus semi-major axis, reflecting the detection biases and selection effects that were partly mentioned in the sections before. A rough classification scheme, according to Sec. 1.1.3, is overplotted.

Despite possible observational biases to be apparent in this distribution, several features can be identified that are thought not to be caused by detection biases or selection effects. A paucity of giant planets is observed in the region around 0.1 au to 0.5 au that separates the hot Jupiters from the cold Jupiters around 1 au or more. As this paucity is also observed in period space (as semi-major axis and period are connected via Kepler's law), it is referred to as the "*period valley*" (Udry et al. 2003; Santerne et al. 2016). A possible reason for this valley is thought to be the so-called type II disk migration (see for example Dawson & Johnson 2018). A prominent feature of the mass distribution is the relative lack of intermediate-mass planets between 20 $M_\oplus$ to 100 $M_\oplus$, and its origin is believed to be a consequence of the runaway gas accretion process in the core-accretion gas capture model (Ida & Lin 2004; Mordasini et al. 2009). The core-accretion gas capture model is one of the two major theories for giant planet formation, the other being the disk instability model (Boss 1997, 2006).

However, the paucity of detected exoplanets with masses similar to or smaller than those of the Earth, and semi-major axes similar to or larger than those of the Earth, is a detection bias caused by the insensitivity to that region of the parameter space by most of the current exoplanet detection techniques. The most Earth-like planet in terms of mass and semi-major axis is OGLE-2016-BLG-1195L b (Shvartzvald et al. 2017), a planet that was discovered using the microlensing method. However, this planet orbits a star with a mass of only 0.08 $M_\odot$. Such a comparison shows that additional information that is not provided in Fig. 1.7, e.g., the host star mass, is necessary to find Earth analogs. Approximated RV semi-amplitudes as a function of the planet's semi-major axis for a 1 $M_\odot$ host star are provided in the plot. Many of the RV planet detections below the

[9] https://exoplanetarchive.ipac.caltech.edu/exoplanetplots/

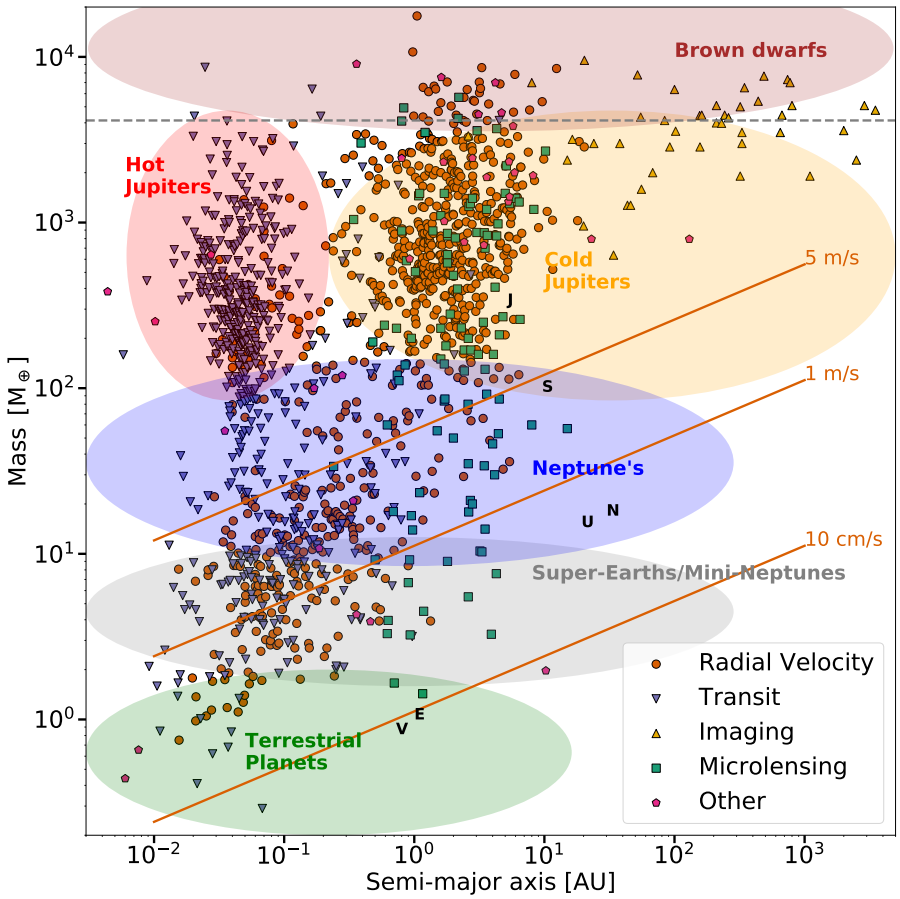


Fig. 1.7.: Diagram of exoplanets with known masses (or minimum masses) as a function of the semi-major axis. Symbols and colors represent different detection methods of the discoveries. The colored ellipses mark approximated regions of a rough classification of exoplanets used within this thesis. The letters are abbreviations according to the IAU for our Solar System planets. Orange lines indicate the approximated RV signal needed for a solar-mass star and a planet with zero eccentricity. One can see that Earth and Venus are at the edge of the detectability for a 10 cm s^{-1} RV instrument. *Credit:* The data for this plot have been obtained from the NASA Exoplanet Archive in February 2021.

line representing a 1m s^{-1} RV semi-amplitude orbit host stars with masses smaller than that of the Sun.

This effect is more clearly visible in Fig. 1.8, where the RV semi-amplitude of the confirmed RV detections is binned to the year of publication. The color-coding, which reflects the stellar mass, shows that most of the planet detections with RV semi-amplitudes around 1m s^{-1} are orbiting stars less massive than the Sun. Such low-mass planets are easier to find around low-mass stars (see Sec. 1.2.1). Figure 1.8 shows that in the last decades, increasingly smaller RV semi-amplitudes

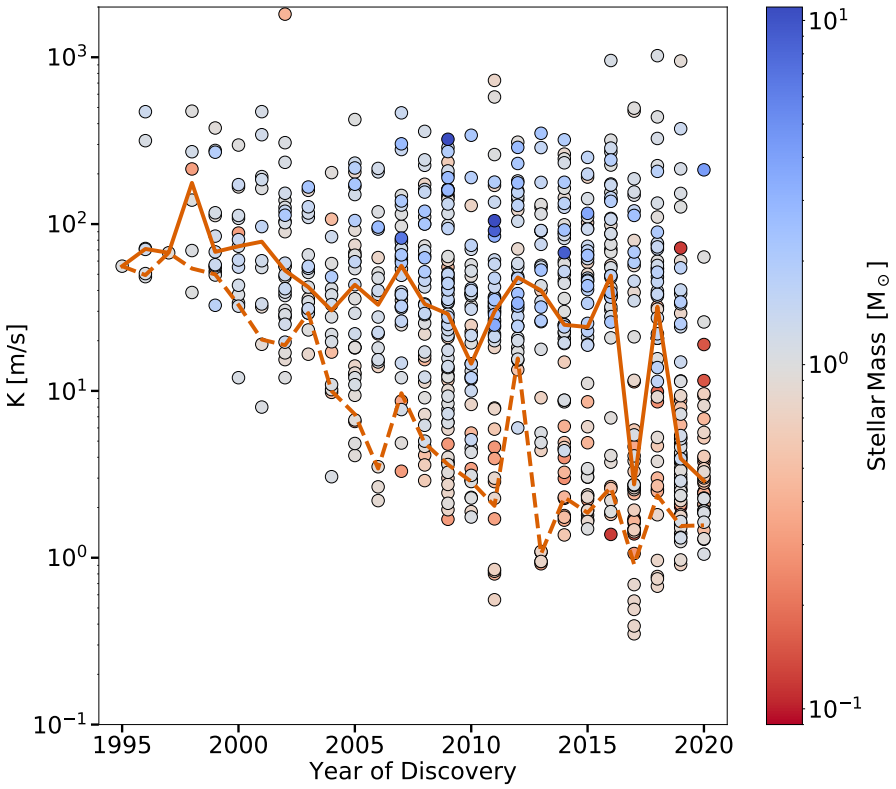


Fig. 1.8.: Radial velocity semi-amplitude binned to the year of discovery. The color-coding shows the stellar mass of the host star. The solid orange line connects the median of the RV semi-amplitude of each year, while the dashed orange line shows the first decile (lowest 10% of the data). *Credit:* The data for this plot have been obtained from the NASA Exoplanet Archive in February 2021.

could be measured, a result of an improving instrumental precision over time (see Sec. 2.1.2 and Sec. 2.1.3). However, in the last years, the RV semi-amplitude improvement slowed down, with only a handful of detections below $1\,\mathrm{m\,s^{-1}}$. The underlying reason is not instrumental, but the astrophysical noise of the host stars themselves can mask planetary signals with small RV semi-amplitudes, as even the most quite stars seem to show RV variations on the order of $1\,\mathrm{m\,s^{-1}}$ (see for example Robertson et al. 2014; Anglada-Escudé & Tuomi 2015, and Sec. 1.2.2). Therefore, an improvement of the instrumental precision is not sufficient to detect planets with smaller RV semi-amplitude, but it has to be accompanied by an improvement of modeling the stellar noise contribution. Several approaches, including physical or stochastic modeling of the stellar astrophysical noise, seem feasible and are discussed further in the following sections.

An additional planetary parameter that can be derived rather well from RV measurements is the orbital eccentricity. Figure 1.9 shows the eccentricity-vs.-semi-major axis plane of all detected

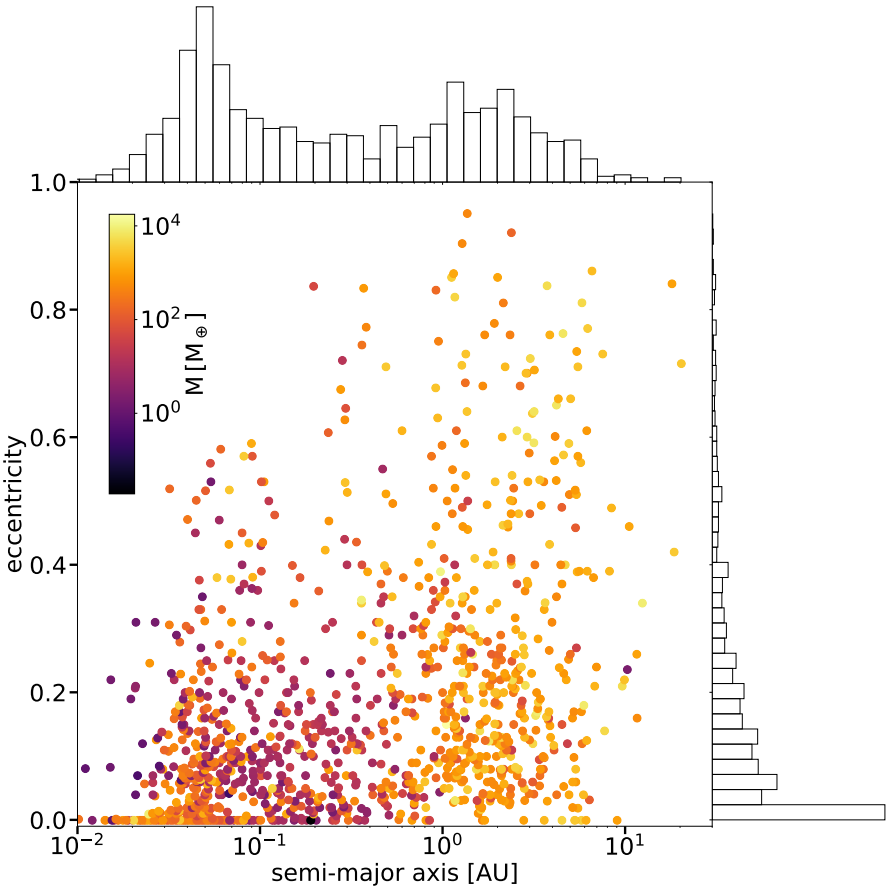


Fig. 1.9.: This plot shows the distribution of orbital eccentricities as a function of the semi-major axis for planets that have both quantities measured as well as a mass estimate. The color-coding indicates the planetary mass. *Credit:* The data for this plot have been obtained from the NASA Exoplanet Archive in February 2021.

planets with a mass, a semi-major axis, and an eccentricity estimate. The distribution shows a wide range of orbital eccentricities up to almost one, something that was not anticipated before the first discoveries of exoplanets and that is significantly different from the observed eccentricities in our Solar System. The overall distribution and its origin are not fully understood and are still debated in the literature (Cumming 2010).

A clear preference for low-eccentricity orbits of close-in planets can be identified in Fig. 1.9. This is expected, as tides circularize such planets. However, as can also be seen from Fig. 1.9, not all close-in planets have zero eccentricity. A possible reason for this could be additional companions that interact gravitationally with the inner planet and excite its orbital eccentricity (Cumming 2010). On the other hand, very few planets on wide orbits show low-eccentricity orbits. The large

scatter in possible eccentricities of the orbits is thought to be a combination of several effects: gravitational interaction of planets in multi-planetary systems with each other (e.g., two-body scattering, see Ford & Rasio 2008), interaction with planetesimals and the protoplanetary disk in the early stages of planet formation (see for example Goldreich & Sari 2003), and last but not least gravitational perturbations by external masses passing by the system (see for example Stock et al. 2020a, and references therein).

1.1.6 Multiplanetary systems

As of February 2021, more than 700 multi-planetary systems were known and confirmed[10], a fraction of about 17% of all known planetary systems. The probability of detecting an additional planet in a system is higher for a two-planet system than a single-planet system (Cumming 2010). This might be a selection effect, as two-planet systems are observed longer and more carefully. Most multi-planetary systems have been found by using the transit method, but about 160 were discovered by the RV method. The detection of multi-planetary systems using the RV method has advantages compared to the detection using transit photometry or any other method. In the best-case scenario, one can detect and constrain orbital inclinations of the planets and mutual inclinations between the planets in the system and derive the most likely masses of the planets.

Multi-planetary systems allow the determination of unique properties of planetary systems and help to constrain formation scenarios. A multi-planetary system consisting of several bodies, particularly tightly packed systems or systems where at least one planet has a large mass, can lead to further gravitational interactions that result in deviations from a simple Keplerian orbit (Laughlin & Chambers 2001). The dynamical interaction between planets can be divided into interactions during the planet formation phase, secular interactions and resonant interactions on timescales of decades or less, and long-term interactions on timescales similar to the host star's lifetime (Laughlin & Chambers 2006). Secular interactions and resonant interactions, in particular, can therefore influence planetary system dynamics on the timescales of the observations. In some cases, it is recommended to include these gravitational interactions into the modeling of the system (see Sec. 2.2.1).

The observation of multi-planetary systems allows assessing the mass spectrum of individual planets that form in a system. It has been found by analyzing multi-planetary systems detected by the Kepler mission that planets in multi-planetary systems have similar sizes and regular orbital spacing (Weiss et al. 2018). Based on Kepler data, Fang & Margot (2013) propose that tightly

[10]NASA Exoplanet Archive: https://nexsci.caltech.edu/

packed systems that are dynamically filled to their maximum capacity are common and the rule. The dynamical state of systems observed today can be closely related to early dynamical processes that have taken place during the formation of the planetary system. Analysis of the dynamics allows constraining possible formation scenarios, e.g., tightly packed systems in resonant chains are well explained by the migration of planets during the disk phase (Lee & Peale 2002; Batygin 2015).

On the other side, one can only observe systems that survived since their time of formation. Therefore, imposing the criterion of long-term stability on a planetary system can be used to define and constrain the planetary system parameters to a level that is difficult to reach purely by observations. This can be achieved by integrating sampled realizations of the observed system within the observational uncertainties using an N-body integrator. For the work presented in this thesis, `SyMBA` (Duncan et al. 1998) and `Mercury` (Chambers 1999) have been used. They are both well-established symplectic N-body integrators suitable for calculating the orbital evolution of multiple interacting planets around one or several stars. N-body integrators numerically iterate over a predefined timespan and calculate each body's position in a system at each time interval by including all relevant gravitational interactions.

Overall, N-body simulations can be classified into two categories: Simulations that recover the initial conditions at the formation of the system by trying to reproduce the observed configuration and simulations that start with the observed initial conditions and predict the future evolution of the system. One downside of N-body integrations is that they cannot prove the system's stability, but only the stability over the time of the integration (Davies et al. 2014). Additionally, the integration of multi-body systems is computationally expensive. The computation time increases with the number of bodies, and it also depends on the time step used for the integration. For systems with smaller orbital periods it is necessary to use a smaller timestep to reduce numerical errors and uncertainties that arise during the integration of the N-body system (Duncan et al. 1998).

The interaction and stability of bodies in a multi-body system depend on the number of bodies, their mass, and separation from each other (Dawson 2018). While the exact behavior of several bodies can only be numerically analyzed using an N-body integrator, it is still common in the literature to use several "*Packing Metrics*" (Dawson 2018) to provide an estimation of strong or weak dynamical interaction between planet pairs. However, no simple metric can describe the system in all its details, particularly for $N > 2$ planets, which is why N-body integrations are usually the preferred choice for the dynamical analysis despite their computational expenses.

Nevertheless, two "*Packing Metrics*" are introduced in the following paragraphs: the orbital period ratio and the Hill spacing. The orbital period ratio is given as

$$\frac{P_{i+1}}{P_i} \sim \frac{p+q}{p}, \tag{1.21}$$

where P_{i+1} is the outer, P_i the inner planet and p and q are integer values. Integer period ratios, so-called period commensurabilities, e.g., 2:1 or 3:2, are often associated with mean-motion resonances (MMR). However, a period commensurability is no clear evidence for a planet pair to be in a real MMR (Murray & Dermott 2000; Tan et al. 2013). The value of q defines the order of the period commensurability, or the resonance order. Two planets are in MMR if their resonance angles, given as

$$\Theta_i = p\lambda_i - (p+q)\lambda_{i+1} + \varpi_i \tag{1.22}$$

and

$$\Theta_{i+1} = p\lambda_i - (p+q)\lambda_{i+1} + \varpi_{i+1}, \tag{1.23}$$

are in libration (Murray & Dermott 2000; Tan et al. 2013; Correia et al. 2018). Here, λ is the mean longitude and ϖ is the longitude of periapsis. MMRs protect the planet pairs from close encounters and stabilize a system. For example, in the case of a 2:1 MMR with resonance angles librating around zero, the inner planet will always be at pericenter at conjunction so that the planets will have the maximum possible distance (Fabrycky 2010). An example of such a system is GJ 876, where planet b and c were found to be in a deep 2:1 MMR, stable on very long-timescales (Marcy et al. 2001; Laughlin & Chambers 2001; Lee & Peale 2002). The GJ 876 system consisting of an M-dwarf host star, is a prime example of planetary systems dynamics. For this system, the orbital inclinations of the planets and the mutual inclinations of planets b and c were derived from the RV data (Bean & Seifahrt 2009; Rivera et al. 2010; Correia et al. 2010). However, it has to be mentioned that systems like GJ 876, where the dynamical interaction between the planets is strong and can be well measured over the time of the observations, are rare and not commonly observed. There are only a handful of systems for which mutual inclinations can be derived from the RV data. For example, the CARMENES survey of about 300 M dwarfs did not detect an analog of GJ 876 thus far.

In addition to two-body resonances, there are also multi-body resonances possible that include more than just two bodies (Murray & Dermott 2000). An example is the Laplace resonance or similar resonances for three bodies for which the Laplace angle needs to be in libration (Murray & Dermott 2000). The Laplace angle for a three-body resonance of the form $p + q + r : p + q : p$ is given as

$$\Theta_{\mathrm{L}} = (p + q)\lambda_{\mathrm{i}} - (2p + 2q + r)\lambda_{\mathrm{i+1}} + (p + q + r)\lambda_{\mathrm{i+2}}, \tag{1.24}$$

and it is common to divide this equation by the largest common divisor (derived with the help of Murray & Dermott 2000, and private communication with Man Hoi Lee). A Laplace resonance is observed in our Solar System for the Galilean moons Io, Europa, and Ganymede, which are in 4:2:1 resonance (Murray & Dermott 2000) and also for the GJ 876 system where a Laplace resonance is found between planets b, c, and e (Rivera et al. 2010). However, other Laplace-like three-body resonances are possible, e.g., the 9:6:4 three-body resonance that can consist of two 3:2 period commensurabilities, and that will be discussed as a possible configuration for the YZ Ceti system later on. A system in a three-body resonance must not be in any two-body MMR and a double two-body MMR does not indicate a three-body resonance (Murray & Dermott 2000). Only if the appropriate resonance angles are in libration the criterion for a specific resonance configuration is met.

The period commensurabilities do not provide any information for the involved planetary masses of the dynamical interaction. The second "*Packing Metric*" introduced is the orbital separation in mutual Hill radii. The Hill radius is the zone in which a body is gravitationally dominant, and it is given as

$$R_{\mathrm{H}} = \left(\frac{m_{\mathrm{i}} + m_{\mathrm{i+1}}}{3M_*}\right)^{1/3} \frac{a_{\mathrm{i}} + a_{\mathrm{i+1}}}{2}. \tag{1.25}$$

The mutual Hill spacing is then given as

$$\Delta = \frac{a_{\mathrm{i+1}} - a_{\mathrm{i}}}{R_{\mathrm{H}}} \tag{1.26}$$

(Davies et al. 2014; Dawson 2018).

Planetary systems that have small values of Δ are prone to destabilization, but the system's stability also depends on the multiplicity (Dawson 2018). Under the assumption of coplanar orbits and initially zero eccentricity, it can be derived analytically for a two-planet system whether

it is so-called Hill stable: the two planets will never experience a close approach, if the Hill separation Δ is larger than $2\sqrt{3}$ (Gladman 1993). Using numerical experiments, Barnes & Greenberg (2007) have found that the Hill stability criterion is a good representation of actual stability. However, some simulated and also real systems that reside within strong MMR were found to be stable even with smaller Hill radius separations (Barnes & Greenberg 2007; Davies et al. 2014), and the GJ 876 system is also an example of such a special circumstance.

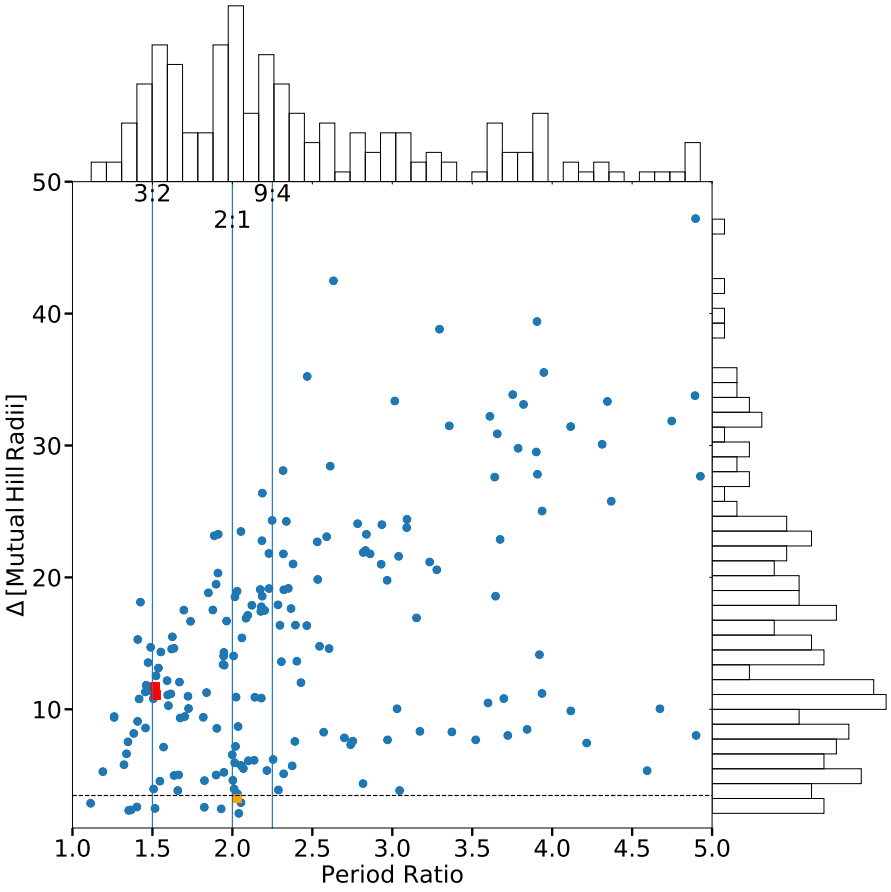


Fig. 1.10.: Separation in mutual Hill radii over the period ratio for all discovered adjacent exoplanet pairs. This also includes adjacent planet pairs in systems with more than two planets. The two red squares mark the planet pairs YZ Ceti b and c, and YZ Ceti c and d, while the orange square marks the pair GJ876 b and c. The 3:2, 2:1, and 9:4 period commensurabilities are marked with the vertical blue lines. The horizontal dashed black line corresponds to the Hill stability criterion for an idealized two planet pair without any additional planet in the system and with zero initial eccentricity and coplanar orbits. *Credit:* The data for this plot have been obtained from the NASA Exoplanet Archive in February 2021.

Figure 1.10 shows the mutual Hill radii of all known adjacent planet pairs over their period ratio in range between $1 < P_{i+1}/P_i < 5$. From the figure, one can see that the majority of planet pairs are found either in a 2:1 or 3:2 period commensurability. Such full integer period commensurabilities, or true resonances in some cases, are footprints of the time of planet formation. They can be well explained as a consequence of planetary migration in the disk phase of newly forming planetary systems (Kley et al. 2005; Dawson & Johnson 2018; Coleman et al. 2019). A third peak in the distribution of the period ratios can be observed around $P_{i+1}/P_i < 5 \sim 2.25 = 9/4$ and it is a significant feature of the period ratio distribution of Kepler multi-planetary systems, as has been shown by using Monte Carlo simulations (Steffen & Hwang 2015). A possible explanation for the peak are unobserved planets between adjacent observed planet pairs. For example, a double 3:2 period commensurability results in a 9:4 commensurability of the outer non-adjacent planet pairs. A more detailed discussion on the possible origin of the peak around $P_{i+1}/P_i \sim 2.2$ is provided in Steffen & Hwang (2015). From Fig. 1.10, one can also see that systems with small period ratios also tend to have smaller mutual hill separations, an indication that these systems are tightly packed and that resonances played an important role in their formation.

Secular perturbations dominate systems that are not in any MMR. Secular perturbations are apparent when the planet pair period commensurabilities are far from any integer ratio. The conjunctions of planet pairs are then distributed equally over all possible orbital positions, and the energy of each orbit is conserved. As a result, there is no change in the semi-major axis or the periods, but the planets exchange angular momentum over long timescales, leading to variations of the eccentricity and inclination (Fabrycky 2010). For planetary systems that are not close to MMR and whose inclinations and eccentricities are small, one can apply the Laplace-Lagrange secular theory and derive the expected dynamical properties analytically (Murray & Dermott 2000). However, the application of this theory to observed systems is difficult (Davies et al. 2014).

In addition to computationally expensive N-body integrations or secular theory, there are many further possibilities to estimate the dynamical properties or long-term stability of a system, but each of them has some drawbacks on their own. A system's stability with more than two planets cannot be estimated analytically (Davies et al. 2014). However, if a system is not close to an MMR, a fast approximation of the stability can be achieved by using the angular momentum deficit (AMD) as a stability criterion (Laskar 1997, 2000; Laskar & Petit 2017; Petit et al. 2018). The AMD is given as

$$\mathrm{AMD} = \sum_k \Lambda_k \left(1 - \cos i_k \sqrt{1 - e_k^2}\right), \tag{1.27}$$

where $\Lambda_k = m_k M_*/(m_k + M_*)\sqrt{G(M_* + M_k)a_k}$ is the angular momentum of planet k (Laskar 1997; Davies et al. 2014). In the case of secular perturbations outside of an MMR, the system's net energy and, therefore, the semi-major axis remain constant. As a result, the AMD is constant, and only the eccentricities and inclinations vary. The amount of the variation is constrained by the AMD and exchanged between the inclination and eccentricity. A system is said to be AMD-Hill stable when the AMD value cannot get large enough to allow crossing orbits and planetary collisions (Laskar & Petit 2017). In the absence of any MMR, this criterion ensures that a system is long-term stable if it is AMD stable on short timescales (Laskar & Petit 2017).

Some other methods try to estimate the long-term stability of a system by using chaos as a fast indicator, e.g., the Mean Exponential Growth factor of Nearby Orbit (MEGNO; Cincotta & Simó 2000) or the Lyapunov indicators (Froeschlé et al. 1997). A planetary system is chaotic if trajectories that are initially separated by a small amount diverge exponentially (Fabrycky 2010). The chaos indicators methodology tries to estimate this divergence on small timescales by integrating the system only for a short time. However, Barnes & Raymond (2004) argue that this method is not well suited and that direct N-body integrations should be preferred. They claim that chaotic motion is not a direct indicator of unstable motion. A good example is our Solar System, whose inner planets are moving on chaotic orbits, but these orbits are stable over the timescale of the planetary system (Dvorak 2007).

1.2 Host stars

Stars are self-gravitating spheres of gas in hydrostatic equilibrium. In their core, energy is generated through the process of nuclear fusion. Some key properties of stars are their mass, radius, luminosity, temperature, and surface gravity. Stars of different masses show different internal structure depending on the dominant type of nuclear fusion, e.g., the proton-proton (p-p) chain or the carbon-nitrogen-oxygen (CNO) cycle. This results in different temperature gradients depending on the star's radius, which play a role regarding the energy transport from the core towards the stellar surface. Intermediate and high mass stars of masses larger than $1.5\,M_\odot$ have a convective core and a radiative envelope. On the other hand, stars with masses less than $1.5\,M_\odot$ consist of a radiative core and a convective envelope while stars below $0.3\,M_\odot$ become fully convective (Ludwig et al. 2002; Stahler & Palla 2005; Carroll & Ostlie 2007). Stars do rotate, a property that results from conservation of angular momentum and is related to the fact that the star was formed out of a gravitationally collapsing cloud that had a small net angular momentum (Carroll & Ostlie 2007). Convection and stellar rotation are the main activity drivers and of

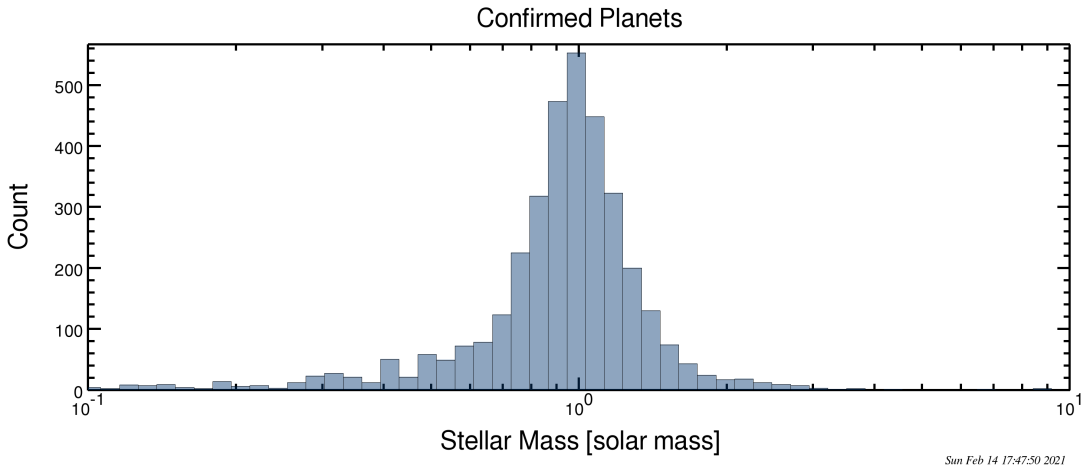


Fig. 1.11.: Frequency of confirmed exoplanets around stars between stellar masses of $0.1\,M_\odot \leq M \leq 10\,M_\odot$. Plot produced in February 2021 by using the NASA Exoplanet Archive ICE plotter.

particular importance regarding the influence of stellar activity signals on RV surveys searching for exoplanets. Convection and rotation poses a severe challenge for the exoplanet detection around active stars.

For almost every detection method, the understanding and correct characterization of the host star is crucial to correctly estimate the planetary properties. In this chapter, I will shortly discuss different types of exoplanet host stars and the implications that arise, in particular for RV surveys. I will introduce the different effects of stellar activity using the Sun as an example since it is the only star whose activity is well studied, as it can be optically resolved. However, I will also show how the activity of M dwarfs differs from solar-like stars, as all planet host stars in this thesis are classified as M dwarfs. For more introductory information and details about stars, their formation, and properties not directly attributed to RV surveys, I refer to a textbook, e.g., Stahler & Palla (2005) or Carroll & Ostlie (2007).

1.2.1 The radial velocity method for different types of host stars

Currently, most confirmed exoplanets are found to orbit F, G, and K stars similar to our Sun (G2V) with masses ranging from $0.8\,M_\odot$ to $1.4\,M_\odot$, because most surveys in the past focused on these targets (Lovis & Fischer 2010; Tal-Or et al. 2018). Fig. 1.11 shows the (biased) distribution of confirmed planets as a function of stellar mass. F, G, and K dwarfs have several advantages when

observed by RV and transit surveys. Their level of stellar activity is better understood and lower overall than for to A and M stars (Lovis & Fischer 2010; Tal-Or et al. 2018) and their number of spectral lines and their spectral intensity distributions are beneficial for RV surveys (Lovis & Fischer 2010). Stars in RV surveys, for example, are often specifically selected according to their variability and photometric stability (see as an example Frink et al. 2001). However, to understand planet formation and properties of exoplanets, it is crucial to search for planets around stars with masses significantly larger or smaller than 1 $M_{\odot}$ (Lovis & Fischer 2010).

The RV method has several problems for intermediate and high mass stars regarding the detection of exoplanets. Stars of spectral class O, B, A with effective temperatures larger than about 10000 K have only a few spectral features, and their rotational broadening, due to high stellar rotation speeds, limits the precision of RV measurements. The lack of spectral features in the stellar atmosphere is caused by the fact that most chemical elements are ionized at such temperatures resulting in fewer electron transitions and, as a result, fewer absorption lines (Lovis & Fischer 2010). Furthermore, stellar activity and pulsations of such stars are more intense compared to FGK stars resulting in a large amount of "stellar jitter". This affects also transit surveys. A method that can be used to mitigate such problems for RV planet searches around high-mass stars is the observation of more evolved evolutionary stages. When a main-sequence star evolves into a red-giant after core hydrogen burning has come to a halt, its envelope expands, and the effective temperature decreases, which allows more spectral features to be apparent in the stellar spectrum. Consequently, this allows precise measurements of radial velocities from so-called "retired A stars" (Johnson et al. 2007; Reffert et al. 2015; Stock et al. 2018; Malla et al. 2020), which are stars of spectral type A in their subgiant, red giant or horizontal branch evolutionary stage, while the term "retired A stars" has been mostly used for the subgiant phase.

Late type stars, e.g., M dwarfs, on the other hand, have effective temperatures ranging from 2000 K up to only 4000 K (see Rajpurohit et al. 2013, and references therein). The stellar atmosphere of such cool stars shows an abundance of molecular bands, e.g. titanium oxide (TiO). The spectral lines of those molecular bands can be so densely packed that the spectra gets too crowded to identify the individual spectral lines, which lowers the precision of RV measurements of these stars. Additionally, not all lines should be treated in the same way. Some lines show variability in their line profile that can be related to the chromospheric activity of the star, e.g., the Calcium H and K lines, Hα, Na D lines, TiO, and several others. Using these lines may lead to wrong conclusions regarding possible planetary signals in the RV data (Queloz et al. 2001a; Desort et al. 2007; Barnes et al. 2011; Robertson et al. 2014, 2015). The above mentioned spectral lines and others can be used as tracers of the stellar activity. If these lines show periodicity with similar timescales as the RV variations, caution is needed when claiming such signals to be of planetary

origin, in particular, since most M dwarfs show signs of intense stellar activity (Johns-Krull & Valenti 1996; Delfosse et al. 1998; Mohanty & Basri 2003; Reiners et al. 2012).

In addition to spectral crowding, late-type stars are much fainter than G-type main-sequence stars, which requires longer exposure times to derive proper signal-to-noise (S/N) ratios for the observations and template spectra. Moreover, late-type M dwarfs have their peak emission in the near-infrared (NIR) instead of the optical wavelength range. As a result, ground-based instruments observing at the NIR need to be cooled and temperature controlled. Furthermore, ground-based spectroscopic NIR observations suffer stronger from telluric absorption lines in the Earth atmosphere when compared to optical observations (Lovis & Fischer 2010, Nagel et al., submitted).

Despite the problems of observing M dwarfs, they have unique advantages that make them attractive for RV and transit surveys of exoplanets. M dwarfs are the most abundant type of stars in the Galaxy and the solar-neighborhood (Kroupa 2001; Chabrier 2003; Henry et al. 2006), which allows to chose from a large variety of potential close-by objects. M dwarfs are good targets to search for temperate or habitable low-mass rocky planets by the RV method. The RV semi-amplitude induced by a low-mass planet is larger if the star has a low mass. Additionally, the habitable zone (HZ) is located closer to the host star due to the lower flux of M dwarfs compared to solar-like stars. The latter results in two additional advantages for the detection of temperate and habitable planets by the RV method. A potential planet in the HZ of an M dwarf will induce a stronger RV semi-amplitude on the host star, when compared to a HZ planet around a solar-like star. Additionally, detecting a significant RV signal takes less time, as the orbital period of the potential HZ planet is smaller.

The HZ is defined as the region in which liquid water can exist (Kasting et al. 1993; Kopparapu et al. 2013). Whether a planet is truly habitable depends on various additional parameters, e.g., planet mass, atmosphere, chemistry. M dwarfs as host stars might be particularly problematic for habitability due to their high level of stellar activity, and it is an unanswered question whether planets around such stars can really host life (Khodachenko et al. 2007; Kay et al. 2016).

1.2.2 Stellar activity

It is crucial to understand the impact of stellar activity on the detection of exoplanets. Intrinsic stellar noise that affects flux and RV measurements stems mainly from the interplay of convection, stellar rotation, and magnetic fields. The stellar noise of flux and RV measurements of stars is mainly dominated by four different effects that occur on different timescales: oscillations,

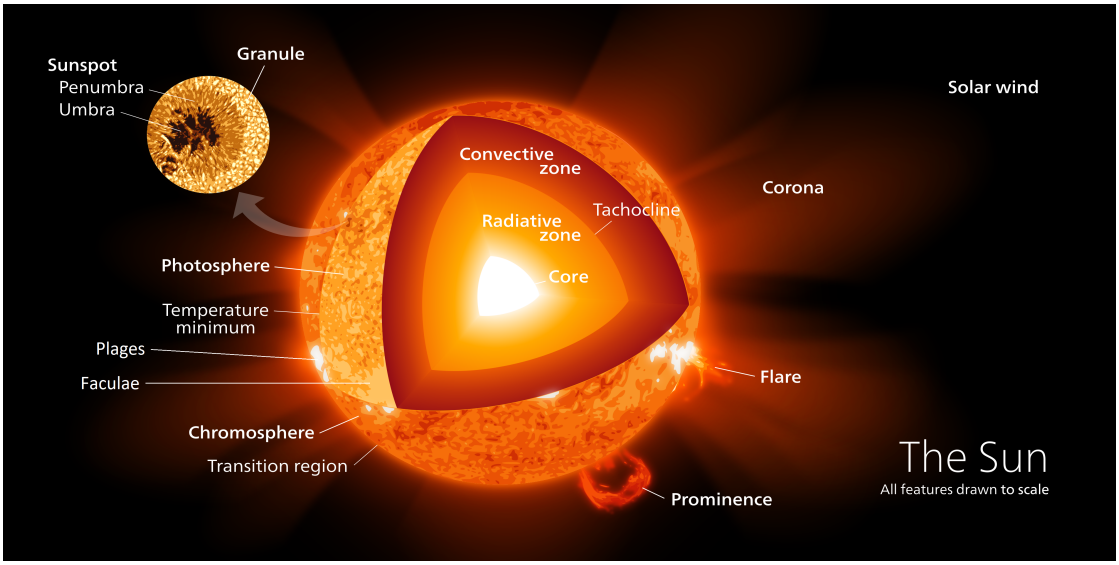


Fig. 1.12.: Cross section of the Sun showing its core, radiative and convective zone as well as different layers of the atmosphere and surface features like spots, faculae, granules and plages. *Credit:* Sun poster by Kelvin Song is licensed under CC BY-SA 3.0, slightly modified.

granulation, active regions and magnetic cycles (Chaplin et al. 2019; Dumusque 2016). For the current and next-generation RV instruments, stellar activity is the main limitation for precise RV measurements (Dumusque 2016). The understanding of solar physics is, therefore, an essential aspect of exoplanetary research. Figure 1.12 shows a picture of the cross section of the Sun, which can also be applied to other Sun-like stars. Most features are similar for fully convective late-type M dwarfs, except that there is no radiative zone.

Oscillations

An intrinsic stellar noise source is stellar oscillation (Lovis & Fischer 2010; Dumusque 2016). These oscillations result from internal pressure fluctuations driven and excited by near-surface convection, which creates acoustic waves (pressure waves, p-modes) that traverse the star's interior. These p-modes lead to dilation and contraction of the stellar surface on timescales of several minutes, typically between 5 minutes and 15 minutes and RV amplitudes of individual modes are on the order of few tens of centimeter per second (Bouchy & Carrier 2001; Kjeldsen et al. 2005; Dumusque 2016; Rodríguez-López 2019). In the end, the overall observed RV variation due to such oscillations is the superposition of many excited modes, which can result in RV variations with an amplitude of a few $\mathrm{m\,s^{-1}}$ (Dumusque 2016). All stars with a convective envelope show such stochastically excited p-mode oscillations, but the overall intensity and

net effect on the RV amplitude decreases for cooler stars and increases for more evolved stars (Christensen-Dalsgaard 2004; Dumusque 2016). For fully convective M dwarfs, these solar-like p-mode oscillations should exist but were not detected thus far as the expected photometric and RV amplitudes are of the order of a few μmag and cm s^{-1}, respectively, making such a detection challenging with current instruments (Rodríguez-López 2019). For solar-like and evolved stars where p-mode oscillations play an important role, it is advisable to mitigate the effect by applying an appropriate observing strategy, e.g., extending exposure times or combining multiple consecutive exposures into one (Dumusque et al. 2011c; Chaplin et al. 2019). According to Lovis & Fischer (2010), an exposure time of 15 minutes reduces the RV contribution of this noise source well below 1 m s^{-1}.

> *One person's data is another person's noise*
>
> **— K.C. Cole**

The field of asteroseismology uses such p-mode oscillations to derive model-independent stellar parameters like mass and radius of the star (see Chaplin & Miglio 2013, and references therein).

Granulation

Granulation on the stellar photosphere is caused by convection in the stellar envelope of Sun-like or later-type stars (Ramírez et al. 2009; Dumusque 2016). Hot bubbles of gas and plasma constantly rise towards the optically thin surface where they radiate away energy, then cool and sink back into the stellar envelope. This convection leads to bright blueshifted up-flows and darker redshifted down-flows visible on the stellar surface. The rising regions are larger than the sinking regions, and as a result, the spectroscopic shift due to the individual granules does not cancel out completely but results in an overall blueshift of the RVs. This affects RV measurements of Sun-like stars on the m s^{-1} level (Palle et al. 1995; Dumusque et al. 2011b). The timescales of individual granules are only on the order of a few minutes for Sun-like stars (Bahng & Schwarzschild 1961), but they tend to appear and disappear at similar positions as they are kept into place by the magnetic field of the star (Getling & Brandt 2002). Therefore, granulation is a positionally correlated noise source that does not average out as easily as stellar oscillations and may lead to systematic RV shifts.

The Sun shows granulation also on a larger scale with groups of granules of similar contrast. This effect is called super-granulation, and such structures have lifetimes of the order of a few days (Rieutord & Rincon 2010). For late-type stars, in particular M dwarfs, granulation and super-granulation is not a dominant noise source on the m s^{-1} level in the RVs as the net RV

effect decreases due to the lower surface temperatures and therefore smaller overall contrast and flow speeds between rising and sinking surface regions (Ludwig et al. 2002; Ramírez et al. 2009). The origin and properties of super-granulation are not investigated and still debated (Lovis & Fischer 2010).

Active regions modulated by stellar rotation

One of the most problematic sources of stellar intrinsic noise for RV measurements, particularly regarding M dwarfs, is stellar activity caused by active regions in the stellar photosphere. Magnetic fields cause these surface features due to the dynamo effect of rotating stars with convective envelopes (Charbonneau 2020). Stellar rotation is a primary driver of activity, and it was found that activity, stellar rotation, and age are correlated with each other (Skumanich 1972; Vilhu 1984; Suárez Mascareño et al. 2015, 2016; Wright et al. 2018). In general, the younger the star, the higher its activity level. For young stars (less than 1 Gyr) the RV variations due to activity can be on the order of several 100 $\mathrm{m\,s^{-1}}$ (Lovis & Fischer 2010; Brems et al. 2019). As a result, most RV surveys focus on old and slow rotating stars. The flux or RV signal of active regions is often modulated by the stellar rotation period, and such activity related Doppler signals can have similar periods and amplitudes as Keplerian signals due to orbiting planets (Boisse et al. 2011). The observing strategy can not fully mitigate such rotationally-related activity signals; on the contrary, it has happened that such signals were mistakenly published as planets.

A dominant reason of photospheric activity are stellar dark spots (starspots), which are regions of cooler temperature compared to the star's photosphere caused by magnetic flux loops emerging from the stellar surface (Solanki 2003). Starspots do not only occur on the Sun (sunspots) but are also observable and investigated on other Sun-like stars (Berdyugina 2005) and M dwarfs (Chugainov 1971; Irwin et al. 2011; West et al. 2015). Schrijver (2002) defines starspots as regions where the convective energy transport is significantly suppressed due to magneto-convective interaction. The connection of starspots to magnetic fields was discovered by the Zeeman splitting of spectral lines in the Sun (Hale 1908). The Zeeman splitting of spectral lines has also been observed for other stars (Semel 1989; Reiners & Basri 2007). Starspots can be explained well by flux tubes, a model abstraction of a cylindrical region where the magnetic fields are parallel to the cylindrical surface and vertical to the stellar surface (Topka et al. 1997). The brightness of flux tubes is a function of their size; small flux tubes are bright (faculae, see below), while large ones are dark and result in starspots (Solanki 1999).

Spots and faculae can cover a significant fraction of the stellar disk. The temperature contrast between the starspots and the quiet photosphere can range from a few hundred Kelvin up to

2000 K, with a strong dependency on the star's effective temperature (Schrijver 2002; Berdyugina 2005). For later type stars, e.g., M dwarfs, the temperature contrast decreases (Berdyugina 2005; Andersen & Korhonen 2015). Starspots will directly affect the measured stellar flux with an amplitude based on the star's covered fraction and the temperature contrast between spot and photosphere, while the modulation is based on the stellar rotation period. This effect is demonstrated in the top plot of Fig. 1.13, where I simulated two starspots for one full rotation of a star, using the tool `starry`[11] (Luger et al. 2019). The effect on the derived RVs, however, is less obvious.

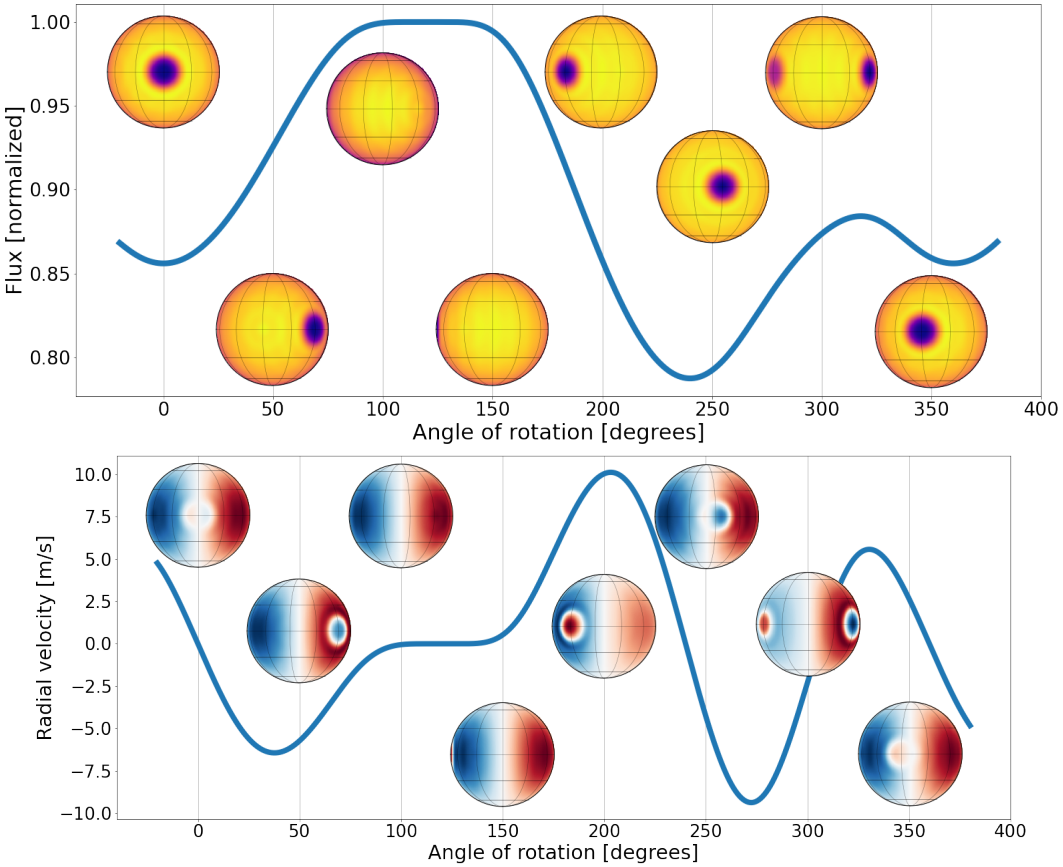


Fig. 1.13.: *Top:* Measured flux of one full rotation of a simulated star with two starspots of different temperature contrast compared to the photosphere and at zero latitudes. The spots have a 120° longitudinal distance from each other. *Bottom:* The stellar surface is color-coded with the appropriate RV shift (blueshift or redshift) of the spectral lines. Limb darkening and differential rotation effects were included for the stellar surface simulations, which adds some additional structure.

[11] https://luger.dev/starry/v1.0.0/

Due to stellar rotation, one half of the visible stellar surface moves towards the observer (blueshifted, negative RVs), and the other half moves away from the observer (redshifted, positive RVs). Without stellar surface features, this would result in a total RV signal of zero. However, the RVs of stars are measured from spectral absorption lines. Inhomogeneities of the photosphere result in asymmetries of the absorption lines leading to measurable RV variations as they slightly shift the measurement of the centroid of the spectral line (Saar & Donahue 1997). Using `starry`, I simulated the radial velocity map of the stellar surface with the same spot configuration as for the flux simulations. The corresponding plot is shown at the bottom of Fig. 1.13. As can be seen, the measurable RV variations due to these two starspots are not strictly sinusoidal but a superposition of signals with varying amplitudes and phases. The amplitude of the flux and RV variations depend on several factors, e.g., the stellar disk size or spot contrast.

The flux and RV signals due to active regions are even more complicated because they show dynamic evolution growing and decaying smoothly (van Driel-Gesztelyi & Green 2015) while traversing the stellar surface due to the stellar rotation. These two properties of active regions lead to quasi-periodic RV signals on timescales related to the stellar rotation. The lifetimes of starspots can range from a few hours to months (Solanki 2003; Dumusque 2016), and show a correlation with the spot size (Martinez Pillet et al. 1993; Hall & Henry 1994; Howard 2000; Robertson et al. 2020), and the effective temperature of the star. For later-type stars, spot lifetimes increase (Giles et al. 2017; Shapiro et al. 2020). The distribution of starspots is difficult to characterize as most stellar surfaces cannot be resolved. It is often only possible to measure the spot filling factors, which is the percentage of the visible surface area of the star that is covered by starspots (Andersen & Korhonen 2015). However, backward modeling of light curves, RV curves, or the spot filling factor is degenerate and may result in a large variety of possible configurations (Andersen & Korhonen 2015) that lead to the same flux or RV signals.

The distribution of sunspots is sometimes simplified as being a random stochastic process over the entire stellar surface, and such spot distributions have also been observed on some stars (Morin et al. 2010). However, observations of the Sun have shown that there are so-called "active longitudes" separated by 180°, where photospheric magnetic activity preferably emerges (Berdyugina & Usoskin 2003; Dumusque et al. 2011b). Such active longitudes were found to exist on other stars than the Sun, in particular on M dwarfs (see Moss 2004; Berdyugina 2005; Järvinen et al. 2005a,b; Lanza et al. 2009; Savanov 2014, and references therein). One caveat is, however, that a study by Jeffers & Keller (2009) showed that light curves of magnetically active stars could be described and approximated by two spots of different sizes and contrast that are 180° apart from each other, independent of the actual spot configuration. Another spot configuration which has been observed is that of only one active longitude (see for example Vida

et al. 2010). Preferred latitudes for the emergence of starspots around the Sun are around ±20° and change slightly over the activity cycles. This, along with the finite lifetimes of spots, lead to the observed so-called butterfly effect (Maunder 1904; Nielsen et al. 2019). For stars more active than the Sun, it seems as if large pole-on spots are possible, as found by Doppler Imaging[12] (see Andersen & Korhonen 2015, and references therein).

Other activity-related surface features include bright faculae and plages that can also be related to magnetic fields and appear close to active regions (Keller et al. 2004). In contrast to starspots, the magnetic field around faculae is not strong enough to suppress the convective flows, but the magnetic field evacuates the flux tubes, reducing the gas pressure and changing the opacity (Parker 1979; Topka et al. 1997). The smaller opacity allows an observer to see deeper into the stellar surface where it is hotter and therefore brighter (Keller et al. 2004). Plages can be related to faculae and are the chromospheric counterparts of them. For the Sun, faculae live longer than stellar spots, and for slow rotating less active stars, or stars in their activity minimum, there is evidence that faculae (and not starspots) are the dominant surface features (Shapiro et al. 2016, 2020). For solar-like and later-type stars, faculae affect the star's photometric variability more substantial than the RVs, which are typically spot-dominated (Bauer et al. 2018; Reinhold et al. 2019).

An additional complicating factor regarding magnetic activity related to stellar rotation is the differential rotation of the stellar surface. Differential rotation of the stellar surface has been observed for the Sun, and it is the result of angular momentum shifts due to the convection within the stellar envelope (Beck 2000). Differential rotation drives the generation of magnetic fields in the convective zone (Berdyugina 2005), and it leads to the fact that active longitudes are not fixed but change over time (Dumusque et al. 2011b). Differential rotation also limits the lifetimes of very large starspots (Berdyugina 2005), and spots at different latitudes rotate at different speeds, which then can complicate the measurement of any rotation period.

Stellar magnetic cycles

The Sun and other stars show magnetic cycles on timescales of several years, leading to a variation of the number of active regions on the stellar surface (Schwabe 1843; Baliunas & Vaughan 1985; Dumusque et al. 2011c). Such long-term activity cycles were also detected for M dwarfs (Savanov 2012; Robertson et al. 2013; Suárez Mascareño et al. 2016). It seems as if all stars with convective envelopes show magnetic cycles (Suárez Mascareño et al. 2016). For example, the

[12]Doppler Imaging monitors line-profile distortions to track the evolution of spots and reproduce stellar surface maps

Sun has a magnetic cycle of approximately 11 yr leading to an increasing and decreasing level of stellar activity (Suárez Mascareño et al. 2016). Additionally, there is a 3.7 yr solar flip-flop cycle responsible for spatial rearrangements of active regions, a consequence of the previously mentioned active longitudes (Berdyugina & Usoskin 2003; Moss 2004; Berdyugina 2005; Suárez Mascareño et al. 2016). Magnetic cycles affect RV and flux measurements due to variations of the filling factor of the active regions on the stellar surface (Dumusque et al. 2011c,b,a; Suárez Mascareño et al. 2016). Additionally, more active regions emerge and decay during a more active epoch, leading to larger RV amplitude variations due to stellar noise contributions.

The radial velocity method

2

> *A planet ten times the mass of Jupiter would be easy to detect, since it would cause the observed radial velocity of the star to oscillate with ± 2 km/s.*
>
> — **Otto Struve**
> (1897-1963)

2.1 Radial velocity techniques

2.1.1 Radial velocity precision

The precise measurement of the radial velocity of stars to detect exoplanets requires understanding, mitigating, and correcting effects that are several orders of magnitudes larger than the signals of the potential companions. This chapter will show how the field has evolved in the last decades to a point where today's modeling of RV data, obtained by state-of-the art instruments, is not limited by instrumental precision, but by the ability to model the stellar intrinsic noise.

The determination of radial velocity via Doppler shift relies on the precise measurement of spectral features. Stars emit most of their radiation from the ultraviolet (UV) to the mid-infrared (MIR), with the number of spectral features increasing towards shorter wavelengths. Since the Earth's atmosphere limits observations in the UV and MIR, most ground-based RV instruments focus on the optical wavelength range. The overall RV precision that can be achieved depends on the S/N of the continuum spectrum, the depth of the spectral line to the continuum of the spectrum, and the width of the spectral line. By assuming a nearly Gaussian shape for the spectral line, one obtains that

$$\sigma_{\mathrm{RV}} \sim \frac{\sqrt{\mathrm{FWHM}}}{C \cdot \mathrm{S/N}}, \tag{2.1}$$

where FWHM is the full width at half maximum of the spectral line and C is the contrast (line depth divided by the continuum level) (Seager 2010).

This equation highlights two limiting factors that affect the precision of RV measurements: spectral lines are intrinsically broadened by the rotation of the star, and measurements are restricted by the resolving power R of the spectrograph according to

$$R = \frac{\lambda}{\Delta\lambda}, \tag{2.2}$$

where $\Delta\lambda$ is the difference of the wavelength that can still be measured at λ. Typical state-of-the-art spectrographs for the detection of exoplanets have resolving powers of $R \sim 50,000$-$100,000$ so that a change of 1 km s^{-1} corresponds to a shift of only one pixel on the CCD (Wright 2018). The transformation from individual pixels to the wavelength is called a wavelength solution. One has to measure the shift of $1/1,000$ of a pixel or less to achieve the necessary precision needed for the detection of signals on the order of 1 m s^{-1} or smaller. This precision cannot be achieved on a single spectral line – this is why it is beneficial to have as many lines available as possible within a stellar spectrum – as long as they do not overlap (Bouchy et al. 2001). An additional problem is that the telescopes and spectrographs are usually not stable at this level of precision. The solution to this problem is a combination of stabilization and calibration (Wright 2018).

The early methods to measure RVs for binaries or galaxies during the 20th century, when the Doppler shift of the light was measured with respect to an emission line or laboratory values, had the problem that the reference lines did not track any changes of the light caused by the instruments and telescopes themselves, and the instruments were not stable enough. Several methods were developed towards the end of the 20th century to increase the precision, and finally, these methods allowed the detection of the first exoplanets. I will discuss the two most prominent methods that are also responsible for the recorded data that was used within this thesis.

2.1.2 Gas cell techniques

To track changes of the light of the star and its spectrum due to instrumental behavior, Campbell & Walker (1979) developed a technique where a sealed glass cell containing hydrogen fluoride (HF) was inserted into the light path of the telescope. The HF absorption spectrum is then superimposed to the stellar spectrum, so that both spectra suffer the same instrumental shifts until they reach the detector. The HF absorption lines serve as a reference grid against which any shift of stellar lines caused by the star — and not the instrument — can be measured. The HF gas

cell method allowed precise wavelength solutions spanning a range of about 50 Å (Campbell & Walker 1979; Seager 2010) and precise RVs down to the level of $10\,\mathrm{m\,s^{-1}}$ (Wright 2018).

The HF gas was later superseded by molecular iodine, which is nowadays the most commonly used gas for this method (Cochran et al. 2008). The iodine cell technique was first used by Butler et al. (1996), and it allowed to achieve an RV precision down to only $3\,\mathrm{m\,s^{-1}}$. The Iodine gas cell technique was used in most exoplanet detections in the first decade of RV surveys searching for exoplanets. The reason is that it was cost-efficient and relatively easy to retrofit older instruments and spectrographs with such an absorption cell and than turn them into planet hunting machines with precisions ranging from $1\,\mathrm{m\,s^{-1}}$ to $10\,\mathrm{m\,s^{-1}}$ (Wright 2018).

The iodine gas cell imprints a rich forest of molecular absorption lines onto the stellar spectrum. The wavelength range is from 5,000 Å to 6,200 Å and much larger than it was for the HF method. Additionally, the iodine absorption lines are dense and narrow compared to the more separate HF molecular lines. The narrower and denser lines are beneficial for modeling small-scale variations caused by the instrument (Cochran et al. 2008). For the instrument's long-term stability, it is required that the column density of the iodine gas in the cell remains constant. The gas cell usually is permanently sealed, and typical cells contain $1/1,000$ atmosphere of I_2 thermally stabilized to about 55° C, where iodine is in its gaseous state.

All gas cell techniques require exact modeling of the gas spectrum and the spectrograph line spread function to achieve the best precision. The observations obtained via the iodine cell technique are modeled as a product of two functions, the intrinsic stellar spectrum and the transmission function of the iodine cell. The product of these two quantities is then convolved with the spectrographs point spread function (PSF) and binned to the wavelength extent of the CCD pixels. The post-processing of the data is, however, difficult as a large number of free parameters have to be fitted for the PSF. For more details on the modeling and data reduction of RV observations obtained by the iodine gas cell technique, I refer to Butler et al. (1996) and Lovis & Fischer (2010). Additionally the precision of this technique is limited to about $1\,\mathrm{m\,s^{-1}}$. In this thesis, I use data from the High Resolution Echelle Spectrometer (HIRES; Vogt et al. 1994) installed at the Keck I telescope in Hawai'i, USA, which uses the iodine gas cell technique.

2.1.3 CARMENES as an example for the simultanous reference technique

Most of today's state-of-the-art high-resolution spectrographs for precise RV observations are stabilized (in temperature and pressure) and use the simultaneous reference technique (SRT).

Examples of such instruments are HARPS (Queloz et al. 2001b), ESPRESSO (Pepe et al. 2010), EXPRES (Jurgenson et al. 2016), SOPHIE (Perruchot et al. 2008) and CARMENES (Quirrenbach et al. 2010). RV data based on the SRT that is used within this thesis has been obtained by the CARMENES, HARPS, and SOPHIE instruments, and the CARMENES instrument has by far provided the most contributions. In this section, I will shortly introduce the CARMENES instrument and, in parallel, discuss the SRT on which the CARMENES instrument is based.

CARMENES is an instrument built explicitly for an exoplanet survey around M dwarfs that targets temperate and HZ planets. It was build and designed to reach long-term stability and radial velocity precision on the order of $1\,\mathrm{m\,s^{-1}}$ (Quirrenbach et al. 2010). The instrument consists of two high-resolution cross-dispersed echelle spectrographs covering the visual (VIS) and near-infrared (NIR) wavelength range. The spectrographs are connected via optical fibers to a front end, attached to the Cassegrain focus of the 3.5 m telescope at Calar Alto Observatory in Granada, Spain. The VIS channel covers the spectral range 0.52–0.96 µm and has a spectral resolution of $R = 93,400$, while the NIR channel covers the 0.96–1.71 µm range with a spectral resolution of $R = 81,800$ (Quirrenbach et al. 2014). Echelle spectrographs are an often used type of spectrograph for high-resolution RV instruments (Baranne et al. 1996). Échelle gratings have a large groove spacing, and their groove profile is shaped explicitly for large blaze angels resulting in high diffraction orders. This is beneficial for reaching a high resolving power. The overall optical layout of the CARMENES VIS spectrograph is provided in Fig. 2.1.

The SRT concept is based on the simultaneous injection and analysis of a science spectrum and a secondary reference spectrum to obtain a wavelength calibration before — and to track instrumental drifts during — the science observations. As such, a spectrograph based on the SRT consists of two channels, the science and the reference channel, and CARMENES is no exception: fiber A feeds the science observations to the CARMENES spectrograph while fiber B is providing the signals for the simultaneous calibration. The underlying assumption that justifies the SRT is that any instrumental changes affect both channels in the same way, as their light follows a similar path in the spectrograph (Lovis & Fischer 2010). The science observations, e.g., the starlight collected by the telescope and the reference spectrum, are generally coupled with fibers to the spectrograph, which has several advantages. The spectrograph does not need to be mounted to the telescope, which reduces mechanical flexure and instrumental vibrations, which are among the main contributors for instrumental RV jitter (Lovis & Fischer 2010).

As an additional side effect, this allows housing the spectrograph in the telescope dome's basement, where it is easier to shield the instrument from temperature and pressure changes. Some instruments are even built inside a vacuum chamber and temperature controlled by a cryostat. Controlling temperature and pressure of the spectrograph mitigates another main contributor of

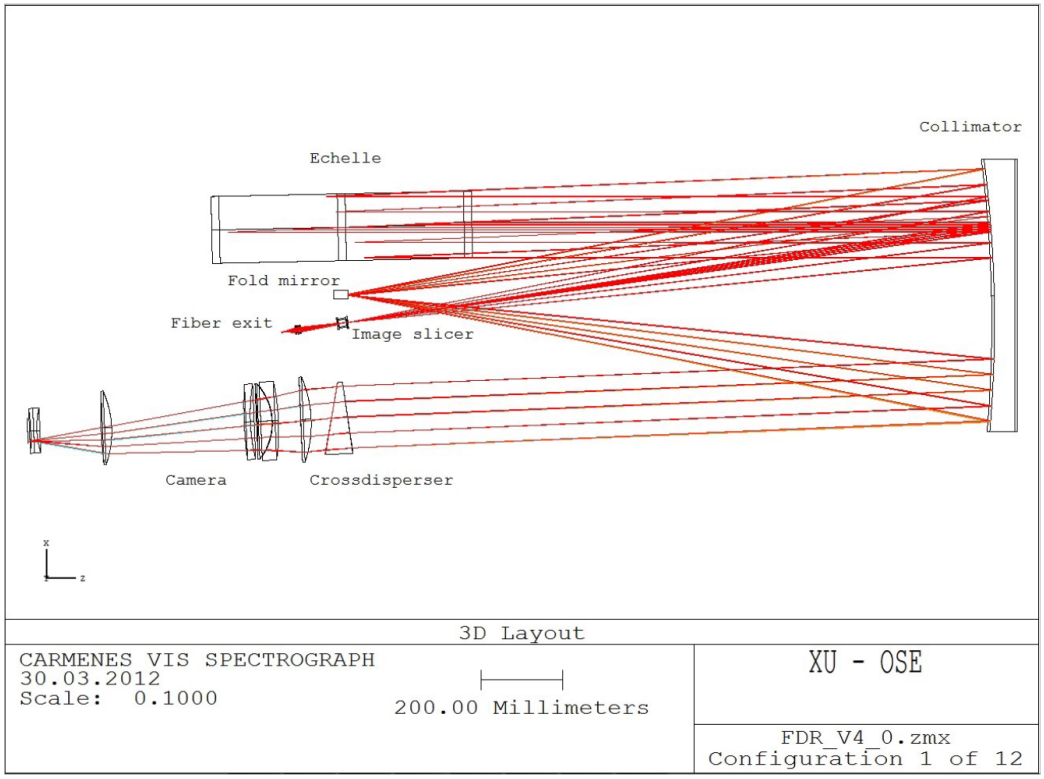


Fig. 2.1.: Layout of the CARMENES VIS spectrograph. *Credit:* Xu & Seifert (2012).

RV instrumental noise, which is variations of the air's refraction index inside the spectrograph (Lovis & Fischer 2010). In case of the CARMENES instrument the VIS channel's temperature is passively stabilized and follows seasonal changes on the order of ±0.2 K resulting into seasonal instrumental RV drifts on the order of 400 to 600 m s^{-1} that need to be tracked (Bauer et al. 2020). The CARMENES NIR channel is actively cooled to 140 K to reduce the noise contribution of the dark current. Last but not least, the coupling of the stellar light to the spectrographs via fibers scrambles the light. As such, it provides the spectrograph with a homogeneously and uniformly illuminated image of the scientific source, which reduces any external noise sources that affect the slit illumination, such as seeing or problems in the telescope guiding (Wright 2018).

The calibration of all SRT spectrographs is similar. Before the science observations start, the wavelength calibrations need to be done at the beginning of the night. This is crucial for the precise measurement of any wavelength shift with respect to the reference spectrum. In particular, the wavelength of the dispersed light that falls onto the detector is unknown, and it needs to be transformed from the pixels of the CCD detector to their absolute wavelength. The wavelength calibrations are carried out by injecting a calibration source into both fibers,

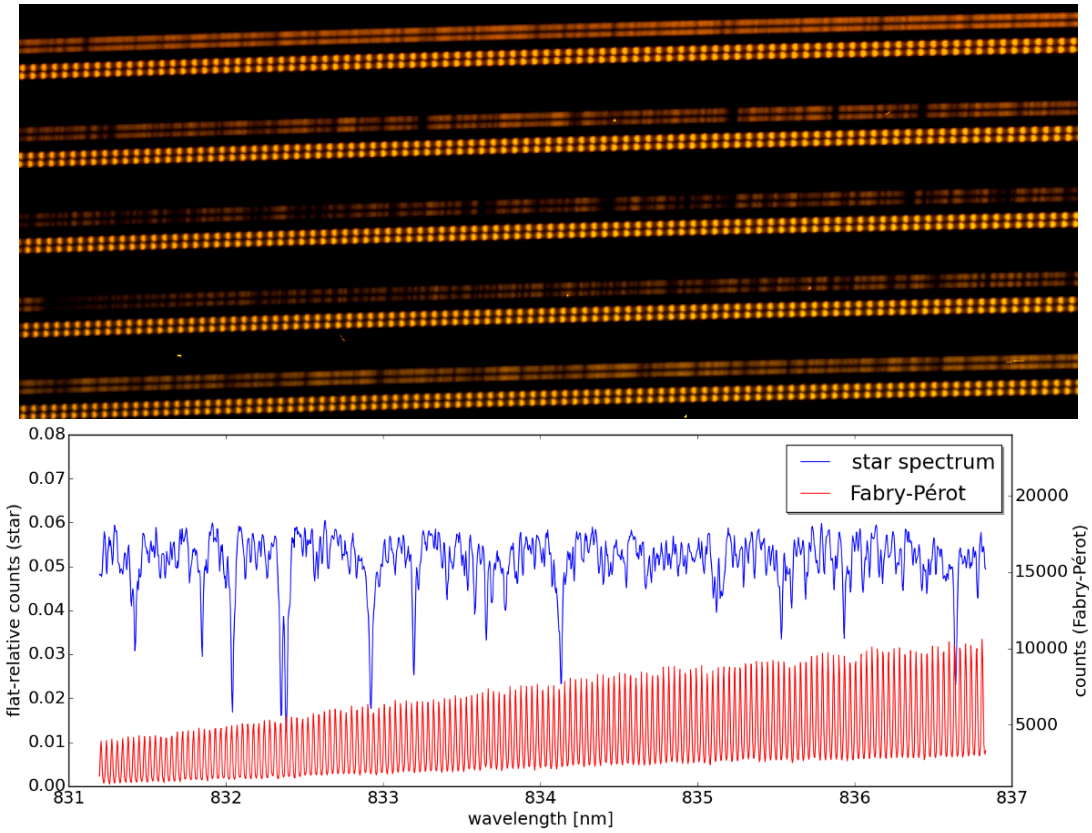


Fig. 2.2.: *Top:* Stellar spectrum and Fabry-Pérot spectrum on the CARMENES-CCD detector. *Bottom:* 1D spectrum of a star and the FP. *Credit:* Image and spectrum provided by Adrian Kaminski.

allowing an independent wavelength solution[1] for both channels. The calibration source is usually a thorium-argon (Th-Ar) lamp (Brown 1990; Baranne et al. 1996). But CARMENES operates in a wavelength regime, where argon would severely affect the obtained spectrum by emitting very bright spectral lines saturating the detector on the timescale that is needed to obtain a good thorium spectrum (Quirrenbach et al. 2018). Therefore, to obtain an optimal wavelength calibration over the complete wavelength coverage of the instrument, we instead use a variety of other lamps, namely thorium-neon (Th-Ne), uranium-neon (U-Ne), and uranium-argon (U-Ar) lamps (Quirrenbach et al. 2010, 2014).

The daily wavelength calibration is only valid for the moment it was obtained. To track any instrumental drifts during the night, the reference channel must be fed continuously with a calibration source. In principle, the calibration source can be one of the hollow-cathode lamps (HCLs)

[1] A function that maps from pixel to wavelength space and that is in general empirically obtained by fitting polynomials to the calibration spectrum.

mentioned before, but more advanced methods include using a Fabry-Pérot (FP) interferometer (Bauer et al. 2015) or a laser frequency comb (Wright 2018). For the CARMENES instrument's simultaneous calibration, we use FP etalons, mainly since the HCLs produce bright noble gas lines that are not favorable for the calibration of the instrument (Quirrenbach et al. 2018). Each channel, NIR and VIS, has its own FP etalon for the simultaneous calibration (Schäfer et al. 2018). Figure 2.2 shows a CARMENES VIS spectrum consisting of a science spectrum and the reference calibration spectrum provided by the FP.

The extraction and data reduction for CARMENES is done as follows. In a first step, standard dark and bias corrections and the tracing of the echelle-orders and wavelength calibration are performed by the reduction pipeline CARACAL (Caballero et al. 2016b). The derivation of RVs from the spectrum can be achieved in several ways. For example, it is common to use the cross-correlation function (CCF) technique to obtain precise RVs from stellar spectra (see for example Hill 1993; Queloz 1995; Pepe et al. 2002). The CCF method uses a binary mask that serves as a template that is correlated with the stellar spectra. The binary mask has only non-zero values at the positions of the rest-wavelengths of the stellar lines (Lovis & Fischer 2010). The template is cross-correlated with the spectrum. The CCF is compressing information of all spectral lines to one average line (Lovis & Fischer 2010). The CCF method is also used within the CARMENES consortium to obtain RVs and CCF activity indicators, like bisectors (see next section). However, the primary reduction pipeline used to derive RVs of the CARMENES instrument is based on the template-matching technique described in the next paragraph.

Anglada-Escudé & Butler (2012) suggested a methodology different from the CCF method to derive RVs from stellar spectra obtained via stabilized SRT spectrographs. Their method uses an individual stellar template of the observed star obtained by co-adding the same spectra used to derive the star's relative RVs. While Anglada-Escudé & Butler (2012) found only a small improvement of their methodology on the RV precision for G and K dwarfs compared to the CCF method, the improvement on the RV precision of M dwarfs was significant. The standard RV pipeline used for the CARMENES instrument is the SpEctrum Radial Velocity AnaLyser (`SERVAL`; Zechmeister et al. 2018), and it is based on the method suggested by Anglada-Escudé & Butler (2012). `SERVAL` determines RVs by co-adding all observed spectra of the target that reach a predefined signal-to-noise threshold and uses them to create one high S/N template of the star. Each spectrum's relative RVs are then derived with respect to the single high S/N stellar template using least-squares fitting (Anglada-Escudé & Butler 2012; Zechmeister et al. 2018).

2.1.4 Difficulties and limitations

Obtaining precise RVs for a star to detect an exoplanet requires to correct for a plenitude of effects that can be several magnitudes larger than the RV variations caused by the potential planet. The radial velocities obtained by high-precision spectrographs like CARMENES are generally corrected for the Earth's barycentric motion, secular perspective acceleration, and instrumental drifts. The quality of these corrections affects the RV precision that can be achieved.

Despite these corrections, CARMENES and other high-resolution spectrographs like HARPS and HIRES show small systematic nightly variations that limit the RV precision (Trifonov et al. 2018; Tal-Or et al. 2019; Trifonov et al. 2020). The origin of these systematic effects is not entirely understood, but for CARMENES there are some indications that it could be related to a differential drift between fiber A and fiber B (Pinto 2019) or the wavelength solution. The current strategy used to mitigate these nightly variations is the calculation of a nightly-zero point (NZP) offset. This is achieved by observing several RV quiet stars with a typical root mean square (RMS) smaller than $10\,\mathrm{m\,s^{-1}}$ during each night. These stars, referred to as "RV standard stars" within the CARMENES consortium, are used to calculate the NZP of the instrument. The NZP of each night is calculated as the weighted-average RV of the observed RV standard stars of that night. Further details on the calculation and different conditions are provided in Appendix A of Tal-Or et al. (2018).

In addition to the instrumental and calibration uncertainties and noise contributions, there is the stellar noise contribution that was previously discussed in Sec. 1.2.2. Spectral lines sensitive to the chromospheric or photospheric activity of the star and line shape analysis, e.g., the shape of the CCF encapsulated in the bisector and linewidth measurement, can indicate RV periodicities caused by stellar activity. Activity related signals will change the line shapes while planetary signals will have no significant effect on it (Hatzes 1996). A similar effect can be observed regarding the wavelength dependence of an RV signal. RVs caused by a planetary motion around the star will affect all RVs independent of the wavelength in the same way and with the same amplitude, but variations caused by stellar activity can be wavelength dependent. As an example: "*rotationally modulated spot-induced RV anomalies should be less pronounced in the infrared, where brightness temperature contrasts are lower*"(Wright 2018). This was one reason why the CARMENES instrument has an NIR arm, as one goal was to differentiate between activity and planetary signals by comparing their derived properties within the NIR and VIS channels.

2.2 Statistics and modeling of radial velocity data

This section presents different models and approaches applied to RV data throughout this thesis to obtain information about planetary parameters, dynamical interaction, stellar parameters, activity, and instrumental jitter. After a short introduction to Kepler and N-body models, I will focus on Bayesian inference. I will introduce Bayesian parameter estimation, define prior, posterior, and likelihood distribution and functions. I will also discuss the marginal likelihood, known as the model evidence, and how it can be used for Bayesian model comparison. Thereafter, I will give a short introduction to posterior estimation by using posterior sampling; in particular, I have used nested sampling throughout this thesis, and I will outline some of its advantages compared to the classical Markov chain Monte Carlo (MCMC) sampling method. Towards the end of this section, I will briefly discuss noise contributions and how they can be dealt with in a Bayesian framework.

2.2.1 Modeling of orbital parameters

Kepler models

In Eq. 1.4 and Eq. 1.10 I have defined the RV semi-amplitude K and how it can be related to the radial velocity. Seven parameters can describe an orbital motion in three dimensions. However, as discussed earlier, the longitude of the ascending node cannot be determined by the RV method, and the inclination and mass (or semi-major axis) can only be derived in combination since these two parameters are degenerate. As a result, a fit to a Keplerian orbit can be described by five observables when based on RV data. Equation 1.4 can be extended to more than one planet, and it is common to include a sixth parameter, the systemic radial velocity γ which represents a constant component of the RV of the system to the solar system barycenter in case of absolute RVs, or in the case of relative RVs an arbitrary instrumental-dependent offset (Dvorak 2007; Perryman 2011; Espinoza et al. 2019). The modeled RV contribution is given by

$$M_{\mathrm{rv}}(t) = \sum_{i=1}^{N} K_i \Big[\cos(\omega_i + \nu_i) + e_i \cos(\omega_i) \Big] + \sum_{j=1}^{I} \gamma_j, \tag{2.3}$$

where $M_{\mathrm{rv}}(t)$ represents the modeled RVs. This results in $5N+I$ parameters for a model of N planets and I instruments. Several realizations of modeled RV curves with different parameter combinations are shown in Fig. 2.3.

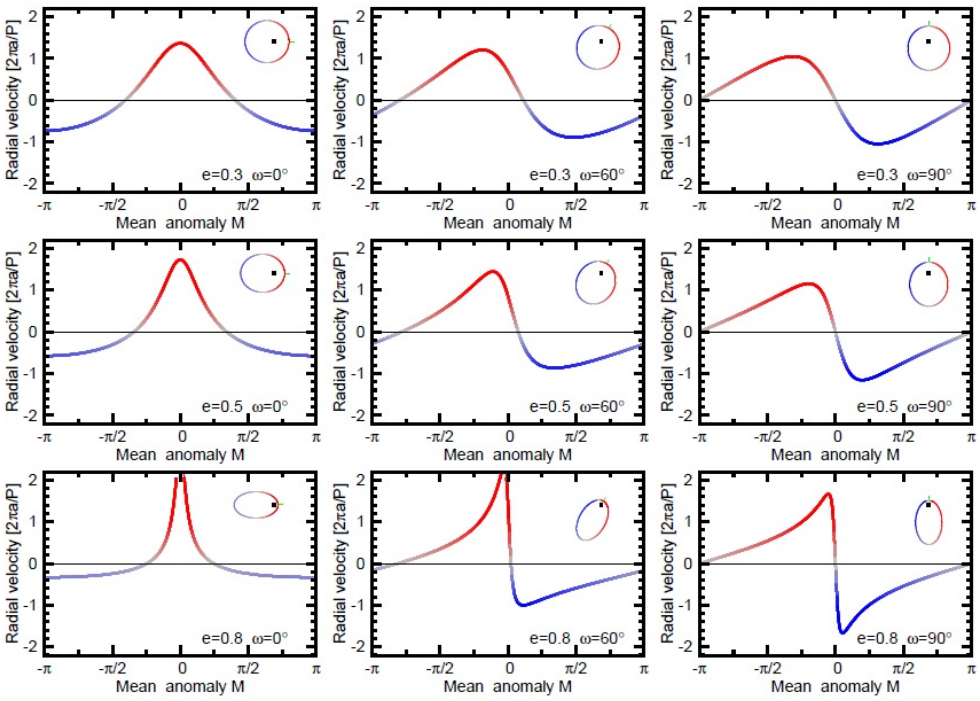


Fig. 2.3.: Calculated RV curves for different parameter realizations. Circular orbits with e=0 are not shown but result in a sinusoidal-like RV curve. The RV curve is color-coded by blue- and redshifted Doppler shifts in the measured spectrum and represent negative and positive RVs, respectively. The orientation of each orbit is given as a small ellipse drawn in the top right corner of each plot. *Credit:* This figure is from Zechmeister (2011).

Radial velocity measurements $v_r(t_n)$ are discrete samples that need to be compared to the predicted model $M_{\rm rv}(t_n)$ at the sampled observations at times t_n. It is common to use numerical methods, e.g., the Levenberg–Marquardt (LM) least-squares method (Press et al. 1992), to minimize the equation

$$\chi^2 = \sum_{t_n} \frac{(M_{\rm rv}(t_n) - v_{\rm rv}(t_n))^2}{\sigma_n^2}, \tag{2.4}$$

where σ_n is the standard deviation of the measured RV. This approach is referred to as χ^2 minimization, and it is, in general, a fast method to find a good model for the RV data. Nevertheless, χ^2 minimization has some drawbacks. One of the main problems is that such minimization techniques are susceptible to local minima of χ^2 and so the derived best-fit does not necessarily represent the global χ^2 minimum of the problem (Dvorak 2007). This can be problematic for large numbers of free parameters, e.g., more planets to be fitted, or data sets that are not sampled

ideally or have poor phase-coverage. For such problems, the χ^2 parameter space tends to be very rugged, and the LM method can be easily trapped in a local minimum.

Additionally, due to the high non-linearity of the RV fitting problem, such minimization techniques are very susceptible to the initially set parameter values. Another problem of the method is the difficulty of the uncertainty estimation of the derived fit parameters that often seem to be underestimated (Press et al. 1992; Ford 2005). The error estimation is particularly problematic when errors are rescaled such that $\chi^2_{\mathrm{red.}} = \frac{\chi^2}{n-p} = 1$, where n is the number of data points and p is the number of parameters. Such error rescaling uses several assumptions that are often not well justified: the errors need to be Gaussian distributed, the model needs to be linear (which often is not the case), and most importantly, by assuming $\chi^2_{\mathrm{red.}} = 1$ one claims that the used model is complete and that it correctly describes the problem (Andrae 2010).

Dynamic Models

For multi-planetary systems, the Keplerian approach to model the planetary orbits is only an approximation, as mutual perturbation between the planets can cause deviations from perfect Keplerian orbits. The deviations from a Keplerian orbit are larger for more massive bodies or tightly packed bodies or bodies in resonant configuration. The procedure to include mutual gravitational perturbation for RV data modeling is referred to as self-consistent, dynamical, or N-body-fitting (Laughlin & Chambers 2001, 2006; Dvorak 2007).

For N-body fits, the model $M_{\mathrm{rv}}(t)$ is calculated numerically by setting the planetary parameters as initial conditions for an N-body integrator and then integrating the system over the timespan of observations. The gravitational perturbations on the host star are then calculated for each observation time and translated to an RV, which is then compared to the measured RV, e.g., by using Eq. 2.4 and the LM method. This process is iteratively repeated for different initial osculating planetary parameters until a good fit of the data is found. Osculating planetary parameters are defined depending on a specific epoch and can change (osculate) over the observation due to the dynamical interaction.

It is common to start the minimization from the parameters obtained by the best multi-Keplerian fit (Laughlin & Chambers 2001), but depending on the system and strength of dynamical interaction it is possible that such a procedure is not sufficient. It seems that finding the correct start parameters for a dynamical fit is in particular difficult for systems with more than two planets, as the "χ^2 *landscape is topologically rugged on large scales*" (Laughlin & Chambers 2006). An alternative method that can be applied to find a dynamical fit solution is to gradually include the

dynamical interaction in an iterative fitting procedure that uses the previous step's fit results as the starting parameters (Laughlin & Chambers 2006).

2.2.2 Bayesian methods for the radial velocity analysis

There are two major approaches to statistical inference: the frequentist approach and the Bayesian approach. There main differences between the two is: in the frequentist view, a hypothesis is tested without applying any probability, whereas in the Bayesian view, a probability is assigned to every hypothesis in the form of a prior probability distribution. The frequentist concept of probability is related to the number of times an event occurs and is only defined for random variables (Díaz 2018). Frequentist methods provide probabilities conditioned only on hypotheses, e.g., the p-value, so any probability is based on the frequency of outcomes over many trial experiments. According to Trotta (2008) the frequentist definition of probability is: "*The number of times an event occurs divided by the total number of events in the limit of an infinite series of equiprobable trials*". The probability $p(x)$ describes how values of x would be distributed among infinitely many trials in the frequentist view. Examples of using the frequentist approach in this thesis include false-alarm probability calculations for periodograms and notably the software tool `AliasFinder` (Stock & Kemmer 2020), which was developed during this thesis.

However, most of the statistical methods that were applied in this thesis are based on Bayesian inference. In the Bayesian view, probability expresses the degree of belief of an event, and it updates that belief based on new evidence (observations) that are made. Bayesian probabilities quantify the uncertainty of the inference. Here, the probability $p(x)$ describes how the probability is distributed over the single possible but uncertain value of x. In contrast to the frequentist approach, the Bayesian approach offers the possibility to consistently combine information from different instruments with different priors. It also allows an adequate, robust, and realistic uncertainty estimation of the derived values as derived values are encoded in probability distributions, and it offers a self-consistent methodology for parameter estimation and model comparison (Parviainen 2018; Díaz 2018).

While in some cases, the Bayesian and frequentist approaches will result in consistent solutions, there are cases where they can differ significantly. As an example, the reliability of stellar masses for giant stars determined via evolutionary models has been discussed within the literature for the past few years, as it seems that some spectroscopic mass determinations are overestimated when compared to mass estimates from model-independent asteroseismic estimates. An analysis of 372 giant stars of the Lick survey based on a Bayesian approach by the author of this thesis (Stock

et al. 2018) was not able to detect a significant overestimation of stellar masses by spectroscopy or evolutionary models. This result was based on the comparison of a subsample of giant stars to independent asteroseismic mass measurements. One key ingredient used within the study by Stock et al. (2018) was the inclusion of priors in the analysis and fitting procedure, in the form of the stellar evolution time and the stellar initial mass function, which was not taken into account in many previous studies. This was also recognized in subsequent literature that extended on this problem: "*Here, we note that Stock et al. (2018), which showed the smallest mass-offset among our comparisons, is the only spectroscopic source that explicitly mention they take the stellar evolution speed into account when estimating the stellar masses*" (Malla et al. 2020).

The Bayesian approach offers more universality and versatility compared to the frequentist approach. It can deal with unique situations much more straightforwardly. It can assign probabilities to future outcomes, and it can take better into account any nuisance parameters that may influence the data (Trotta 2008). However, depending on the problem, both approaches can be valid. A recommended discussion of the frequentist and Bayesian approaches on the future of astrostatistics is provided within Loredo (2012). The complete modeling of RV data in this thesis is based on a Bayesian approach. I shortly outline the critical properties of such an approach.

Bayes' Theorem

The critical ingredient of Bayesian inference is Bayes' theorem, given as

$$P(\boldsymbol{\Theta}|\mathbf{D}, M) = \frac{P(\mathbf{D}|\boldsymbol{\Theta}, M)P(\boldsymbol{\Theta}|M)}{P(\mathbf{D}|M)}, \tag{2.5}$$

where $\boldsymbol{\Theta}$ is the parameter vector of the model M for the data $\mathbf{D}$, $P(\boldsymbol{\Theta}|\mathbf{D}, M) \equiv P(\boldsymbol{\Theta}, \mathbf{D})$ is the posterior probability distribution (hereafter often abbreviated as posterior), $P(\mathbf{D}|\boldsymbol{\Theta}, M) \equiv \mathcal{L}(\boldsymbol{\Theta})$ is the likelihood function, $P(\boldsymbol{\Theta}|M)$ is the prior probability distribution (hereafter often abbreviated as prior) and $P(\mathbf{D}|M) \equiv \mathcal{Z}$ is the marginal likelihood, also referred to as the Bayesian evidence or simply evidence (Trotta 2008). Bayes' theorem can be seen as a recipe to learn from previous experience and update the knowledge of a problem (Trotta 2008). In the following, I shortly discuss each ingredient of Bayes' theorem.

Likelihood function

The likelihood $P(\mathbf{D}|\mathbf{\Theta}, M) \equiv \mathcal{L}(\mathbf{\Theta})$ is a measure for the probability of data given specific parameters of a model (Díaz 2018), but it does not represent a probability distribution as its integral can be indefinite. The likelihood plays an essential role in parameter estimation. In the case of uncorrelated uncertainties (so-called white noise) and a deterministic, parameterizable model, the likelihood is given as the product of the independent likelihoods $\mathcal{L}(\mathbf{\Theta}) = P(\mathbf{D}|\mathbf{\Theta}) = \prod_i P(D_i|\mathbf{\Theta})$. Whereas if the errors are Gaussian distributed, the joint likelihood is given as

$$\mathcal{L} = \prod_{i=1}^{N} \frac{1}{\sqrt{2\pi}\sigma_i} \exp\Big(- \frac{(d_i - m(t_i, \mathbf{\Theta}))^2}{2\sigma_i^2} \Big), \tag{2.6}$$

where $m(t_i, \mathbf{\Theta})$ is the model function, given some independent time variable t_i and the parameter vector $\mathbf{\Theta}$ (Díaz 2018).

The likelihood function has an extensive dynamical range. Therefore, for numerical reasons, it is common to use the natural logarithm given as

$$\ln(\mathcal{L}(\mathbf{\Theta})) = -\frac{N}{2}\ln(2\pi) - \frac{1}{2}\sum_{i=1}^{N} \ln \sigma_i^2 - \frac{1}{2}\sum_{i=1}^{N} \frac{(d_i - M(t_i, \mathbf{\Theta}))^2}{\sigma_i^2}, \tag{2.7}$$

where $-\frac{N}{2}\ln(2\pi)$ is a constant and $\frac{1}{2}\sum_{i=1}^{N} \frac{(d_i - M(t_i,\mathbf{\Theta}))^2}{\sigma_i^2} = \frac{\chi^2}{2}$ is equivalent to the χ^2 statistic. The middle term $\frac{1}{2}\sum_{i=1}^{N} \ln \sigma_i^2$ prevents the likelihood from becoming arbitrarily large when including an additional nuisance parameter for error rescaling or jitter estimation into the model (Baluev 2009; Díaz 2018). However, the likelihood and log-likelihood will always increase, or at least stay constant, when adding more parameters to the model, due to the increased flexibility of the model.

Prior distribution

The prior distribution $P(\mathbf{\Theta}|M) \equiv \pi(\mathbf{\Theta})$ plays a fundamental role in Bayesian inference to derive any posterior distribution (Trotta 2008). It sits at the core of the Bayesian methodology and is an inherent feature. *"The guiding principle of Bayesian probability theory is that there can be no inference without assumptions"* (Trotta 2008). However, prior distributions have been a controversial feature of Bayesian theory as, at first glance, it seems as if results based on the Bayesian methodology are sensitive to subjective assumptions, which however is not the case

(Trotta 2008; Díaz 2018). Even though the prior distribution includes assumptions on the problem and represents the initial degree in the belief of the parameters given the data (Díaz 2018), its definition follows some specific objective rules.

In cases where no or little information about a possible prior distribution is available, so-called ignorance priors, "*i.e., priors reflecting a state of indifference with respect to symmetries of the problem considered*" (Trotta 2008), should be used. The most common prior distribution in this family is the uniform distribution, also referred to as "flat" prior, and it is given by

$$P(\mathbf{\Theta}|\mathbf{D}) = \text{const} \quad \forall\, \mathbf{\Theta} \in [\mathbf{a}, \mathbf{b}], \tag{2.8}$$

where **a** and **b** are the lower and upper boundaries of each parameter of the parameter vector. The notation $\mathcal{U}(a_i, b_i)$ is used throughout this thesis and it is an abbreviation for a uniform prior with the boundaries a_i and b_i. The uniform prior is an uninformative prior that does not prefer any specific values of the parameters as long as it is within the boundaries that, by definition, still represent some prior belief. However, the boundaries can, in principle, be arbitrarily set to small and large values. The uniform prior should be preferentially used in cases where the functions depending on $\mathbf{\Theta}$ are linear, and not much information about possible parameter values is known before considering the data.

In cases of non-linear functions on $\mathbf{\Theta}$, flat priors can be dangerous as they are not uniform on that function. As an example, if the possible parameters span a sizable dynamical range, it can be better to use the log-uniform prior, also known as log-flat or Jeffreys prior, given as

$$P(\mathbf{\Theta}|\mathbf{D}) = \frac{\text{const}}{\mathbf{\Theta}} \quad \forall\, \mathbf{\Theta} \in [\mathbf{a}, \mathbf{b}] \tag{2.9}$$

(Jeffreys 1946; Díaz 2018) and abbreviated as $\mathcal{J}(a_i, b_i)$ for a certain parameter.

In cases where a-priori knowledge of the parameters is better constrained, either by physical or mathematical fundamental knowledge or any previous observations on some data, it is common to use more informative priors. For example, it is possible to use the normal distribution (see Eq. 3.1), abbreviated as $\mathcal{N}(\mu, \sigma)$ as an objective prior.

As different as prior distributions can be, as long as they include regions where the likelihood is large, they will converge to a common objective solution of the problem (Trotta 2008). Although, in theory, this always should be the case, in practice, one is sometimes limited by the quality of the data resulting in posterior probabilities that still depend on the prior. Such cases are

complicated and need to be well analyzed to infer to which degree the solution is based on the prior. Nevertheless, even in cases where different prior lead to different non-consistent solutions, an objective outcome is provided by Bayesian methodology, which is that data quality is not sufficient to constrain the problem or model. Therefore, any results or wrong conclusions obtained from the Bayesian methodology are often subject to wrong assessments by the user and not a cause of the methodology itself.

Bayesian evidence

The Bayesian evidence $\mathcal{Z} \equiv P(\mathbf{D}|M)$ is the probability of the data, given the model, and it serves as the normalization factor of the parameter posterior distribution. It can be obtained by integration of the posterior over the entire parameter space. As such, it can be calculated as

$$\mathcal{Z} \equiv P(\mathbf{D}|M) = \int_{\Omega_{\mathbf{\Theta}}} \mathcal{L}(\mathbf{\Theta})\pi(\mathbf{\Theta})d\mathbf{\Theta}, \tag{2.10}$$

where the integral is spanning the entire domain $\Omega_{\mathbf{\Theta}}$ of $\mathbf{\Theta}$. For complex data and large dimensions, this integral cannot be analytically derived, and numerical methods, which often come along with high computational costs, have to be used (Parviainen 2018). While the Bayesian evidence can usually be ignored for parameter estimation, it is extremely powerful and useful regarding model comparison, which will be discussed at the end of Sec. 2.2.2.

Posterior distribution

The posterior distribution provides information about the parameters $\mathbf{\Theta}$ of the model, given the prior and likelihood (Parviainen 2018). "*The posterior is the relevant quantity for Bayesian inference as it represents the state of belief about the hypothesis after considering the information in the data*" (Trotta 2008). It is common to use some estimator, e.g., the mean or median, to specify the properties and the degree of uncertainty of the posterior distribution of a parameter of interest.

Parameter inference within a Bayesian framework

Here I shortly outline how Bayesian inference works and then I show how the RV data within this thesis is modeled. The general approach is outlined as the follows. A physically motivated

model with parameters $\boldsymbol{\Theta}$ has to be chosen, together with a prior for each parameter. These can be "flat" for uncertain prior knowledge or represent a previous estimate's posterior distribution on the parameter. As an example for the latter, the posterior of the rotation period provided by photometry can be used as an estimate for the rotation period prior when taking into account the stellar activity contribution in the RV data with a noise model.

The primary step within the inference process is constructing a likelihood function that represents the problem and measurements. In the case of measurements with Gaussian noise, one can use the likelihood function that is given in Eq. 2.7. With a likelihood function and a prior distribution, it is then possible to obtain the joint posterior distribution of all parameters by using Bayes' theorem. The Bayesian evidence as a normalization factor can be ignored for the parameter inference. One can marginalize (see Sec. 3.2.3 for a short and intuitive introduction to marginalization) over the nuisance parameters to obtain the posterior of the parameter of interest from the joint posterior distribution

$$p(\phi|\mathbf{D}, M) \propto \int L(\phi, \psi) p(\phi, \psi|M) d\psi, \tag{2.11}$$

where the parameter vector $\boldsymbol{\Theta}$ is divided in nuisance parameters ψ and parameters of interest ϕ (Trotta 2008). In most cases, it is not possible to derive the posterior distribution analytically. However, one can estimate the posterior distribution by drawing samples from the posterior using numerical methods, e.g., Markov Chain Monte Carlo (see Sec. 2.2.3) or Nested Sampling (see Sec. 2.2.3). In the last step of the process, it is common to summarize the posterior by some summary statistic, e.g., the posterior distribution's median values.

Model comparison within a Bayesian framework

New computational methods, e.g., nested sampling (Skilling 2004), have reduced the computation time of the Bayesian evidence and allowed Bayesian model comparison to become popular among astronomers. Bayesian model comparison, which uses the Bayesian evidence (defined in Eq. 2.10), is a powerful method to compare distinct or nested models with different numbers of parameters and complexity with one and other. Since the Bayesian evidence $P(\mathbf{D}|M)$ is the probability of the data given the model, one can calculate the posterior of the model given the data by applying Bayes' theorem resulting into

$$P(M|\mathbf{D}) = \frac{P(\mathbf{D}|M)P(M)}{P(\mathbf{D})}, \tag{2.12}$$

where $P(M)$ is the prior distribution of the model and $P(\mathbf{D})$ a normalization factor that only depends on the data. The models' prior is usually assigned as $1/N_m$, where N_m is the number of models, so no model is preferred (Trotta 2008). Similar to the inference of the parameters, one can neglect the normalization factor if one is only interested in the posterior distribution of the model, so that $P(M|\mathbf{D}) \propto P(\mathbf{D}|M) \cdot P(M)$. In the case shown in Eq. 2.12 the Bayesian evidence fills the role the likelihood had in the parameter estimation. It is now possible to compare two models by calculating the ratio of the posterior probabilities, also referred to as posterior odds given as

$$\frac{P(M_0|\mathbf{D})}{P(M_1|\mathbf{D})} = B_{01} \frac{P(M_0)}{P(M_1)}, \tag{2.13}$$

where B_{01} is the Bayes factor given as

$$B_{01} = \frac{P(\mathbf{D}|M_0)}{P(\mathbf{D}|M_1)} = \frac{\mathcal{Z}_0}{\mathcal{Z}_1} \tag{2.14}$$

and represents the ratio of the models' evidence (Trotta 2008). In the case of equal prior probabilities for the models, these simplify to unity, and the model comparison can be made using only the Bayes factor. As for the likelihood, it is common to use the log-evidence $\ln(\mathcal{Z})$ instead of the evidence. Since $\ln(\frac{\mathcal{Z}_0}{\mathcal{Z}_1}) = \ln(\mathcal{Z}_0) - \ln(\mathcal{Z}_1)$ one can compute the difference of the log-evidence of the models given as $\Delta \ln(\mathcal{Z})$. To assess the strength of the evidence in favor of one model, it is common to use the so-called Jeffreys' scale, which has been empirically calibrated (Jeffreys 1961; Trotta 2008). Thresholds are at $\Delta \ln(\mathcal{Z}) = 1$, $\Delta \ln(\mathcal{Z}) = 2.5$, and $\Delta \ln(\mathcal{Z}) = 5$ with odds of about 3:1, 12:1, and 150:1, respectively and within this thesis I follow the convention of Trotta (2008) that these represent weak, moderate, and strong evidence in favor of the model with higher log-evidence.

The main property which makes the Bayesian evidence so powerful for model comparison is the automatic trade-off between the model fit and the model complexity, which refers to the Ockham's razor principle: "*Pluralitas non estponenda sine neccesitate*"(William of Ockham, ca. 1285-1349) which is Latin and translates to "*entities should not be multiplied without necessity*". In the sense of Bayesian model comparison, this means that the simplest model explaining the data should be preferred. Choosing the model with the highest likelihood is not an appropriate method for choosing the best model since increasing the parameters will in most cases lead to a better fit of the data resulting in over-parameterization and a poor generalization of the model for future data points.

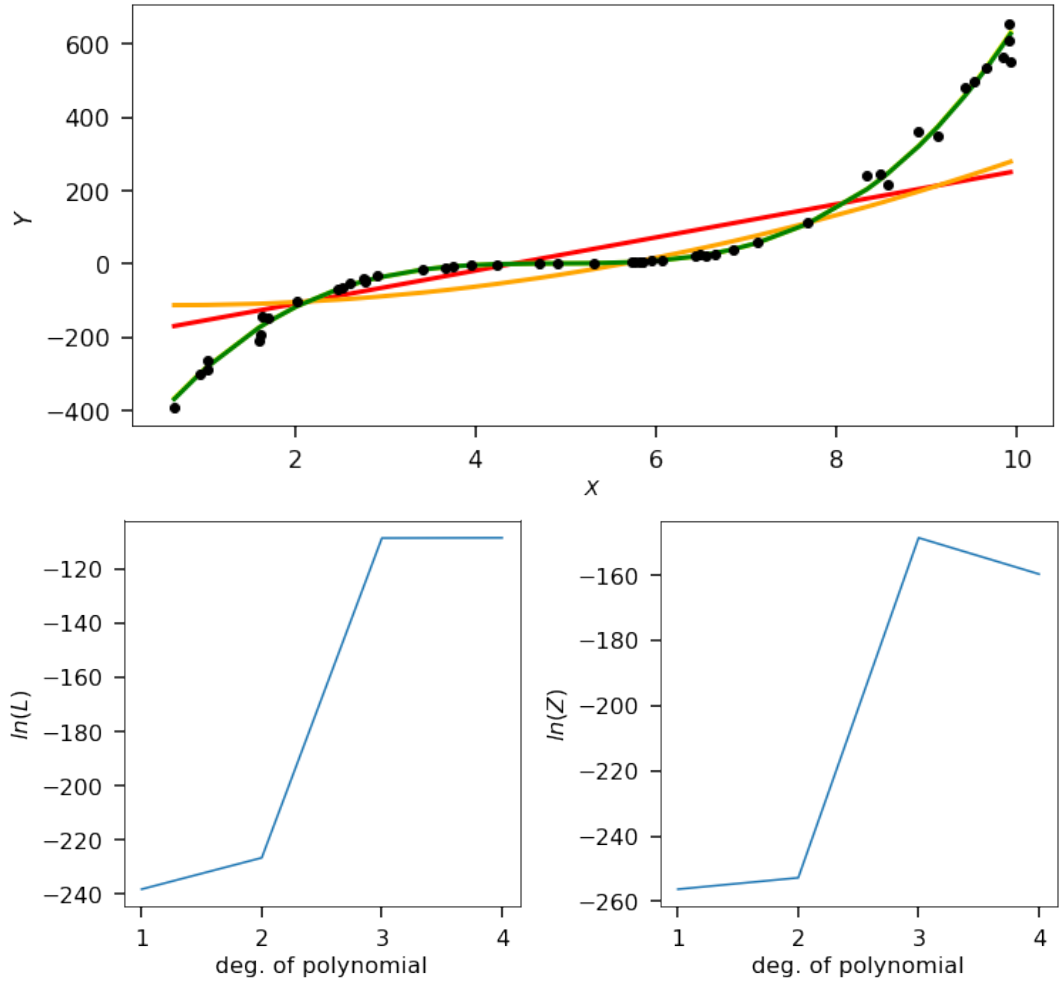


Fig. 2.4.: *Top:* Polynomials of order one, two, three and four were fitted to data that follows a polynomial of order three by using posterior nested sampling. *Bottom left:* Log-likelihood of the fits. *Bottom right:* Log-evidence of the fits.

An example is the fitting of polynomials to data points. The higher the order of polynomials, the better they may fit the data, increasing the maximum likelihood and the computation time. Additionally, such overfitted high-order polynomials will, in most cases, perform poorly when estimating new data. An example is shown in Fig. 2.4 where 50 data points based on the polynomial function $f(x) = 5(x-5)^3 + 2(x-5)^2 + (x-5) + 1$ were simulated together with some white noise assumption for each data point. Nested sampling (see Sec. 2.2.3 below) with `dynesty` (Speagle 2020) was then used to estimate the evidence and sample the posterior for polynomial models of the form of $a_0(x-5)^0 + a_1(x-5)^1 + ... + a_n(x-5)^n$ up to $n = 4$. A uniform prior for each parameter of the form $a_n = \mathcal{U}(-1000, 1000)$ has been adopted for this example.

As can be seen, the log-likelihood and the log-evidence increase up to the polynomial model of order three. Higher orders resulted in a stagnation of the log-likelihood and a decrease of the log-evidence. Therefore, as expected, the best model is the polynomial model with order three. It has a significant log-evidence difference of $\Delta \ln(\mathcal{Z}) = 11.1$ compared to the second-best model, which was the polynomial of order four. Since the prior distribution included zero, the parameter a_4 was estimated to be zero within uncertainties for the fourth-order polynomial.

Since the Bayesian evidence is the integral spanning the entire domain of possible parameter values, it is smaller when the parameter space, in this particular case also referred to as prior volume, is larger but does not include a significant log-likelihood contribution. This is why the log-evidence of the example provided above decreased while the quality of the model fit stayed constant. Therefore, the Bayesian evidence can be regarded as the "*average of the likelihood under the prior for a specific model choice*"(Trotta 2008). This average is larger when there is a small volume with high likelihood, and the average is smaller for large volumes where the likelihood is small on most of the volume. Additionally, a larger uniform prior will reduce the evidence estimate since it reduces the contribution of high-likelihood posterior regions. Therefore it is of utmost importance to take care when choosing the priors for model comparisons.

It is worth noting that the model comparison is taking place on a level that is above the parameter inference. However, it does not replace the inference, which still needs to be performed for each model. As the Bayesian evidence also depends on the prior probabilities of the parameters, it is sensitive to the choice of prior, and, therefore, it is essential to analyze the sensitivity of the model comparison result based on the prior choice. In cases where nested models are compared with each other, this means, in particular, to not apply any changes to the prior volume of the subset of the parameters in the underlying nested model.

2.2.3 Posterior sampling

The derivation of the posterior probability from the likelihood and prior distribution can be complicated, and in many cases, it is not possible to obtain this distribution analytically. However, several numerical methods are capable of estimating the posterior distribution. This chapter will introduce two such methods: MCMC and nested sampling. The focus is on nested sampling since it was mainly used within this thesis.

Markov chain Monte Carlo

A widely used approach to estimate posterior distributions is the MCMC method. There are various variations of the MCMC method, and here I discuss the widely used Metropolis-Hastings algorithm (Metropolis et al. 1953; Hastings 1970). This method's basic idea is to start a chain from some (random or arbitrary) point in the parameter space, and each new step of the chain is proposed through a random walk. A caveat is therefore given by the fact that an initial parameter vector is required. In general, a new point is accepted if the likelihood is better than that of the previous point. Nevertheless, to estimate the posterior distribution, points of smaller likelihood must be accepted in some cases. A new point is accepted by calculating the posterior density ratio between the proposed and current location. The probability for acceptance is given as

$$p_{\mathrm{acc.}} = \frac{p_{\mathrm{prop.}}}{p_{\mathrm{curr.}}} = \frac{\frac{P(\mathbf{D}|\mathbf{\Theta}_{\mathrm{prop.}},M)P(\mathbf{\Theta}_{\mathrm{prop.}}|M)}{P(\mathbf{D}|M)}}{\frac{P(\mathbf{D}|\mathbf{\Theta}_{\mathrm{curr.}},M)P(\mathbf{\Theta}_{\mathrm{curr.}}|M)}{P(\mathbf{D}|M)}} = \frac{\pi(\mathbf{\Theta}_{\mathrm{prop.}})\mathcal{L}(\mathbf{\Theta}_{\mathrm{prop.}})}{\pi(\mathbf{\Theta}_{\mathrm{curr.}})\mathcal{L}(\mathbf{\Theta}_{\mathrm{curr.}})}\frac{P(\mathbf{D}|M)}{P(\mathbf{D}|M)} \tag{2.15}$$

(Trotta 2008; Díaz 2018). Given this equation, the MCMC algorithm will visit high posterior probability regions more often than regions of low posterior probability. However, any point is saved within the chain to estimate the posterior distribution later on. It is common to remove some samples of each chain's start, as these tend to be at low posterior density positions. This is referred to as chain warm-up or burn-in (see Parviainen 2018, and references therein). Additionally, as can be seen from Eq. 2.15 the Bayesian evidence $P(\mathbf{D}|M)$, which is difficult to calculate, cancels out and is not required when estimating the posterior distribution using MCMC methods. Most MCMC methods cannot compute the Bayesian evidence and tend to have problems estimating multi-modal posterior distributions (Trotta 2008; Parviainen 2018; Díaz 2018; Speagle 2020).

MCMC methods approximate the posterior distribution asymptotically by the convergence of the chains. However, an inherent problem of MCMC algorithms is to decide when to end the sampling and estimate chain convergence. Several analytical tools were developed to test the convergence of chains. To improve convergence time, to test convergence, and reduce problems for multi-modal posterior distributions, it is common to run large numbers of chains in parallel starting at different parameter space locations. Comparing the chains with each other can be used as a diagnostic tool of chain convergence, e.g., the Gelman-Rubin diagnostic (Gelman & Rubin 1992).

Nested Sampling

Nested sampling (Skilling 2004) is a Monte Carlo sampling method that is very efficient in calculating the Bayesian evidence. In contrast to MCMC, which estimates the posterior density distribution directly by sampling from it, nested sampling focuses on estimating the Bayesian evidence, and the posterior density distribution follows as a by-product. Advantages of nested sampling are a well-defined stopping criterion for the sampling, generation of a sequence of independent samples, and a trivial parallelization of the sampling algorithm (Speagle 2020). Furthermore, nested sampling is well suited for estimating multi-modal posterior distributions, and it is more efficient than MCMC for such problems (Feroz & Skilling 2013; Speagle 2020). Additionally, no initial parameter vector is required for nested sampling, as it samples from the whole prior volume.

The fundamental concept of nested sampling is based on the concept of estimating the Bayesian evidence by reducing the multi-dimensional integral of the evidence through re-factorization into a one-dimensional integral that is taken over the prior volume X of an enclosed parameter space (Speagle 2020). The idea is to use a likelihood threshold λ to define an iso-likelihood contour $\mathcal{L}(\boldsymbol{\Theta}) \geq \lambda$ that constrains the prior volume, so that this prior volume is given as

$$X(\lambda) = \int_{\Omega_{\boldsymbol{\Theta}}:\mathcal{L}(\boldsymbol{\Theta})\geq\lambda} \pi(\boldsymbol{\Theta})\mathrm{d}\boldsymbol{\Theta}, \tag{2.16}$$

and the integral extends over the region of parameter space contained within the iso-likelihood contour. The prior distribution is a normalized quantity, and therefore it follows that $X(\lambda \to 0) = 1$ and $X(\lambda \to \infty) = 0$, which then allows the transformation of the Bayesian evidence integral to

$$\mathcal{Z} = \int_{\Omega_{\boldsymbol{\Theta}}} \mathcal{L}(\boldsymbol{\Theta})\pi(\boldsymbol{\Theta})\mathrm{d}\boldsymbol{\Theta} = \int_0^1 \mathcal{L}(X)\mathrm{d}X, \tag{2.17}$$

where $\mathrm{d}X = \pi(\boldsymbol{\Theta})\mathrm{d}\boldsymbol{\Theta}$, and $\mathcal{L}(X)$ is the inverse of Eq. 2.16 and a monotonically decreasing function of X, where $0 < X_i < ... < X_1 < X_0 < 1$ is a sequence of decreasing values (Skilling 2006; Feroz & Skilling 2013; Speagle 2020). The transformation from $\boldsymbol{\Theta}$ to X means that the unit prior volume is divided into small sub-elements, which are then sorted by their likelihood. It is then possible to approximate the evidence by using the weighted sum

$$\mathcal{Z} = \sum_{i=1}^{M} \mathcal{L}_i w_i, \tag{2.18}$$

where $\mathcal{L}_i = \mathcal{L}(X_i)$ are the sorted likelihoods at the finite and decreasing values of X_i and the weights are usually calculated by the trapezium rule so that $w_i = \frac{1}{2}(X_{i-1} - X_{i+1})$ (Feroz & Skilling 2013). Nevertheless, this estimate of the evidence has some uncertainty as it is difficult to assess the prior volume.

The function $\mathcal{L}(X)$ can be approximated by using random Monte Carlo sampling from the prior distribution. Since the prior distribution, by definition, is known exactly, it is possible to sample a number i of different $X_i(\boldsymbol{\Theta})$ within the provided prior volume to obtain a noisy estimate of $X(\boldsymbol{\Theta})$ and $\mathrm{d}X = \pi(\boldsymbol{\Theta})\mathrm{d}\boldsymbol{\Theta}$ (Speagle 2020). The basic nested sampling algorithm works in the following way. An initial number of i different samples $\{\boldsymbol{\Theta}_1 ... \boldsymbol{\Theta}_i\}$ are drawn from the predefined prior distribution, referred to as live points. Each live point corresponds to a specific computable likelihood value $\mathcal{L}_i$, hence to prior volume X_i. After computing the likelihood of all initial samples, the live point with the lowest likelihood is removed, and its likelihood and value are stored. Then a new live point is drawn that meets the criterion that its likelihood is larger than that of the removed live points ($\mathcal{L}_{i+1} > \mathcal{L}_i$). By this definition, the new live point is positioned within a smaller prior volume region in a new iso-likelihood contour. This process is repeated until the sampler meets the stopping criterion. After the sampling has stopped, the live points are uniformly redistributed within the final prior volume. Since nested sampling provides an estimate of the Bayesian evidence, a well-suited stopping criterion is given when the sampling process reaches a certain log-evidence improvement threshold per iteration. Mathematically this means that sampling is stopped if $\Delta\hat{\mathcal{Z}}_i \equiv \ln(\hat{\mathcal{Z}}_i + \Delta\hat{\mathcal{Z}}_i) - \ln(\hat{\mathcal{Z}}_i) < \epsilon$, where $\Delta\hat{\mathcal{Z}}_i$ is the estimated remaining evidence and ϵ is the tolerance that needs to be defined for the sampler (Speagle 2020).

While nested sampling provides several benefits mentioned at the beginning of this section, there are also some downsides. It is important to note that unlike MCMC, nested sampling depends on correctly specified priors. The prior probability distribution has to be integrable to unity since nested sampling draws randomly from the prior distribution, e.g., uniform priors need to be bounded. It is also essential to understand that the evidence is dependent on the prior volume, as discussed already. Another problem is that the remaining evidence $\Delta\hat{\mathcal{Z}}_i$ is unknown. Although an upper bound can be estimated by $\Delta\hat{\mathcal{Z}}_i \leq \mathcal{L}_{\max} X_i$ where $\mathcal{L}_{\max}$ is the maximum likelihood value obtained within the prior volume and X_i the prior volume at the current iteration, there exists a small possibility that the sampler stops too early. This can happen for problems where there is a likelihood peak which is too narrow within the prior volume that has not been discovered by the live points.

Additionally, Speagle (2020) mentions the following drawbacks, which I summarize here: most nested sampling algorithms rely on sampling from a uniform prior distribution, hence it is essential

to know the appropriate prior transform for more general distributions. Additionally, the evidence depends on the size of the prior volume to be integrated over. Therefore the runtime of the sampler depends on the prior volume and prior distribution. Less informative and broad priors lead to a significant increase in the computation time until the sampler reaches the stopping criterion. Because the number of live points is fixed initially and kept constant during the sampling process, the integration rate over the posterior is the same, independent of where live points lie within the prior volume. Increasing the number of live points does increase the accuracy of the estimation of posterior and evidence at the same time. This comes at the cost of a more extensive runtime (Speagle 2020). However, the last point can be solved using so-called dynamic nested sampling, which is used within this thesis. Dynamic nested sampling adjusts the number of live points during the sampler's runtime, allowing higher resolution close to posterior overdensities and lower resolution at low posterior density regions. The weighting of the live points' positions can be defined in advance by giving weights through an importance function to the sampler. This allows employing either an accurate estimation of the posterior distribution, the evidence, or a mixture of both. For further details on this improved nested sampling methodology and additional technical peculiarities, e.g., on the bounding distributions or sampling methods, I refer to Speagle (2020) and Higson et al. (2019).

2.2.4 Radial velocity modeling within this thesis

Within this thesis, the publicly available tool `juliet` (Espinoza et al. 2019) has been used to model the photometric or RV data. `juliet` uses additional publicly available packages, and further details on those are provided in Sec. 5.4. In particular `juliet` uses nested sampling as its primary fitting method, and therefore it provides the Bayesian evidence and the posterior distributions of the parameters. Here, I summarize, primarily based on Espinoza et al. (2019), the key aspects of the modeling which is applied for the data within this thesis.

For data used within this thesis and modeled with `juliet` each datapoint $y(t_{i,l})$ at time $t_{i,l}$ is given by a model of the form

$$y(t_{i,l}) \sim M_i(t_{i,l}) + \epsilon_i(t_{i,l}), \tag{2.19}$$

where $M_i(t_{i,l})$ is the photometric or RV model of instrument i, ϵ_i is a zero-mean noise term for instrument i, and the index l defines each individual datapoint of instrument i (Espinoza et al. 2019).

In the case of RV modeling, the model is similar to Eq. 2.3 and given by

$$M_i(t_{i,l}) = K(t_{i,l}) + \gamma_i + Q(t'_{i,l})^2 + At'_{i,l} + B, \tag{2.20}$$

where $K(t_{i,l})$ is a Keplerian model of N planets, γ_i is the instrumental dependent systemic velocity, and Q, A, and B are quadratic and linear terms as well as the corresponding intercept (Espinoza et al. 2019). The three latter terms are optional and can be used to model a long-term RV trend due to a companion on a wide orbit.

The Keplerian model $K(t_{i,l})$ can be parametrized in several different ways, and within `juliet` the standard parameters are the orbital period P, the RV semi-amplitude K, the eccentricity of the orbit e, the argument of periastron w, and the time-of-transit center t_0. Note that the time-of-transit center can be converted to the time of periastron t_p, by

$$t_p = t_0 - \frac{P}{2\pi}\Big(E - e\sin(E)\Big) = t_0 - \frac{P}{2\pi}M, \tag{2.21}$$

where M, in this particular case, is the mean anomaly, and E is the eccentric anomaly that can be calculated by

$$E = 2\arctan\left(\tan\left(\frac{0.5\pi - \omega}{2}\right)\sqrt{\frac{1-e}{1+e}}\right). \tag{2.22}$$

For low-eccentricity orbits, the argument of periastron is not well defined which can lead to problems when sampling the posterior distribution by MCMC or nested sampling algorithms (Parviainen 2018). `juliet` allows two alternative parameterizations, $e\cos\omega$ and $e\sin\omega$, which has been suggested by Ford (2005), as well as $S_1 = \sqrt{e}\sin\omega$ and $S_2 = \sqrt{e}\cos\omega$, which has been suggested by Anderson et al. (2011). The latter parametrization has the advantage that a uniform prior on the parameters S_1 and S_2 lead to a uniform prior on e and ω, which is not the case for the former parametrization (Anderson et al. 2011; Parviainen 2018). Within this work I make use of the parametrization by Anderson et al. (2011).

Of primary interest is the zero-mean noise term ϵ_i for which several noise models can be assumed. The most straightforward and simple model is a white noise model in which the data points are assumed to be uncorrelated and normally distributed so that

$$\epsilon_i(t_{i,l}) \sim \mathcal{N}(0, \sigma^2_{w,i} + \sigma^2_{t_{i,l}}), \tag{2.23}$$

where $\mathcal{N}(\mu, \sigma^2)$ denotes a normal distribution with mean μ and variance σ^2, $\sigma_{t_{i,l}}$ is the measurement uncertainty of each data point, and $\sigma_{w,i}$ is a jitter term that is added in quadrature to each uncertainty and that can be either fixed or left as a free parameter during the fit of the data. Such a jitter term assumes that the measurement uncertainty is overestimated or underestimated or that other physical processes that are not directly modeled are taking place in the background, e.g., stellar oscillations.

In most cases, however, underlying stochastic or physical processes result in correlated noise, and data points are not distributed as in Eq. 2.23. Such noise components should also be modeled as they can significantly influence the derivation of the deterministic model's parameters, e.g., the Keplerian planetary parameters. Correlated and uncorrelated noise can be modeled with Gaussian processes, a non-parametric form of modeling, and the next chapter is fully dedicated to this type of noise model. A mixture of both correlated and uncorrelated noise is also possible and often applied.

Regarding the calculation of the likelihood, `juliet` can distinguish between two different types of models for the data. The type which has been mostly used within this thesis is the so-called global model, where the noise model of the correlated noise is the same for each instrument. The global model assumes that the observed noise is independent of the instrument and has the same origin. This form of noise modeling is well suited for physical processes like stellar rotation, which is intrinsic to the observed star and should be observable, independent of the instrument. However, since the contribution of stellar activity is different across different wavelengths, the instrument's bandpass can affect the noise contribution, which is one of the reasons why `juliet` also allows to have an instrument-by-instrument noise model.

For the global model, the likelihood of all the data points $\mathbf{y}$, given the parameters $\boldsymbol{\Theta}$, has the form

$$\ln P(\mathbf{y}|\boldsymbol{\Theta}) = -\frac{1}{2}\Big(N_I \ln 2\pi + \ln|\Sigma_I| + \mathbf{r}^T\Sigma_I^{-1}\mathbf{r}\Big), \tag{2.24}$$

where $N_I = \sum N_i$ is the sum of datapoints for all instruments, Σ_I is the covariance matrix (an example of the functional form is given in Eq. 3.9), and $\mathbf{r}$ is the residual vector given as

$$r(t_{i,l}) = y(t_{i,l}) - M_i(t_{i,l}). \tag{2.25}$$

The instrument-by-instrument model assumes different noise models for each instrument, so each instrument experiences a different noise process realization. This can be due to instrumental noise,

a noise contribution caused by Earths' atmosphere, or different bandpasses of the instruments with different sensitivities for certain noise contributions (Espinoza et al. 2019). For the instrument-by-instrument model, the log-likelihood is calculated individually for each instrument. The complete log-likelihood of all the instruments is provided as the sum of the log-likelihood and is given as

$$\ln P(D_I|\mathbf{\Theta}_p, \mathbf{\Theta}_1, \mathbf{\Theta}_2, ...) = \sum_{i=0} \ln P(\mathbf{y}|\mathbf{\Theta}_p, \mathbf{\Theta}_i) \tag{2.26}$$

where D_I is the data of all instruments, $\mathbf{\Theta_p}$ are the physical parameters and $\mathbf{\Theta_i}$ the instrumental parameters (Espinoza et al. 2019). The log-likelihood of each instrument can be calculated as

$$\ln P(\mathbf{y}|\mathbf{\Theta_p}, \mathbf{\Theta_i}) = -\frac{1}{2}\left(N_i \ln 2\pi + \ln |\Sigma_i| + \mathbf{r}^T \Sigma_i^{-1} \mathbf{r}\right), \tag{2.27}$$

where each instrument has a different covariance matrix Σ_i. Specifying which approach is best for a specific data set depends on the type of noise one wants to model, but the decision can also be made by comparing both approaches' resulting evidence. This can provide information about whether there is a significant difference in the noise between the instruments, which would justify additional independent parameters.

3 Gaussian processes for radial velocity modeling

> *All models are wrong, but some are useful.*
>
> **— George E. P. Box**
> (1919-2013)

3.1 Motivation

As discussed in the last chapters, RV instruments and especially the stars themselves harbor additional correlated and uncorrelated intrinsic noise which can interfere with the measured RVs caused by gravitational perturbations of an object orbiting the host star. This increases the difficulty to detect or characterize planetary candidates within the data. Instrument precision and stability have reached a level where the stars' intrinsic stellar activity has become the limiting factor for state-of-the-art and next-generation spectrographs in search of Earth-like planets (Rajpaul et al. 2015).

The active regions on the stellar surface have limited lifetimes and are constantly evolving as the star rotates. Correlated stellar noise, caused by stellar activity, often shows up as quasi-periodic (QP) variations of the measured radial velocity. In most cases, a simple sinusoid is not an appropriate model to account for such a signal, as the QP signal might differ significantly from the sinusoidal model at certain epochs. Therefore, modeling such QP signals with sinusoids runs the risk of introducing spurious signals into the residuals.

A physical model of the stellar surface capable of predicting the measured RVs or light curve would be extremely useful in modeling such variations. However, as shortly discussed in Sec. 1.2.2, such models and their parameters are degenerate, e.g., many starspot surface configurations can result in similar or equal RV variations. Additionally, the computational expenses for such investigations are quite large as each simulated spot — there can be quite a large number of

them — has several parameters that have to be taken into account by a complete physical model, e.g., the starspot's position on the sphere and its lifetime, resulting in a vast parameter space.

Recently it has become popular in the RV community to mitigate correlated time variations by applying noise models in the framework of Gaussian process (GP) regression models (see, for example, Haywood et al. 2014; Rajpaul et al. 2015; Ribas et al. 2018). These stochastic models fit the stellar and instrumental noise contribution within RVs or light curves. However, the implementation of such noise models is still discussed in the exoplanet community. Some people criticize that the flexibility of GP models may affect the measured planetary parameters or even absorb potential planetary signals. I will discuss this towards the end of this chapter.

3.2 Basics for Gaussian Processes

The following sections, although basic, will finally result in an elegant and straightforward intuition of how Gaussian process models are built and how they function.

3.2.1 The univariate Gaussian distribution

GP regression models can be used to perform non-linear regression of observed data. The basis of a GP model is the multivariate Gaussian distribution (also known as normal distribution), which is the generalization of the univariate Gaussian distribution for $k > 1$ dimensions. The univariate Gaussian distribution is given as

$$f_X(x) = \frac{1}{\sigma\sqrt{2\pi}} e^{-\frac{1}{2}\left(\frac{x-\mu}{\sigma}\right)^2}, \tag{3.1}$$

where σ is the standard deviation and μ the mean or expectation of the distribution (Arens et al. 2010). The random variable X is normally distributed, written as $X \propto N(\mu; \sigma^2)$, when Eq. 3.1 is the probability distribution of X. The univariate Gaussian distribution is a probability density function (PDF) over scalars.

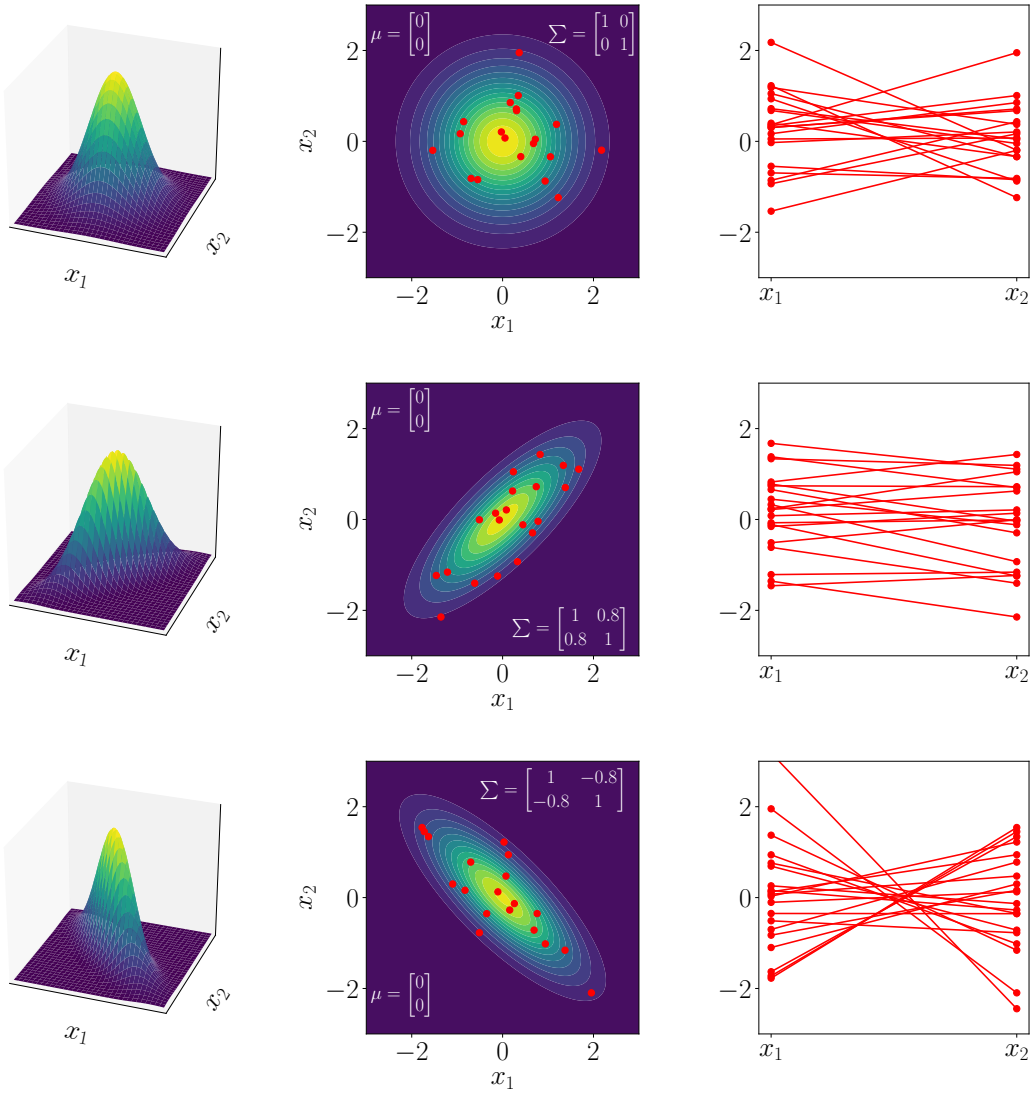


Fig. 3.1.: These plots show different bivariate Gaussian distributions and 20 samples drawn from them. Each column shows different types of visualizations, which are (from left to right): three-dimensional, two-dimensional, and parallel coordinate visualization. Each row shows a realization of a bivariate Gaussian distribution with different covariance matrix: the top row shows a realization with no correlation, the middle row shows a realization with positive correlation, and the bottom row shows a realization with negative correlation. The appropriate mean vectors and covariance matrices are provided in the middle plot of each row.

3.2.2 The multivariate Gaussian distribution

The generalization for $k > 1$ dimensions is given by the multivariate Gaussian distribution, given for a random vector $\mathbf{X} = (X_1, ..., X_k)^T$ as

$$f_{\mathbf{X}}(\mathbf{x}) = f(x_1, ..., x_k) = \frac{1}{\sqrt{(2\pi)^k |\mathbf{\Sigma}|}} e^{-\frac{1}{2}\left(\mathbf{x}-\boldsymbol{\mu}\right)^T \mathbf{\Sigma}\left(\mathbf{x}-\boldsymbol{\mu}\right)}, \tag{3.2}$$

where $|\mathbf{\Sigma}|$ is the determinant of the covariance matrix $\mathbf{\Sigma}$, $\boldsymbol{\mu}$ the expectation vector, and $\mathbf{x}$ is the column vector (Arens et al. 2010). The multivariate Gaussian distribution is a PDF over vectors. The diagonal elements of the covariance matrix $\mathbf{\Sigma}_{i,j}$ for $i = j$ can be referred to as the standard deviation of each Gaussian distribution in each dimension. The non-diagonal elements $\mathbf{\Sigma}_{i,j}$ for $i \neq j$ determine the correlation of the Gaussian distributions in each dimension between each other. Values of zero indicate no correlation, whereas positive or negative values result in a positive or negative correlation, respectively. In Fig. 3.1, three bivariate Gaussian distributions with different covariance matrices are shown in three different visualizations: a three-dimensional plot, a two-dimensional plot, and a parallel coordinate plot. The parallel coordinate visualization (see, for example, Inselberg 1997) represents randomly drawn samples of the underlying distribution. It is beneficial for dimensional cases of $k > 2$ and can be helpful for an intuitive understanding of Gaussian processes.

3.2.3 Marginalization and conditioning

An essential property of multivariate Gaussian distributions is that any resulting distribution after conditioning or marginalization (integrating out the nuisance variable) is also Gaussian distributed. The marginal probability for the discrete random variables $\mathbf{X}$ is given as

$$P(\mathbf{X}_1) = \sum_y P(\mathbf{X}_1, \mathbf{X}_2 = x_2) \tag{3.3}$$

under the joint distribution $P(\mathbf{X}) = P(\mathbf{X}_1, \mathbf{X}_2)$. In case of continuous variables, the sum in Eq. 3.3 is replaced by an integral over $d\mathbf{X}$ (Rasmussen & Williams 2006). A marginal distribution is the distribution of a subset of a collection of random variables from the original distribution. It characterizes the densities of the subset's variables without a reference to the values in the original distribution. A practical example of the marginalization property is the following case of the

marginalization of the joint probability $\mathbf{X}$ with multivariate normal random variables X_1, X_2, X_3, mean vector $\boldsymbol{\mu} = [\mu_1, \mu_2, \mu_3]$, and covariance matrix

$$\boldsymbol{\Sigma} = \begin{bmatrix} \Sigma_{11} & \Sigma_{12} & \Sigma_{13} \\ \Sigma_{21} & \Sigma_{22} & \Sigma_{23} \\ \Sigma_{31} & \Sigma_{32} & \Sigma_{33} \end{bmatrix} \tag{3.4}$$

to the joint distribution $\mathbf{X}_{13}$, which is multivariate normal and has random variables X_1, X_3, mean vector $\boldsymbol{\mu} = [\mu_1, \mu_3]$ and the covariance matrix

$$\boldsymbol{\Sigma} = \begin{bmatrix} \Sigma_{11} & \Sigma_{13} \\ \Sigma_{31} & \Sigma_{33} \end{bmatrix}. \tag{3.5}$$

Another example of a marginalization for a bivariate Gaussian distribution is given in the left plot of Fig.3.2.

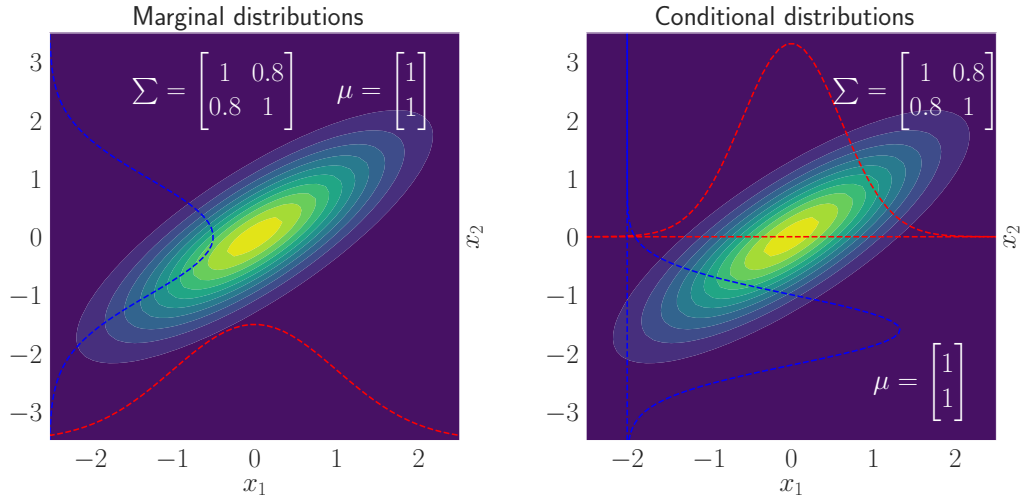


Fig. 3.2.: Plots of a bivariate Gaussian distribution. *Left:* In case of a two-dimensional multivariate normal distribution, the marginal distributions are the univariate distributions with $P(\mathbf{X}_1) = \mathcal{N}(\mu_1, \Sigma_{11})$ and $P(\mathbf{X}_2) = \mathcal{N}(\mu_2, \Sigma_{22})$. *Right:* Conditional distributions $P(\mathbf{X}_1|\mathbf{X}_2 = 0.0)$ and $P(\mathbf{X}_2|\mathbf{X}_1 = -2)$. A comparison of the conditional distribution $P(\mathbf{X}_1|\mathbf{X}_2 = 0.0)$ with the marginal distribution $P(\mathbf{X}_1) = \mathcal{N}(\mu_1, \Sigma_{11})$ highlights the effect of the conditioning which is the reduction of the standard deviation of the univariate Gaussian distribution.

In contrast to marginalization, where information was ignored, conditioning allows incorporating additional information. Conditioning can be used to calculate the probability of one variable given another variable. The conditional probability function is given as

$$P(\mathbf{X}_1|\mathbf{X}_2) = \frac{P(\mathbf{X}_1, \mathbf{X}_2)}{P(\mathbf{X}_2)}, \tag{3.6}$$

with $P(\mathbf{X}_2) > 0$ (Rasmussen & Williams 2006), and it can be shown that if $\mathbf{X}_1$ and $\mathbf{X}_2$ are jointly normally distributed, adding information about $\mathbf{X}_2$ will result in a new conditional distribution for $\mathbf{X}_1$ that is again Gaussian (Rasmussen & Williams 2006).

Note that this operation generally requires a matrix inversion of an $n \times n$ matrix, where n is the number of dimensions for $\mathbf{X}_2$. This operation is computationally costly but crucial for a GP prediction given some data, which is discussed later in this chapter. A graphical example of conditioning in two dimensions is provided in the right plot of Fig. 3.2.

3.3 Gaussian processes

3.3.1 Definition

Figure 3.3 shows a family of five curves (realizations) from three different 5-dimensional multivariate Gaussian distributions, with mean vectors of zero, but different covariance matrix for each row in the plot. The parallel coordinate visualization in each row's middle plot allows to assess the effect of the covariance matrix, given in the left panel of Fig 3.3. From this example, it is straightforward to create a link to GPs. Intuitively one can think of a GP as a multivariate Gaussian with infinite random variables, an infinite mean vector, and an infinite-by-infinite covariance matrix. A GP is the generalization of a multivariate Gaussian distribution to infinitely many variables. This non-parametric model that, in general, can have infinite dimensions is computationally calculable due to the above-mentioned marginalization property, which allows computing marginals and conditionals for any finite subset of variables. Rasmussen & Williams (2006) provides the rigorous mathematical definition of a GP, which is:

Definition 1 *A Gaussian process is a collection of random variables, any finite number of which have a joint Gaussian distribution.*

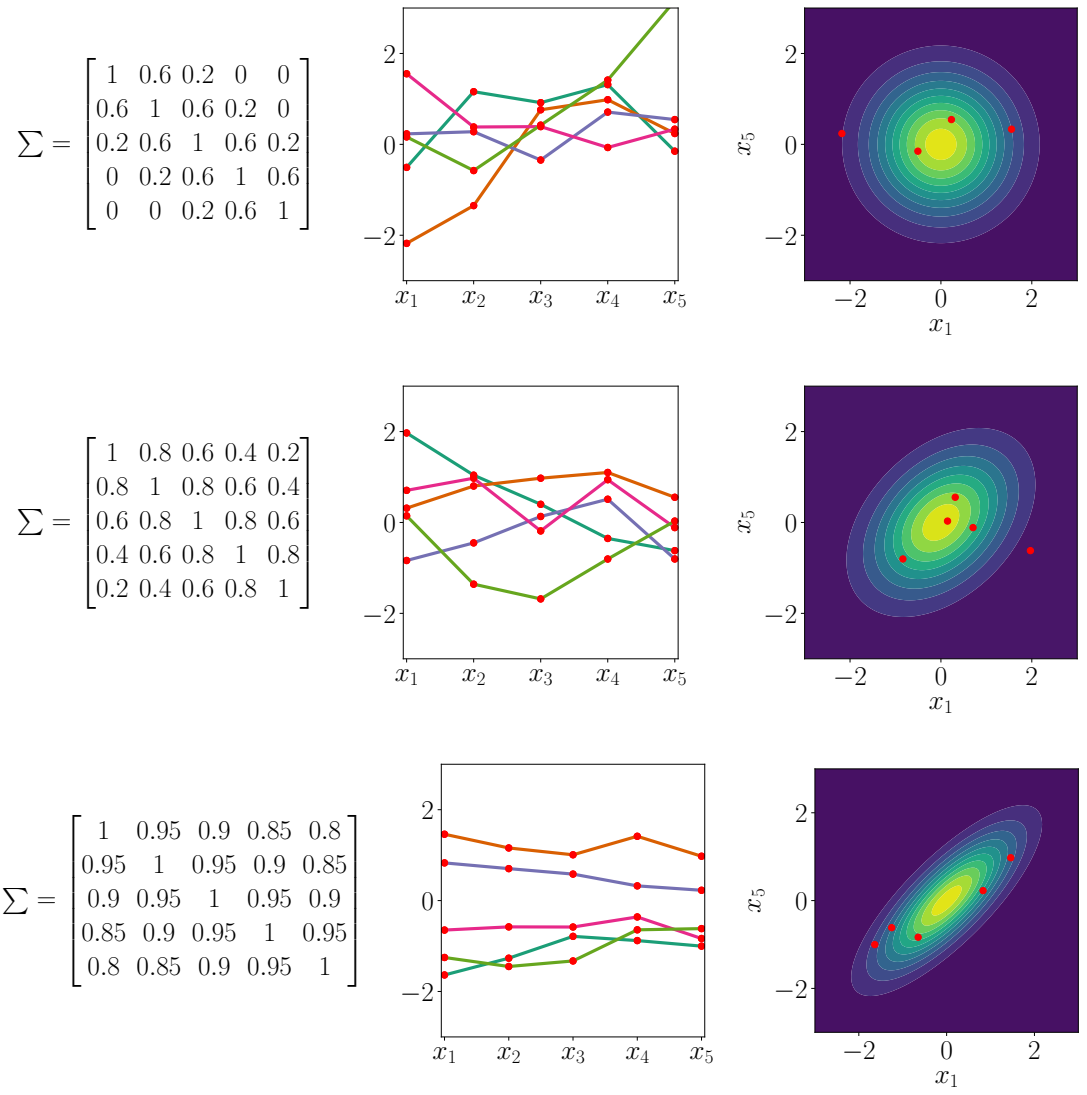


Fig. 3.3.: This graphic shows five different random realizations of multivariate Gaussian distributions in the middle panel of each row. Each row is specified by a different 5-dimensional multivariate Gaussian distribution with mean vector of zero. The appropriate covariance matrix is provided in the left panel of each row. The right panels show the covariance between the first and last dimension of this multivariate Gaussian distribution as well as the five drawn realizations of the curves given in the middle panels.

While multivariate Gaussian distributions are fully specified by a mean vector $\boldsymbol{\mu}$ and covariance matrix $\boldsymbol{\Sigma}$, a GP is completely specified by a mean function $m(x)$ and a covariance function $k(x, x')$ (Rasmussen & Williams 2006). The covariance function is a recipe that defines the covariance between pairs of random variables and allows to compute any specific finite number of values.

This is the important step that makes the difference between a GP and a multivariate Gaussian. Mathematically, a GP is written as

$$f(x) \sim \mathcal{GP}(m(\mathbf{x}), k(\mathbf{x}, \mathbf{x}')) \tag{3.7}$$

(Rasmussen & Williams 2006).

A GP is a Gaussian distributed PDF over possible functions. While it is common to set the GP's mean to zero, in general, one can use any fixed deterministic mean function $m(\mathbf{x})$ instead. In the specific case of RV modeling, the mean function often corresponds to all the deterministic models, e.g., the Keplerian planetary signals. The stochastic signals, e.g., the stellar activity, are taken care of by the covariance function $k(\mathbf{x}, \mathbf{x}')$ which also controls the smoothness and shape of the possible functions.

3.3.2 Kernels, hyperparameters, and predictions

A variety of covariance functions, hereafter referred to as GP kernels, are possible. A widely applied kernel function which is also used within this thesis is the squared-exponential kernel given as

$$k_{\mathrm{exp}}(\mathbf{x}, \mathbf{x}') = \sigma_{\mathrm{GP}}^2 \exp\left(\frac{(\mathbf{x} - \mathbf{x}')^2}{2l^2}\right), \tag{3.8}$$

where l is a characteristic length-scale and σ_{GP}^2 the variance of the signal (see ,for example, Rasmussen & Williams 2006). Therefore, σ_{GP} can be interpreted as an amplitude of the GP. These parameters do not directly shape any model curve, but they define only the covariance between each finite number of variables (data points). For this reason, and to emphasize that these are parameters of a non-parametric model, they are referred to as hyperparameters (Rasmussen & Williams 2006).

Based on the mean and covariance function properties, one can draw an arbitrary number of samples of functions evaluated for any random finite number of test points. These test points define the grid, and this operation corresponds to the marginalization, which was mentioned for multivariate Gaussian distributions in the sections before. In the Bayesian framework, this sample of functions corresponds to the prior distribution of functions defined by the set of hyperparameters. In the case of a zero-mean function, the distribution of all possible functions

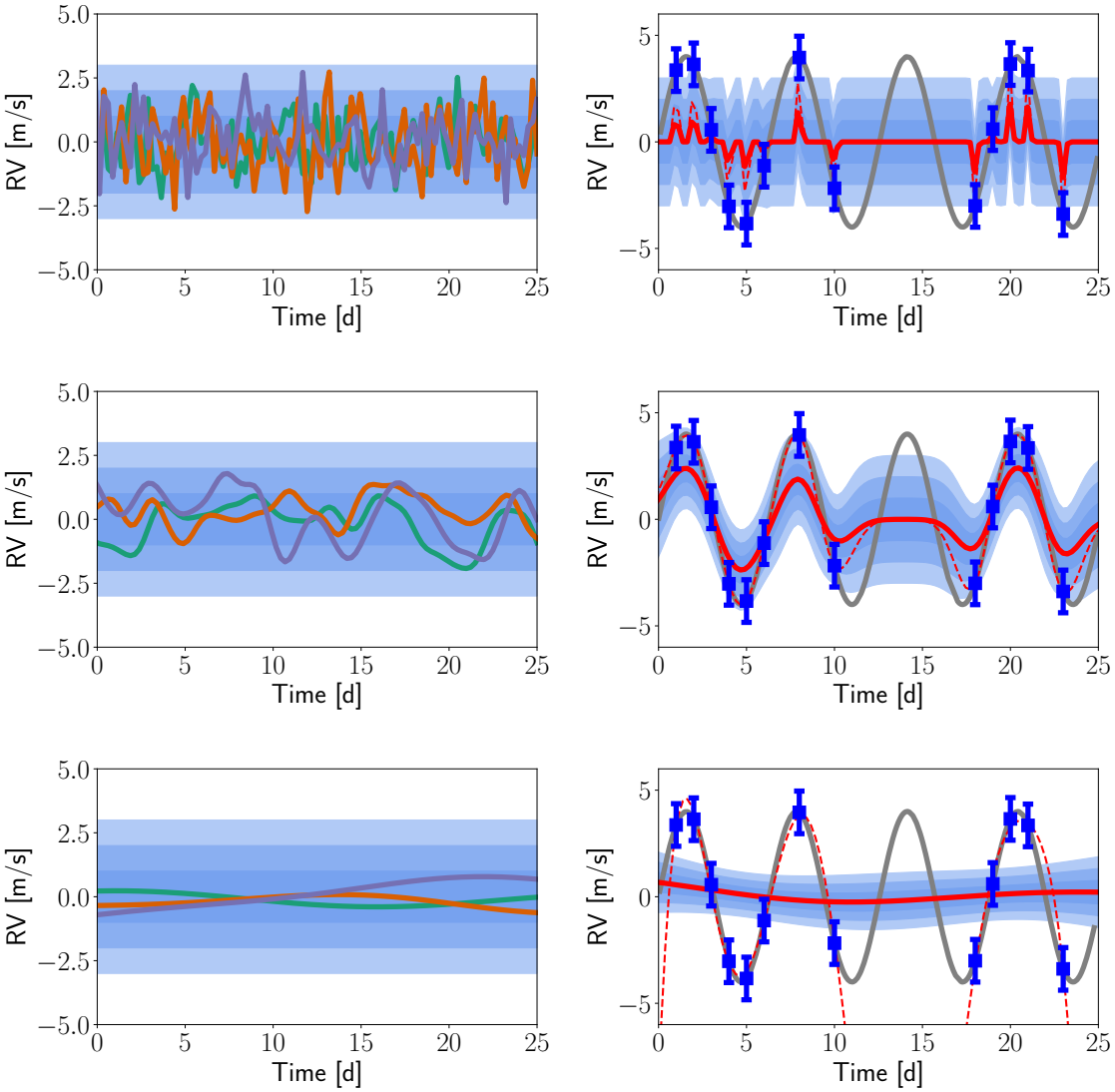


Fig. 3.4.: *Left:* Three random functions drawn from a GP prior distribution with a mean function of zero and a squared-exponential kernel that has an amplitude of 1 m s^{-1} but a short length-scale (top), intermediate length-scale (middle) and long length-scale (bottom). The 1σ, 2σ and 3σ uncertainty of prior distribution is illustrated by the blue shaded area. *Right:* Median GP model for training points (blue squares) that follow a sinusoidal signal (solid gray line) given the GP prior distribution of the left panel. The red-dashed line is the median GP model without any white noise contribution, while the solid red line represents the median GP model with a white noise contribution of 1 m s^{-1} as indicated by the error bars of the training set. The 1σ, 2σ and 3σ uncertainty of the latter GP posterior distribution with white noise is illustrated by the blue shaded regions.

revolves around zero. Examples of possible functions from a GP prior distribution with a squared-exponential GP kernel and a mean function of zero are shown in in the left panels of Fig. 3.4.

However, in most cases, one is interested in predicting new function values $\mathbf{f}$ for specific input data. In this context, the observed data is often referred to as training points, while the predictions are evaluated on the test points. Using Bayes' theorem (see Eq. 2.5), it is possible to derive the posterior GP distribution by using the GP prior distribution and the likelihood of the training data. This operation corresponds to the conditioning which was mentioned for multivariate Gaussian distributions in the previous sections. The mathematical details of this operations in the case of GPs are given in chapter 2.2. of Rasmussen & Williams (2006). Intuitively, this process can be thought of as if random functions are drawn form the prior distribution, and only those functions that fit all the training points are kept for the GP posterior, although this process would be far less efficient than the conditioning operation. The resulting GP posterior, which is also normal distributed, can then be used to make predictions on additional input values.

In the case of n real measurements, it is common to have a white noise contribution (Gaussian distributed noise). In such cases, the covariance matrix consists of two components: the sum of the GP kernel and an identity matrix with the noise contribution σ_n^2 of each data point on its diagonal component. In index notation, this can be written as

$$\Sigma_{l,m} = k(\mathbf{x}_l, \mathbf{x}_m) + \sigma_n^2 \delta_{l,m}, \tag{3.9}$$

where $\delta_{l,m}$ is the Kronecker's delta, σ_n^2 is the variance of the white noise and $k(\mathbf{x}_l, \mathbf{x}_m)$ is the GP kernel.

3.3.3 Controversial aspects of GPs

As can be seen from Fig. 3.4, a GP has high flexibility in fitting data. As a result, if there are any numbers of finite functions inside the GP prior distribution that fit the data, it will fit the data by its definition. Only if white noise is included in the GP model, the variance at the training points is allowed to be non-zero, and the median GP model will then include a large number of different GP realizations that do not need to fit each data point directly. It is important to emphasize that the inference, which is taking place for the GP prediction, is one step below the inference of the hyperparameters, as for a given set of fixed hyperparameters there is a prior distribution $p(\mathbf{f}|X)$ of function values $\mathbf{f}$. This leveling of inferences can be referred to as *"hierarchical models"*

(Rasmussen & Williams 2006). At the bottom level, the posterior is derived using the prior function values defined by the hyperparameters. As this prior is Gaussian distributed and the likelihood of the training data $p(\mathbf{y}|\mathbf{f}, X)$ is also a factorized Gaussian, it is possible to analytically derive the marginal-likelihood (evidence) for the GP prediction which is

$$\log p(\mathbf{y}|X) = \log\left(\int p(\mathbf{y}|\mathbf{f}, X)p(\mathbf{f}|X)\mathrm{d}\mathbf{f}\right) = -\frac{1}{2}\mathbf{y}^{\mathrm{T}}\Sigma^{-1}\mathbf{y} - \frac{1}{2}\log|\Sigma| - \frac{N}{2}\log 2\pi, \tag{3.10}$$

where $\Sigma = K + \sigma_n^2 I$ is the covariance matrix that includes the white noise term (Rasmussen & Williams 2006). The "parameters" of the non-parametric GP model that are used for the calculation of the likelihood $p(\mathbf{y}|\mathbf{f}, X)$ are the noise-free function values at the position of the training data (Rasmussen & Williams 2006). More training points result in more parameters when it comes to this first (lowest) level of inference. Note that the last part of Eq. 3.10 is identical to Eq. 2.7 and Eq. 2.27, respectively. So the evidence of the first level of inference plays the role of the likelihood when it comes to the estimation of the hyperparameter posterior distribution.

As the likelihood used for the calculation of the posterior of the hyperparameter is the marginal likelihood of the first level of inference based on the "parameters", it includes all the benefits discussed in Sec. 2.2.2. In particular a GP fit includes a complexity penalty by the inclusion of the term $-\frac{1}{2}\log|\Sigma|$. Even though a large variety of different hyperparameters can fit the data, there is a set of hyperparameters for which the GP prediction's marginal log-likelihood will be maximized. This maximum does not correspond necessarily to the set of hyperparameters that allow the largest flexibility of the GP model. This can also be understood intuitively by looking at the resulting predictions of Fig. 3.4. For a very short length-scale of the squared-exponential kernel, the GP acts as a white noise model, and it loses much predictive power not far away from the training points, which is visible by the larger area of the uncertainty of the GP compared to the intermediate length-scale GP model used for this data. On the other side, the model with the highest length-scale results in a GP that performs similar as a constant model with some added white noise. Therefore it seems plausible that some intermediate model would win in the provided example, as the underlying model of the data was neither some white noise nor constant, but a sinusoidal. There is, however, no guarantee that the marginal log-likelihood has only one mode, since several combinations of hyperparameters may in principle perform similar for some data, although this does not seem to be a very common problem (Rasmussen & Williams 2006).

Within `juliet`, the log-likelihood of the global models is evaluated according to Eq. 2.7 or, equivalently, according to Eq. 3.10. In the case of additional parametric models that are modeled with the noise process, e.g., Keplerian models, the parametric model is part of the residual vector,

and its parameters define the residuals that are modeled by the covariance matrix. Therefore, the GP log-likelihood is calculated using the RV-offset-subtracted, Keplerian-subtracted RVs. This operation can be performed since the "fit" is a sampling operation. Whether some signal can be modeled more properly by a GP or by a Keplerian, can be used as a diagnostic tool to decide whether the signal has a planetary or stellar origin. However, it is worth noting that such analyses should be treated with caution, as there can be a certain degree of degeneracy between the GP model and parametric models like Keplerians. Therefore, it is recommended to use additional diagnostic tests to verify these results.

In particular, it can be difficult for a correlated noise model to distinguish whether the origin of the "noise" is a planet or some stellar activity. In general, the GP has no way of knowing the generated noise process, especially if there are many variabilities present in the data. Therefore, the danger of absorbing signals of planetary origin into the noise model cannot be entirely neglected (see, for example, Cabot et al. 2021) and is further investigated in this thesis (see Sec. 3.5.3). Hence, it is essential to explore a range of different models, and the metric of the log-evidence can be a useful tool for such analyses (see Sec. 3.5.4).

Additionally, within this thesis, several additional methodologies have been used or developed to reduce the probability that the GP has absorbed planet signals. A significant planetary signal modeled by a GP should be visible in a periodogram decomposition of the GP model, which is why I advocate this test as an additional ingredient of the analysis. It is essential to understand the origin of any significant peak in this periodogram. Furthermore, it can be useful to investigate the GP hyperparameters' posterior distributions to identify any possible physical origin of the noise, e.g., the stellar rotation. This can only be done when the GP hyperparameters have some meaningful physical interpretation, which is not the case for many kernels. The opinion about the question whether only those GP kernels should be used which allow physical interpretation differs between authors and studies. However, a physical interpretation is advantageous as it allows us to understand the noise generating process, reducing the possibility of wrong conclusions. This can also be related to the hyperparameters' prior volume as constraining this volume by physically related priors constrains the GP models posterior distribution and also increase the marginal likelihood. In a combined RV data fit of planet and GP model, constraining the GP will improve the detection efficiency of any planetary signals and the precision of the derived planetary parameters (Gilbertson et al. 2020). Within the next sections, some of the controversial aspects of GPs are qualitatively investigated for the physically motivated QP-GP kernel that has been used within this thesis.

3.4 The quasi-periodic kernel for radial velocity data

3.4.1 GP kernel and hyperparameters

A GP kernel that has been widely used to model stellar variability within RV and photometric data is the QP kernel (Haywood et al. 2014; Rajpaul et al. 2015; Angus et al. 2018; Nava et al. 2020; Gilbertson et al. 2020). The QP-GP kernel consists of a multiplication of the squared-exponential kernel and the exponential-sine-squared kernel. It can be written as

$$k_{\exp}(\mathbf{x}, \mathbf{x}') = \sigma_{\mathrm{GP}}^2 \exp\left(\frac{(\mathbf{x}-\mathbf{x}')^2}{2l^2} - \Gamma \sin^2\left(\frac{\pi(\mathbf{x}-\mathbf{x}')^2}{P}\right)\right), \tag{3.11}$$

where the first term represents the squared-exponential kernel and the second term represents the exponential-sine-squared kernel consisting of the hyperparameter P defining a timescale of periodicity (in units of the data) within the covariance structure and Γ representing a term that gives relative importance between the periodic and exponential kernel by affecting the amplitude of the sine-squared term (see, for example, Haywood et al. 2014; Rajpaul et al. 2015; Angus et al. 2018; Nava et al. 2020; Gilbertson et al. 2020). For RV and photometric time series it is common that $(\mathbf{x}-\mathbf{x}')^2$ is a time.

Figure 3.5 shows the covariance matrix, the covariance over time, and some example functions drawn from a QP-GP to highlight the properties of the GP hyperparameters for this kernel. The effect of the rotation hyperparameter P is straightforward. It correlates points that are roughly one period apart from each other. The amplitude hyperparameter σ^2 defines the absolute strength of the covariance and results in larger amplitudes for any drawn example function from the GP. The length-scale parameter l defines how strongly points are correlated with each other depending on how far away from each other they are. Large values of the length-scale lead to a strong correlation for those points, while small values lead to weak or no correlation. The hyperparameter Γ is responsible for the complexity of the harmonic content: for small values of Γ, points with a different distance, other than a multiple of P, are higher correlated than for large values of Γ where points are less correlated if they are not close to one rotation P.

3.4.2 Physical motivation

The QP-kernel usage for the GP fitting of activity signals in RV and photometric time series has several advantages. The GP is infinitely differentiable and results in very smooth functions,

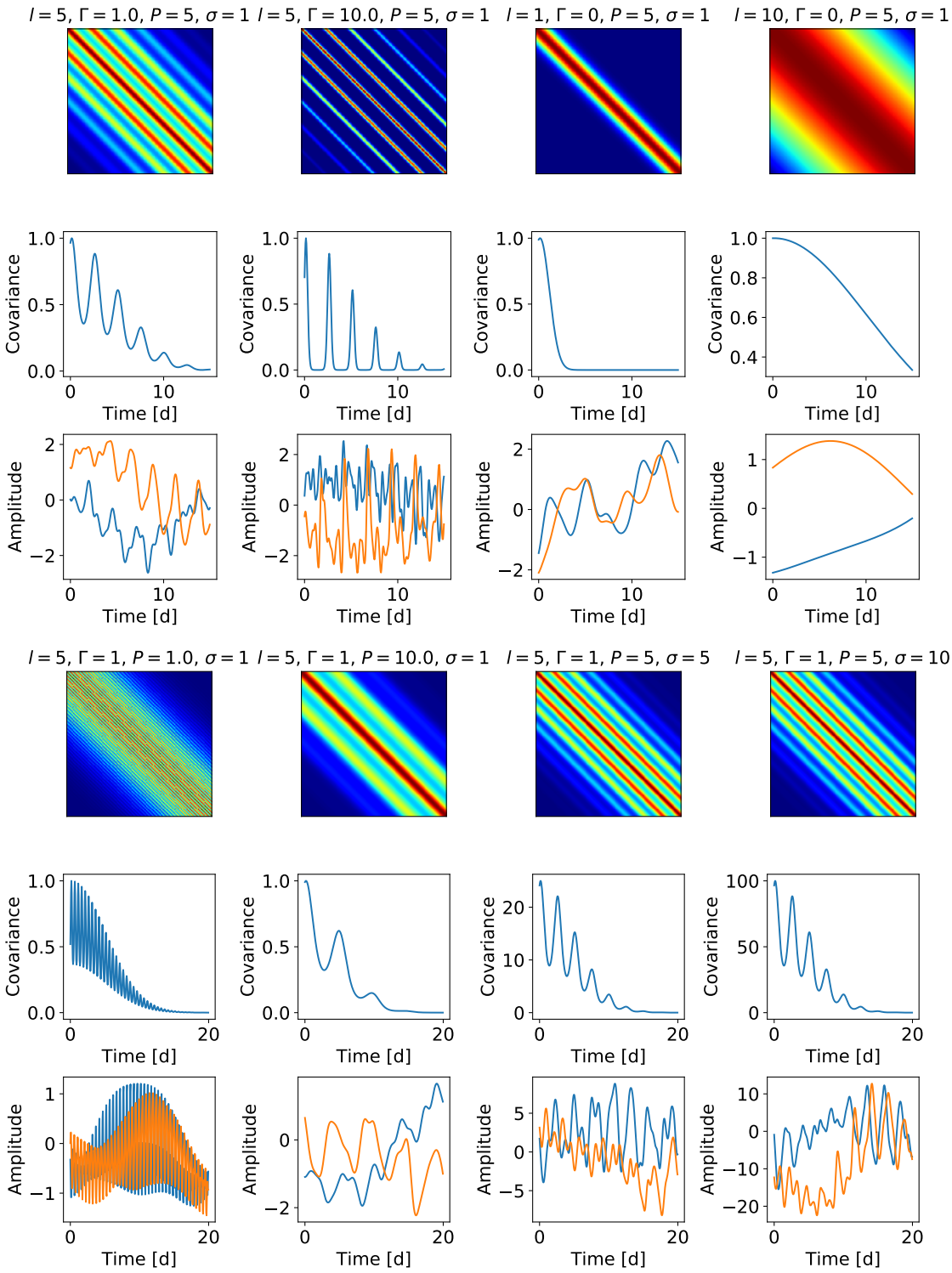


Fig. 3.5.: This figure shows some properties of the QP-GP kernel for different combinations of hyperparameters. For each combination, there is a 1×3 matrix of plots. The top panel of this matrix shows the covariance matrix and the warmer the color of the color-coding, the stronger the correlation. The middle panel shows the covariance over time and the bottom panel shows two random GP realizations from the GP prior distribution. The hyperparameters are provided on top of each 1×3 matrix (l and P in days, σ in $\mathrm{m\,s^{-1}}$).

as can be seen from Fig. 3.5. However, an essential feature is that the kernel is physically motivated (Rajpaul et al. 2015; Angus et al. 2018). The GP can, therefore, generate functions that can, in principle, represent quasi-periodic signals in photometric and RV time series quite well, whose origins could be due to stellar activity rather than a planet. The amplitude hyperparameter $\sigma^2_{\rm GP}$ models the strength of the activity signal, and it could be related to the spot size, number of visible spots on the stellar surface, or temperature contrast. However, this is a degenerate problem considering these parameters, and a few others, can all affect the amplitude of the activity signal. The length-scale l defines the decay of the signal, and it can be related to the evolutionary timescale of any activity features, e.g., stellar spots (Rajpaul et al. 2015). The hyperparameter P can be interpreted as the stellar rotation period, which is responsible for magnetic active regions moving in and out of the observed stellar disk. As the Γ hyperparameter describes the harmonic complexity, it can be related to the number of variations (or local maxima and minima) between one full rotation of the star. Therefore, this hyperparameter provides information about the average distribution of active regions on the stellar surface (Angus et al. 2018; Nava et al. 2020).

3.4.3 Physically motivated hyperparameter priors

As the hyperparameters can be related to the star's physical properties, it is possible to motivate some physical priors for these hyperparameters. The amplitude parameter $\sigma^2_{\rm GP}$ is challenging to constrain physically due to the large degeneracy of parameters affecting it. The distribution of this hyperparameter usually is chosen to be uniform, and its upper boundary can be chosen to be of the order of the maximum observed amplitude of the time series data.

For the prior of the GP rotation period, it is common to use a uniform or log-uniform prior that spans the range of physically possible stellar rotation periods, which, depending on the type of star and its age, can span from less than a day to several hundreds of days. Without any further knowledge, a uniform prior spanning this whole range is appropriate. However, in some cases, there is already an estimate of the rotation period, or some auxiliary data, e.g., photometric time series, can be used to derive the stellar rotation period more easily. In such cases, it is common to use this estimate as a normal prior for this hyperparameter in any following analysis (Angus et al. 2018). The mean and standard deviation of the normal prior are set according to the previous estimate. Depending on the previous estimates' reliability, it is recommendable and useful to relax the normal prior of the GP rotation hyperparameter by using a larger standard deviation than the previous estimates uncertainty, especially since many estimates of stellar rotation periods seem to show underestimated uncertainties, whether derived by periodograms, auto-correlation

functions or GPs. Within these three methodologies to derive stellar rotation periods, Angus et al. (2018) have found that GPs, in particular the QP-GP, provide the most realistic and robust uncertainties. An additional motivation to relax the prior is given by the fact that differential rotation of the stellar surface, together with the wavelength dependence of some activity features could lead to small differences between photometry, RVs, or different instruments.

The length-scale parameter l is essential when it comes to modeling a meaningful rotational signal. For example, a small length-scale parameter leads to a dominating squared-exponential kernel, and the signal decays before one rotation has finished. Therefore, this hyperparameter is usually set in accordance with the rotation period. If the rotation period is unknown, it is common to use a uniform prior that spans over all physically possible values ranging from less than days up to several years. In cases, where the rotation period is known, it is common to set the lower boundary of the prior to values which satisfy the rule that the length-scale is larger than the rotation period $l > P_{\mathrm{rot.}}$ (Angus et al. 2018).

Large values of the harmonic complexity parameter Γ allow the GP to become very flexible, which allows the GP to fit the data without any variations of the period. Therefore, it is recommended to impose an informative prior or an upper constraint on Γ. Jeffers & Keller (2009) have shown that, in first approximation, *"two unequally strong spots that are 180 degrees apart can explain any light curve"*, independent of the complexity of the spot distribution on the stellar surface. This roughly corresponds to two active longitudes on the stellar surface, and its RV signal can be modeled by one to three local maxima of the GP within one full rotation period. Therefore, an upper limit of Γ can be around ten as this corresponds to this number of local maxima. Within the literature, there are cases where even more informative priors than the one used within this thesis were applied to the GP model, e.g., normal priors (see, for example, Nava et al. 2020, and references therein).

3.5 Investigations on quasi-periodic Gaussian processes

3.5.1 Goals and assumptions of this analysis

The goal of this section is to investigate, mostly on a qualitative basis, some of the discussed controversial aspects of GPs. Firstly, how well do the hyperparameters of a QP-GP capture the physical properties of stellar activity, in particular the rotation period and the spot lifetime? Secondly, how well can planets be recovered and detected in cases where the Keplerian signal is

Tab. 3.1.: Relevant parameters used to simulate the stellar activity.

Parameter	Value	Units	Description
		general	
λ_{min}	380	nm	Lower boundary of spectral range of RV instrument
λ_{max}	690	nm	Upper boundary of spectral range of RV instrument
T_{Obs}	220	d	Time of simulations
Δt	60	min	Time cadence
		RV	
Δv_{CCF}	15	km/s	CCF velocity range
Mask	M2	...	Spectral mask (G2 or K5 or M2)
		star	
T_{eff}	3500	K	Stellar effective temperature
ΔT_{Spot}	400	K	Spot temperature contrast[1]
$\Delta T_{\mathrm{Faculae}}$	0	K	Faculae temperature contrast
P_{rot}	22	d	Stellar rotation period
R	0.36	$R_{\odot}$	Stellar radius
$\log(g)$	5	dex	Stellar surface gravity
[Fe/H]	0	...	Stellar metallicity
$[\alpha/\mathrm{Fe}]$	0	...	Stellar alpha element abundance
Q	0	...	Faculae to spot area ratio
i	90	deg	Axis inclination
k_{rot}	0	deg/d	Stellar differential rotation
		spots	
a_{rd}	0.5	deg/d	Spot size evolution rate
R_{Spot}	$\mathcal{T}(6, 2, 4, 8)$ [2]	deg	Spot radius
P_{life}	44 or 110 or 220	d	Spot lifetime
$\sigma_{P_{\mathrm{life}}}$	$10^{-3} P_{\mathrm{life}}$	deg	Spot lifetime standard deviation
$\bar{N}_{\mathrm{Spot}}$	3 or 9	...	Average number of spots on surface at any time

[1] The spot temperature contrast for a dwarf star with $T_{\mathrm{eff}} = 3500\,\mathrm{K}$ has been set according to the results of the purple and red empirical fits to M dwarf spot temperature contrasts shown in fig. 2 of Andersen & Korhonen (2015).
[2] The prior labels $\mathcal{T}(\mu, \sigma, a_{\mathrm{lower}}, b_{\mathrm{upper}})$ represents a truncated normal.

of the same order as the noise due to the stellar activity, that is modeled by a QP-GP? In particular, are Keplerian signals absorbed by the noise model and can the metric of the log-evidence help in some cases? Last but not least, are planetary parameters affected if stellar activity is inherent in the RV data and if it is not fitted for by a GP or, as could be asked from another perspective, does fitting for a GP affect the planetary parameters?

The parameter space which influences the stellar activity signal is large. These investigations will, therefore, be carried out on a small grid of different physical input values that are expected to have the strongest contribution on the properties of the activity signal, and, therefore, also on the derivation of the hyperparameters and the performance of the QP-GP in general. However, most of the stellar parameters have been fixed to values corresponding to "an average M dwarf". These parameters and some more important parameters for the modeling of the stellar activity are provided in Table 3.1. In particular, the rotation period has been fixed to 22 d and differential rotation as well as faculae have been neglected. The only modeled activity features are, therefore, stellar spots, which are assumed to have circular shape.

For the modeling of the RV activity signal, the tool `StarSim`[1] (Herrero et al. 2016) has been used. A detailed description of the `StarSim` code is provided within Herrero et al. (2016). `StarSim` models RVs by dividing the stellar surface into a grid of different effective temperatures, depending on whether there is an activity surface feature (spot or faculae) or not (quit photosphere) at the position of the grid element. Each of the three different surface regions is then assigned a synthetic Phoenix spectra (Husser et al. 2013) based on the effective temperature and other relevant stellar parameters, e.g., $\log g$. Additionally, each grid element is Doppler shifted depending on the velocity of the surface grid. `StarSim` then calculates the CCF of each of the three different spectra and then integrates the entire grid of surface elements in terms of CCFs instead of spectra to speed up the calculations. `StarSim` provides pre-defined masks for the CCFs calculations. For this thesis, a mask suitable for the HARPS instrument as well as for an M2 star has been used. Limb darkening effects, convection effects and limb brightening are also included into `StarSim`. RVs are then derived from the CCFs for a defined grid of epochs. While `StarSim` is only a physical model of a simulated stellar surface, that might have some limitations, e.g., circular spot shape, it is a sufficient tool for the qualitative analysis of the QP-GP properties presented in this chapter.

The grid, on which the performance of the QP-GP is investigated, is defined by different spot lifetimes, different spot surface distributions, and two different activity levels, represented by the average number of spots on the surface at any time. The grid of spot lifetimes is given by 2, 5 and 10 times the length of the rotation period, corresponding to 44 d, 110 d and 220 d. The uncertainty of the spot lifetime has been set to a value of 0.1% of the actual spot lifetime, so effectively no variation in the spot lifetime is allowed. For the investigations within this thesis, the grid has been further extended by applying two different levels of activity corresponding to the occurrence of 3 or 9 spots at each time. These spot lifetimes and spot numbers were based on values used within Basri & Shah (2020).

[1] https://github.com/rosich/starsim-2

The different spot distributions were inspired by the works of Perger et al. (2021). Three configurations have been used: Firstly, a random spot distribution for which spots can emerge anywhere at the surface at any time. Secondly, a spot distribution with one active longitude for which spots occur at one longitude according to a truncated normal distribution with $\mathcal{T}(90°, 45°, 0°, 180°)$, where 90° represents the mean, 45° the standard deviation, 0° the lower, and 180° the upper boundary. For this spot distribution, the butterfly effect (see Sec. 1.2.2) has been additionally simulated by applying two truncated normal distributions to the colatitudes with $\mathcal{T}(70°, 20°, 55°, 85°)$ and $\mathcal{T}(110°, 20°, 95°, 125°)$. Thirdly, a spot distribution with two active longitudes for which spots occur at longitudes which are separated by 180° according to the truncated normal distributions $\mathcal{T}(90°, 45°, 0°, 180°)$ and $\mathcal{T}(270°, 45°, 180°, 0°)$. Similar to the case of one active longitude, the butterfly effect has been additionally simulated by applying two truncated normal distribution to the colatitudes.

Regarding the simulated RV observations, 110 RV measurements over 220 days have been semi-randomly drawn from the 60 minute grid of the calculated `StarSim` model. The drawing of the measurements was based on a combination of two distributions, a uniform, and a Gaussian distribution, that have been properly set to provide a realistic observation pattern, e.g., that the observations only take place during nighttimes and that observations usually are carried out close to the culmination of the star. The period over which observations are simulated, the number of measurements, and the number of iterations of the simulations per individual configuration have been defined according to these criteria to reduce the computation time of the GP fits. However, they do not significantly differ from common RV data sets.

`StarSim` only models RVs based on the rotation of active regions and does not incorporate any white noise contribution or measurement uncertainty. Therefore, each synthetic RV measurement has been perturbed by adding a random RV offset, based on a Gaussian distribution with mean around the RV measurement and a standard deviation of $1.5\,\mathrm{m\,s^{-1}}$. This represents white noise contributions that are not modeled by `StarsSim` and that can be caused by stellar granulation, stellar oscillations, observational conditions, and instrumental behavior. The uncertainties of each synthetic RV measurements have been drawn from a truncated normal distribution with $\mathcal{T}(1.5\,\mathrm{m\,s^{-1}}, 0.5\,\mathrm{m\,s^{-1}}, 0\,\mathrm{m\,s^{-1}}, 200\,\mathrm{m\,s^{-1}})$ which represents realistic median RV uncertainty of CARMENES and HARPS for these type of stars.

Based on the presented parameters that are varied, the grid consists of 18 different configurations: three different spot lifetimes (44 d, 110 d, 220 d) for an average number of three or nine spots, respectively, occurring on the surface at any time, replicated for three different spot distributions: random distribution, one active longitude, and two active longitudes. For each of these 18 configuration, ten random realization have been simulated. Given the small number of iterations,

a robust statistical analysis is not pursued. Nevertheless, the analysis should qualitatively assess the performance of the QP-GP for some cases of stellar activity that scientist often have to face without any prior knowledge.

3.5.2 Derivation of stellar activity properties by the QP-GP

The first step has been to test whether the QP-GP can derive the star's correct rotation period or whether it fails to do so for specific configurations. The resulting rotational and length-scale hyperparameters are compared to the actual simulated stellar rotation period and spot lifetime. The amplitude and harmonic complexity hyperparameters were not investigated in detail, mainly because these two quantities cannot be directly connected to a single physical property of the host star. For example, the rotation period, the spot temperature contrast, the spot number, and the spot size, all of these mentioned quantities affect the measured RV amplitude, and, therefore, also the amplitude hyperparameter. Although the harmonic complexity hyperparameter Γ can be interpreted as a quantity that reflects the spot distribution, it is not well constrained. The further investigations of Γ and σ_{GP} are, therefore, postponed to the future.

All 18 configurations with ten iterations each, as defined in the previous subsection, have been analyzed, resulting in 180 GP fits. The parametrization of the length-scale hyperparameters of the QP-GP within `juliet` is slightly different compared to Eq. 3.11. The public code `juliet` uses an inverse length-scale α, which, according to eq. 8 and footnote 6 in the `juliet` paper (Espinoza et al. 2019), is given as $1/(2l^2)$. However, during the analysis of this chapter it has been found that the correct transformation is $\alpha = 1/(l^2)$, which has been used throughout this chapter[2].

The priors of the hyperparameters of the GP for the analysis in this section have been set as given in Table 3.2 for GP prior I. In order to assess the significance of the GP fit to the data, the log-evidence has been compared to a flat model with white noise, i.e., a model which only fits for jitter. The log-evidence difference to the white-noise model and the results of the rotation and

[2]The QP-GP kernel used in `juliet` is a multiplication of an exponential-squared kernel and an exponential-sine-squared kernel in `george` (see kernel definitions here: https://george.readthedocs.io/en/latest/user/kernels/). The exponential-squared kernel is defined in `george` as $\exp(-r^2/2)$, where r corresponds to τ in the `juliet` paper. The length-scale in `george` is proportional to $\exp(-r^2/(2\Theta))$ (see how k_1 is defined in the `george` tutorial here: https://george.readthedocs.io/en/latest/tutorials/hyper/). Within `juliet`, the inverse of this length-scale. $\Theta = 1/\alpha$, is defined, so the kernel being fitted by `juliet` is $\exp(-\alpha \cdot r^2/2)$ and not $\exp(-\alpha \cdot r^2)$ as written in eq. 8 of the `juliet` paper. This circumstance has been confirmed via private communication with first author Nestor Espinoza. I have been unaware of this wrong implementation of `george` within the `juliet` code when Chapters 5 and 6 have been produced. Fortunately, this does not significantly affect the results of this thesis. An error is only introduced when the inverse length-scale α is transformed to units of days.

Tab. 3.2.: Gaussian process priors used within `juliet` for the investigations of this chapter.

Parameter name	Prior	Units	Description
		GP prior I	
$\sigma_{\rm GP}$	$\mathcal{U}(0, 20)$	$\mathrm{m\,s^{-1}}$	Amplitude of GP component
$\Gamma_{\rm GP}$	$\mathcal{J}(10^{-1}, 10^{1})$	...	Amplitude of GP sine-squared component
$\alpha_{\rm GP}$	$\mathcal{J}(10^{-8}, 10^{0})$	$\mathrm{d^{-2}}$	Inverse length-scale of GP exp. component
$P_{\rm rot,\,GP}$	$\mathcal{U}(1, 100)$	d	Period of the GP QP component
$\sigma_{\rm jitter,\,GP}$	$\mathcal{J}(10^{-2}, 10^{1})$	$\mathrm{m\,s^{-1}}$	Extra jitter term
		GP prior II	
$\sigma_{\rm GP}$	$\mathcal{U}(0, 20)$	$\mathrm{m\,s^{-1}}$	Amplitude of GP component
$\Gamma_{\rm GP}$	$\mathcal{J}(10^{-1}, 10^{1})$	...	Amplitude of GP sine-squared component
$\alpha_{\rm GP}$	$\mathcal{J}(10^{-8}, 10^{-2})$	$\mathrm{d^{-2}}$	Inverse length-scale of GP exp. component
$P_{\rm rot,\,GP}$	$\mathcal{N}(22.0, 2.2)$	d	Period of the GP QP component
$\sigma_{\rm jitter,\,GP}$	$\mathcal{J}(10^{-2}, 10^{1})$	$\mathrm{m\,s^{-1}}$	Extra jitter term

The prior labels $\mathcal{U}$, $\mathcal{N}$,, and $\mathcal{J}$ represent uniform, Normal and Jeffrey's distributions (Jeffreys 1946).

length-scale hyperparameters for all 180 fits are visualized in boxplots. These are provided in Fig. 3.6 for a spot lifetime of 10 $P_{\rm rot}$ (220 d), in Fig. 3.7 for a spot lifetime of 5 $P_{\rm rot}$ (110 d), and in Fig. 3.8 for a spot lifetime of 2 $P_{\rm rot}$ (44 d).

In general, the rotation period was derived very accurately and precisely by the QP-GP for the majority of cases in which the spot lifetime $P_{\rm life}$ has been either 5 $P_{\rm rot}$ or 10 $P_{\rm rot}$. Nevertheless, one can see an effect on the precision and accuracy of the determined value based on the corresponding spot distribution. In general, the estimated median of the rotation period deviated stronger from the true value of the rotation period, and the interquartile range (IQR) spanned a wider range for random spot distributions. However, even in cases in which the absolute deviation of the derived median rotation period from the true rotation period has been considerable, the real value has been within the model uncertainty. Exceptions have been realizations where the QP-GP captured a signal at half of the rotation period, or GPs with insignificant evidence compared to a white-noise model.

In cases where the spot lifetime is close to the stellar rotation timescale ($P_{\rm life} = 2P_{\rm rot}$), the estimates of the rotation period by the QP-GP has been less precise. This is expected, as the signal's coherence decreases if the positions, size, and number of stellar spots on the surface change significantly within one rotation. The determination of the rotation period is particularly hampered if the spot distribution is, in addition to the short spot lifetime, positionally uncorrelated,

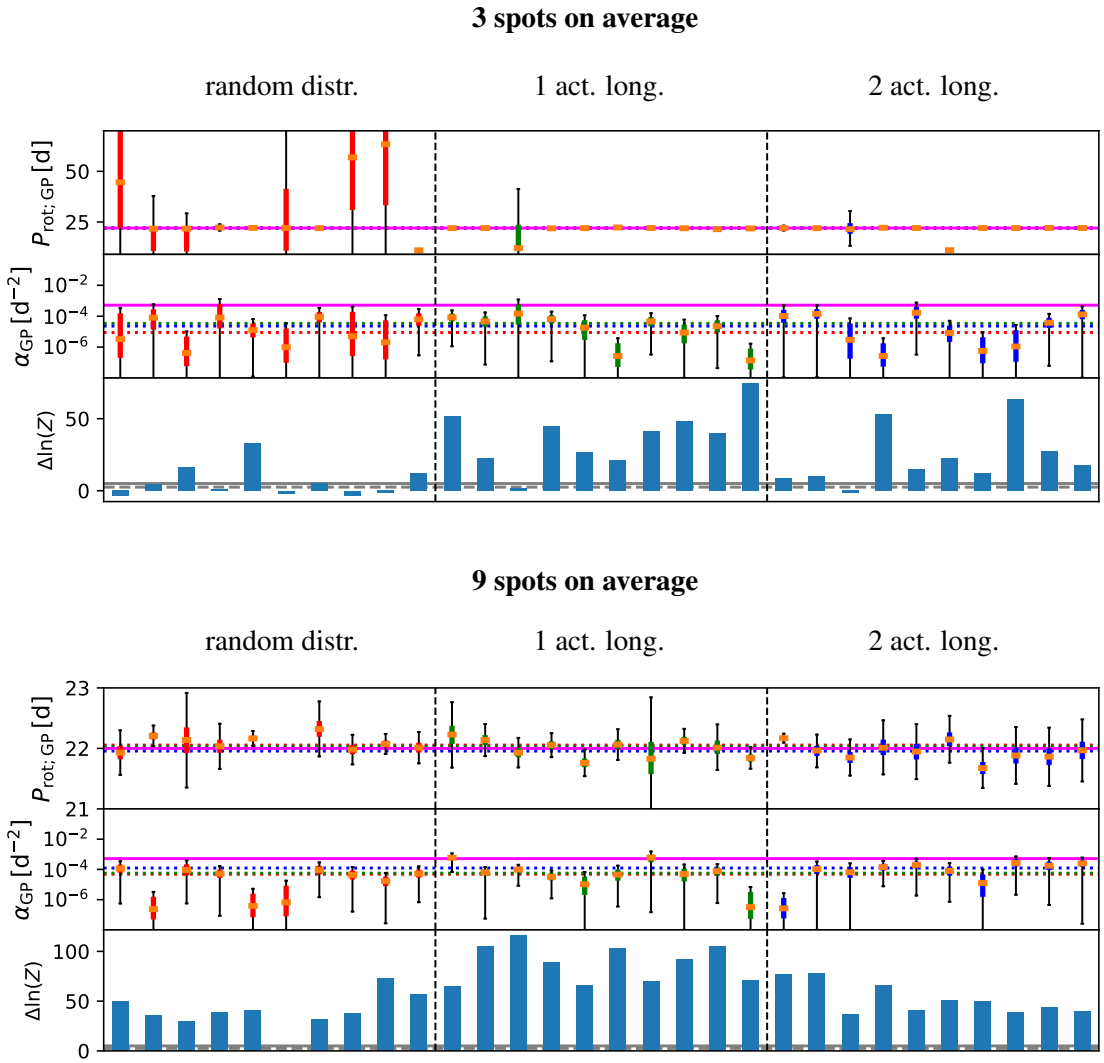


Fig. 3.6.: Boxplots of the derived GP rotational and GP inverse length-scale hyperparameter for simulated stars with $P_{\mathrm{rot}} = 22\,\mathrm{d}$ and spot lifetime of $P_{\mathrm{life}} = 10P_{\mathrm{rot}}$. The top panels visualize the results for a lower activity case of three spots on average at any time; the bottom panels show the results of a more active case with nine spots on average. The color of each box's interquartile range represents different cases of spot distributions: red represents a random spot distribution, green represents one active longitude, and blue represents two active longitudes. The difference of these spot distributions is additionally marked by two vertical dashed black lines in each plot. The horizontal dashed lines mark the median value of the ten simulated cases per spot distribution while the horizontal solid magenta line marks the simulated true value by `StarSim`, with the assumptions that P_{GP}=P_{rot} and $l = 1/\sqrt{\alpha_{\mathrm{GP}}} = P_{\mathrm{life}}$. The bottom row of each panel provides the log-evidence difference of the GP fit with respect to a flat model that included white-noise. The horizontal dashed and solid lines in the bar plot represent the boundaries of moderate and strong evidence according to Trotta (2008), respectively.

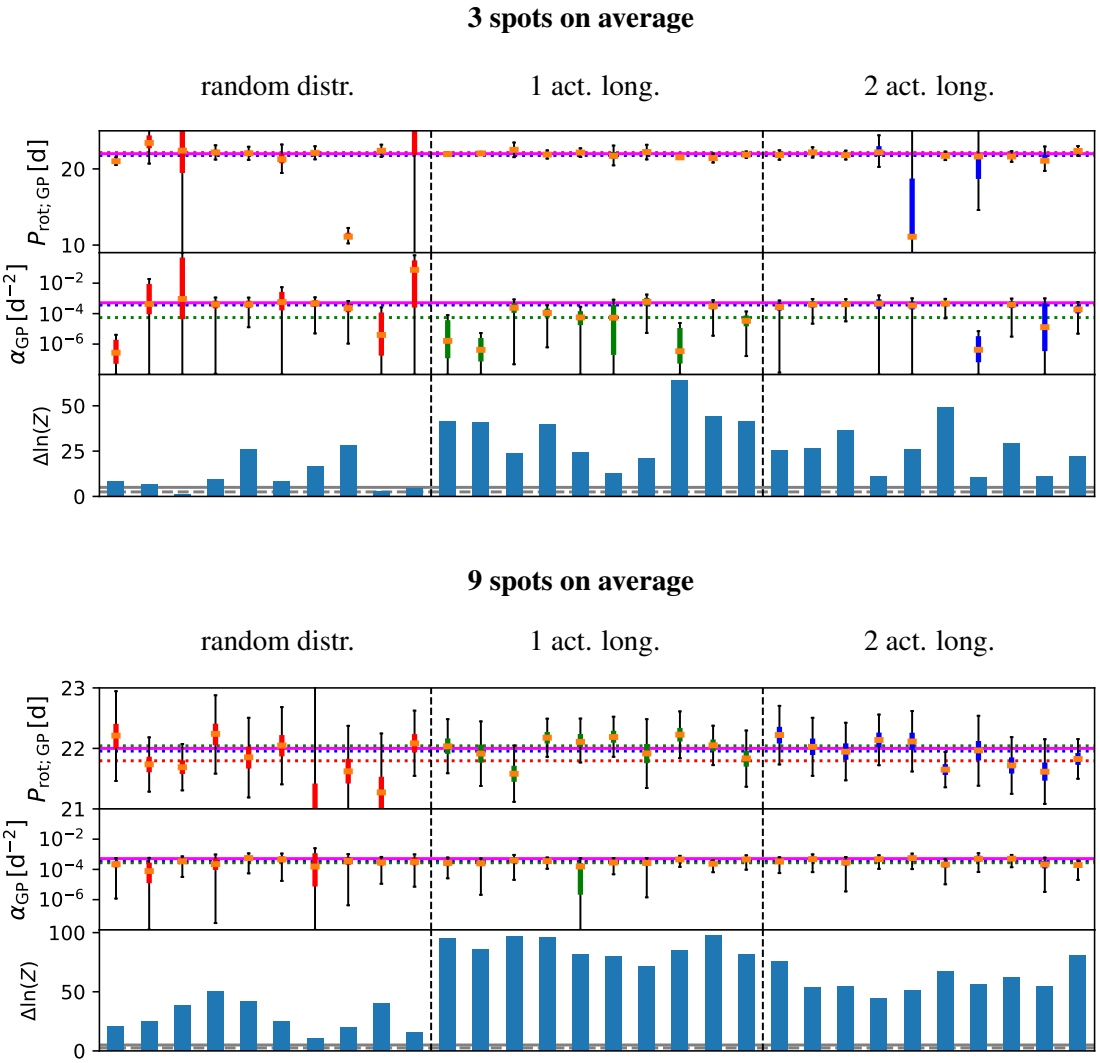


Fig. 3.7.: Same as in Fig. 3.6 but for a spot lifetime of $P_{\mathrm{life}} = 5P_{\mathrm{rot}}$.

i.e., a random spot distribution. In five out of ten of these cases, a flat model with a white noise component performed better or equal to the GP in terms of log-evidence (see, for example, top panel of Fig. 3.8). However, even for short spot lifetimes or unfavorable spot distributions, an accurate estimate has been derived, as the real rotation period lies in most cases within the uncertainty of the derived rotation period.

The analysis and results of this chapter and the following chapters indicate that it can be informative to investigate the two-dimensional distribution of the inverse length-scale hyperparameter α_{GP} over the rotation hyperparameter P_{GP}. A small inverse length-scale corresponds to a larger decay

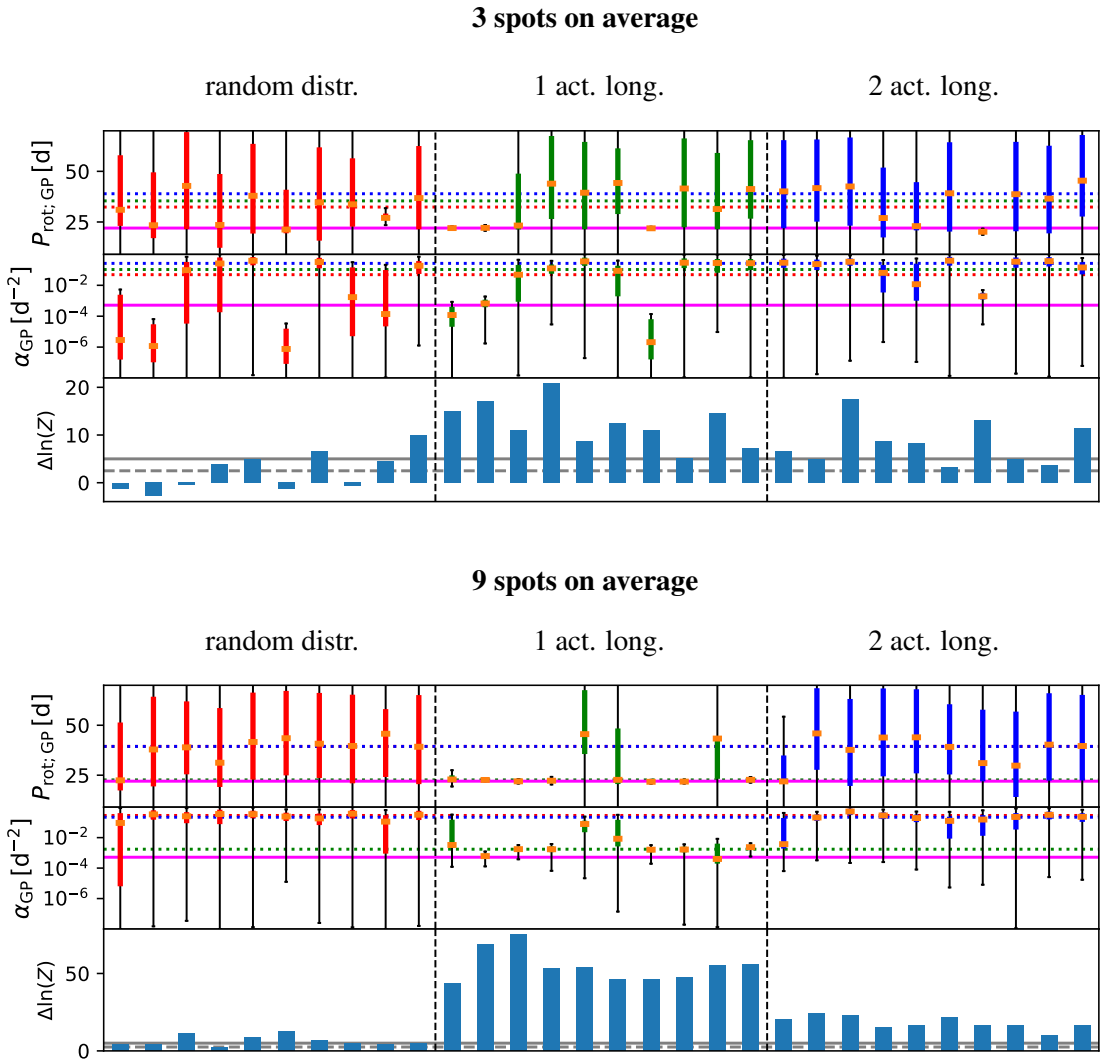


Fig. 3.8.: Same as in Fig. 3.6 but for a spot lifetime of $P_{\mathrm{life}} = 2P_{\mathrm{rot}}$.

time of the active regions, and, therefore, to a more coherent signal. In the best-case scenario, one can observe a well-defined peak within this two-dimensional distribution, which could be referred to as "o-shaped". A "prototype" of such a structure is shown in Fig. 3.9. However, if the lifetime of active regions is smaller or similar to the stellar rotation period, the signal's coherence decreases fast. Within the RV data short spot lifetimes will result in correlated noise on short timescales or white noise, depending on the observations' cadence and the particular spot distribution. Such noise can be identified as a plateau of posterior solutions with large α_{GP} with no preference for any rotation period within the α_{GP}-vs.-P_{GP} diagram. This is caused by the fact that the rotation hyperparameter within the exponential-sine-squared kernel gets meaningless if

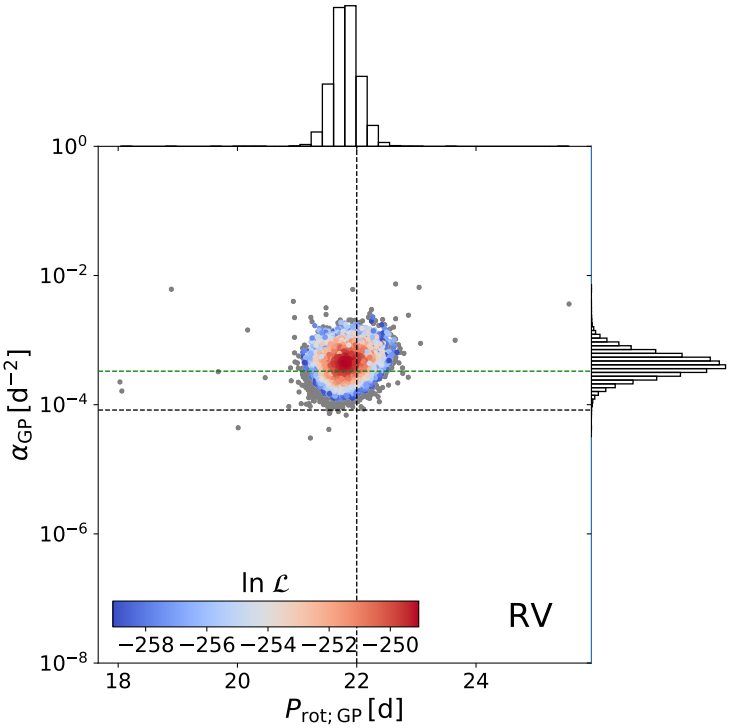


Fig. 3.9.: Posterior distribution of the GP fit to one simulated RV data set in the α_{GP}-vs.-P_{rot} plane for a star with $P_{life} = 5\,P_{rot}$ and two active longitudes. The two-dimensional posterior is well constrained and "o-shaped". The color-coding shows the log-likelihood normalized to the highest value in the posterior sample. Gray samples indicate solutions with $\Delta \ln L > 10$ compared to the best solution. The true rotational period modeled with `StarSim` is overplotted as the vertical line. The horizontal lines mark the simulated spot lifetimes under the assumption that either the length-scale is equal the spot lifetime (in black) or that two times the length-scale is equal the spot lifetime (in green), which has been empirically calibrated in this thesis.

the signal significantly decays on timescales smaller than one rotation, resulting into a dominant exponential-squared term. Nevertheless, by fitting a QP kernel, the GP model will try to identify any sign of coherence within the signal that is preserved for at least one or more rotations. This can lead to a characteristic structure, where posterior solutions close to the rotation period tend to populate also smaller α_{GP} values, resulting in an observed "v-shape" within the α_{GP}-vs.-P_{GP} diagram. This kind of structure is shown in Fig. 3.10. As can be seen, this structure can be used to indicate the position of the rotation period, even if the corresponding one-dimensional posterior distributions are rather unconstrained. The color-coding with each posterior solution's likelihood can further help to identify these structures.

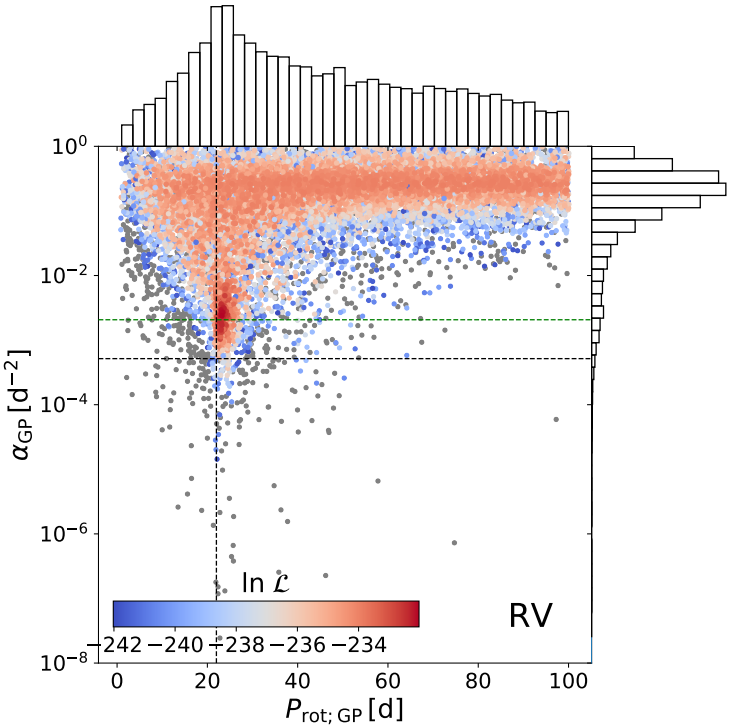


Fig. 3.10.: Same as in Fig. 3.9 but for a star with $P_{life} = 2\,P_{rot}$ and a random spot distribution. The posterior solutions form a plateau with a "v-shape" of higher likelihood, corresponding to the rotation period.

Although it has not been tested within the simulations of this thesis [3], it seems plausible that this "v-shaped" structure can also be observed if the spot lifetime is smaller than the rotation period, at least if the occurrence of the active regions on the stellar surface is positionally correlated, e.g., in the case of active longitudes. However, this estimate then might not be directly connectable to the spot life time of individual spots. By comparing the two-dimensional distributions of the cases with active longitudes to the cases that have a random spot distribution for $P_{life} = 2\,P_{rot}$, one finds that the cases with active longitudes show, in general, a more pronounced "v-shaped" structure at the rotation period.

In one-third of the simulated cases, the spot lifetime equaled the timespan of observations. For these cases or cases in which spots emerge on a similar longitude the posterior solutions can form an "i-shape" at the rotation period that spans towards the lower boundary of the prior volume that has been set for α_{GP}. Such a shape is caused by the fact that the decay of the signal cannot be

[3] It would have been interesting to test configurations with $P_{life} \leq P_{rot}$, however, due to an observed unresolved problem with `StarSim` these configurations could not be reliably simulated and tested before submission of this thesis and will be postponed and investigated in the future.

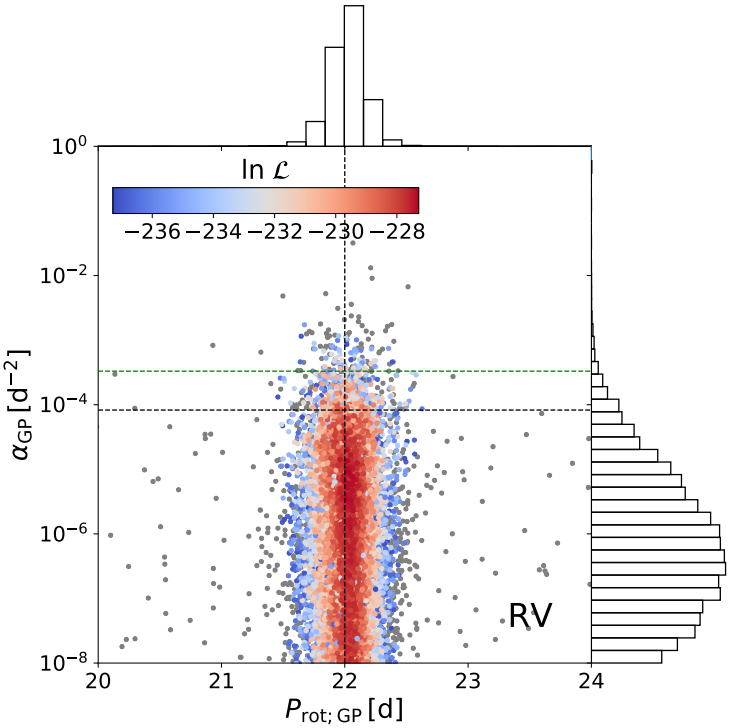


Fig. 3.11.: Same as in Fig. 3.9 but for a star with $P_{life} = 10\,P_{rot}$ and two active longitudes. The posterior solutions form an "i-shape" at the rotation period because the decay timescale is unconstrained due to the long spot lifetime compared to the time of observations, as well as the fact that several long-lived spots formed at similar longitudes resulting into a long-lived, stable and coherent correlation.

constrained given the data, therefore, the spot lifetime is estimated to "infinity" resulting in valid solutions for any small α_{GP} that is larger than the time on which the GP can constrain the decay. Such a shape in the α_{GP}-vs.-P_{GP} diagram can be interpreted as a signal that is coherent over the entire time of observations. This can be either due to long spot lifetimes, similar longitudes of recurring spots, or both. However, in most of the cases with spot lifetime equal to the timespan of the observations, a single "o-shaped" peak and, therefore, a decay time scale could still be derived. Therefore, the lower boundary of the prior α_{GP} should be allowed to span a slightly larger range than the timespan of observations.

Within some of the simulated cases, the α_{GP}-vs.-P_{GP} diagram showed a "characteristic structure" with high likelihood, unrelated to the rotation period. This has been particularly the case for the lower stellar activity simulations, i.e., three spots on average at any time. The occurrence of spots within `StarSim` is in general uniformly distributed over the time the model is calculated including a buffer on both sides so that spots can be present before the first observation. However,

by coincidence, it can happen that within some simulations there are periods in which the number of spots is significantly higher than for other times. This represents a random activity effect on small timescales that is similar to the effect of longterm magnetic cycles that also affects the number of spots. A close inspection of these cases reveals the following: the period at which this "i-shape" structures can also occur, if not related to the stellar rotation, is related to the period of the amplitude modulations, i. e., the envelope of the signal. Since in most simulated cases these spot overdensities occur only once or twice within the time-domain, the period is larger than the rotation period and the signal is not decaying over the time of observations. Therefore, it is reasonable to expect that it should be possible to also identify magnetic cycles with the QP-GP if long time-baseline observations are available. However, the highly flexible mean of the GP may "filter" these amplitude variations on large time scale without the need of an additional quasi-periodic component. In principle, it may be possible to combine two QP-GP kernels with different length-scales and periods to model these cases more physically.

Up until now, the length-scale hyperparameter has been interpreted as a decay time scale of the active regions on the stellar surface but not as a direct measure of the spot lifetime as defined by `StarSim`. Within `StarSim`, the spot lifetime is defined as the time the spot emerges, lives, and decays. A linear grow (and decay) is assumed within this spot lifetime until the final spot size is reached. The derived length-scale parameter of the QP-GP has been compared with the spot lifetime that has been used within `StarSim` to model the RV activity signal. The results indicate an offset between these two quantities. This is also visible in the "o-shaped" case shown in Fig. 3.9 and by looking at all the results given in Figs. 3.6, 3.7, and 3.8.

The effect of the posterior plateau or the "i-shape" cannot fully explain the observed offset, especially not for well constrained signals. By using only those estimates that are "o-shaped" in their two-dimensional posterior distributions, meaning that the two-dimensional posterior distribution of α_{GP} and P_{GP} consists of a single precise peak of posterior samples with high-likelihood, a correction factor, hereafter called η, between the simulated spot lifetime and the length-scale hyperparameter has been derived. The equation $P_{\mathrm{life}} = \eta / \sqrt{\alpha} = \eta \cdot l$ was solved for η for all posterior samples of "o-shaped" cases, therefore, resulting in a global distribution of η. The derivation of the correction factors based on the global posterior for each spot lifetime has yielded values of $\eta_{P_{\mathrm{life}}=2P_{\mathrm{rot}}} = 1.71^{+0.48}_{-0.60}$, $\eta_{P_{\mathrm{life}}=5P_{\mathrm{rot}}} = 2.02^{+0.64}_{-0.57}$, and $\eta_{P_{\mathrm{life}}=10P_{\mathrm{rot}}} = 2.03^{+1.55}_{-0.84}$ which base on 7, 38, and 29 "o-shaped" cases, respectively. The case of combined posterior samples of all three configurations yields a value of $\eta = 1.99^{+0.88}_{-0.69} \approx 2$.

The simulations of this chapter, therefore, indicate that the length-scale l of the QP-GP cannot be directly interpreted as the spot lifetime of active regions as defined by `StarSim`. This result is, however, based on a small number of simulations and a small number of different configurations.

In particular the ensemble of spots were not allowed to follow a distribution of spot lifetimes but were set to one specific spot lifetime. Additionally, a small effect on the value between random spot configurations and active longitudes is seen. For active longitudes the spots emerge on similar longitudes, and thus they result in a more coherent correlation of the signal. The value of $P_{\rm life} = 1.99^{+0.88}_{-0.69} \cdot l$ derived in this thesis is consistent with a recently derived value of $P_{\rm life} = (1.7 \pm 0.1) \cdot l$ by Perger et al. (2021) who propose a new kernel, the quasi-periodic and cosine (QPC) kernel that uses $l_{\rm QPC} = 2l_{\rm QP}$ to represent *"the average spot lifetime more closely"* (Perger et al. 2021). Additionally, they also find a slight difference between random spot distributions and active longitudes.

From the mathematical perspective, it seems reasonable that the characteristic length-scale cannot be a direct measure of the spot lifetime. The covariance of points that are exactly one length-scale ($\mathbf{x} - \mathbf{x}' = l$) apart is given by the kernel that follows a Gaussian form as $K = \exp(l^2/(2l^2)) = \exp(1/2) \approx 0.61$. This implies that the data is still correlated to a high degree, and that the spot cannot be fully dissolved. Additionally, it implies that the signal is decaying exponentially, which a-priori is not clear for a single spots, let alone an ensemble of spots, e.g., within `StarSim` a linear decay for each spot is assumed. Therefore, a "typical lifetime" may be difficult to define for signals whose amplitudes are not decreasing exponentially. Nevertheless, in the case that $\mathbf{x} - \mathbf{x}' = \eta l = 2l$, one obtains $K \approx 0.14$ which is much closer to zero correlation. Note that due to the exponential form of the decay in the covariance, it is not beneficial to increase η to arbitrarily large values.

This result has an implications for the setting of the prior of the length-scale parameter. As mentioned before, it is common to set $l > P_{\rm rot}$. However, as can be seen in Fig. 3.10, such a boundary condition would remove a large amounts of high-likelihood posterior solutions. Even if the length-scale is set to $l > P_{\rm rot}/2$, one would remove the lower half of the high-likelihood posterior solutions in the example of Fig. 3.10. Therefore, it seems reasonable to use less restricted and less informative priors on the length-scale parameter. A good prior of the length-scale l, or $\alpha_{\rm GP}$ in case of the `juliet` parametrization, can also be empirically constrained by setting the boundary of the prior with respect to the lower boundary of the observed plateau of posterior solutions of a GP fit with unconstrained and uninformative prior on the length-scale hyperparameter. From the results of the simulations it seems as if this is a very good approach to restrict the length-scale parameter of the QP-GP which is why it is used in this work.

Within the last decades, periodograms have been a frequently used diagnostic tool to infer stellar rotation periods. Periodograms generally assume sinusoidal signals, however, stellar activity is rarely strictly sinusoidal. For the 180 simulated cases, the performance of the GP has been compared with the GLS periodogram (generalized Lomb-Scargle periodogram; see Sec. 4.1.4 or

Zechmeister & Kürster 2009). The results of the GLS periodogram are based on the highest peak between 1 d and 100 d. Additionally, the false-alarm probability (FAP) had to be smaller than 1%. For the GP, the posterior medians were used and the log-evidence of a GP compared to a white noise model had to be larger than 2.5, representing moderate evidence according to Trotta (2008). Both of these detection threshold are not too conservative and are often used in the literature. For the GP, 92% of the fits reached the detection threshold while for the GLS periodogram only 82% of the simulated data sets showed a peak with an FAP smaller than 1%.

Figure 3.12 shows the histogram of the derived rotation period. The results presented in this figure show that in more than half of the cases the GLS periodogram has its highest peak close to half of the rotation period (the first harmonic of the signal) and not at the true rotation. Only in the case of one active longitude, the GLS periodogram is robust in detecting the correct period. On the other side, the GP is extremely efficient in detecting the true rotation period and only few solutions correspond to the first harmonic. A few GP solutions are close to a rotation period of 40 d, twice the true period, which, at first glance, seems indicative. However, inspecting those solutions showed that these are solutions with a "plateau" in the α_{GP}-vs.-P_{GP} plane. The rotation period of 40 d is a consequence of the prior distribution of P_{GP}, spanning uniformly from 0 d to 100 d, along with a small constraint of the data forming the "v-shape" around the rotation period, and, therefore, pushing the median to values smaller than 50 d. Applying the findings from the prior discussions in the previous paragraphs would result in better precision of the derived rotation period by the GP.

An additional aspect of a model is the reliability on its uncertainty estimate. The GP is not only more efficient in detecting the correct period, but it also offers a probabilistic uncertainty estimate based on a Bayesian approach. The right plot of Fig. 3.12 shows the distance of the estimated rotation period to the true value in terms of standard deviations. As can be seen, the uncertainty estimates of the GP are more realistic compared to the uncertainty provided by the GLS periodogram[4] which have been underestimated most of the time.

The results obtained within this subsection prefer the use of the QP-GP to the use of the GLS periodogram. The GP is a reliable tool to derive the stellar rotation periods of stars. The GP is the more flexible model that allows a better adaption to the QP behavior of stellar activity. However, some simulations, that showed drastic changes in the amplitude modulation, e.g., a change from a periodic signal with high amplitude to a flat line for the remaining observations. For these cases it was difficult for the QP-GP to model the flat part. Despite the flexibility of the GP, some residual variations caused by the model were introduced, although the effect is much smaller

[4]The uncertainty of the GLS periodogram is estimated by the GLS routine from the local χ^2 curvature of sinusoidal fits with different period to the data.

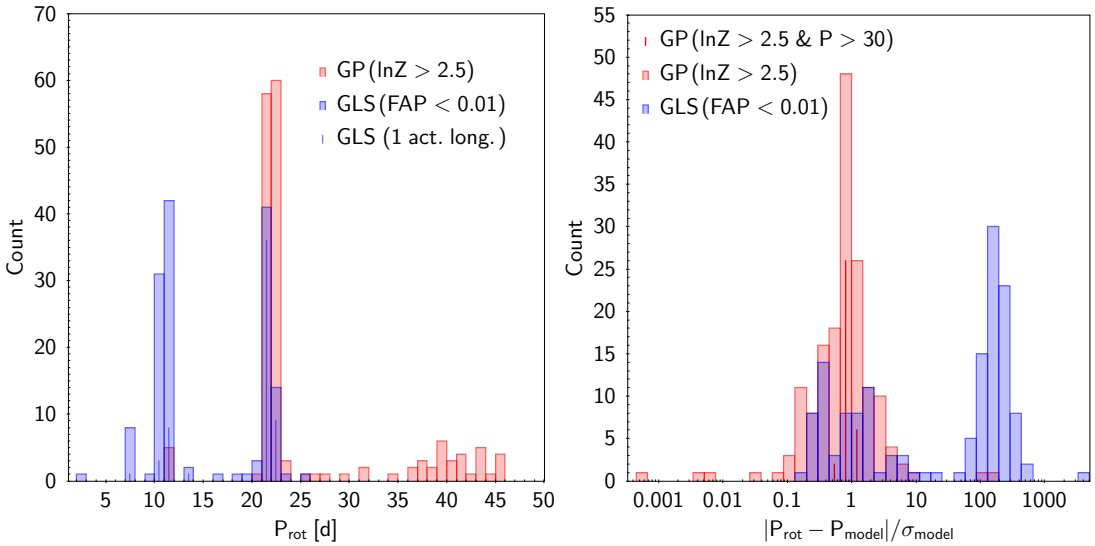


Fig. 3.12.: *Left:* This histogram shows the derived rotation period using the GP (in red) and using the GLS periodogram (in blue). The blue peaks show the periodogram estimates for the case of one active longitude on the stellar surface. *Right:* This histogram shows the absolute difference between simulated rotation period and the derived model estimate in units of standard deviations. It should be noted that the x-axis is in logarithmic scale. The red peaks show the uncertainty distribution of GP estimates with periods larger than 30 d that are visible in the left histogram.

than if the activity were to be modeled by sinusoidal functions. While the analysis within this subsection has been made on RV data, the conclusions are also applicable to photometric data as the main characteristics of stellar activity signals are not significantly different for these data. In particular, ground-based photometric data is not contaminated by Keplerian signals, therefore, the derivation of the stellar activity parameters is more robust on photometric data, as the GP will absorb the Keplerian signals within RV data in most cases (see Sec. 3.5.3). In case of RV data of real systems, the α_{GP}-vs.-P_{GP} plot should only be used for deriving the rotation period, after all Keplerians have been identified and are fitted simultaneously with the GP. The following sections will show how this can be reliably achieved, even in cases where no prior information of the system properties is available which is typically the case.

3.5.3 Absorption of planetary signals by quasi-periodic Gaussian processes

The aim of this section is to investigate if GP models absorb planetary signals if they are fitted to data sets that include a Keplerian signal. In the following analysis, Keplerian signals have

been added to the simulated activity-contaminated RV data. The grid of investigations from the last chapter is extended, by injecting two Keplerian signals with the following parameters $K = 3\,\mathrm{m\,s^{-1}}, P = 5\,\mathrm{d}$, $e = 0$, $\omega = 0$, and $M = 0$, hereafter referred to as signal K5, and $K = 3\,\mathrm{m\,s^{-1}}$, $P = 44\,\mathrm{d}$, $e = 0$, $\omega = 0$, and $M = 0$, hereafter referred to as signal K44. The Keplerians were injected independently of each other, i.e., only one of the signals, either K5 or K44, has been added to the simulated RV data at the same time. As for the activity-contaminated RV data sets, only the high activity cases, i.e., the cases with nine spots on average per time interval have been further investigated, as these high activity cases are of more interest. The RV semi-amplitude of the injected Keplerian signal has been set to $K = 3\,\mathrm{m\,s^{-1}}$ as it is on the order of, or in most cases even smaller than, the activity signal, which makes its detection more challenging.

Two different GP models have been fitted to the data sets without simultaneously fitting a Keplerian model for the injected Keplerian signal. The first GP-only model has uniform priors on the GP rotation hyperparameter and an unconstrained inverse length-scale hyperparameter (GP prior I, given in Table 3.2). The second GP-only model has a normal prior on the GP rotation hyperparameter and a slightly more constrained inverse length-scale hyperparameter (GP prior II, given in Table 3.2). The investigation of the simulated RV data, the GP model itself, and the RV residuals with the GLS periodogram can be informative regarding any potentially absorbed signal by the GP model. Figure 3.13 shows the periodograms for these three components for the simulations with the injected K5 signal and Fig. 3.14 shows the periodograms for these three components for the simulations with the injected K44 signal.

The results show that the GP-only model can absorb the Keplerian signal in many cases, despite not simultaneously fitting a Keplerian model. However, various results can be deduced. In the case of the K5 signal, the GP has absorbed the Keplerian signal in far less cases and with less strength than in the case of the K44 signal. For example, the periodograms of the RV residuals reveal that the planetary signal is the strongest remaining signal when the K5 signal is injected. In some cases, specifically those for which the spot lifetime has been longer, the periodograms of the RV residuals has larger relative power compared to the periodogram of the RV data since the astrophysical noise is removed. However, for short spot lifetimes (44 d) or a random spot distribution, the K5 signal has also been absorbed in many cases by the GP. These are configurations for which the α_{GP}-vs.-P_{GP} plot preferably shows a plateau with posterior solutions that have very small length-scales. The period of the Keplerian component with respect to the length-scale of the GP affects how strongly the signal is absorbed by the GP. This is the reason why the K44 signal is much stronger absorbed by the GP model. As a consequence, one would assume that further constraining the GP to the presumed quasi-periodic signal should affect

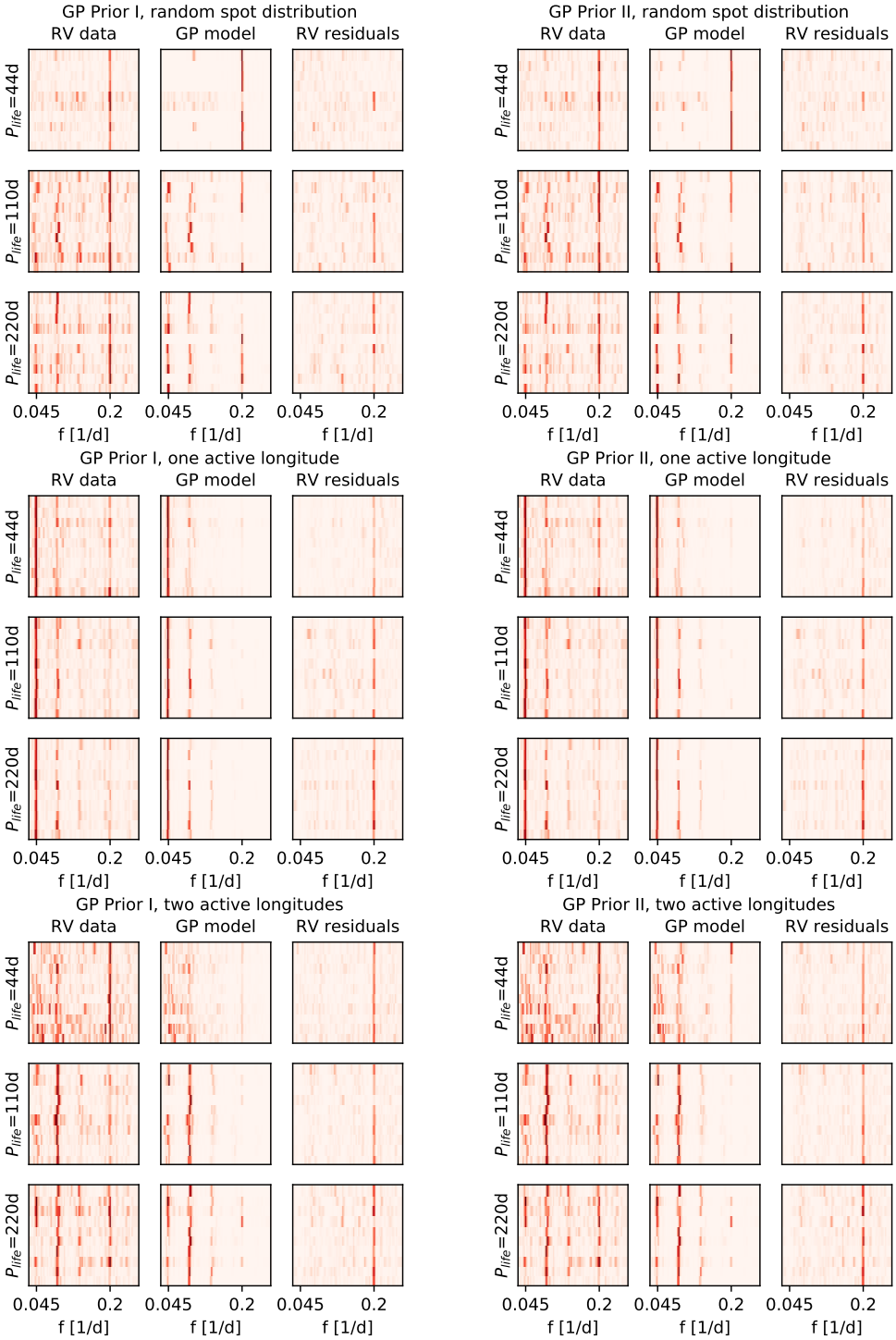


Fig. 3.13.: Each 3×3 matrix represents a certain spot distribution. Within each 3×3 matrix, a row corresponds to a different spot lifetime and a column represents the GLS periodogram of the RV data (left), GP model (middle) and RV residuals (right). Within each window, a row represents one of ten simulated cases while the x-axis represents the frequency of the periodogram. The power of the periodograms is color-coded with respect to the highest power (in dark red) achieved within the periodograms of the RV data, GP model, or RV residuals of that data set. The left column of 3×3 matrices represent fits with GP prior I and the right column of 3×3 matrices represent fits with GP prior II. The K5 signal ($f = 0.2\,\mathrm{d}^{-1}$) has been injected.

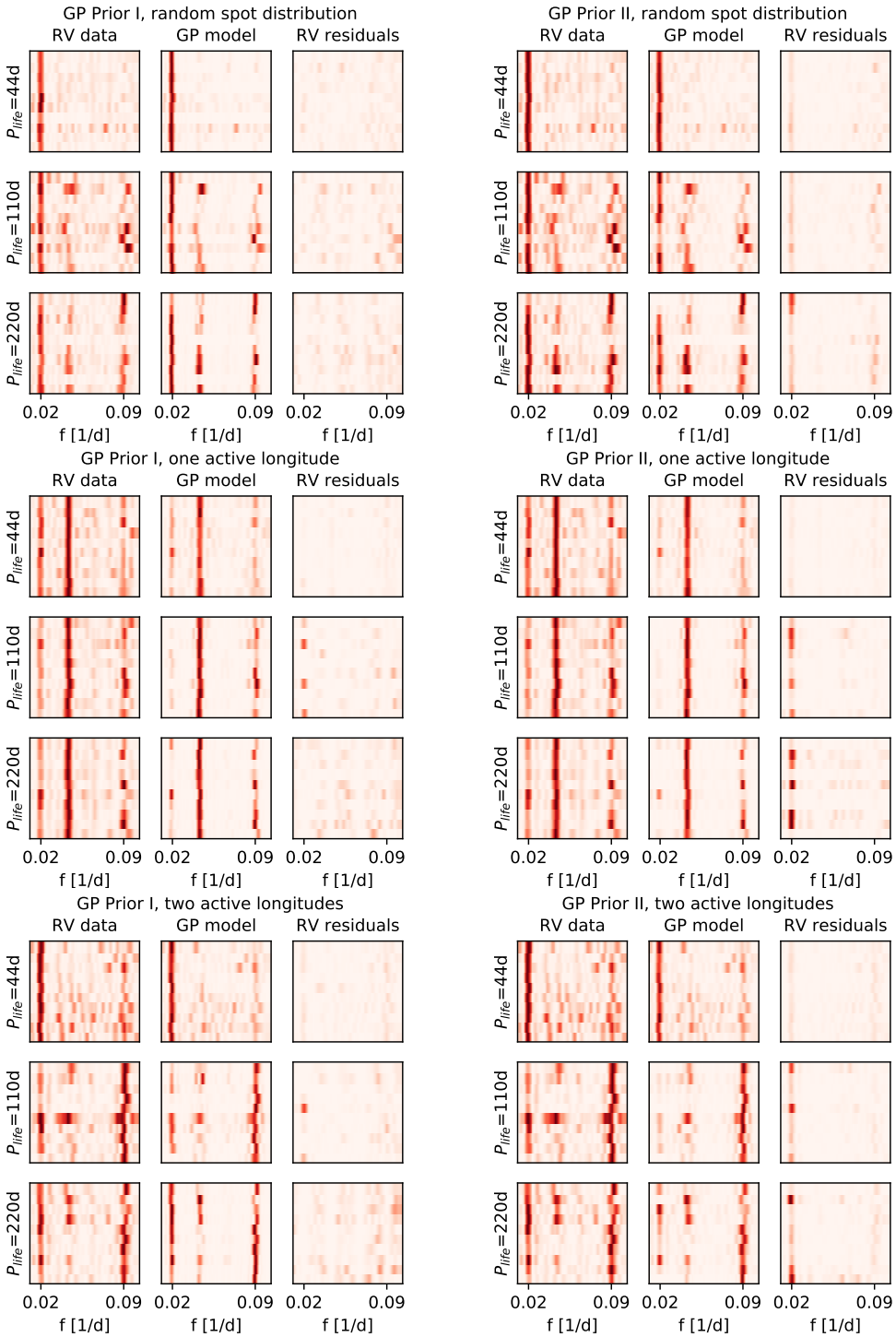


Fig. 3.14.: Same as in Fig. 3.13 but for the injected K44 signal ($f \approx 0.02\,\mathrm{d}^{-1}$).

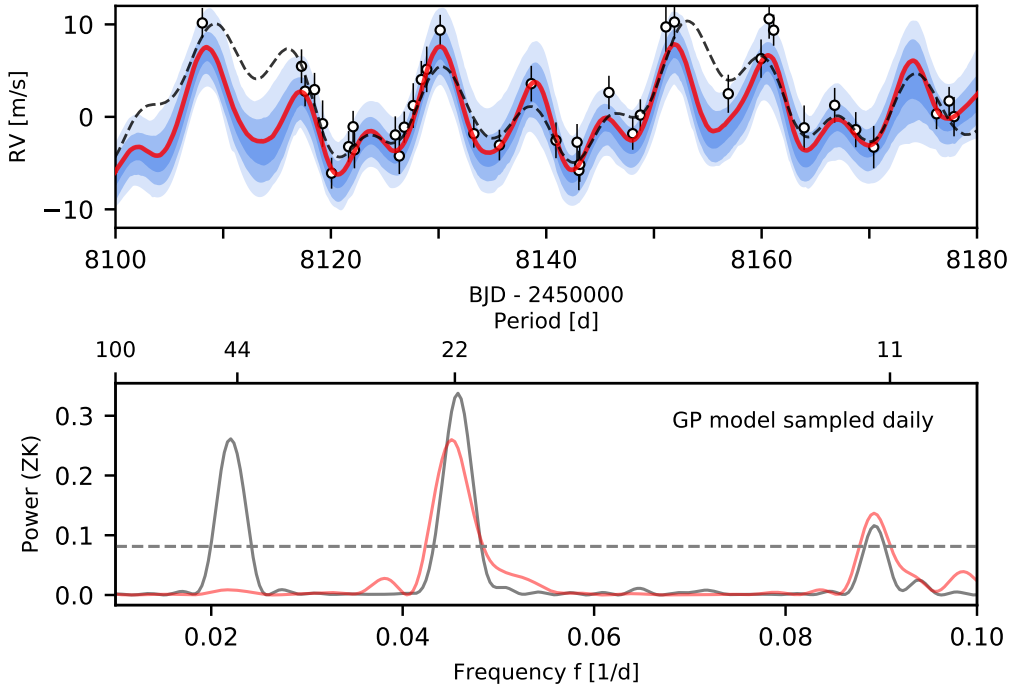


Fig. 3.15.: *Top:* Enlarged view of the constrained GP model with the GP Prior II (in red) that has been fitted to synthetic activity contaminated RV data with an additional Keplerian signal injected at 44 d. The 68%, 95%, and 99% confidence levels are shaded in blue. The unconstrained GP model with GP Prior I (dashed-black line) that absorbed the injected Keplerian signal is shown, as well. *Bottom:* GLS periodogram of the constrained GP model (in red) and of the unconstrained GP model (in black). The dashed-black horizontal line indicates an FAP of 0.1%. The periodogram of the less-constrained GP shows a clear peak at the planetary period at 44 d.

the strength by which the Keplerian component is absorbed. Indeed, if one compares the RV residuals of the more constrained GP fits with those of the less constrained fits, particularly for the K44 signal, one can see that in case of a GP constrained to the rotation period of the star and with a stronger constraint on the length-scale, the Keplerian component is absorbed less often. An example where the prior has significantly influenced the Keplerian absorption by the GP is provided in Fig. 3.15.

Despite the improvement with a constrained GP prior distributions, pre-whitening in general, and in particular pre-whitening using GPs, is not a valid approach. The GP is a red-noise model that will try to fit all variability within the residuals, independent of its origin, given the allowed flexibility provided with the hyperparameters. However, the solution to this problem is the

simultaneous modeling of GPs and Keplerian models and constraining the GP model given any prior information that is available. Model comparison in the framework of the Bayesian evidence should be able to find the best combination of models given the data. The reliability of this approach is investigated in the next section. The periodogram decomposition of the GP model that has been used in the current section can be used as a tool to reveal which periodic components are fitted by the GP model. It is then advisable to test by means of model comparison whether any significant periodicity within the GP model could also be equally modeled by a Keplerian signal.

3.5.4 Model comparison in a Bayesian framework: Keplerian model vs. QP-GP model

Efficient nested sampling, and in particular the powerful metric of the log-evidence, can help to distinguish planetary signals from stellar activity. A numerical experiment to assess the robustness of this metric has been performed. The following analysis has been carried out on the simulation that included the K44 signal, as this signal has been absorbed stronger by the GP than the K5 signal.

In the simulated RV data sets with Keplerian signals, three signals appear, in most of the cases, at periods of 11 d, 22 d, and either 5 d or 44 d (as can be seen in Fig. 3.14). The following experiment assumes that the origin of these signals within the RV data is unknown, and no additional information on the nature of these signals is available i.e., no photometry or activity indicators. The idea is to test whether it is possible to identify the origin of the signal by comparing GP models and Keplerian models in the framework of Bayesian evidence. As no information on the signals is given, the unconstrained GP with GP prior I, as given in Table 3.2, has been used.

The Keplerian models' prior ranged all possible parameter values for e, M, and ω. The prior of the semi-amplitude K was uniform between $0\,\mathrm{m\,s^{-1}}$ and $20\,\mathrm{m\,s^{-1}}$. The GLS periodogram has informed the prior of the orbital period of the data, and it has been set to a uniform distribution around the period, with a lower and upper boundary, corresponding to a 10% difference of the absolute value from the true value. As an example: the Keplerian model fitted to the 44 d signal had the prior $\mathcal{U}(39.6\,\mathrm{d}, 48.4\,\mathrm{d})$ for the orbital period.

In the first step, four models have been compared, a flat model (F), a Keplerian model fitted for 44 d (K44), a GP model, and a combined GP and Keplerian model (GP/K44). All these models included an additional jitter term. The results of this experiment are visualized in Fig. 3.16 which shows the log-evidence difference between these models for each simulated data set. As additional

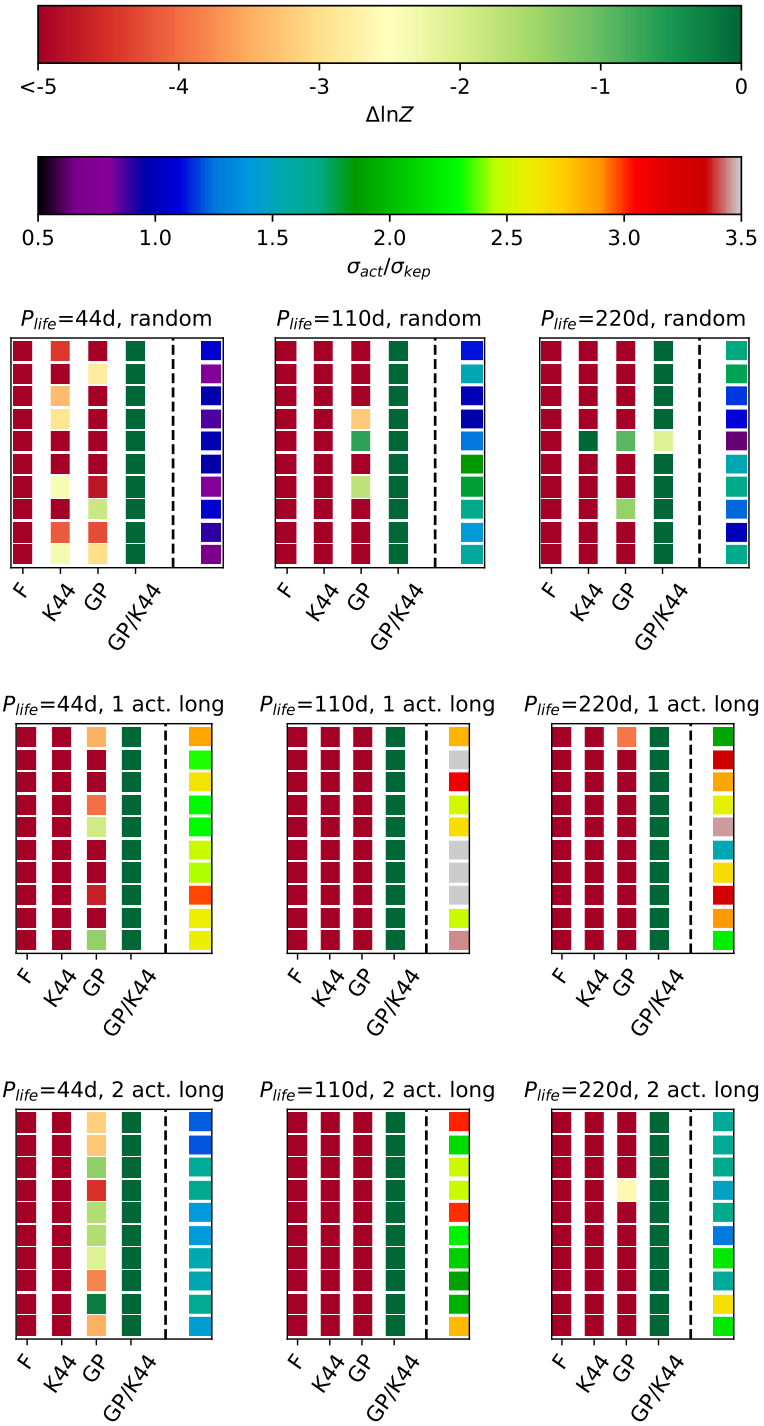


Fig. 3.16.: This figure visualizes the differences in the log-evidence between models fitted to the simulated data. Each subplot corresponds to one out of nine different stellar activity configurations. Within each subplot each row represents one out of ten random realizations of the stellar activity configuration. Each column left to the vertical-dashed line represents a different model fitted to the data. The color bar represents the difference in the log-evidence with respect to the best model of the row, which is set to a log-evidence of zero (in dark green). The column right to the vertical-dashed line represents an approximated amplitude ratio $\sigma_{\rm act}/\sigma_{\rm kep}$ with its own color-bar provided on the top.

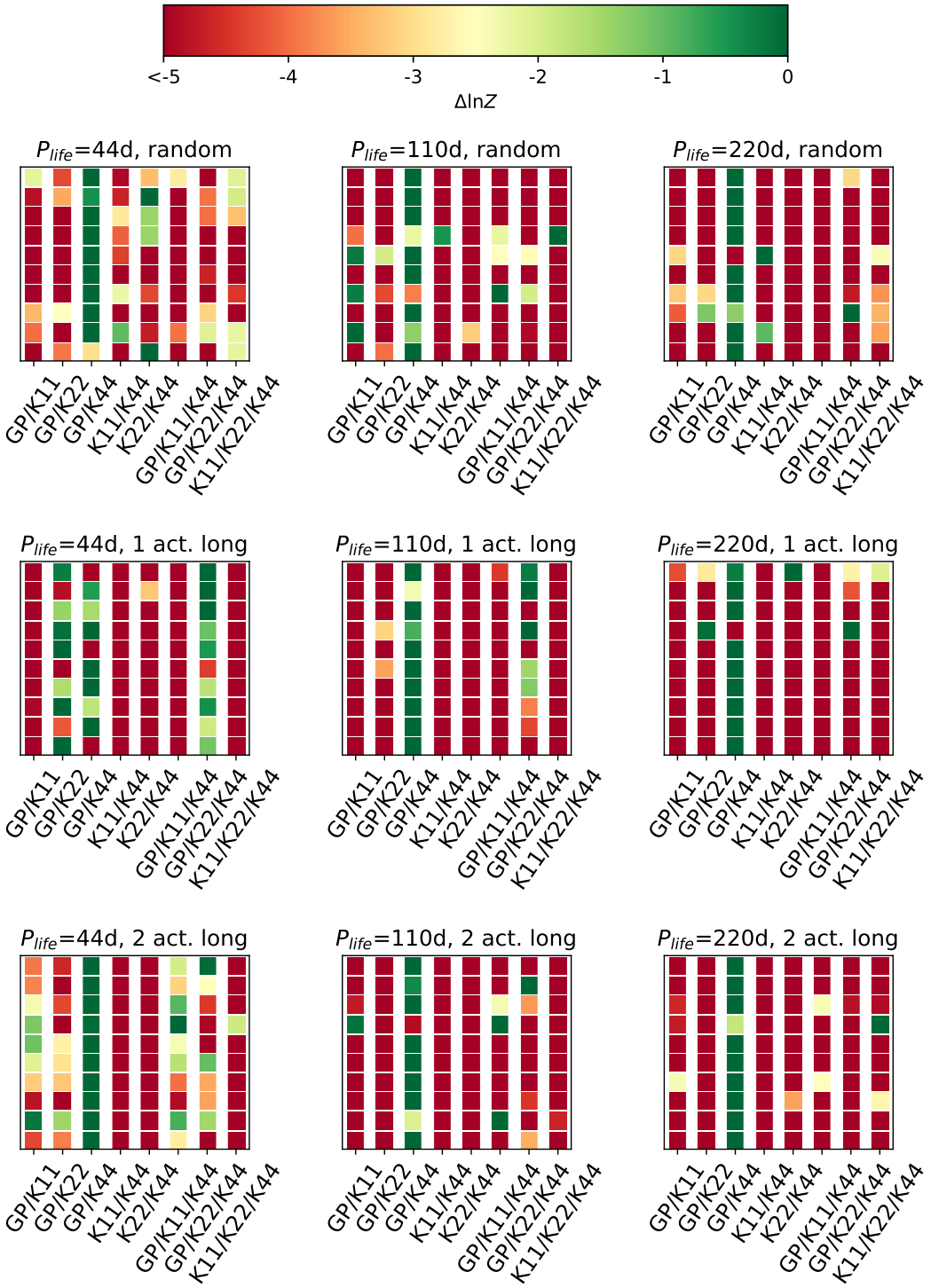


Fig. 3.17.: Same as in Fig. 3.16 but without the approximated amplitude ratio for each simulated data set for which the value can be obtained in the previous figure on the left page. The rotation period of the star is at $P_{\mathrm{rot}} = 22\,\mathrm{d}$, the planet signal at 44 d. K11, K22 and K44 denote Keplerian models fitted to 11 d, 22 d and 44 d.

information an activity-to-Keplerian signal ratio ($\sigma_{\mathrm{act}}/\sigma_{\mathrm{kep}}$) is color-coded as a second quantity. Its value for each data set has been derived by numerically determining the standard deviation of the noise-free `StarSim` model and dividing this by $\sigma_{\mathrm{kep}} = K/\sqrt{2}$ of the injected circular Keplerian signal. As can be seen from this figure, the GP and Keplerian simultaneous fit reached the highest evidence in all cases, except for one data set, for which the Keplerian model had slightly higher evidence ($\Delta \log \mathcal{Z} \sim 2$). However, models for which the log-evidence difference is smaller than 2.5, meaning less than moderate evidence in favor of the better model, are basically indistinguishable (Trotta 2008). Additionally, for this single case, the activity-to-Keplerian signal ratio has been strongly in favor of the Keplerian model and the activity signal has been very small. This shows that the log-evidence does not favor the inclusion of a GP in cases where the activity level is very small. Overall, the results show that, although the QP-GP is a powerful and flexible model, it is not capable of explaining all the variability within the data if a Keplerian signal is apparent, even if that Keplerian signal's amplitude is of the same order, or smaller, than the activity signal's amplitude. The correct approach to investigate an unknown system with several signals is to test various possible model combinations for the observed variations.

Therefore, if the origin of the signals is unknown, one must also compare Keplerian signals for the variations of the simulated rotation period at 22 d and its observed first harmonic at 11 d. Figure 3.17 shows a variety of additional model combinations that have been tested. It is encouraging that the correct model combination (GP/K44) has won, or is within the best indistinguishable models, in the vast majority of the cases. This shows that this approach is, in general, robust, in particular, if any additional information on the nature of these signals is available, for example, the rotation period derived by photometric observations or activity indicators.

Nevertheless, for a few data sets, a Keplerian model for one or both activity-related signals, in addition to the GP, has been significantly ($\Delta \log \mathcal{Z} > 5$; GP/K44 marked in red for 6 of 90 data sets) or moderately significantly ($\Delta \log \mathcal{Z} > 2.5$; GP/K44 marked in orange/yellow for 4 of 90 data sets) favored. It is expected that a Keplerian signal can have similar performance for an activity signal that has long lifetimes and is relatively stable. However, it might be unexpected that in the case of short spot lifetimes, an additional Keplerian component for the activity related signal has been favored more often than in the case of long spot lifetimes. Short spot lifetimes result in less coherent RV signals with varying amplitude and the signal, therefore, deviates stronger from a perfect sinusoidal or Keplerian signal, in contrast to the cases with longer spot lifetimes. However, it is precisely this characteristic that apparently makes it more difficult for the QP-GP to model the periodic variations as well, which is why the evidence favors an additional sinusoidal-like model component. As explained before, it is common to observe a

plateau of posterior solutions with no meaningful rotation hyperparameter for short spot lifetimes because the GP length-scale is shorter than one period. This results in an unconstrained rotation hyperparameter for the GP model, and the median QP-GP kernel is effectively turned into an exponential-squared kernel. Therefore, it is beneficial for most posterior solutions in the plateau of such a model that an additional sinusoidal or Keplerian model component fits any periodic variations. Then, the GP component only takes into account any additional short-term deviation from this sinusoidal-like structure. This behavior has been observed in many of those cases that showed a plateau in the α_{GP}-vs.-P_{GP} plane.

As an example, the left panels of Fig. 3.18 show several different GP models for a data set with a spot lifetime of 44 d and one active longitude where the GP/K44 model has been significantly worse than the GP/K22/K44 model. As can be seen from the α_{GP}-vs.-P_{GP} plot in the right panels of Fig. 3.18, the additional Keplerian model removes the posterior samples at smaller α_{GP} belonging to larger length-scales. A solution for this problem can be achieved by constraining the GP to only allow longer length-scales. A fit with the GP prior II as given in Table 3.2 resulted in a much higher agreement of the GP model with the noise-free `StarSim` model. Additionally, the derived eccentricity of the Keplerian signal (injected with zero eccentricity) has been reduced from $e = 0.70^{+0.10}_{-0.10}$ from the GP/K44 fit to $e = 0.66^{+0.15}_{-0.21}$ in the GP/K22/K44 fit, to $e = 0.49^{+0.23}_{-0.30}$ in the case of the constrained GP/K44 fit with GP prior II. The effect on the planetary parameters will be discussed in the following section.

The results of the investigated cases in this thesis show that, in contrast to the concerns, the model comparison in the framework of the Bayesian log-evidence does not allow a QP-GP to absorb an apparent Keplerian signal in the data without penalizing it. The inclusion of an additional Keplerian model for the injected signal has been favored in all cases. However, the opposite has been observed – for a small number of data sets, a stable periodic variation, e.g., a Keplerian model, can absorb parts of the stellar activity and support the GP model. This shows that the QP-GP still has limited flexibility, so that the model cannot properly take into account both short-term and long-term correlated noise. Therefore, one would either have to extend the kernel function with an additional term, taking into account these short-term variations, or decide how to tune the hyperparameters of the QP-GP to model the variations affecting the data the most. The approach used within this thesis has been to tune the QP-GP, in terms of period and length-scale, to the signal related to the star's rotation period. The noise on short time scales is taken into account by absorbing these as "jitter". As has been shown in Sec. 3.5.2, this is, to a certain degree, sufficient, as for some configurations with short spot lifetimes and random spot distributions a flat model assuming white-noise had a similar or better performance than the QP-GP in terms of log-evidence.

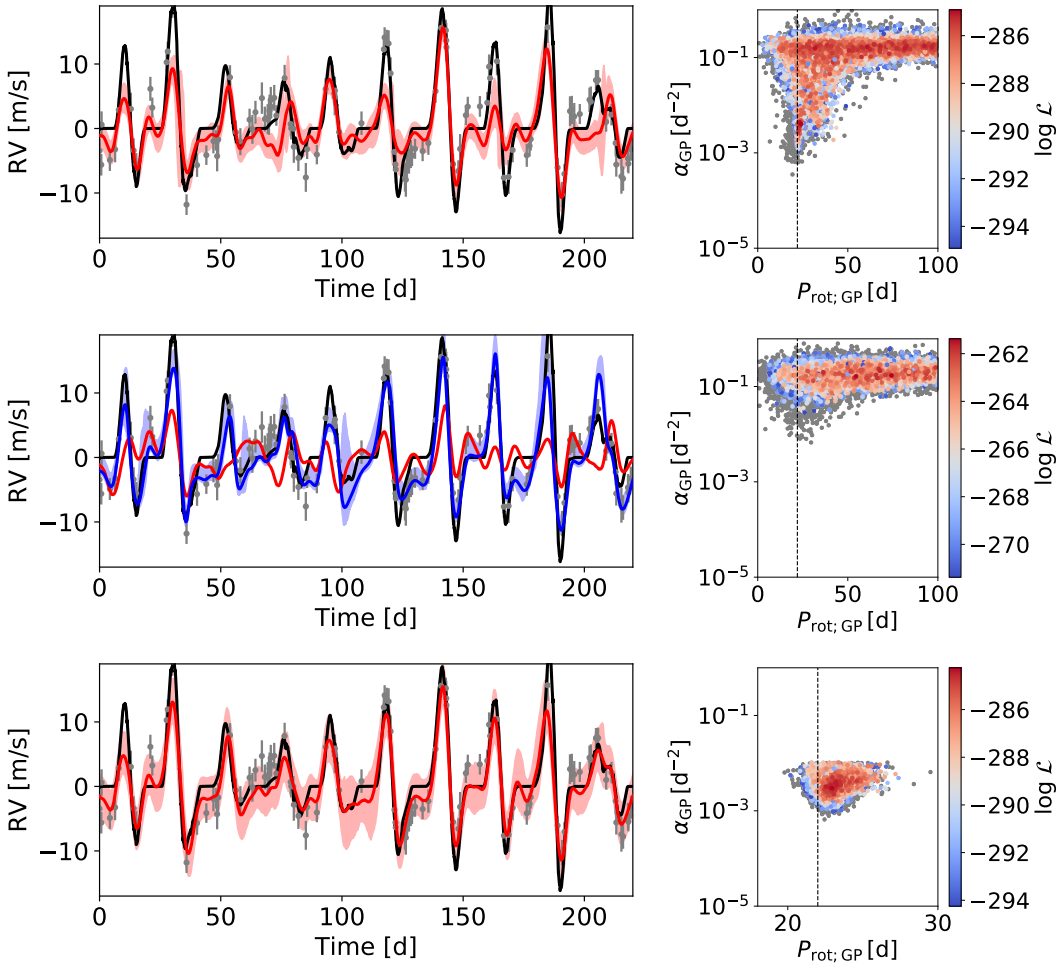


Fig. 3.18.: *Top left:* The GP model of the GP/K44 combined fit is plotted as red line, the noise-free `StarSim` model is plotted in black, the RV data is represented by gray points. *Top right*: α_{GP}-vs.-P_{GP} plot of the GP in the GP/K44 combined fit. *Middle left:* The combined GP/K22 model is plotted as the blue line, the GP model of the GP/K22/K44 combined fit is plotted as the red line, the noise-free `StarSim` model is plotted in black, the RV data is represented by gray points. *Middle right*: α_{GP}-vs.-P_{GP} plot of the GP in the GP/K22/K44 combined fit. *Bottom left:* Constrained GP model with GP prior II as in given in Table 3.2 of a combined GP/K44 fit is plotted as the red line, the noise-free `StarSim` model is plotted in black, the RV data is represented by gray points. *Bottom right*: α_{GP}-vs.-P_{GP} plot of the constrained GP in a GP/K44 combined fit.

While the analysis provided in this section has shown that the log-evidence metric coupled with the QP-GP and Keplerian models is robust in most cases, the results show the benefit of having additional prior knowledge on the nature of the signals. This can either be derived from photometric observations, activity indicators, or some other measure, e.g., a wavelength

dependency of the signal or any loss of coherence of the signals over the time of observations. Within this thesis, the following criteria have been used to declare a planetary signal. A Keplerian fit for the signal must have a significant log-evidence improvement compared to a GP model. Additionally, this signal must be coherent, and it is not allowed to show any significant counterpart within the spectroscopic activity indicators or to be consistent with the photometrically derived rotation period within the uncertainties.

3.5.5 Investigations on planetary parameters

In this last section of this chapter, it is investigated how precisely and accurately the planetary parameters of the injected Keplerian signals can be recovered. Three models have been compared: a model that included only a Keplerian fit to the injected planetary signal, a model that included a simultaneous unconstrained GP (GP Prior I) in addition to the Keplerian model, and a model that included a more constrained GP (GP Prior II) in addition to the Keplerian model. The derived planetary parameters for the K5 and K44 signal are visualized for the derived eccentricity in Fig. 3.19, while Figs. 3.20 and 3.21 show the same for the derived RV semi-amplitude and for the derived orbital period, respectively. These three parameters were most affected regarding the different models. The difference in the effect on determined planetary parameters between the two differently constrained GP models was small, except for cases with a short spot life-time, for which the more constrained GP resulted in slightly more precise and accurate estimates of the planetary parameters. Therefore, Figs. 3.21, 3.20, and 3.19 show only the results of the Keplerian fit without GP and the results of the fits which included the constrained GP (GP Prior II).

The strongest effect of the activity signal on the modeled planetary parameters can be observed for the derived eccentricity of the planet. The determined value of the eccentricity in the RV model depends on the form of the RV curve (see, for example, Fig. 2.3 in Sec. 2.2.1) which can be easily changed by an additional correlated signal that is apparent in the data that is not modeled properly. The eccentricity is, therefore, capable to absorb such signals more easily than the period parameter. In the case of the K5 signal, the median of the derived eccentricities of all fits has been reduced from 0.25 to 0.12 if the stellar activity has been fitted with a GP. Additionally, the median absolute uncertainty of the eccentricity has been reduced by a factor of two. So the overall precision and accuracy of the estimate has increased significantly by adding a GP.

The more interesting case, however, is the K44 signal. The period of this injected Keplerian has not arbitrarily been set to twice the rotation period of the star. Anglada-Escudé et al. (2010) has shown that planets in 2:1 period commensurabilities can be confused with a single planets with

high eccentricities. This is caused by the fact that the RV signal of two Keplerians in a period commensurability is on first order identical to a single high-eccentricity signal (Anglada-Escudé et al. 2010). Within this thesis, a similar effect has been found for YZ Ceti b (see Chapter 5), but the second signal is an alias of a quasi-periodic signal caused by stellar activity. By setting the planetary period to twice the simulated rotation period, this potential effect has been further investigated in the simulations. In Fig. 3.19, this effect is observable in the simulated data sets. For the injected planetary signal with circular orbit ($e = 0$), the median derived eccentricity of all Keplerian fits that neglected the modeling of the stellar activity has been $\tilde{e}_{\mathrm{K44}} = 0.62$. More importantly, the median of the absolute uncertainty has been only $\tilde{\sigma_{\mathrm{e}}} = 0.09$ resulting in the fact that the median distance of the derived value from the true eccentricity has been larger than 4.4 standard deviations. The small uncertainty of the estimate implies a high precision but the estimate is not accurate. This picture is significantly different for fits that included a GP. Here, the median of all derived eccentricities is $\tilde{e}_{\mathrm{K44}} = 0.28$, which is much closer to the true value, and, although the absolute uncertainty has increased, the values are more realistic as the median distance between the true value and the derived values is only ~ 1.5 standard deviations. So while including the GP results in less precision in this case, it allows much higher accuracy. The larger uncertainties of the GP-Keplerian fit reflect the difficulty to disentangle the stellar activity signal from the first harmonic of the orbital period that contains information about the eccentricity of the planetary signal.

Regarding the RV semi-amplitude, similar conclusions can be drawn from the results as for the eccentricities. The determined RV semi-amplitude is connected to the eccentricity, therefore, the RV semi-amplitude parameter is also overestimated in cases that neglected to model the stellar activity contribution. Regarding the planetary orbital period, the effect of the GP is much less obvious although apparent. While the median of the derived orbital periods, absolute uncertainties and model distances to the true model in standard deviations performs similar, it does not reflect that the fits without GP resulted in a few cases with larger deviation from the true value as for cases in which a GP has been included. Nevertheless, the orbital period is less susceptible for errors than the eccentricity in the presence of an additional correlated noise signal in the data.

The results of these investigations show that it is strongly advisable to model all apparent periodic variations within the RV data in order to derive precise and accurate planetary parameters. An approach, that can sometimes still be found in the literature, is to neglect those signals that are attributed to the stellar activity even if they result in significant signals within the residuals. As can be seen, this has the disadvantage that the planetary parameters are less accurate and precise, at least if the planetary signal amplitude is of the same order or smaller than the stellar noise contribution. Only the high-activity cases, with nine spots on average per time interval, have

been used for the investigations of the Keplerian signals in this chapter. However, there is one simulated data set, that was mentioned in the last section, for which the amplitude ratio was in favor of the Keplerian signal, and for which the Keplerian fit had slightly higher evidence than a GP-Keplerian combined fit (see the top right panel in Fig. 3.16). This single data set is the only exception for which the Keplerian model provided more precise and accurate parameters than the combined fit. Here, the eccentricity has been determined to $e_{\mathrm{K}} = 0.09^{+0.11}_{-0.06}$ for the Keplerian-only fit, while for the Keplerian and GP simultaneous fit the eccentricity has been determined to $e_{\mathrm{K+GP}} = 0.15^{+0.18}_{-0.11}$. So the inclusion of the GP model should be justified by an apparent activity signal and a higher evidence. A final note, regarding the distribution of the eccentricity: it is beneficial to compare models of fixed-zero eccentricity to models with free eccentricity to investigate whether the inclusion of an eccentricity parameter, given the data, can be justified, as it can sometimes happen that the eccentricity cannot be well constrained from the data and the resulting posterior distribution of the eccentricity is consistent with zero.

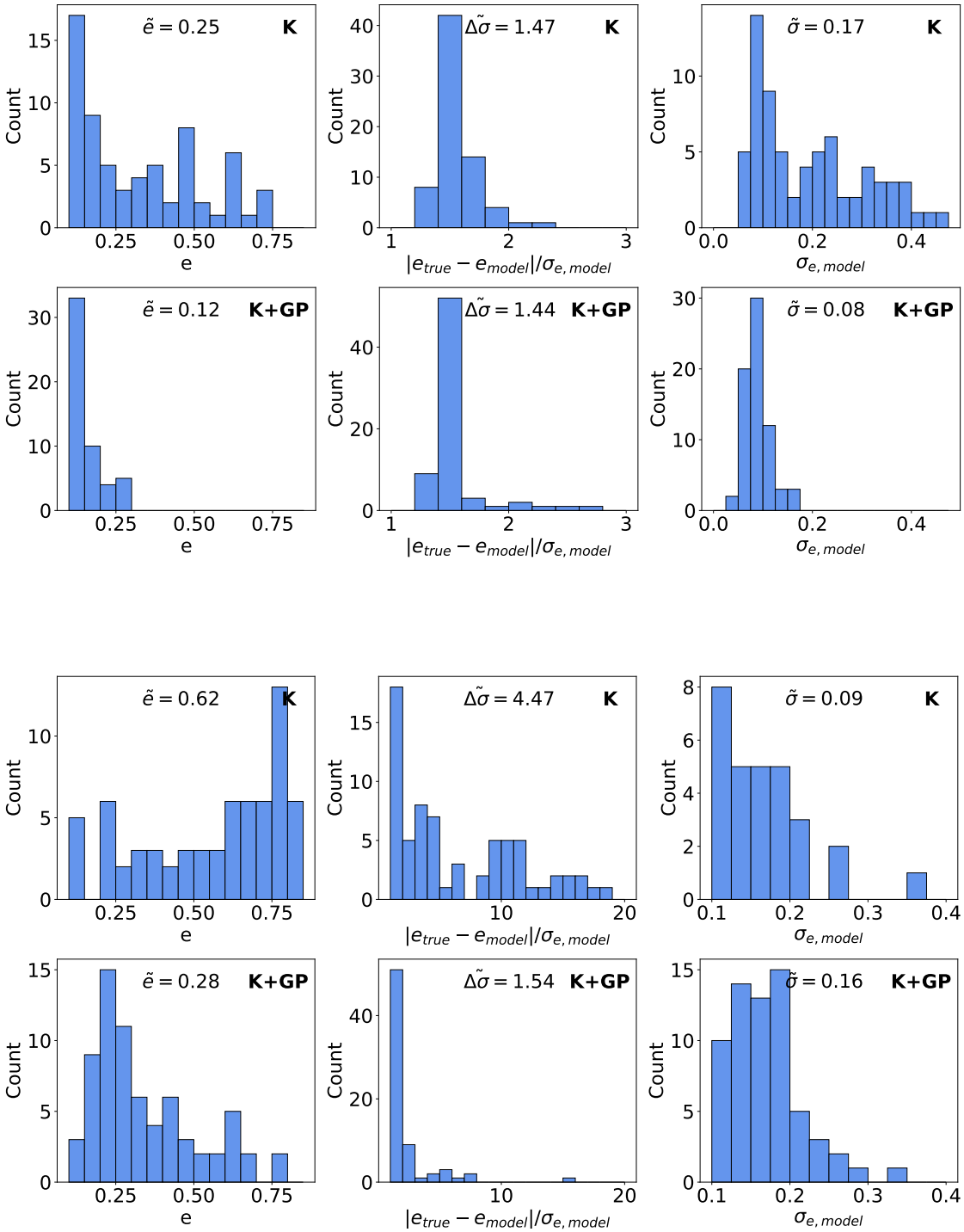


Fig. 3.19.: The first two rows in the top panels show the derived eccentricities (left column), the difference between fitted and simulated value in terms of standard deviation (middle column), and the absolute uncertainties (right column) for the models of the injected Keplerian at 5 d. The median of each quantity is provided in the histograms, as well as the fitted model, where K denotes the Keplerian-only model and K+GP the combined Keplerian and GP model. The last two rows in the bottom show the results for the injected Keplerian at 44 d. The injected eccentricity is $e = 0$.

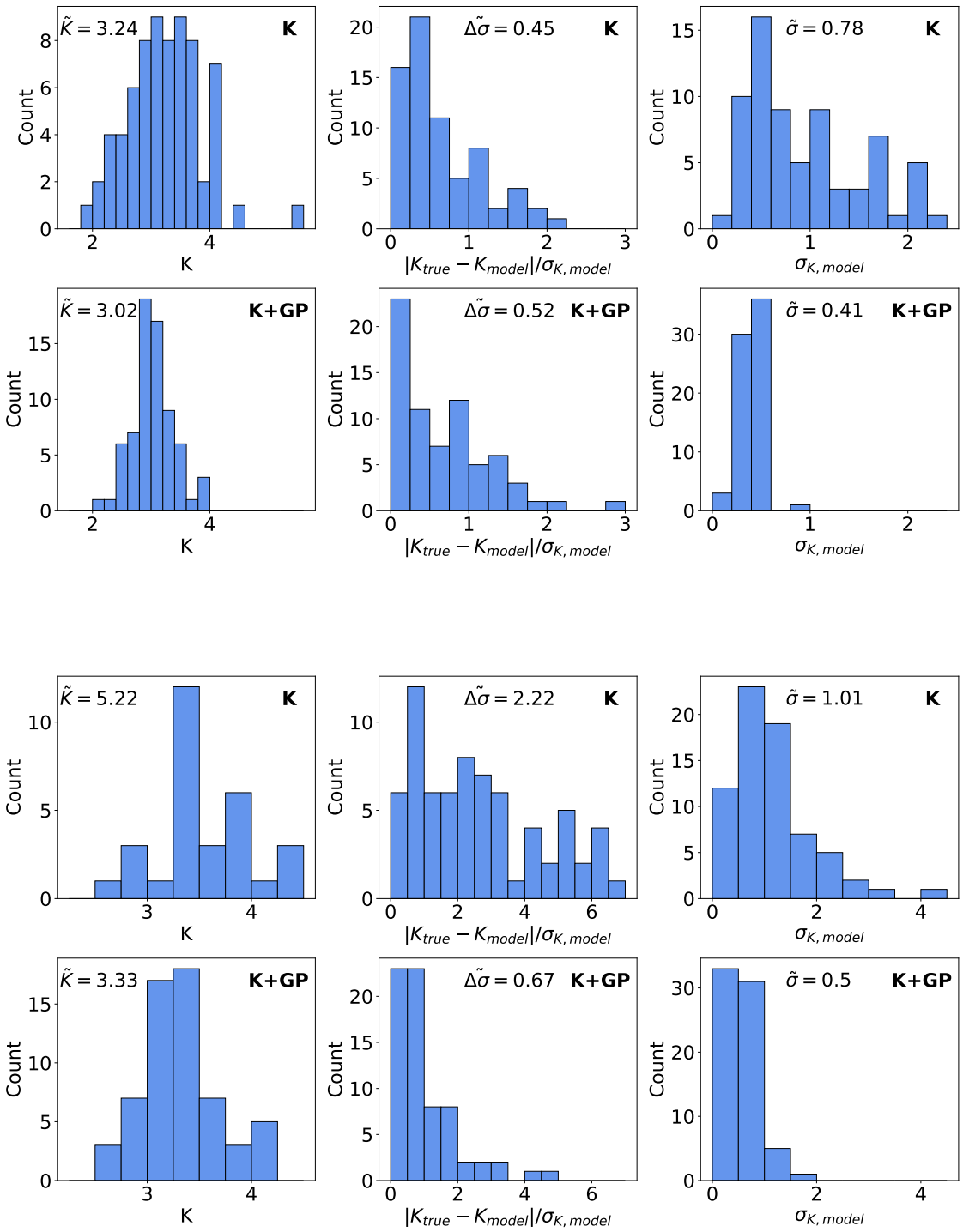


Fig. 3.20.: Same as in Fig. 3.19 but for the RV semi-amplitude. The injected semi-amplitude is $K = 3\,\mathrm{m\,s^{-1}}$.

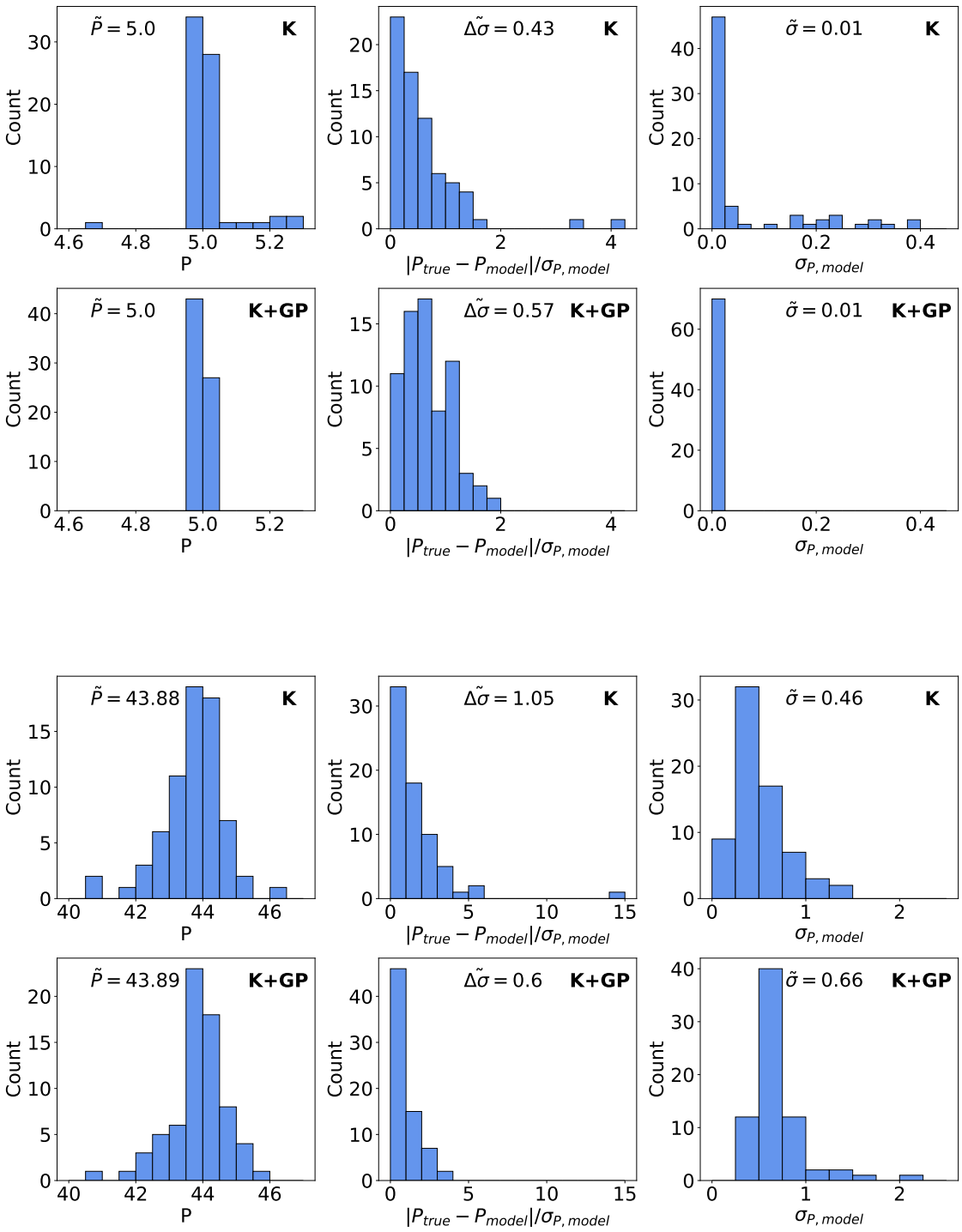


Fig. 3.21.: Same as in Fig. 3.19 but for the orbital period. The injected orbital periods are 5 d (top two rows) and 44 d (bottom two rows).

4 `AliasFinder`: A tool to de-alias radial velocity data

> *Most of the fundamental ideas of science are essentially simple, and may, as a rule, be expressed in a language comprehensible to everyone.*
>
> — **Albert Einstein**
> (1879-1955)

Details of authorship: *Some content and text passages of this chapter are based on already published work (Stock & Kemmer 2020) which has been written by the author of this thesis. The text has been slightly changed, updated and divided into two parts (Sec. 4.1.1 and Sec. 4.2.2 in this chapter). The main functionalities of the* `AliasFinder` *code, in particular the simulations, the plotting, and the science orientated parts of the code, have been programmed by the author of this thesis, with some parts of the code making use of public packages that are named in section 4.2.2. The co-author Jonas Kemmer helped to bring the code into a publishable format, which meets the technical requirements for a publication in the Journal of Open Source Software (JOSS), including a restructuring of the code, the creation of an API documentation and some improvements on the user interface capabilities.*

4.1 Introduction

4.1.1 Motivation

The detection of exoplanets using the RV method often relies on finding periodic signals in noisy time-series data. However, discrete measurements and gaps in the observations (for example, optical ground-based observations cannot take place during the day), can result in strong aliases

of any signal. The effect that spurious signals appear, due to the sampling of the data, that are indistinguishable from the true signal, is called aliasing. Aliases can occur at

$$f_{\text{Alias}} = f_{\text{True}} \pm m \cdot f_{\text{Sampling}}, \tag{4.1}$$

where f_{True} is the true signal, f_{Sampling} is the sampling frequency and m is an integer value. This makes it difficult to determine the true period of the planet, and this problem has already led to incorrectly published orbital periods, see, for example, 55 Cnc e (McArthur et al. 2004) corrected by Dawson & Fabrycky (2010) and YZ Ceti b (Astudillo-Defru et al. 2017) corrected by Stock et al. (2020b).

4.1.2 Fourier transform

To visualize and identify possible periodic signals astronomers often make use of periodograms. Here, I briefly outline their concepts which are based on Fourier transformations. The Fourier transform of a continuous time-dependent signal $g(t)$ can be written as

$$F\{g\} = \hat{g}(f) = \int_{-\infty}^{\infty} g(t) e^{-2\pi i f t} \mathrm{d}t, \tag{4.2}$$

where $i \equiv \sqrt{-1}$ is the imaginary unit, f is the frequency of the continuously sampled signal, and t is the time. In the case of discrete measurements, the Fourier transform can be written as

$$\hat{g}(f) = \sum_{n=0}^{N} g_n e^{-2\pi i f n \Delta t}, \tag{4.3}$$

where g_n is a sampled signal at times of regular spacing Δt, and N is the number of the discrete measurements (VanderPlas 2018).

The key properties that make the Fourier transform a powerful method for the analysis of periodic signals is its linearity $F\{A(h(t) + g(t))\} = AF\{h(t)\} + AF\{g(t)\}$, the fact that each Fourier transform of a sinusoidal signal with frequency f_0 is a pair of Dirac Delta functions $\delta(f)$ at $\pm f_0$ (Dirac 1958), and that a time shift results in a phase in the Fourier transform (VanderPlas 2018; Arens et al. 2010). For RV measurements, it is of particular interest to discuss the Fourier transform behavior

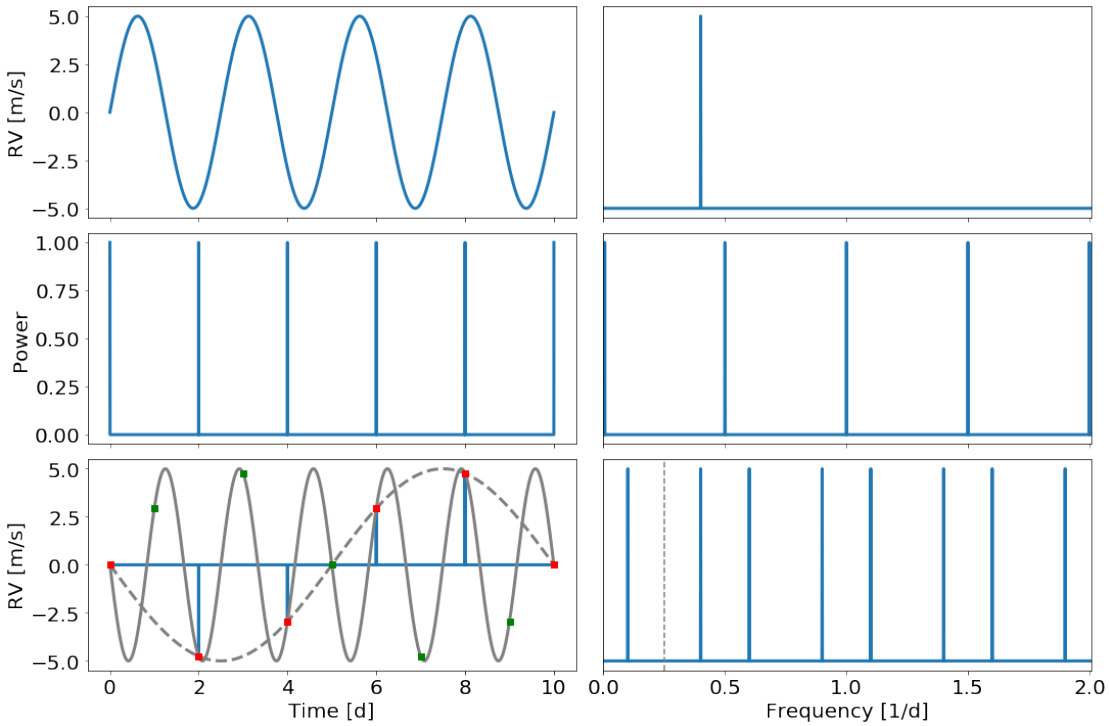


Fig. 4.1.: *Top left:* Simulated sinusoidal signal with $S_0(t) = 5\,\mathrm{m\,s^{-1}}\sin((2\pi/2.5\,\mathrm{d})t)$ in blue. *Top right:* Fourier transform of the simulated signal. *Middle left:* Dirac comb with $T = 2\,\mathrm{d}$. *Middle right:* Fourier transform of the Dirac comb. *Bottom left:* Convolution of the simulated sinusoidal signal and the Dirac comb plotted in blue. Red points represent artificial measurements based on the true signal $S_0(t)$. Two sinusoidal functions of the form $S_1(t) = 5\,\mathrm{m\,s^{-1}}\sin((2\pi \cdot 0.1\,\mathrm{d^{-1}})t - \pi)$ (dashed line) and $S_2(t) = 5\,\mathrm{m\,s^{-1}}\sin((2\pi \cdot 0.6\,\mathrm{d^{-1}})t)$ (solid line) that are consistent with the measurements are overplotted in gray. The green points represent additional artificial measurements that would allow to discard $S_1(t)$ as the generating signal of the measured data. *Bottom right:* Fourier transform of the convolution of the simulated sinusoidal signal $S_0(t)$ with the spectral window. The dashed-gray line presents the Nyquist-limit for $f_{\mathrm{Sampling}} = 0.5\,\mathrm{d^{-1}}$.

for two types of functions, the simple sinusoid and the Dirac comb[1]. This discussion is beneficial for understanding periodograms, the spectral window of RV observations, and aliasing.

4.1.3 Evenly sampled data and the spectral window function

In the top left plot of Fig. 4.1, a sinusoidal signal with a period of 2.5 d ($f_{\mathrm{True}} = 0.4\,\mathrm{d^{-1}}$) and an amplitude of $5\,\mathrm{m\,s^{-1}}$ has been modeled and its Fourier transform has been calculated. As expected one can find a single Dirac delta function in the Fourier transform at a frequency of

[1]The Dirac comb is an infinite series of Dirac delta functions with uniform intervals T between them.

$f_{\text{True}} = 0.4\,\text{d}^{-1}$. It should be noted that, due to complex conjugation, there also exists a peak at a negative frequency ($f_{\text{True},2} = -0.4\,\text{d}^{-1}$) which is not shown in the plot as it is unphysical. The power of the peak depends on the amplitude of the signal.

Assuming that the sinusoidal signal is measured exactly every two days, the sampling itself can be regarded as a Dirac comb with $T = 2\,\text{d}$ and with a power of one, representing a measurement, while zero means no measurement has been taken. This Dirac comb and its Fourier transform are provided in the two middle plots of Fig. 4.1. As can be seen, the Fourier transform of a Dirac comb is another Dirac comb with distance $f_{\text{Sampling}} = 1/T = 1/2\,\text{d}^{-1} = 0.5\,\text{d}^{-1}$. The Fourier transform of the Dirac comb specifying the measurements can be interpreted as the observations' spectral window function. Roberts et al. (1987) has defined the spectral window function as

$$W(f) = \frac{1}{N}\sum_{n=1}^{N} e^{-2\pi i f t_n}, \tag{4.4}$$

where N is the number of measurements and t_n the time at each measurement. This form follows from the definition of the discrete Fourier transform (Roberts et al. 1987).

If a signal is represented by discrete sampling, the resulting Fourier transform of the signal shows properties of the spectral window function and the continuous signal. Mathematically, the combination of the spectral window function with the signal is a convolution $[f * g](t) = \int_{-\infty}^{+\infty} f(\tau)g(t-\tau)\text{d}\tau$ (VanderPlas 2018; Arens et al. 2010). This is shown in the bottom two panels of Fig. 4.1, where the bottom right panel shows the derived Fourier transform of this convolution. In the range between $0\,\text{d}^{-1}$ and $2\,\text{d}^{-1}$, one can count eight peaks with equal power at frequencies of $f_{\text{Alias}}(0\,\text{d}^{-1} < f < 2\,\text{d}^{-1}) : \{0.1, 0.6, 0.9, 1.1, 1.4, 1.6, 1.9\}\,\text{d}^{-1}$ and $f_{\text{True}} = 0.4\,\text{d}^{-1}$. The alias frequencies can be calculated by applying Eq. 4.1. A negative result of the alias frequencies can be switched to a positive one by shifting the signal phase by π. It is easy to see that it is impossible to derive the correct period of the sampled signal in this constructed case by having only the red RV measurements in the bottom left panel and the resulting Fourier transform in the bottom right panel. This is shown in the bottom left panel of Fig. 4.1 where two sinusoidal functions based on $f_{\text{Alias}} = 0.1\,\text{d}^{-1}$ and $f_{\text{Alias}} = 0.6\,\text{d}^{-1}$ were plotted to the data points, which are marked in red.

The sampling frequency in this example is $f_{\text{Sampling}} = 0.5\,\text{d}^{-1}$. The observed structure of aliases in the Fourier transform of the discrete signal is caused by the Nyquist sampling limit, which is defined as $f_{\text{Nyquist}} = 0.5 \cdot f_{\text{Sampling}}$ (Arens et al. 2010). According to the Shannon-Nyquist theorem (Shannon 1949), all signals have to be smaller than the Nyquist frequency to be reconstructable

in the case of evenly sampled data. Therefore, the sampling frequency should be twice as high as the signal one wants to record. In the provided example, this means that one can only reliably differentiate between frequencies that are smaller than $f < 0.25\,\mathrm{d}^{-1}$. For frequencies larger than this value, there will be aliasing. It is important to note that this does not mean that any signal at a higher frequency cannot be the real signal. On the contrary, as shown in the example, the true signal is at $f_{\mathrm{True}} = 0.4\,\mathrm{d}^{-1}$ and below the optimal sampling frequency. It would be incorrect to conclude that the signal at $f_{\mathrm{Alias}} = 0.1\,\mathrm{d}^{-1}$ is the true signal only because it is smaller than the Nyquist limit. The only way to distinguish the true period from this alias period in the case of evenly sampled data is to sample with a frequency $f_{\mathrm{Sampling}} > 2 \cdot f_{\mathrm{True}}$. In such a case, one can see that $f_{\mathrm{Alias}} = 0.1\,\mathrm{d}^{-1}$ cannot be the true period. We show this in the bottom left panel of Fig. 4.1 where the additional green data and the red data are sampled with a frequency of $f_{\mathrm{Sampling}} = 1\,\mathrm{d}^{-1}$, which is not large enough to differentiate between $f_{\mathrm{Alias}} = 0.6\,\mathrm{d}^{-1}$ and $f_{\mathrm{True}} = 0.4\,\mathrm{d}^{-1}$.

Besides that, it is essential to make clear that for real observations, which are taken over a finite time interval, the Fourier transform of sinusoidal signal is not given by a Dirac delta function, but that the peaks will have a finite width given by $1/T_{\mathrm{Obs}}$, where T_{Obs} is the time interval of all observations (VanderPlas 2018). This is caused by the fact that an additional window function, representing the time interval of the observations, will be convolved with the observations. The Fourier transform of the window function is a sinc function, leading to the peaks' finite width. Therefore, the example in Fig. 4.1 represents an idealized case.

4.1.4 Periodograms and unevenly sampled data

The classical periodogram by Schuster (1898) is defined as

$$P(f) = \frac{1}{N}\left|\sum_{n=1}^{N} g_n e^{-2\pi i f t_n}\right|^2, \tag{4.5}$$

where g_n is the discrete measurement n at time t_n of a continuously measured signal $g(t)$ with frequency f. Note that $|\sum_{n=1}^{N} g_n e^{-2\pi i f t_n}|^2 = |F\{g\}|^2$ is the power spectral density which is defined as the squared amplitude of the Fourier transform. In the case of evenly sampled data, this form of the periodogram has a well-defined behavior (VanderPlas 2018).

However, astronomic measurements are rarely sampled evenly due to telescope scheduling, weather conditions, seasonal and daily cycles, and further observational constraints. For such unevenly sampled data, the classical periodogram is less useful, as one of its main properties

breaks apart, which is that the periodogram distribution can be analytically expressed (Groth 1975; Scargle 1982; VanderPlas 2018). Scargle (1982) and Lomb (1976) have derived a generalized version of the classical periodogram, referred to as the Lomb-Scargle (LS) periodogram, whose main advantage is that the periodogram distribution is analytically computational for unevenly sampled data. Additionally, the LS-periodogram reduces to the simple classical form for the evenly sampled cases. A particularly useful property of the LS-periodogram is that its Fourier interpretation (see, for example, Eq. 10 in Scargle 1982) is equivalent to a least-square interpretation, where a sinusoidal function of the form $y(t; f) = A \sin(2\pi f(t - \phi_f))$ is fitted for each trial frequency f, and the parameters A and ϕ_f are derived by minimizing the function $\chi^2 = \sum_n (y_n - y(t))^2$ for each frequency (VanderPlas 2018). The periodogram power at each frequency is then derived by the χ^2 goodness of the fit at each frequency.

Zechmeister & Kürster (2009) further improved the LS periodogram allowing for measurement uncertainties by including weights and allowing the periodogram calculations to have a floating mean. Their form is known as the generalized Lomb-Scargle periodogram (GLS). By including measurement uncertainties, the χ^2 value at every frequency is derived in analogy to Eq. 2.4. This improves the estimate of the power of the periodogram at each frequency in case of noisy observations. The second advantage of the GLS is the floating mean due to the possibility of a varying zero-point. In contrast to the LS periodogram, where the mean is defined by the mean of all available data, the GLS allows for an offset so that $y(t; f) = A \sin(2\pi f(t - \phi_f)) + y_0(f)$ (Zechmeister & Kürster 2009; VanderPlas 2018). This has the advantage of improving the detection efficiency of periodic functions in data with insufficient phase-coverage. A good example is a case, in which there is an observational gap whenever the sinusoidal approaches its maximum amplitude. While the GLS would derive a correct estimate of the signal period, as it will shift the offset during the minimization process, the LS periodogram will struggle to detect the signal's correct period. Within this thesis and particularly for the tool `AliasFinder` the GLS periodogram, that is available on a GitHub repository of M. Zechmeister[2], has been used.

4.1.5 Aliasing in the case of irregularly sampled data

For irregularly sampled data, the spectral window function (the Delta functions' transformation at the observed times t_i) is not a Dirac Comb anymore. Due to the measurements' random times, the Fourier transform will consist of peaks at random positions and random heights (VanderPlas 2018). The spectral window function will appear more noisy than the Fourier transform in Fig. 4.1, which, for example, can be seen in Fig. 4.2 that shows the spectral window function of

[2] https://github.com/mzechmeister/GLS

the SOPHIE RV data for Lalande 21185. The periodogram of the observed sampled signal is the convolution of the real underlying signal with the spectral window function of the observations, and, therefore, it will also be affected by the random noise caused by the uneven sampling of the data. In the case of evenly sampled data, the Nyquist limit has been a consequence of the regular spacing of Dirac delta functions in the spectral window. As a result, theoretically, there is no Nyquist limit for unevenly sampled data.

A well established approximation for the Nyquist limit of irregularly sampled data is that of Eyer & Bartholdi (1999) and their concept is straightforward to understand. The idea is that the Nyquist limit can be derived using $f_{\text{Nyquist}} = 1/(2p)$, where p is the largest factor that satisfies the equation $t_i = t_0 + n \cdot p$ (t_0 is the starting time and n must be an integer). For example, the Nyquist frequency of the time-series $[0, 0.1, 0.6, 2, 2.3, 3, 5]$ (in arbitrary units) is given by $f_{\text{Nyquist}} = 1/(2 \cdot 0.1) = 5$. A result of this definition is that, if there is a pair of observations whose ratio is irrational, there is, in principle, no Nyquist limit, e.g., the time-series $[0, e, \pi, 2e, 2\pi, ..., ne, n\pi]$. However, due to the finite precision of time measurements, in time-series data of real observations there is always a Nyquist-limit (VanderPlas 2018). If the precision of time measurements would be three decimals the Nyquist limit would be around $f_{\text{Nyquist}} = 1/(2 \cdot 0.001) = 500$ for the sequence $[0, e, \pi, 2e, 2\pi, ..., ne, n\pi]$. Therefore, the Nyquist limit of irregular sampled measurements can be defined by the precision of the time measurements (Koen 2006; VanderPlas 2018).

The fact that there is effectively no Nyquist limit for irregularly sampled data, as it is at very high frequencies, reduces the effects of aliasing in the case of astronomical measurements. However, an approximated aliasing effect can also be caused by a structure similar to a Dirac delta function in the observations' spectral window function. The observations of astronomical targets are affected by seasonal cycles, the day/night cycle, and further constraints. As a result, the sampling is semi-regular, which means it is the sum of random time measurement with a regular pattern (Scargle 1982). This circumstance leaves an imprint on the observations' spectral window function, and it results in peaks at the frequencies of the regular patterns. For example, from the ground and in the visual band, stars can only be observed during night, which results in an observed 1 d peak in the spectral window function. This peak can have a similar effect as the Dirac delta function in regularly sampled data. Therefore, aliasing can still affect irregular measurements, and it can be challenging to disentangle the real signal (Deeming 1975; Scargle 1982; Dawson & Fabrycky 2010; VanderPlas 2018).

However, due to the finite and irregular sampling of the data, the peaks and phase values (given by $e^{2\pi i f t_n}$) at each frequency of the spectral window function will span a finite width (Dawson & Fabrycky 2010). The phase value at each frequency is a superposition of all the values possible at each finite sampled time t_n. As a result of the peaks and phases' finite widths, the alias power is

reduced for higher orders that are farther away from the real signal in frequency space (VanderPlas 2018). In principle, this allows the determination of a signal's correct frequency, despite the occurrence of strong aliases due to unfavorable sampling, by performing an accurate analysis of all alias peaks and of all their properties. The tool `AliasFinder`, based on the method of Dawson & Fabrycky (2010), is intended to help identifying the correct sampled signal.

4.2 `AliasFinder`

4.2.1 The conceptual basis of `AliasFinder`

As discussed in the previous sections, within irregularly sampled data, aliases should not have the same power as the original peak. For idealized noise-free data, this is almost always the case (see Dawson & Fabrycky 2010). However, noise within the data can affect the peak heights in the periodogram as it may interfere with the data so that one alias peak will have larger power than the true signal. This effect is particularly observable when the signal-to-noise ratio of the data is small, either due to a small number of observations, small amplitudes of the signal under investigation, or large noise contributions from stellar activity or from the instrument. This is the case for many low-mass planet signals in current RV surveys.

The idea of Dawson & Fabrycky (2010) is to simulate a noise-free sinusoidal with the period of the signal to be investigated. This signal should be simulated on the same time grid as the observations. The convolved window function of the original data and the simulated signal will, as a result, be identical. By comparing the simulated periodogram with the data periodogram, one can derive conclusions about the real sampled signal. In addition to comparing the peak heights, one should also use the phases at the peak positions as an additional dimension and criterion to compare simulated signal and data periodograms, as the phase values at each peak will also be affected by the noise. If the peak heights and peak phases of both periodograms sufficiently match each other, the correct period was determined (Dawson & Fabrycky 2010). Otherwise, another possible frequency needs to be simulated. If none or several simulated periodograms representing the possible true signals match well with the data periodogram, additional data is needed to differentiate the periods.

4.2.2 AliasFinder as a tool

AliasFinder is a Python script which has been developed to identify the true sampled signal within RV time series data. The script is based on a method described in Dawson & Fabrycky (2010), however, AliasFinder uses some improvements[3]. To the best of our knowledge, there are no other public packages to perform alias testing based on this methodology. The basic principle is to simulate an ensemble of noisy time-series based on the original data sampling and noise level and inject one of the original data's signals into this time-series. AliasFinder will then plot the median GLS periodogram (Zechmeister & Kürster 2009) from the simulations of the injected signal overplotted with the original data periodogram. From the comparison of the signal properties (signal power, frequency, or phase) at the injected frequency and its aliases between these two periodograms, one can assess the signal's true period.

AliasFinder is written explicitly for Python 3 and should run with a standard Anaconda distribution including a small number of additional packages. These packages include Astropy (Astropy Collaboration et al. 2013), a community-developed core Python package for Astronomy (Astropy Collaboration et al. 2018). We made use of NumPy (Oliphant 2006), tqdm (da Costa-Luis 2019), SciPy (Virtanen et al. 2020) and matplotlib (Hunter 2007). AliasFinder is executed by passing a YAML parameter file with important information about the star, planetary system, and the measured RV signals.

AliasFinder has been developed to be used by astronomers searching for exoplanets in RV data. Nevertheless, in principle, the software can be used by anyone who needs to distinguish a possible signal from its aliases within noisy time-series, if the correct input format is respected. The script is already used within Stock et al. (2020b,c) and will be used in further studies in the future. AliasFinder is designed to be fast (multi-core support) and user-friendly, and produces high-quality publication plots, as in Fig. 4.2. This software will encourage the usage of alias testing within future scientific publications based on time-series data, particularly RV data, and the software has the potential to reduce the number of incorrectly published orbital periods for exoplanets.

[3]These improvements are discussed further in Sect. 5.4.2.

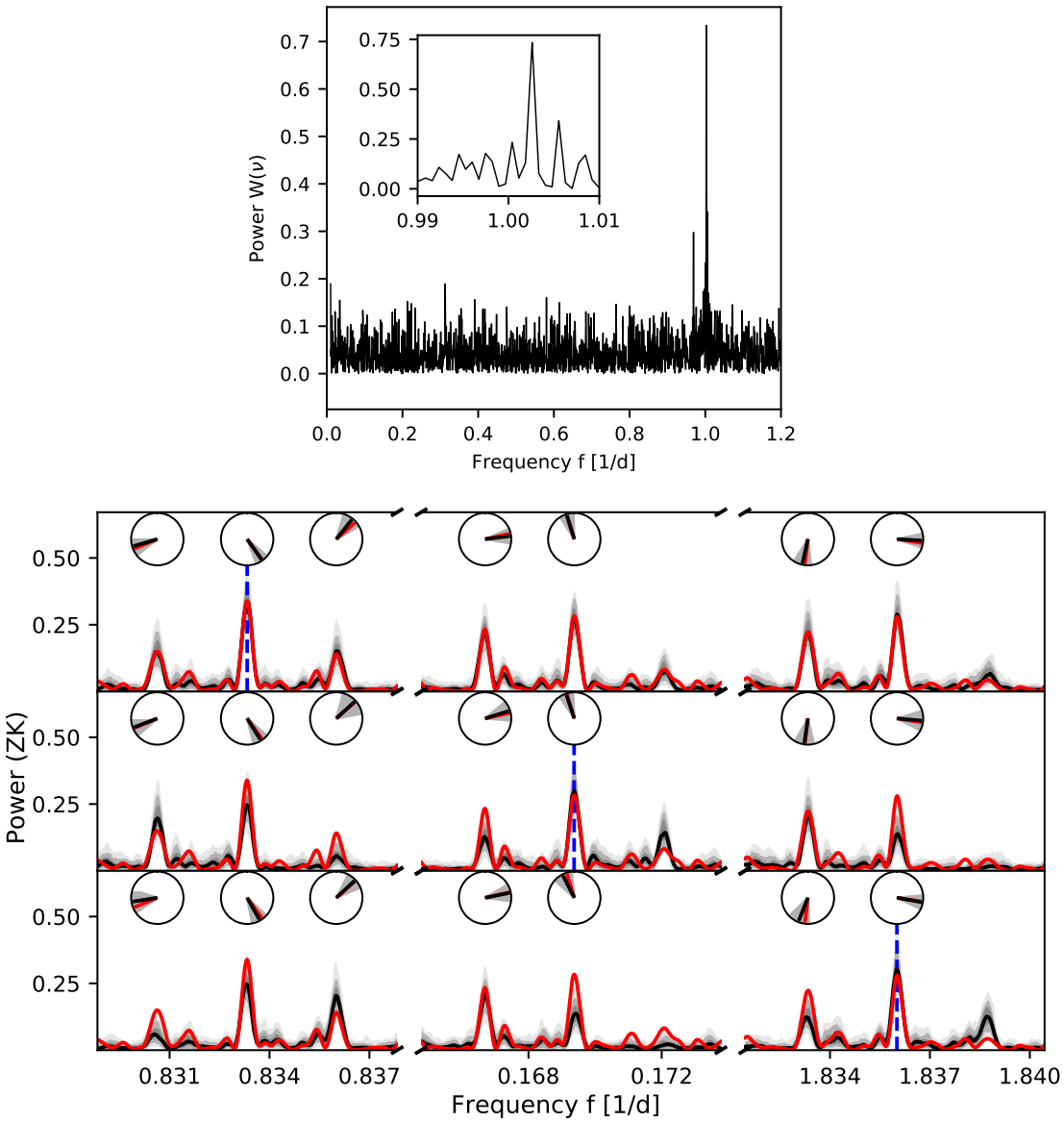


Fig. 4.2.: *Top:* Spectral window function of SOPHIE data for Lalande 21185. The highest peak is at $f_{\text{Sampling}} = 1.00261\,\text{d}^{-1}$. *Bottom:* A signal with $f = 0.8333\,\text{d}^{-1}$ has been injected into the SOPHIE data for Lalande 21185 after removing the real planet Lalande 21185 b. It is tested whether the injected signal's period can be recovered. This plot shows the GLS periodogram of the data (in red) and the median of simulated periodograms calculated on the same observations but with different white noise contributions (in black). The different columns show the region around $f = 0.8333\,\text{d}^{-1}$ and its two first order aliases. Each row corresponds to a different set of simulations and the vertical blue dashed line indicates the injected frequency for these simulated periodograms. The gray shaded area indicate the IQR and the 90% and 99% credibility interval, respectively. The clock diagrams indicate the phase of the signal at the peaks. The phase of the data is given as the red clock, and the angular mean of the simulated phases and its circular standard deviations are provided as the black clock and gray shaded area. Although it is a difficult case, one can see that the first row, corresponding to simulations with an injected signal at $f = 0.8333\,\text{d}^{-1}$, fits best to the observed data periodogram.

5 Characterization of the nearby ultra-compact multi-planetary system YZ Ceti

> *Somewhere, something incredible is waiting to be known*
>
> — **Carl Sagan**
> (1934-1996)

Details of authorship: *The content and text passages of this chapter are almost entirely based on already published work in Stock et al. (2020b). The manuscript, as well as all major scientific work, calculations and conclusions contained therein, have been prepared by me. Before submission and during the review process I included suggestions and corrections by the co-authors and reviewer. The text has been slightly adjusted and extended at some parts to make this work more consistent with the rest of this thesis. Additionally, for this thesis I have slightly adjusted the format of figures and tables to better suit the one column style. The appendix of this work has been shifted to the appendix of this thesis.*

5.1 Motivation

By July 2019, 665 multiplanetary systems were known, 148 of them discovered by precise Doppler spectroscopy. Only 11 of those Doppler spectroscopy-detected systems had stellar masses lower than 0.3 $M_\odot$. Such a low-mass star is YZ Ceti (GJ 54.1), which was reported to host three planets (Astudillo-Defru et al. 2017). It is the closest multiplanetary system to our Solar System published so far. Astudillo-Defru et al. (2017) announced that YZ Ceti is orbited by at least three Earth-mass planets at periods of 1.97 d, 3.06 d, and 4.66 d. The low amplitude of the signals (on the order of 1–2 m s^{-1}) together with the spectral window make the radial velocities of the system prone to strong aliasing. Although the system has been the subject of several

studies (Astudillo-Defru et al. 2017; Robertson 2018; Pichierri et al. 2019) the true configuration of the planets is still highly disputed. For example, Robertson (2018) pointed out that the true configuration of the system could not be uniquely determined with the HARPS data available to Astudillo-Defru et al. (2017). In particular, the signal of planet c (P = 3.06 d) had a strong alias at 0.75 days.

Astudillo-Defru et al. (2017) also mentioned a fourth tentative signal slightly above a one-day periodicity at 1.04 d. On the other hand, Tuomi et al. (2019), who used only 114 radial velocity measurements by HARPS and 21 from HIRES, supported the existence of only two planet candidates for YZ Ceti at periods of 3.06 d and 4.66 d.

Determining the true configuration of a planetary system and constraining its parameters is of the utmost importance for any attempt to perform a dynamical characterization or to understand its formation. Recent planet formation results suggest that ultra-compact planetary systems around stars similar to YZ Ceti should be common, where the planets are typically locked in long resonant chains, exhibiting both two-body and three-body resonances (Coleman et al. 2019). We took additional radial velocity (RV) data for YZ Ceti with CARMENES and HARPS to address the open questions regarding the exact planetary configuration, the possibility of additional companions, the modeling, the influence of stellar activity, and the dynamical properties of this multiplanetary system.

This work is organized as follows. The data and instruments used in this study are described in Sec. 5.2. We discuss the basic stellar properties of YZ Ceti and the analysis of the photometry and activity indicators in Sec. 5.3. In Sec. 5.4 we examine the RV data for additional planet candidates, resolve the alias issues raised in the literature, and present strong evidence for the correct planetary configuration of the system. In Sec. 5.5 we describe the modeling with a Gaussian process (GP) and the influence of the stellar activity on the eccentricity of the innermost planet, while in Sec. 5.5.2 we constrain our posterior parameters even further by adopting the criterion of long-term stability for the multiplanetary system. The results of this study are summarized and discussed in Sec. 5.6.

5.2 Data

5.2.1 CARMENES

We observed YZ Ceti as one of the 324 stars within our CARMENES[1] Guaranteed Time Observation program (GTO) to search for exoplanets around M dwarfs (Reiners et al. 2018a). CARMENES is a precise échelle spectrograph mounted at the 3.5 m telescope at the Calar Alto Observatory in Spain. It consists of two channels: the visual (VIS) covers the spectral range 0.52–0.96 µm with spectral resolution of $R = 93,400$, and the near-infrared (NIR) the 0.96–1.71 µm range with spectral resolution of $R = 81,800$ (Quirrenbach et al. 2014). We obtained 111 high-resolution spectra in the VIS and 97 spectra in the NIR between January 2016 and January 2019. Three spectra of the VIS and NIR arm were without simultaneous Fabry-Pérot drift measurements and were therefore excluded from our RV analysis. The data were reduced using CARACAL (Caballero et al. 2016b), and we obtained the radial velocities using `SERVAL` (Zechmeister et al. 2018). `SERVAL` determines RVs by coadding all available spectra of the target with signal-to-noise ratio (S/N) higher than 10 to create a high S/N template of the star and by deriving the relative RVs with respect to this template using least-squares fitting. The radial velocities were corrected for barycentric motion, secular perspective acceleration, instrumental drift, and nightly zero points (see Trifonov et al. 2018; Tal-Or et al. 2018, for details). For the VIS we achieved a median internal uncertainty, including the correction for nightly zero points, of 1.55 m s^{-1} and a root mean square (rms) of 3.00 m s^{-1} around the mean value. For the NIR we achieved a median internal uncertainty, including the correction for nightly zero points, of 5.71 m s^{-1} and an rms of 7.17 m s^{-1} around the mean value. Due to the small amplitudes of the planetary signals of less than 2 m s^{-1} in the YZ Ceti system, we only used the VIS data for our analysis.

The radial velocity time series and their uncertainties for all data sets used within this work are listed in Table B.1 and is only available at the CDS via anonymous ftp `tocdsarc.u-strasbg.fr(130.79.128.5)` or via `http://cdsarc.u-strasbg.fr/viz-bin/cat/J/A+A/636/A119`

5.2.2 HARPS

The High Accuracy Radial velocity Planet Searcher (HARPS; Mayor et al. 2003) is a precise échelle spectrograph with a spectral resolution of $R = 110,000$ installed at the ESO 3.6 m

[1] `http://carmenes.caha.es`

telescope at La Silla Observatory, Chile. HARPS covers the optical wavelength regime, and was the first spectrograph that reached a sub-m s^{-1} precision. We retrieved 334 high-resolution spectra from the ESO public archive, of which 59 were collected by the Red Dots program (Dreizler et al. 2020). As with the CARMENES data we used `SERVAL` to obtain the RV from the corresponding spectra. Only 326 spectra were used for the coadding of the template, as eight spectra had a S/N of less than 10. We then calculated the corresponding RVs for all 334 spectra. From these 334 we removed two extra measurements: one at BJD 2456923.73068 as it was an obvious outlier with very low S/N of 3.6 and one at BJD 2458377.92388 due to an RV uncertainty larger than 83 ms^{-1}. This resulted in a total of 332 RV measurements by HARPS. We divided the HARPS RV data due to a fiber upgrade on May 28, 2015 (Lo Curto et al. 2015), into pre- and post-fiber data and fitted an offset for it. For the pre-fiber upgrade data sets we achieved a median internal uncertainty of 1.92 m s^{-1} and an rms of 2.88 m s^{-1} around the mean value. For the post-fiber upgrade data sets we achieved a median internal uncertainty of 1.86 m s^{-1} and an rms of 3.72 m s^{-1} around the mean value.

5.2.3 Photometry

Details of observations from five photometric facilties are given below.

ASAS. The All-Sky Automated Survey (Pojmanski 1997) has been monitoring the entire southern and part of the northern sky since 2000. We retrieved 461 ASAS-3 measurements of YZ Ceti taken between November 2000 and November 2009.

ASAS-SN. The All-Sky Automated Survey for Supernovae (ASAS-SN) (Shappee et al. 2014; Kochanek et al. 2017) uses 14 cm aperture Nikon telephoto lenses, each equipped with a 2048 × 2048 ProLine CCD camera with a field of view (FOV) of 4.5 deg^2 at different observatories worldwide. We extracted about six years of photometric observations (2013-2019) in the *V* band from the ASAS-SN archive[2] for YZ Ceti.

[2] https://asas-sn.osu.edu/

MEarth. The MEarth project (Berta et al. 2012) is an all-sky transit survey. Conducted since 2008 it uses 16 robotic 40 cm telescopes, 8 located in the northern hemisphere at the Fred Lawrence Whipple Observatory in Arizona, USA, and 8 in the southern hemisphere located at Cerro Tololo Inter-American Observatory, Chile. The project monitors several thousand nearby mid- and late M dwarfs over the whole sky. Each telescope is equipped with a 2048x2048 CCD that provides a FOV of 26 arcmin^2. MEarth generally uses an $RG715$[3] long-pass filter, except for the 2010-2011 season when an $I_{715-895}$ interference filter was chosen. In the case of YZ Ceti, we used archival data from MEarth telescopes T11 and T12 released in the seventh data release (DR7[4]). The set from T11 consists of 40 epochs with a time span of 102 days between May and August 2017, while the set from T12 consists of 25 epochs with a time span of 68 days between June and August 2017.

ASH2. The Astrograph for Southern Hemisphere II (ASH2) telescope is a 40 cm robotic telescope located at the San Pedro de Atacama Celestial Explorations Observatory (SPACEOBS) in Chile. The telescope is equipped with a STL11000 $2.7k \times 4k$ CCD camara and has a FOV of 54×82 arcmin^2. We carried out the observations in the V and R bands and in two runs. Run 1 consisted of 14 observing nights during the period September to December 2016, with a time span of 65 days and about 650 data points collected in each filter. Run 2 consisted of 28 observing nights between July and October 2018, with a time span of 91 days and about 500 data points collected in each filter.

SNO. The Sierra Nevada Observatory (SNO) in Spain operates four telescopes. The T90 telescope at Sierra Nevada Observatory is a 90 cm Ritchey-Chrétien telescope equipped with a CCD camera VersArray $2k \times 2k$, FOV 13.2×13.2 arcmin (Rodríguez et al. 2010). We carried out the observations in both Johnson V and R filters on 38 nights during the period August to December 2017, with a time span of 125 days and about 1850 data points collected in each filter.

[3] https://www.pgo-online.com/intl/curves/optical_glassfilters/RG715_RG9_RG780_RG830_850.html

[4] https://www.cfa.harvard.edu/MEarth/DR7/README.txt

Tab. 5.1.: Stellar parameters of YZ Ceti.

Parameter	Value	Ref.
	Name and identifiers	
Name	YZ Ceti	
Alias name	GJ 54.1	Gli95
Karmn	J01125–169	Cab16
	Coordinates and spectral type	
α	01 12 30.64	*Gaia*
δ	–16 59 56.4	*Gaia*
Sp. type	M4.5 V	Alo15
G [mag]	10.4294 ± 0.0006	*Gaia*
J [mag]	7.26 ± 0.02	2MASS
	Parallax and kinematics	
$\mu_\alpha \cos\delta$ [mas/yr]	+1205.176 ± 0.170	*Gaia*
μ_δ [mas/yr]	+637.758 ± 0.120	*Gaia*
π [mas]	269.36 ± 0.08	*Gaia*
d [pc]	3.712 ± 0.001	*Gaia*
V_r [m/s]	+27272 ± 112	Laf19
U [km/s]	−28.087 ± 0.020	This work
V [km/s]	−0.441 ± 0.012	This work
W [km/s]	−23.03 ± 0.11	This work
	Photospheric parameters	
$T_{\rm eff}$ [K]	3151 ± 51	Sch19
$\log g$ [dex]	5.17 ± 0.07	Sch19
[Fe/H] [dex]	−0.18 ± 0.16	Sch19
$v \sin i$ [km/s]	< 2.0	Rei18
	Physical parameters	
L [$L_\odot$]	0.002195 ± 0.00004	Sch19
R [$R_\odot$]	0.157 ± 0.005	Sch19
M [$M_\odot$]	0.142 ± 0.010	Sch19
Age [Gyr]	3.8 ± 0.5	Eng17

2MASS: Skrutskie et al. (2006); Alo15: Alonso-Floriano et al. (2015); Cab16: Caballero et al. (2016a); *Gaia*: Gaia Collaboration et al. (2018); Gli95: Gliese & Jahreiß (1979); Laf19: Lafarga et al. (2020); Rei18: Reiners et al. (2018a); Sch19: Schweitzer et al. (2019); Eng17: Engle & Guinan (2017).

5.3 Properties of YZ Ceti

5.3.1 Basic physical parameters

YZ Ceti (GJ54.1) is an M4.5 V star at a distance of approximately 3.7 pc (Gaia Collaboration et al. 2018), making it the 21st nearest star to the Sun[5]. We provide an overview of the basic stellar parameters in Table 5.1. For our analysis we adopted the stellar parameters of Schweitzer et al. (2019). The effective temperature $T_{\rm eff}$, surface gravitiy $\log g$, and metallicity [Fe/H] were determined by fitting PHOENIX synthetic spectra (Husser et al. 2013) to CARMENES spectra using the method of Passegger et al. (2018). The luminosity was derived by integrating broadband photometry and adopting the parallax measurement from *Gaia* DR2. The stellar radius R of $0.157 \pm 0.005\,\mathrm{R}_\odot$ was determined by applying the Stefan-Boltzmann law. With a linear mass-radius relation we then obtained $0.142 \pm 0.010\,\mathrm{M}_\odot$ for the stellar mass (see Schweitzer et al. 2019, for details). We computed the Galactocentric space velocities UVW as in Cortés-Contreras (2016) with the latest equatorial coordinates, proper motion, and parallax from *Gaia* DR2 and the latest absolute RV of Lafarga et al. (2020). With these UVW values, YZ Ceti kinematically belongs to the Galactic thin disk and has never been assigned to a stellar kinematic group (Cortés-Contreras 2016). Apart from flaring activity, which is very frequent in intermediate M dwarfs of moderate ages, the star does not display any feature of youth. Engle & Guinan (2017) estimated an age of 3.8 ± 0.5 Gyr from the stellar rotation and X-ray emission, which is consistent with the star kinematics.

5.3.2 Photometric analysis

Astudillo-Defru et al. (2017) estimated the rotation period of YZ Ceti to be 83 d by analyzing ASAS photometry and the FWHM of the cross-correlation function ($\mathrm{FWHM_{CCF}}$) of the radial velocity data obtained by HARPS. However, shortly after publication Jayasinghe et al. (2017) determined the photometric rotation period at $P_{\rm rot} = 68.3$ d using an ASAS-SN lightcurve of 854 photometric measurements in the V band obtained between 2013 and 2017. This result was confirmed by Engle & Guinan (2017), who estimated a rotation period of $P_{\rm rot} = 67 \pm 1.8$ d based on V-band photometry taken between 2010 and 2016 with the 1.3 m Robotically Controlled Telescope. Both of these estimates are in good agreement with the value of $P_{\rm rot} = 69.1$ d determined by Suárez Mascareño et al. (2016) and $P_{\rm rot} = 69.2 \pm 0.4$ d determined by Díez Alonso et al. (2019). Furthermore, Fig. 1 in Astudillo-Defru et al. (2017) shows that the second highest

[5] http://www.recons.org/TOP100.posted.htm

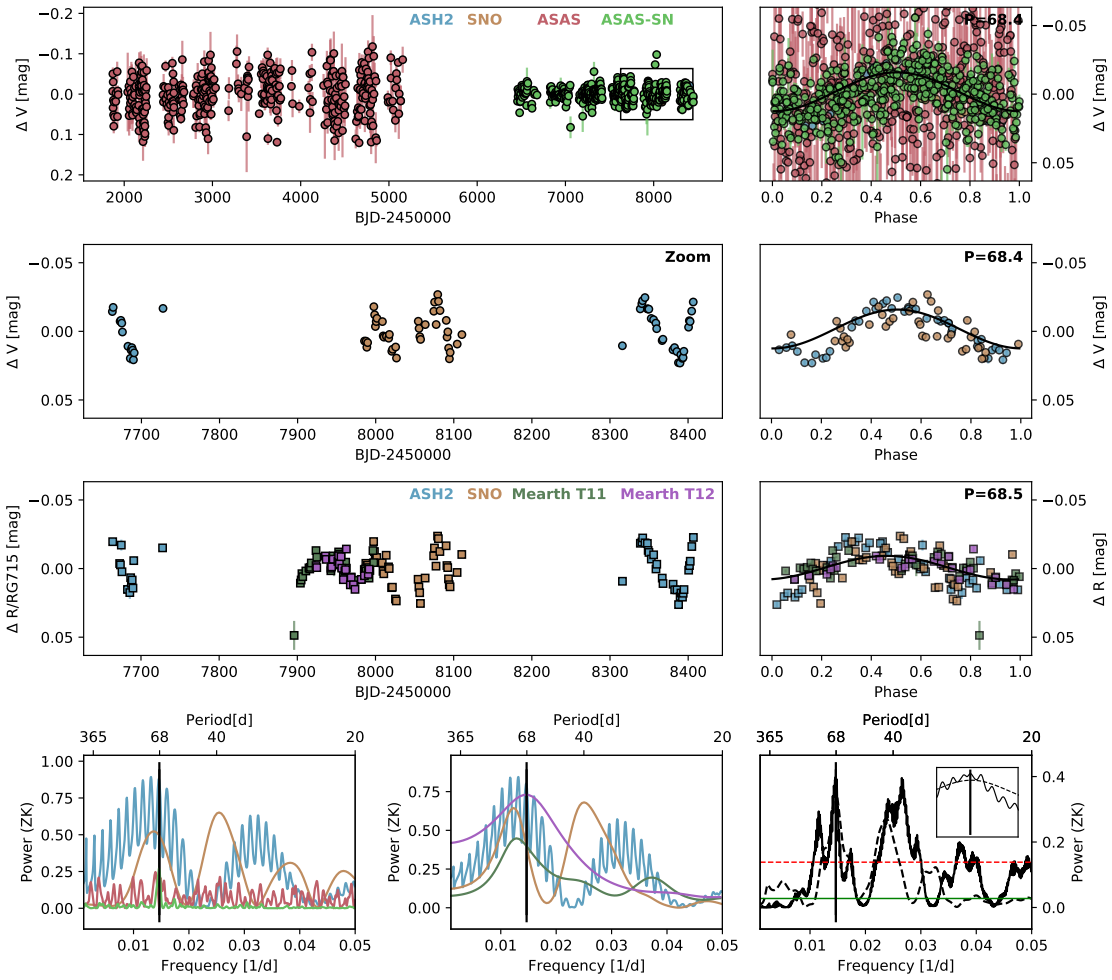


Fig. 5.1.: Top three rows: Nightly binned photometric time series (*top*: all data in the *V* band, *middle*: zoom to ASH2 and SNO data in the *V* band, *bottom*: all data in the *R* band) and a phase plot to the determined rotation period. Bottom row: Periodograms of the different instruments in the *V* band (left), *R* band (middle), and the combination of all instruments in each band (right). The periodograms for the analysis on individual instruments are color-coded (*blue:* ASH2, *brown:* SNO, *red:* ASAS, *green:* ASAS-SN, *dark green:* MEarth T11, *purple:* MEarth T12), while the combined periodograms are plotted in black. The solid line represents the combined *V*-band periodogram and the dashed line the combined *R*-band periodogram. For the combined periodograms we show the FAP level of 0.001 (green solid line for *V* band and red dashed line for *R* band). The vertical black line in each periodogram represents the determined rotation period of 68.4 d and 68.5 d, respectively.

peak of the periodogram of the ASAS data, as well as the highest peak of the $FWHM_{CCF}$ between JD 2457100 to JD 24577000, was around 68 days.

We combined the public archive data from ASAS, ASAS-SN, and MEarth telescopes 11 and 12 (Sec. 5.3.2) with our own observations with ASH2 and SNO T90 to carry out the most extensive combined photometric analysis of the rotation period of YZ Ceti. For each instrument and photometric filter we created generalized Lomb-Scargle (GLS) periodograms (Zechmeister & Kürster 2009) on the nightly binned data. We show the obtained GLS peaks for each instrument in Table 5.2. All instruments except ASAS directly show a highly significant peak at around 68 d. However, for some instruments the highest peak was either a yearly alias or close to half the rotational period of this ~ 68 d periodicity. The formal uncertainties on the frequency, and therefore for the period for each peak, are estimated by the GLS routine from the local χ^2 curvature. This estimate does not account for incorrect choices of alias peaks, hence real uncertainties can be larger. We have also done a combined analysis of all instruments in the *R* and *V* bands by fitting for an offset and jitter term for each instrument within the two different bands. We also do a combined analysis for the SNO *R*-band data and the MEarth T 11 as they have no peak at 68 d; instead, they have a single broad peak close to the yearly alias, which however includes the 68 d period. Combining both data sets yields 41.63 ± 0.85 d as the highest and 69.31 ± 2.52 d as the second highest peak, both with a false-alarm probability (FAP) below 0.001.

In Fig. 5.1 we show the nightly binned photometric time series of each instrument in the *V* band and *R* band as well as the phase plots corresponding to each time series. The bottom row of panels displays the GLS periodograms of each single instrument in the corresponding photometric band (left *V*, middle *R* and *I*) and a combination of all instruments in the *V* band and combined *R* and *I* bands.

In some of our data sets we recognized periodicities near 80 d and 57 d. The former period is close to the rotation period adopted by Astudillo-Defru et al. (2017). Fitting a sinusoid for either the 68-day signal or the 80-day signal removes the other, a strong sign of aliasing. In all data sets the 80-day signal can be reproduced by strong aliases due to annual sampling effects in the window function together with the 68-day periodicity. There are no strong signs of the 80-day periodicity in the combined *R*-band data nor in many individual *R*- and *V*-band data sets. These subsets did not show large annual peaks in the window function, so we are confident that the true rotation period is around 68 days.

Tab. 5.2.: Highest GLS peak (P_{high}) and alternative GLS peak consistent with a common rotation period (P_{rot})[a].

Band	Instrument	P_{high} [d]	P_{rot} [d]
	Single Instruments		
V	ASH2	75.96 ± 0.27	68.29 ± 0.25[b]
V	SNO	39.29 ± 1.03	72.32 ± 4.95[b]
V	ASAS	3.752 ± 0.001	67.38 ± 0.16[c]
V	ASAS-SN	68.49 ± 0.21	68.49 ± 0.21
R	ASH2	75.85 ± 0.33	68.67 ± 0.31[d]
R	SNO	78.21 ± 1.96	78.21 ± 1.96
I	MEarth T 11	78.21 ± 7.03	78.21 ± 7.03
I	MEarth T 12	70.12 ± 7.72	70.12 ± 7.72
	Combined Instruments		
V	All	68.40 ± 0.05	68.40 ± 0.05
R+I	SNO+MEarth T 11	41.63 ± 0.85	69.31 ± 2.52[b]
R+I	All	68.46 ± 1.00	68.46 ± 1.00

[a] We show only peaks with P>1.2 days and FAP below 10^{-3}. We also show the formal 1σ uncertainties provided by the GLS analysis. [b] Second highest peak of GLS. [c] Highest peak after fitting a sinusoidal for P_{high}. [d] Third highest peak of GLS. Error bars denote the 68% posterior credibility intervals.

From the $R+I$ band combined GLS analysis we determined a rotation period of 68.5 ± 1.00 d with an amplitude of 8.6 ± 0.7 mmag, and we independently determined from the V band a rotation period of 68.40 ± 0.05 d with an amplitude of 14.2 ± 0.5 mmag[6].

5.3.3 Spectroscopic activity indicators

YZ Ceti is an active M dwarf identified as a flare star (Kunkel 1970; Shakhovskaya 1995; Montes et al. 2001). Reiners et al. (2018a) estimated an upper limit of $v \sin i < 2\,\mathrm{km\,s^{-1}}$, which corresponds to a slow rotational velocity. The equatorial rotation speed estimated from the radius and rotation period of the star is $2\pi R \sin i / P \approx 0.12 \sin(i)\,\mathrm{km}\,s^{-1}$, well below the directly estimated upper limit of $2\,\mathrm{km}\,s^{-1}$. In addition to the photometric observations, we analyzed several spectral activity indicators from the CARMENES and HARPS spectra. We searched for periodicities of the chromatic index (CRX), Hα, and differential line width (dLW) within all data sets (see Zechmeister et al. 2018, for CRX and dLW), and the Ca II IRT lines within the CARMENES data. These indicators are directly provided by SERVAL. From the CARMENES data we also determined the full width half at maximum (FWHM), contrast, and bisector span (BIS) of the cross-correlation function (CCF, see Reiners et al. 2018a). The GLS periodograms for each of these indicators are shown in Fig. 5.2. We identified a forest of significant peaks that include both the 80 d and 68 d periods visible from photometry within the CARMENES CRX, CARMENES dLW, CARMENES FWHM, CARMENES contrast. Within the HARPS activity indicators we identify a significant peak in the HARPS-POST dLW at 69.68 ± 0.23 d, where the error represents the 1σ uncertainty. These indicators (CRX, dLW, and FWHM) are sensitive to the photosphere of the star and are in agreement with our derived photometric rotation period of the star. However, we did not find a significant correlation between the the CARMENES RVs and CARMENES CRX at this period. We did not see any significant signals for the remaining activity indicators. The forest of significant signals could be explained by adopting a period of around 68 days and calculating possible yearly aliases due to the window function of the radial velocity observations. Overall, we found a good agreement between the spectral activity indicators and the derived photometric rotation period. In particular, we did not find any signs of activity close to the periods of the planetary signals, or their aliases (see below).

[6]For this thesis, I have done a reanalysis of the photometry of YZ Ceti, by using a QP-GP. The priors of this GP have been set similar as for the QP-GP fitted to the photometry of GJ 251 in Chapter 6. The derived rotation period by the QP-GP is $69.1^{+0.31}_{-0.32}$ d and consistent with the GLS estimates. The α_{GP}-vs.-P_{GP} diagram is given in Fig. A.2 in Appendix A, although it was not part of the original publication.

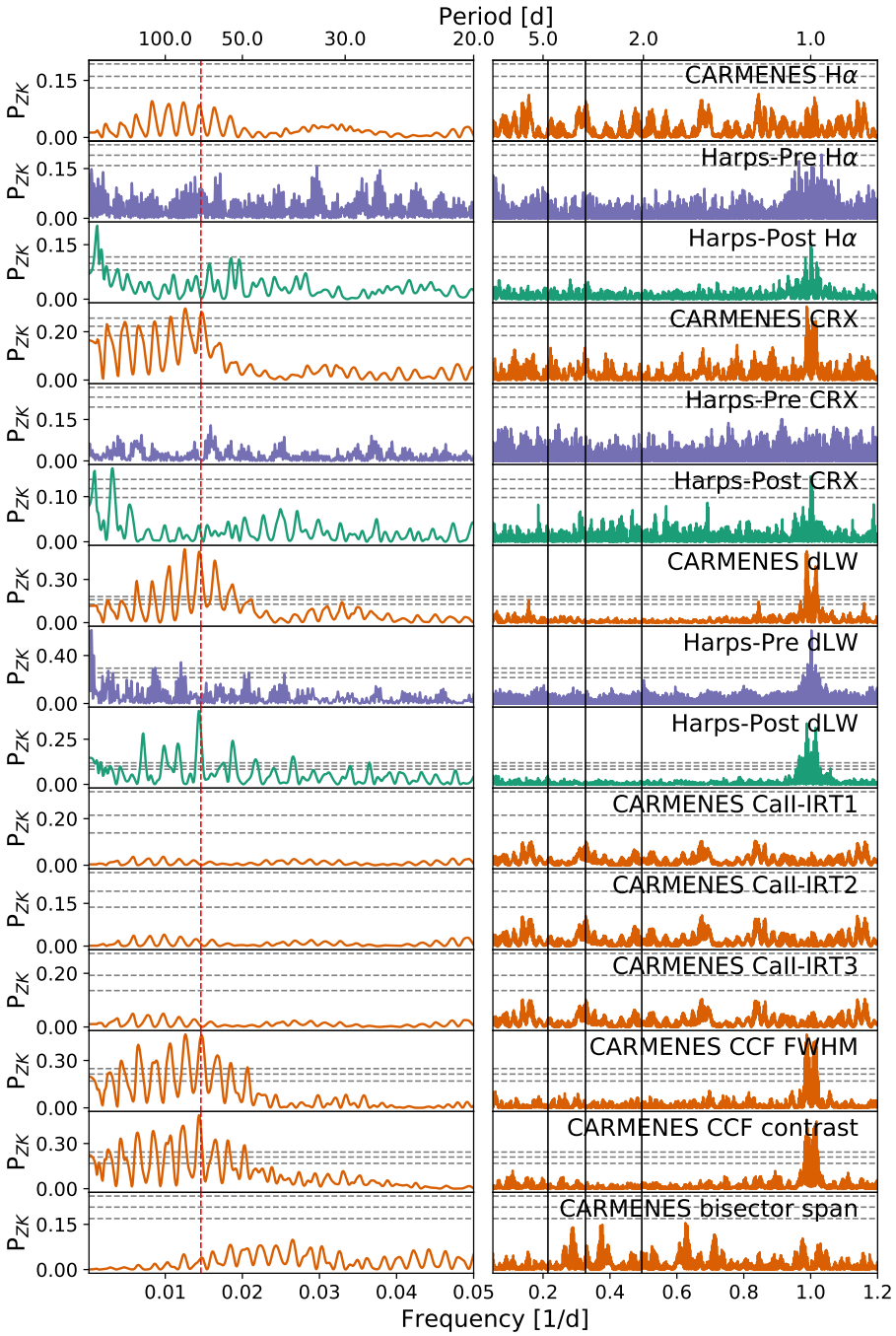


Fig. 5.2.: GLS periodograms of several activity indicators in the CARMENES and HARPS data. The periodograms are separated and show different frequency regimes to better display the significant peaks within the low-frequency regime. The red dashed line shows the photometric rotation period and the black solid lines highlight the planetary frequencies.

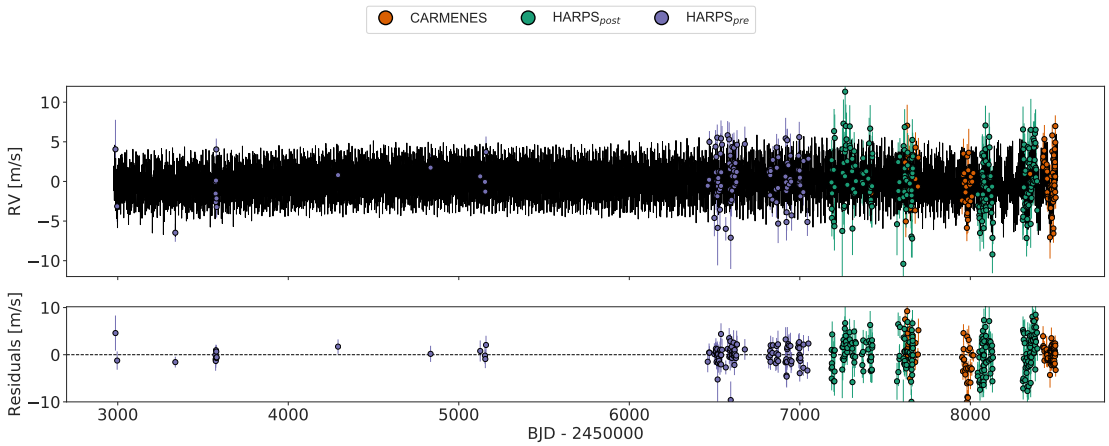


Fig. 5.3.: Radial velocity data and final stable fit including the Gaussian process model for the activity signal (see Sec. 5.5 and Sec. 5.5.2).

5.4 YZ Ceti planetary system

5.4.1 Search for planetary signals

Compared to the discovery paper with 211 data points, we obtained 121 additional data points from HARPS and 108 from CARMENES, resulting in a total of 440 radial velocities for YZ Ceti, which more than doubles the number of available RV measurements in previous studies of this system; for example, both Astudillo-Defru et al. (2017) and Robertson (2018) used only 211 data points taken by HARPS before October 2016. For a major fraction of the CARMENES observations, we took two observations per night in order to break possible degeneracies due to daily aliasing. In Fig. 5.3 we show the RV data and the final stable fit (see Sec. 5.5.2). For the fitting of planetary signals, we used the tool `juliet` (Espinoza et al. 2019), which allows fitting of photometric and/or RV data by searching for the global maximum of the Bayesian evidence within the provided prior volume of the fitting parameters. It does so by using nested sampling algorithms, for example `MultiNest` (Feroz et al. 2009), `PyMultiNest` (Buchner et al. 2014), and `dynesty` (Speagle 2020). For the modeling, `juliet` uses many different publicly available packages, for example `batman` (Kreidberg 2015) for transits, `radvel` (Fulton et al. 2018) for radial velocities, and `george` (Ambikasaran et al. 2015) and `celerite` (Foreman-Mackey et al. 2017) for GP. The priors of the planetary parameters for the fits are shown in Table A.1.

We did a periodogram analysis of the RV data and fitted for the strongest signal until no significant peak with a FAP of less than 0.001 was observed in the residuals periodogram. The FAPs were

Tab. 5.3.: Bayesian log-evidence for models of different number of planets and their log-evidence difference to the best model.

Model	Periods [d]	$\ln \mathcal{Z}$	$\Delta \ln \mathcal{Z}$
0 Planets	...	-1163.8 ± 0.2	76.7
1 Planet	3.06	-1127.3 ± 0.2	40.2
2 Planets	3.06; 4.66	-1110.7 ± 0.3	23.6
3 Planets	2.02; 3.06; 4.66	-1090.1 ± 0.3	3.0
3 Planets[a]	2.02; 3.06; 4.66	-1089.8 ± 0.3	2.7
3 Planets[b]	2.02; 3.06; 4.66	-1088.8 ± 0.3	1.7
3 Planets[c]	2.02; 3.06; 4.66	-1087.1 ± 0.3	...

[(a)] Three-planet model with circular orbits. [(b)] Three-planet model with circular orbits for planet c and d. [(c)] Three-planet model with circular orbits for planet c only.

determined by bootstrapping using 10000 realizations. In order to test whether fitting $n+1$ planets was significantly better than fitting for n planets, we compare the Bayesian log-evidence of the corresponding models. The resulting log-evidence for each model are displayed in Table 5.3. As suggested by Trotta (2008), we regard the difference between two models as strongly significant if their log-evidence differs by $\Delta \ln \mathcal{Z} > 5$. The residual periodograms for these runs are shown in Fig. 5.4; the strongest signal in the periodogram was at 3.06 d. After fitting this signal, the next highest peak was at 4.66 d, and thereafter at 2.02 d. After fitting for three planets, the resulting periodogram did not show any remaining significant signal (no signal with FAP < 0.01; see also Fig. 5.4).

Examining the orbital parameters of the three planets, we found that planet b at 2.02 d has an unusually high eccentricity $e_b = 0.41^{+0.14}_{-0.17}$ $[0.12, 0.67]$, where the errors are 1σ uncertainties and the values inside the bracket represent the 95% density interval. The eccentricity is not significantly different when we choose the alias at 1.97 d, which was the favored period by Astudillo-Defru et al. (2017) for YZ Ceti b. The high eccentricity of most of the posterior samples led to instability for the majority of the samples on very short timescales as shown by integrations using an N-body integrator (see Sec. 5.5 and Table 5.7). Therefore, we compared the Bayesian log-evidence of different configurations where we fixed the eccentricity for all or certain combinations of planets to zero (shown in Table 5.3). This procedure reduced the number of parameters per planet from five to three (as ω is not defined for e=0). We find that a model where we fix the eccentricity for planet c to zero but keep e_b and e_d open performs moderately better than a fit that fits eccentric orbits for all planets ($\Delta \ln \mathcal{Z} = 3 > 2.5$) or fixes eccentricity to

zero for all planets ($\Delta \ln \mathcal{Z} = 2.7 > 2.5$). As a result, there is moderate evidence to fit eccentric orbits for planets b and d (Trotta 2008). The residual periodogram of a three-planet circular fit showed several remaining peaks. The strongest of them was at 67.69 d, and then the peaks at 69.22 d and 68.28 d, all with FAP < 0.01, and at 0.98 d and 1.02 d with a FAP < 0.1. All these peaks could be directly attributed to the stellar rotational period, which is known from photometry to be 68.4 d. The peaks at 67.69 d and 69.22 d are yearly aliases of the 68.28 d period, and 1.02 d and 0.98 d are its daily aliases. We also identified a peak at 28.37 d with FAP < 0.1. However, by fitting a simple sinusoid to the activity signal around 68 d, the 28.37 d singal is removed, a strong indication that this signal is connected to activity.

We tested the coherence of the 28.37 d signal over time with the stacked-Bayesian GLS periodogram (s-BGLS) method (Mortier et al. 2015; Mortier & Collier Cameron 2017). These BGLS periodograms allow comparison of the probabilities of the signals with each other, while the stacking allows assessment of the coherence of the signal with increasing number of observations. As in Mortier & Collier Cameron (2017) we normalized all s-BGLS periodograms to their respective minimum values.

We found that the 28.37-day signal ($f \approx 0.035\,\mathrm{d}^{-1}$) was not very stable over the observed time interval, which can be seen in Fig. 5.5. In particular, this period was not prominent within CARMENES spectra. From these BGLS periodogograms we also deduce that the activity related to the 68-day signal increased over time.

From our GLS analysis we also identified a signal at 7.05 d with FAP just slightly above a FAP of 0.1 in the residuals of the three-planet circular fit. After fitting a three-planet model simultaneously with a GP to model the activity (see Sec. 5.5), we find that this signal increases slightly; it is the highest remaining signal in the residuals, but still below our detection threshold. The signal has an amplitude of roughly $0.6\,\mathrm{m\,s}^{-1}$, and is close to an optimal 3:2 commensurability with regard to the period of YZ Ceti d, hinting at the possibility that there might be a fourth planet in the system. However, the signal requires more data to either confirm or refute its presence.

With the data analyzed to date we thus cannot find statistically significant evidence for an additional fourth planet in the YZ Ceti system. In particular, the tentative signal mentioned by Astudillo-Defru et al. (2017) at 1.04 d ($f \approx 0.962\,\mathrm{d}^{-1}$) has decreased in significance (see also Fig. 5.5, left). In contrast to these signals, our s-BGLS analysis shows that the additional observations increase the probability of the signals at the frequencies of the three planets, further strengthening the possibility of a planetary origin of these signals.

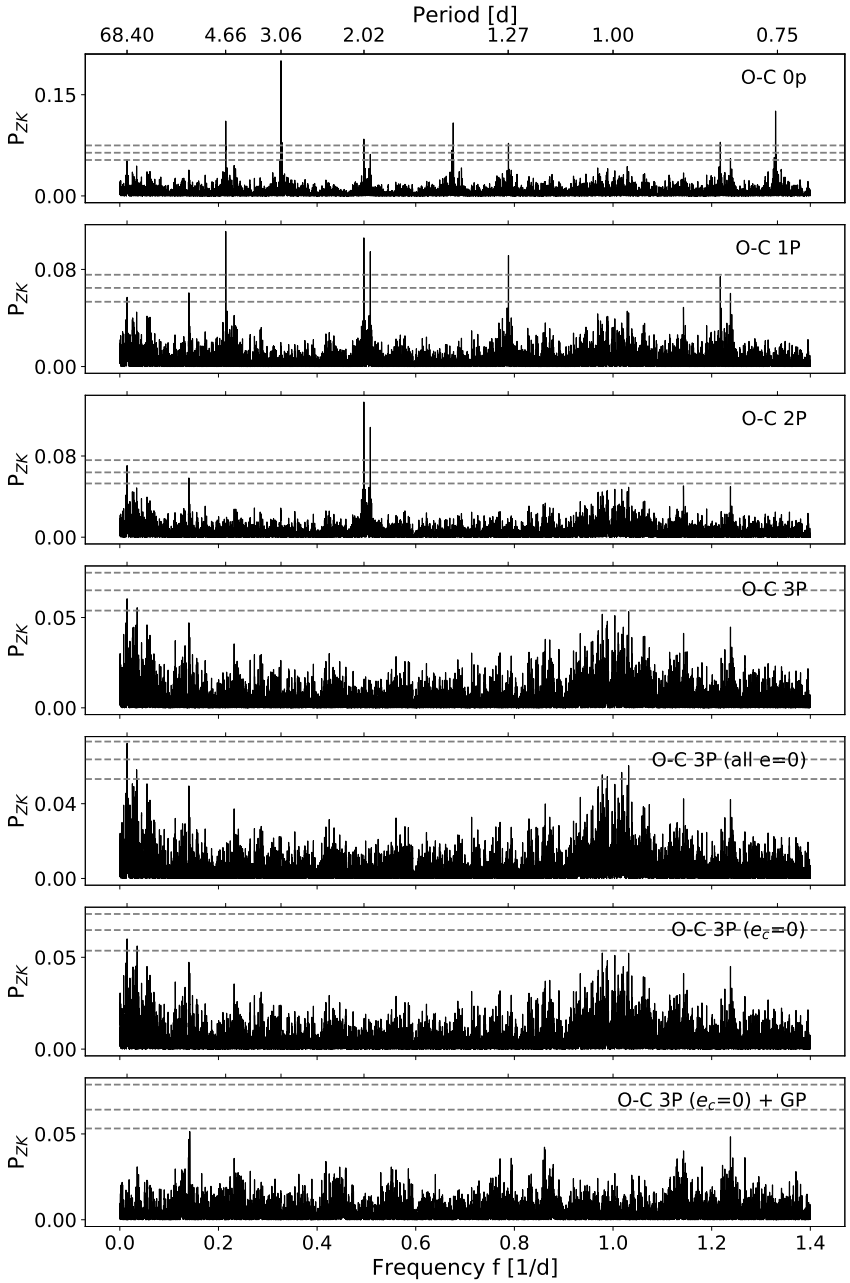


Fig. 5.4.: Generalized Lomb-Scargle periodograms of the data and different fit models from Table 3, and the final GLS periodogram after fitting for the activity with a GP (see Sec. 5.5).

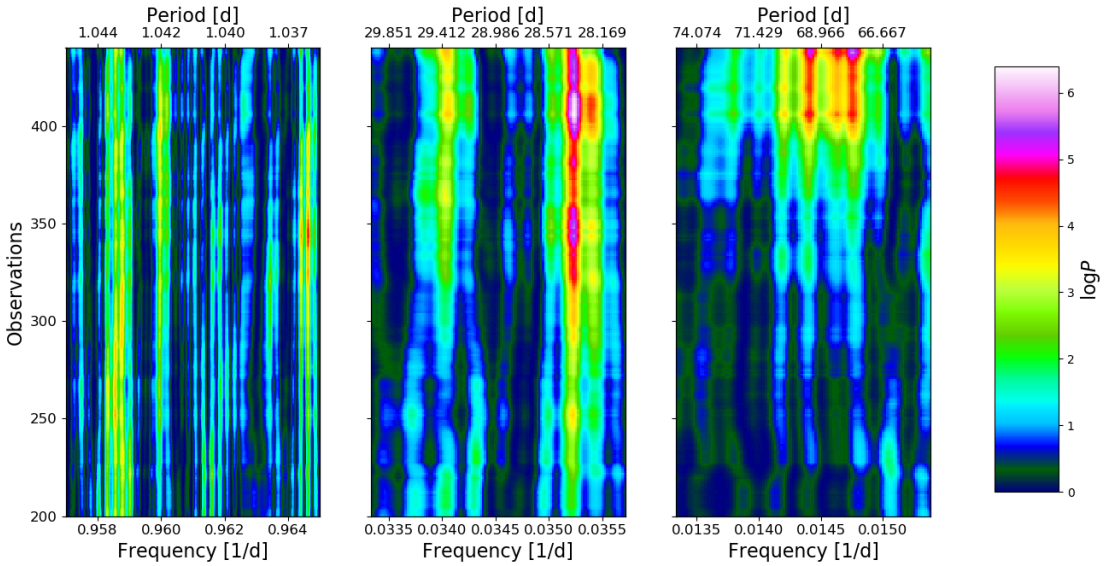


Fig. 5.5.: S-BGLS periodograms after subtracting the three planetary signals. *Left*: Around the frequency of the tentative signal mentioned by Astudillo-Defru et al. (2017), *middle*: 29.36-day signal visible as remnant power in a circular three-planet model, *right*: 68-day signal attributed to the stellar rotation.

5.4.2 Configuration of the system

Each of the three planetary signals had at least one strong alias, making it difficult to pin down the correct period for the planets. The three strong alias pairs are $P_b = 1.97/2.02$ d, $P_c = 0.75/3.06$ d, and $P_d = 1.27/4.66$ d. Astudillo-Defru et al. (2017) published the configuration $P_b = 1.97$ d, $P_c = 3.06$ d, and $P_d = 4.66$ d while Robertson (2018) favored the orbital configuration $P_b = 1.97$ d, $P_c = 0.75$ d and $P_d = 4.66$ d. Here we show that the most likely configuration of YZ Ceti is $P_b = 2.02$ d, $P_c = 3.06$ d, and $P_d = 4.66$ d and that we can robustly determine the configuration of the system with our data. We use two distinct methods. First, we compared the maximum log-likelihood, similar to Robertson (2018), of different realizations of periods for the three-planet models by sampling each possible configuration within `juliet`. When we fitted for the different aliases we only changed the prior of the period and ensured that the posterior is well sampled and not truncated within this volume; for example, to fit planet c at 0.75 d instead of 3.06 d we simply adopted $\mathcal{U}(0.7, 0.8)$ instead of $\mathcal{U}(3.0, 3.1)$. The log-likelihood is more robust to changes in the prior than the log-evidence when comparing the same model with equal number of free parameters but different realizations. The achieved maximum log-likelihoods for each sample of this analysis are summarized in Table 5.4. The data significantly favors a model with planets at

Tab. 5.4.: Maximum achieved log-likelihood for different three-planet models and their difference to the best model.

Periods [d]			max(ln $\mathcal{L}$)	$\Delta \ln \mathcal{L}$	Remarks
P_b	P_c	P_d			
1.97;	0.75;	1.27	−1072.5	35.6	...
2.02;	0.75;	1.27	−1066.3	29.4	...
1.97;	0.75;	4.66	−1065.7	28.8	Rob18
2.02;	0.75;	4.66	−1058.0	21.1	...
1.97;	3.06;	1.27	−1053.1	16.2	...
1.97;	3.06;	4.66	−1043.5	6.6	AD17
2.02;	3.06;	1.27	−1043.4	6.5	...
2.02;	3.06;	4.66	−1036.9	0	This work

AD17: Astudillo-Defru et al. (2017); Rob18: Robertson (2018).

2.02 d, 3.06 d, and 4.66 d ($\Delta \ln \mathcal{L} = 6.5 > 5$, with respect to the best model). In particular, the models with the proposed alias by Robertson (2018) adopting $P_c = 0.75$ d perform worse.

As outlined by Dawson & Fabrycky (2010), the best fitting model does not necessarily represent the true configuration of the system. Therefore, model comparison can only be a strong indication of the way to disentangle aliases. Hence, we also applied a slightly modified version of the method described by Dawson & Fabrycky (2010). The basic idea is to simulate periodograms of the candidate frequencies and their possible aliases by investigating the periodogram of the spectral window function (Roberts et al. 1987), which we show for our data in Fig. 5.6. Using the same sampling as for the original data, a signal with the same properties (phase, amplitude period) is injected into a simulated time series. A periodogram analysis is used to compare the signal properties at the proposed true frequency and at each alias frequency of the simulated and the data periodograms. If the periodogram of one of the simulated frequencies matches the observed data significantly better than the others, this frequency can be considered to be the true one. The original Dawson & Fabrycky (2010) method did not include any noise for the simulated periodograms. Dawson & Fabrycky (2010) stated that only if the noiseless simulated periodograms matches the data periodogram well can it be regarded as a good match. Such a noiseless periodogram, which only includes the true frequency, tends to look very clean with sharp peaks. This makes it in some cases difficult to compare with the noisier data periodogram. In an attempt to break the period degeneracies for YZ Ceti, Robertson (2018) used the method by Dawson & Fabrycky (2010) and included noise by adopting the uncertainties of the radial velocities at each time together with a white noise model of the star based on its derived jitter value.

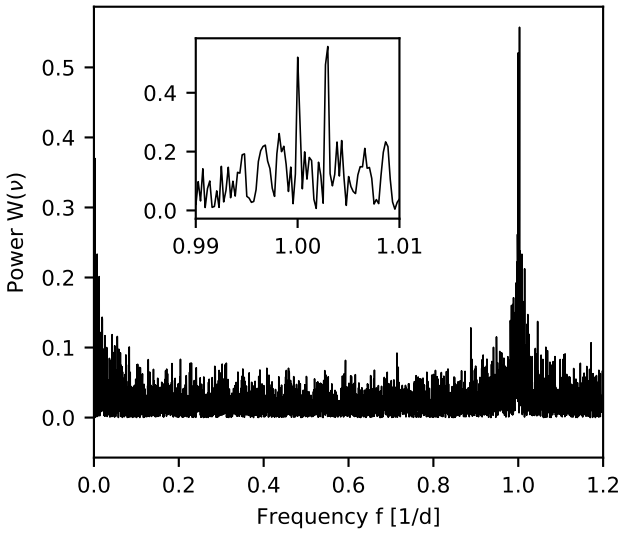


Fig. 5.6.: Periodogram of the spectral window function for the data used in our analysis.

Nevertheless, with the data available at that time, Robertson (2018) was unable to constrain the true frequencies of YZ Ceti b and c with this test. Care should always be taken if noise is included in the simulations. Dawson & Fabrycky (2010) already mentioned that noise can interfere with the candidate periods resulting in the possibility that the power of the alias frequency is higher than the power of the true frequency in the data periodogram. Creating only one realization, a simulated periodogram with noise can therefore lead to incorrect conclusions. Most importantly, however, the inclusion of noise can have a significant effect on the derived phases, as small errors of the determined phase value can accumulate to significant phase differences for peaks that are far away from the injected signal in frequency space. This can be easily seen and tested by injecting two signals with slightly different phases into a simulated time series and examining the phase of their aliases.

Therefore, if noise is included it is necessary to also account for the uncertainties of the determined phase values. We recommend the addition of noise via this method, but suggest the following approach: coupling the method with a Monte Carlo technique and creating 1000 different versions of the simulated data sets. For each time series we used a white noise model, as in Robertson (2018), so that we draw for each realization i from a Gaussian distribution with $\sigma_i^2 = \sigma_{\mathrm{RV},i}^2 + \sigma_{\mathrm{jitter}}^2$. To compare the simulated data with the observations, we created a master periodogram, which is

Tab. 5.5.: Planetary orbital frequencies f_p and their first-order aliases for a sampling frequency of $f_s = 1.0027\,d^{-1}$.

Planet	P [d]	f_p [1/d]	$f_\mathrm{p} + f_\mathrm{s}$ [1/d]	$f_\mathrm{p} - f_\mathrm{s}$ [1/d]
c	3.06	0.32680	1.32950	−0.67590
d	4.66	0.21460	1.21729	−0.78811
b	2.02	0.49505	1.49775	−0.50765

the median of the periodograms from all simulations. This was repeated for the expected true frequency and its first-order aliases. The aliases were thereby calculated using the equation

$$f_\mathrm{alias} = f_\mathrm{p} \pm m \cdot f_\mathrm{s}, \tag{5.1}$$

where f_p is the planetary orbital frequency, f_s the sampling frequency (in our case the largest peak of the window function periodogram), and m the order of the alias. We show the results from this analysis in Fig. 5.7.

The first row in each plot corresponds to the simulation for the strongest peak in the observed periodogram (the expected true frequency f_p), while the second and third row correspond to its first-order daily aliases of $f_\mathrm{alias} = f_\mathrm{p} - f_\mathrm{s}$ and $f_\mathrm{alias} = f_\mathrm{p} + f_\mathrm{s}$ respectively ($f_\mathrm{s} = 1.0027\,d^{-1}$). The signal that is most likely underlying the observed periodogram is the one whose simulated periodograms fits best all three subsets compared to the simulations in the other rows. Such a plot is recommended for any system where possible strong aliases exist. We provide the script used for the alias-testing on github[7] (Stock & Kemmer 2020).

The key frequencies and periods for the following analysis are summarized in Table 5.5. We started with the strongest signal in our data at 3.06 d ($f \approx 0.327\,\mathrm{d}^{-1}$) which was the signal called into question by Robertson (2018). The top panel of Fig. 5.7a shows a significantly better agreement between the simulated periodogram and the observed data when the 3.06-day signal is injected into our simulation compared to when we use its aliases. Injecting the alias at 1.48 d ($f \approx 0.676\,\mathrm{d}^{-1}$, see Fig. 5.7 a, middle panel) did reproduce the phase values of all peaks well, but not the peak height at 0.75 d ($f \approx 1.332\,\mathrm{d}^{-1}$). Injecting the 0.75-day periodicity (Fig. 5.7a, lower panel) resulted in large phase differences for the other two aliases, and the peak height of the signal at 1.48 d was not well reproduced. From this result and the previous results based on the log-likelihoods we concluded that the true period of YZ Ceti c is indeed 3.06 d.

We subtracted this signal from the periodogram using a simple sinusoid and tested the candidate periods of YZ Ceti d, the second strongest signal in the data, for its possible aliases. In the top

[7] https://github.com/JonasKemmer/AliasFinder

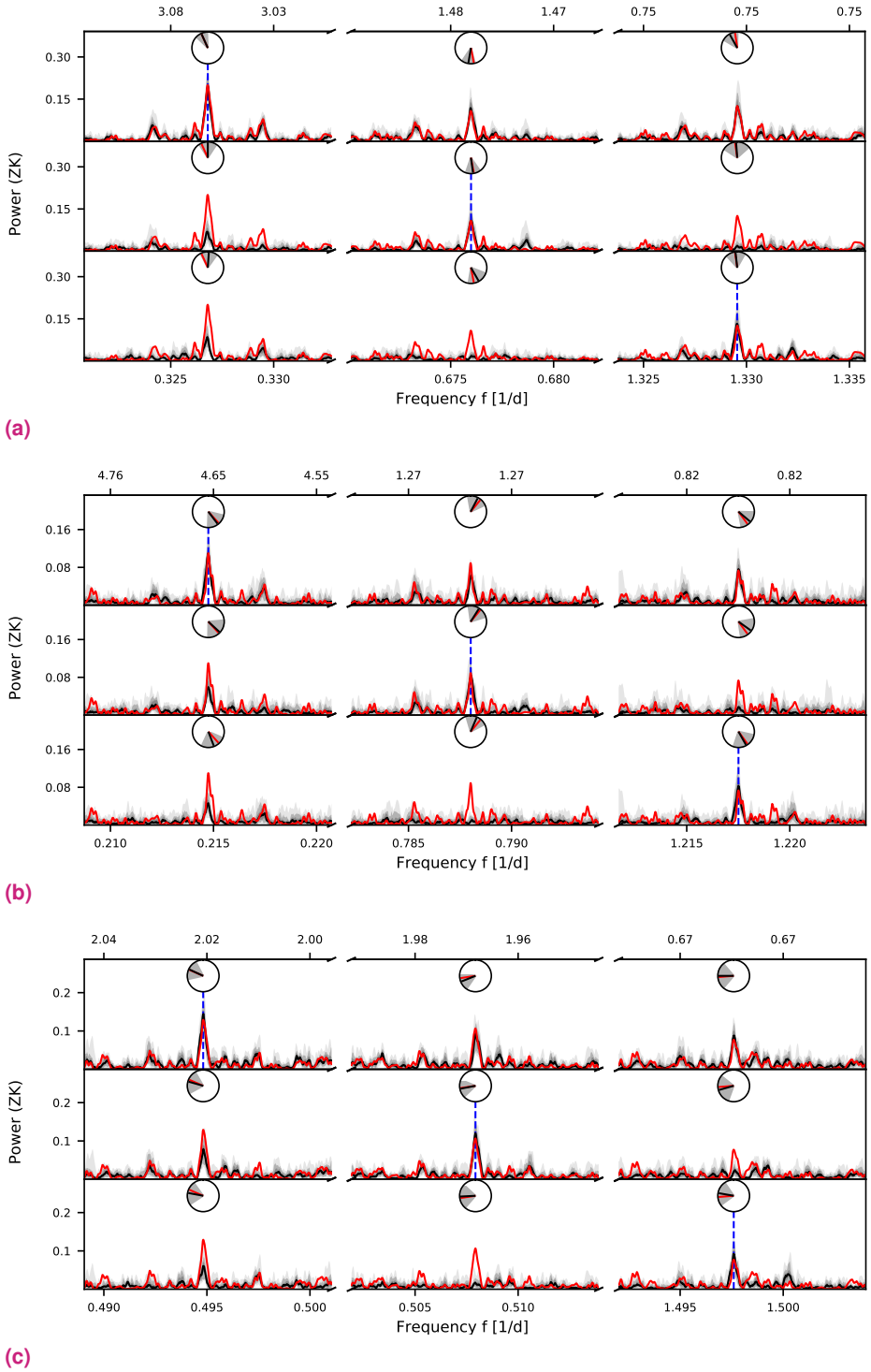


Fig. 5.7.: Alias tests for the periods of 3.06 d (a), 4.66 d (b), and 2.02 d (c). In each plot, each row corresponds to one set of simulations. The frequency of the injected signal is indicated by a vertical blue dashed line. From 1000 simulated data sets each, the median of the obtained periodograms (black solid line), the interquartile range, and the ranges of 90% and 99% (shades of gray) are shown. For comparison, the periodogram of the observed data is plotted as a red solid line. Additionally, the angular mean of the phase of each peak and its standard deviation of the simulated periodograms are shown as clock diagrams (black line and grays) and can be compared to the phase of the peak in the observed periodogram (red line).

panel of Fig. 5.7b, the simulated periodogram with a period of 4.66 d ($f \approx 0.215\,\mathrm{d}^{-1}$) fits the peak heights and phases of the data periodogram well. Injecting the signal of 1.27 d ($f \approx 0.788\,\mathrm{d}^{-1}$; see Fig. 5.7b, middle panel) did not reproduce the peak at 0.82 days ($f \approx 1.218\,\mathrm{d}^{-1}$) and resulted in larger differences in the phase values of the other two peaks. Instead, the 0.82-day signal (Fig. 5.7 b, lower panel) did not reproduce the 1.27-day peak. We concluded that YZ Ceti d orbits at 4.66 d as stated by Astudillo-Defru et al. (2017) and Robertson (2018). We subtracted this signal and analyzed the aliases for YZ Ceti b.

Regarding the simulated periodograms for YZ Ceti b in the top panel of Fig. 5.7 c, we found that the simulated periodogram with the period of 1.97 d ($f \approx 0.508\,\mathrm{d}^{-1}$) published by Astudillo-Defru et al. (2017) performs worse than the alternative period of 2.02 d ($f \approx 0.495\,\mathrm{d}^{-1}$; see Fig. 5.7c, middle panel). The 1.97-day signal did not reproduce the peak at 0.67 d ($f \approx 1.497\,\mathrm{d}^{-1}$) at all, as the peak heights of the simulated periodograms deviated significantly from the data periodogram, and the data periodogram is not in the range of 99% of the simulated periodograms. The same is true for the peak at 1.97 d when simulating the 0.67-day signal (Fig. 5.7c, lower panel). We therefore adopted a period of 2.02 d for YZ Ceti b, in line with our results by `juliet` and in contrast to the published period by Astudillo-Defru et al. (2017) and Robertson (2018). We also tested subtracting the alternative alias solutions from the periodograms before doing the analysis for YZ Ceti b and d. This had no significant influence on the results presented in Fig. 5.7.

With more data, some RV measurements taken twice per night and with observations taken from multiple observatories (Calar Alto, Spain and La Silla, Chile), which have a ~4 h difference in longitude, we have improved sampling and therefore were able to solve the alias problem for this system. Overall, we found from our analysis on aliases and the model comparison within the framework of Bayesian statistics that the most probable configuration of the YZ Ceti multiplanetary system, as derived from the current data, is a three-planet system with planets at periods of 2.02 d, 3.06 d, and 4.66 d. Coincidentally, attributing YZ Ceti b to a period of 2.02 d instead of 1.97 d brings the system configuration closer to a 3:2 period commensurability for both pairs of neighboring planets.

5.5 Simultaneous fitting of stellar activity and Keplerians

As in Astudillo-Defru et al. (2017), we simultaneously modeled the stellar activity by using GP regression models as we found that correlated noise seems to influence the derived planetary parameters. This is in contrast to Robertson (2018), who did not use a GP to model the YZ Ceti system. Compared to sinusoidal signals, a GP has the advantage that is is more flexible, and

can therefore capture more features resulting from the stellar activity. However, GPs may also potentially lead to overfitting the data and so to absorbing noise or planetary signals into the presumed stellar activity. We used `juliet` to model the activity signal simultaneously with the Keplerian models. We used an exp-sin-squared kernel multiplied with a squared-exponential kernel (Ambikasaran et al. 2015). This kernel has the form

$$k_{i,j} = \sigma_{GP_i}^2 \exp\left(-\alpha_i \tau^2 - \Gamma_i \sin^2\left(\pi\tau / P_{\mathrm{rot},i}\right)\right), \tag{5.2}$$

where σ_{GP_i} is the amplitude of the GP component given in $m\,s^{-1}$, α_i is the inverse length scale of the GP exponential component given in d^{-2}, Γ_i is the amplitude of GP sine-squared component and dimensionless, $P_{\mathrm{rot},i}$ the period of the GP quasi-periodic component given in d, and τ is the time-lag. The α value is a measure of the strength of the exponential decay of the quasi-periodic kernel. A lower α describes a more stable periodic signal and stronger correlation between data points. The quasi-periodic kernel is a kernel widely used in the literature for the modeling of stellar activity with a GP. We also tested the `celerite` approximation to a quasi-periodic kernel and the `celerite` Simple Harmonic Oscillator (SHO) kernel (Foreman-Mackey et al. 2017). Both of these had significantly worse evidence than the quasi-periodic kernel and were for most of the runs also not able to reproduce the rotational period of YZ Ceti.

We performed runs with different priors for the GP hyperparameters in order to investigate the influence of the GP modeling on the planetary parameters. YZ Ceti is a rather compact system, so we also used the dynamical stability of the derived orbits to test whether our posterior distributions for the planetary parameters are realistic (see Sec. 5.5.2). The following runs were all done by using the `dynesty` (Speagle 2020) dynamic nested sampling with 1500 live points and the sampling option slice, which is needed for our high-dimensional parameter space.

Our very first GP model used uninformative priors of the GP hyperparameters that spanned a very wide parameter range, especially for the rotation period, for which we used $\mathcal{U}(30, 100)$. From the posterior samples of this run, we found that only for rotation periods around 68 d the GP model allowed very low α values, consistent with a rather stable periodic signal. This period range is consistent with the photometric rotation period. However, we also observed a plateau of a large number of possible solutions that range over the complete prior volume but have rather high values of α between $10^0\,\mathrm{d}^{-2}$ and $10^{-4}\,\mathrm{d}^{-2}$. Therefore, only a few samples modeled the stellar rotational signal.

In the four GP runs, which we describe in detail below, we constrained the prior on the rotation period to sample more dense around the period range of the photometric rotation period. The reason was that we wanted to use the GP primarily as a model for the stellar rotational signal

and not for any other residual noise (e.g., instrumental). Our analysis showed that the correlated signal originating from the stellar rotational signal affects the planetary parameters the most, especially for YZ Ceti b at 2.02 d. We therefore note that the following approach might be unique for YZ Ceti and systems that suffer from a similiar problem.

The GP priors used for these runs are listed in Table 5.6, where we also show the posteriors of the hyperparameters as well as the evidence of the run, the maximum achieved log-likelihood, and the eccentricity of planet b as this parameter is rather sensitive to the modeling of the stellar activity. The Bayesian log-evidence of all these runs was significantly better than a simple three-planet Keplerian fit to the data. In Fig. 5.8 we show the scatter plots of the sampled α values of the quasi-periodic kernel over the sampled rotational periods. Since the influence of the activity on the RV data is wavelength dependent, and HARPS and CARMENES operate across different wavelength regimes, we also tested for each run whether it is justified to use distinct GP amplitudes (σ_{GP} and Γ) for the two spectrographs separately. For all our runs with distinct GP amplitudes we achieved less log-evidence while increasing the number of parameters. The derived planetary parameters and remaining non-amplitude GP parameters were not significantly different from runs where we did not use distinct GP amplitudes for the instruments. Therefore, we stayed with the simplest GP model which has fewer hyperparameters and a higher log-evidence, but global amplitude hyperparameters.

Tab. 5.6.: Four runs with different GP priors done with `juliet` for modeling the activity of YZ Ceti.

Run	Priors	σ_{GP} [m s^{-1}]	α_{GP} [10^{-4}d^{-2}]	Γ_{GP}	P_{GP} [d]	$\ln \mathcal{Z}$	max($\ln \mathcal{L}$)	e_b
a	σ_{GP}: $\mathcal{U}(0.1, 5)$ α_{GP}: $\mathcal{J}(10^{-8}, 10^{0})$ Γ_{GP}: $\mathcal{J}(10^{-2}, 10^{2})$ P_{GP}: $\mathcal{U}(65, 70)$	$1.65^{+0.18}_{-0.17}$ [1.32, 2.01]	$357.562^{+954.387}_{-352.145}$ [0.003, 1930]	$13.0^{+17.3}_{-12.7}$ [0.0, 43.9]	$67.52^{+1.70}_{-1.76}$ [65.24, 70.00]	$-1052.7^{+0.3}_{-0.3}$	−996.1	$0.16^{+0.15}_{-0.11}$ [0.00, 0.41]
b	σ_{GP}: $\mathcal{U}(0.1, 5)$ α_{GP}: $\mathcal{J}(10^{-8}, 10^{-4})$ Γ_{GP}: $\mathcal{J}(10^{-2}, 10^{2})$ P_{GP}: $\mathcal{U}(65, 70)$	$1.50^{+0.24}_{-0.21}$ [1.09, 1.99]	$0.121^{+0.674}_{-0.090}$ [0.002, 0.942]	$15.3^{+11.9}_{-6.8}$ [3.2, 40.2]	$68.18^{+0.42}_{-0.53}$ [67.00, 69.98]	$-1057.1^{+0.3}_{-0.3}$	−997.4	$0.11^{+0.12}_{-0.08}$ [0.00, 0.32]
c	σ_{GP}: $\mathcal{U}(0.1, 5)$ α_{GP}: $\mathcal{J}(10^{-8}, 10^{-5})$ Γ_{GP}: $\mathcal{J}(10^{-2}, 10^{2})$ P_{GP}: $\mathcal{U}(65, 70)$	$1.48^{+0.29}_{-0.21}$ [1.04, 2.09]	$0.041^{+0.032}_{-0.022}$ [0.008, 0.094]	$14.4^{+14.0}_{-7.0}$ [2.4, 43.0]	$68.28^{+0.22}_{-0.26}$ [67.70, 68.71]	$-1056.0^{+0.3}_{-0.3}$	−997.2	$0.10^{+0.11}_{-0.07}$ [0.00, 0.30]
d	σ_{GP}: $\mathcal{U}(0.1, 5)$ α_{GP}: $\mathcal{J}(10^{-8}, 10^{0})$ Γ_{GP}: $\mathcal{J}(10^{-2}, 10^{2})$ P_{GP}: $\mathcal{N}(68.5, 1)$	$1.65^{+0.18}_{-0.17}$ [1.31, 2.00]	$251.689^{+1013.743}_{-247.547}$ [0.005, 1852]	$14.1^{+17.5}_{-13.7}$ [0.0, 45.5]	$68.6^{+1.06}_{-0.96}$ [66.72, 70.74]	$-1056.3^{+0.3}_{-0.3}$	−995.4	$0.15^{+0.15}_{-0.11}$ [0.00, 0.40]

[(a)] The prior labels $\mathcal{U}$ and $\mathcal{J}$ denote uniform and Jeffrey's distributions. We also list the posteriors of the GP hyperparameters, the log evidence and maximum likelihood achieved by the sampling, and the median from the posterior of the eccentricity for the innermost planet. Error bars denote the 68% posterior credibility intervals. We report the 95% highest-density interval within square brackets.

For run a we set up a narrow uninformative uniform prior around the region of the suspected stellar rotational period. From the results of the posterior samples we found that the GP still did not predominantly model the rotation period of the star in most of the samples. The posterior of the GP rotational period was mostly flat and not well constrained, as $[65.24, 70.00]$ which populates almost the complete provided prior range of this parameter. In Fig. 5.8a we see the same plateau as before, in the range of α values from $\sim 0.1\,\mathrm{d}^{-2}$ to $1\,\mathrm{d}^{-2}$, corresponding to decay timescales of several days ($\tau \sim \alpha_{\mathrm{GP}}^{-1/2}$). The plateau spanned the range between $10^{0}\,\mathrm{d}^{-2}$ and $10^{-4}\,\mathrm{d}^{-2}$ in α for this run. These solutions were dominated by the exponential decay term of the GP model. The high likelihood of such solutions showed that the GP tends to favor models in which the data set for YZ Ceti is not dominated by the stellar rotation and in which there is no strong correlation between neighboring data points. The GP may also have a tendency to fit for such high α values due to the sampling of the RV data together with the intrinsic flexibility of the GP model. Nevertheless, we identified an interesting feature in Fig. 5.8a around a period of 68 days, with samples that have likelihood values similar to the samples in the plateau. For such periods, the GP allowed very low values for α_{GP}, which are more consistent with a rather stable quasi-periodic signal. We now tuned the quasi-periodic GP to model only the stellar rotational signal and sample this local maximum. In the following we show how this affects the log-evidence and derived planetary parameters, in particular the eccentricity of the planets.

The following two runs (*b, c*) show what happens if the GP is tuned to specifically model only the signal that can be directly attributed to the rotation period of the star. We constrained the prior of the α parameter to lower values, so that the GP will predominately fit more periodic signals. This tuning was physically motivated in our case, and forces the GP to not primarily model short-term correlated or uncorrelated noise and act more like a sinusoid, but it still allows changes in the amplitude or phase shifts making it more flexible than a simple sinusoid. Since our prior for α excludes a number of high-likelihood samples distributed over the whole prior volume, it is expected that the log-evidence of a model with such a strong constraint is smaller than a model that can fit these solutions. If the GP is forced to predominantly fit the rotational signal of the star but no other unknown systematics (e.g., jitter), the median of the posterior of the derived eccentricity for the innermost planet and the upper boundary of the 95% density interval shift towards lower values (Table 5.6), which is exactly what we expected. However, there seems to be a "sweet spot" where further constraining of the α value leads to significantly lower maximum likelihood achieved within the sample distribution and to significantly worse log-evidence. This was the case when we further constrained α to values below 10^{-6} as we were then sampling only the tail of the contribution from the stellar rotation signal.

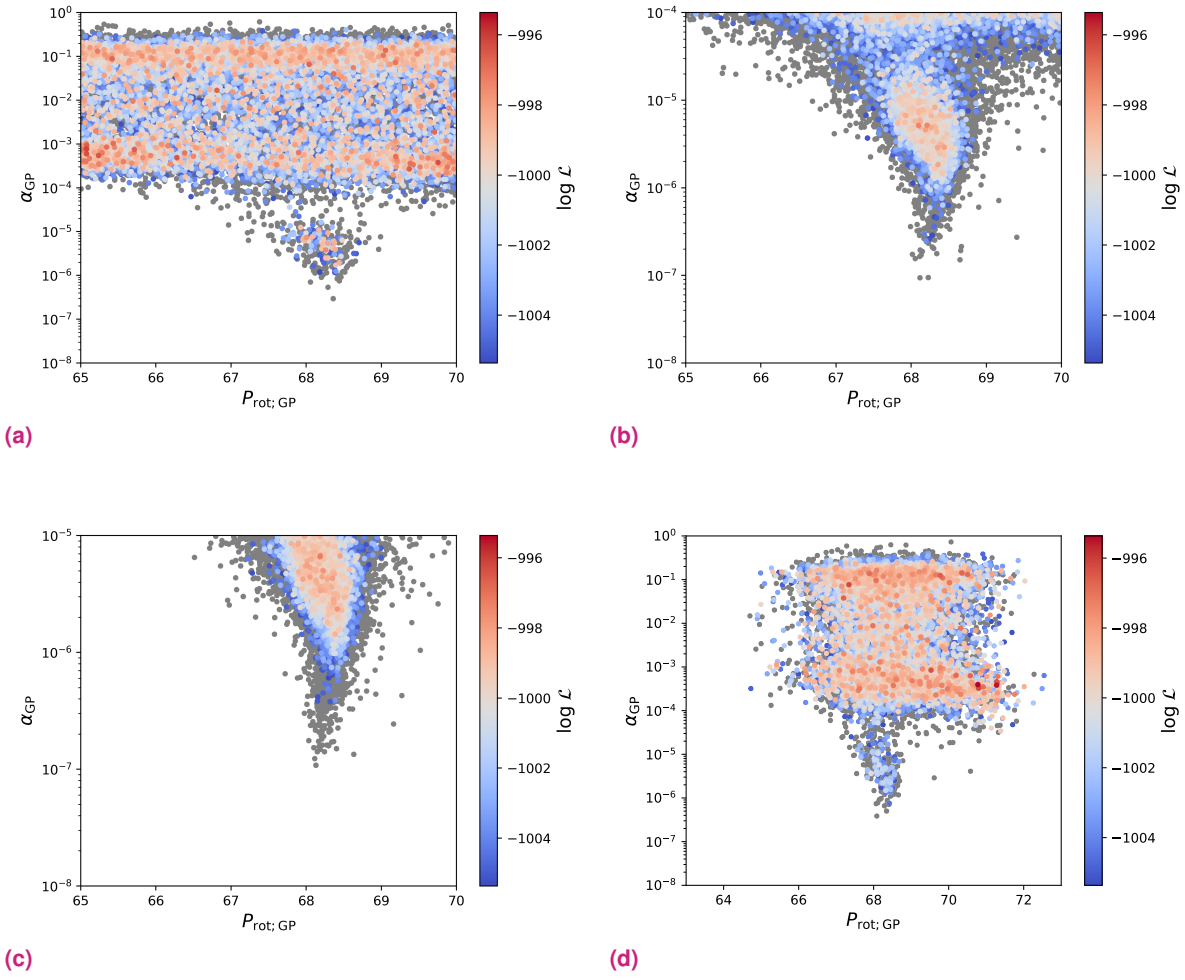


Fig. 5.8.: Gaussian-process alpha-period diagram (α_{GP} vs. P_{GP}) for four runs with different priors listed in Table 5.6. The color-coding shows a likelihood range of $\Delta \ln \mathcal{L} \leq 10$ normalized to the highest achieved log-likelihood within all four runs, and can be compared between the different subplots and runs. Samples with a $\Delta \ln \mathcal{L} > 10$ compared to the highest achieved likelihood are shown in gray.

A widely used approach if a rotation period of the star is available from photometry is to use this information as an informative normal prior within the radial velocity fitting. We tested this approach in run *d* by adopting a normal prior based on the photometric rotation period, and uncertainty derived from the *R* band as it has the largest uncertainty. In the specific case of YZ Ceti, this constraint has no influence on the derived planetary parameters compared to run *a* as the GP model still fits predominantly for high α values. The uncertainty of the GP rotational period equals the prior range for this hyperparameter, showcasing the same problem as for run *a*, namely that most of the posterior samples favor that the GP models to a lesser extent correlated effects and short-term noise, which seem to dominate over the contribution from the stellar rotational period. Only a constraint on α is able to change this behavior of the GP. It is reassuring that in the case of run *c* this constraint on α results in a distribution of the posterior of the rotation period for the GP that is close to a normal distribution and consistent with the photometric observations even without the need of an informative normal prior on the rotation period. We also tested whether any other period between 30 d and 100 d is consistent with such low α values by applying a broader uniform prior on the rotation period ranging from 30 d to 100 d as in the very first run that we performed, but keeping the constraint of run *c* on α. For this test we still found only one single mode for the posterior of the rotation period of the GP, which peaked at the same period as for run *c*, and the GP α-*P* diagram looked almost as in Fig. 5.8c. Additionally, the derived planetary parameters from run *c* were more consistent with a much simpler analysis that used sinusoids as activity models. Run *c* also led to more dynamically stable solutions than run *a*. For the physically motivated reasons mentioned before, we adopted run *c* as our final GP model for YZ Ceti.

5.5.1 Transit search with *TESS*

In addition to the extensive long-term photometry presented in Sec. 5.3.2, short-cadence observations from the *TESS* satellite (Ricker et al. 2015) were also available. YZ Ceti was observed in Sector 3 (Camera 1, CCD 1) from 20 September to 10 October, 2018. However, there were no *TESS* objects of interest (TOIs) listed on the *TESS* data alerts public website for this target. As in Luque et al. (2019) we performed an independent signal search applying the transit least-squares (TLS; Hippke & Heller 2019) algorithm on the Pre-search Data Conditioning Simple Aperture Photometry (PDCSAP) light curve provided by the Science Processing Operations Center (SPOC; Jenkins et al. 2016) on the Mikulski Archive for Space Telescopes (MAST)[8]. No signals were found in the process.

[8] https://mast.stsci.edu/portal/Mashup/Clients/Mast/Portal.html

We therefore investigated whether we could rule out transits of the three known planets, and thus use this information to further constrain the minimum inclination of the system assuming coplanar orbits. YZ Ceti b has the highest transit probability ($p \approx R_*/a_b$) with $p \approx 4\%$, while YZ Ceti c and d have transit probabilities of $p \approx 3\%$. However, as it is also the smallest planet in the system, the transit signal of YZ Ceti b would be the most difficult to detect. To calculate the planetary radius we used the semi-empirical mass-radius relationship from Zeng et al. (2016). We derived $R_b \approx 0.93\,R_\oplus$, $R_c \approx 1.05\,R_\oplus$, and $R_c \approx 1.04\,R_\oplus$. Assuming a circular orbit, the transit depth of YZ Ceti b would thus be about $(r_b/R_*)^2 \approx 0.29\%$ and the transit duration $\Delta t \approx 0.73$ h. The standard deviation of the *TESS* PDCSAP light curve is 0.16%, which means that the planet would be easy to detect if it had a full transit. This was also confirmed by injecting fake box-transits into the data set and running the TLS signal search.

We concluded that the maximum inclination of the system must be such that a full transit of YZ Ceti b is excluded. This yields $i_{\max} = \arccos(R_*/a_b) = 87.43$ deg.

5.5.2 *N*-body integrations

We tested the long-term stability of the YZ Ceti system by using the `SyMBA` *N*-body symplectic integrator (Duncan et al. 1998), which was modified to work in Jacobi coordinates (e.g., Lee & Peale 2003). Each posterior sample was integrated for a maximum of one million orbits of the inner planet with time steps of 0.02 d. However `SyMBA` reduces the time step during close encounters to ensure an accurate simulation. `SyMBA` also tests whether there are planet-planet or planet-star collisions, or planetary ejections, and if so interrupts the integration. A planet is considered lost and the system unstable if, at any time, (*i*) the mutual planet-planet separation is below the sum of their physical radii, assuming Jupiter mean density (i.e., planets undergo collision); (*ii*) the star-planet separation exceeds twice the initial semi-major axis of the outermost planet ($r_{\max} > 2a_{\mathrm{d\ init}}$), which we define as planetary ejection; (*iii*) the star-planet separation is below the physical stellar radius ($R \approx 0.00074$ au), which we consider a collision with the star; and (*iv*) the semi-major axis receives a change of 30% compared to the initial value. These criteria efficiently detect unstable configurations and save computation time.

The inclination of YZ Ceti, $i_{\max} < 87.43$ deg, was applied for the stability analysis under the assumption of co-planar orbits. In Table 5.7 we show the further constrained posterior parameters that we derived by allowing only solutions stable up to one million orbits of the inner planet. Compared to our previous estimates, we found lower values for the eccentricities. We also found that about 17.1% of the samples of our favored model (run *c*) were stable, showing that the

Tab. 5.7.: Posterior parameters of fits obtained for YZ Ceti using `juliet`.

Parameter[a]	3 Planet	3 Planet + GP (run *c*)	Stable 3 Planet + GP (run *c*)
		Planet b	
P (d)	$2.02084^{+0.00007}_{-0.00006}$	$2.02087^{+0.00007}_{-0.00008}$	$2.02087^{+0.00007}_{-0.00009}$
$t_0 - 2450000$ (BJD)	$2996.57^{+0.19}_{-0.26}$	$2996.25^{+0.21}_{-0.18}$	$2996.25^{+0.21}_{-0.17}$
K (m s^{-1})	$1.65^{+0.27}_{-0.23}$	$1.35^{+0.15}_{-0.15}$	$1.31^{+0.15}_{-0.14}$
e	$0.42^{+0.14}_{-0.16}$	$0.10^{+0.11}_{-0.07}$	$0.06^{+0.06}_{-0.04}$
ω (deg)	197^{+15}_{-16}	205^{+101}_{-152}	197^{+110}_{-133}
		Planet c	
P (d)	$3.05994^{+0.00011}_{-0.00011}$	$3.05988^{+0.00010}_{-0.00010}$	$3.05989^{+0.00010}_{-0.00010}$
$t_0 - 2450000$ (BJD)	$2997.56^{+0.16}_{-0.16}$	$2997.62^{+0.15}_{-0.16}$	$2997.62^{+0.15}_{-0.16}$
K (m s^{-1})	$1.93^{+0.16}_{-0.17}$	$1.85^{+0.14}_{-0.15}$	$1.84^{+0.14}_{-0.15}$
e	0.00 (fixed)	0.00 (fixed)	0.00 (fixed)
ω (deg)	N/D[b]	N/D[b]	N/D[b]
		Planet d	
P (d)	$4.65654^{+0.00028}_{-0.00030}$	$4.65629^{+0.00027}_{-0.00031}$	$4.65626^{+0.00028}_{-0.00029}$
$t_0 - 2450000$ (BJD)	$2996.77^{+0.30}_{-0.30}$	$2996.97^{+0.33}_{-0.30}$	$2996.83^{+0.30}_{-0.29}$
K (m s^{-1})	$1.48^{+0.18}_{-0.17}$	$1.59^{+0.15}_{-0.15}$	$1.54^{+0.14}_{-0.15}$
e	$0.22^{+0.15}_{-0.13}$	$0.19^{+0.10}_{-0.10}$	$0.07^{+0.04}_{-0.05}$
ω (deg)	214^{+29}_{-44}	209^{+29}_{-38}	200^{+53}_{-62}
		RV parameters	
$\gamma_{\text{HARPS-PRE}}$ (m s^{-1})	$2.89^{+0.20}_{-0.20}$	$2.75^{+0.45}_{-0.44}$	$2.74^{+0.44}_{-0.45}$
$\sigma_{\text{HARPS-PRE}}$ (m s^{-1})	$0.86^{+0.33}_{-0.53}$	$0.08^{+0.33}_{-0.06}$	$0.10^{+0.35}_{-0.08}$
$\gamma_{\text{HARPS-POST}}$ (m s^{-1})	$-7.72^{+0.20}_{-0.20}$	$-7.72^{+0.46}_{-0.45}$	$-7.72^{+0.46}_{-0.47}$
$\sigma_{\text{HARPS-POST}}$ (m s^{-1})	$2.17^{+0.19}_{-0.18}$	$1.76^{+0.20}_{-0.19}$	$1.78^{+0.20}_{-0.20}$
γ_{CARMENES} (m s^{-1})	$-0.23^{+0.23}_{-0.22}$	$-0.18^{+0.48}_{-0.48}$	$-0.19^{+0.49}_{-0.49}$
σ_{CARMENES} (m s^{-1})	$1.54^{+0.23}_{-0.22}$	$0.20^{+0.48}_{-0.17}$	$0.24^{+0.50}_{-0.20}$
		GP hyperparameters	
$\sigma_{\text{GP,RV}}$ (m s^{-1})	...	$1.48^{+0.29}_{-0.21}$	$1.48^{+0.31}_{-0.21}$
$\alpha_{\text{GP,RV}}$ (10^{-4} d^{-2})	...	$0.041^{+0.032}_{-0.022}$	$0.040^{+0.033}_{-0.022}$
$\Gamma_{\text{GP,RV}}$	...	$14.4^{+14.0}_{-7.0}$	$13.4^{+13.1}_{-6.4}$
$P_{\text{rot;GP,RV}}$ (d)	...	$68.25^{+0.22}_{-0.27}$	$68.28^{+0.21}_{-0.28}$

[a] Error bars denote the 68% posterior credibility intervals. [b] Argument of periapsis not defined. Priors and descriptions for each parameter can be found in Table A.1.

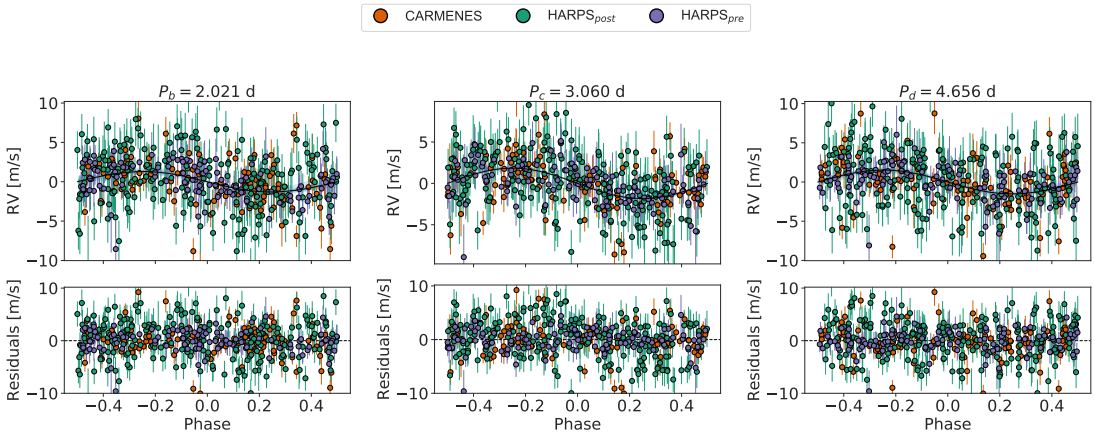


Fig. 5.9.: Phase-folded RVs to the planetary periods based on the median posterior parameters of the stable solutions (Table 5.7).

compactness of the planetary orbits in the YZ Ceti system allows only a narrow range of planetary eccentricities. For comparison, the stable fraction of posterior samples without modeling the activity with a GP was only 1.7%. Figure 5.9 shows the phase plot of the RV models based on the posterior of the stable solutions. A corner plot of all the derived fit parameters for run *c* using `juliet` is displayed in Fig. A.1. In this plot we also highlight the stable sample (in blue). Additionally, we used our stability analysis to search for a lower limit on the inclination. We found that for an inclination of $i_{\mathrm{min}} = 0.9\,\mathrm{deg}$ no sample solution was stable, providing a weak upper limit. Based on the stable solutions we derived some additional planetary parameters which are given in Table 5.8.

The median GP model of the stable solutions and its GLS periodogram are shown in Fig. 5.10. With the GLS periodogram we verified which periods are fitted by the GP. The plot also shows that the amplitude of the GP increases over the observational time span, indicating that the contribution of the radial velocity variations caused by the stellar rotation increased over time.

The dynamics of the YZ Ceti multiplanetary system has only been sparsely investigated since its discovery by Astudillo-Defru et al. (2017). From our 17.1% of the stable Kepler sample, we found that a fraction of about 22% of the solutions showed clear libration of the three-body Laplace angle Θ_{L} given as

$$\Theta_{\mathrm{L}} = 2\lambda_1 - 5\lambda_2 + 3\lambda_3, \tag{5.3}$$

where λ_1, λ_2, and λ_3 are the mean longitudes of YZ Ceti b, c, and d. This result is in agreement with a purely theoretical result by Pichierri et al. (2019) based on the measured period ratios

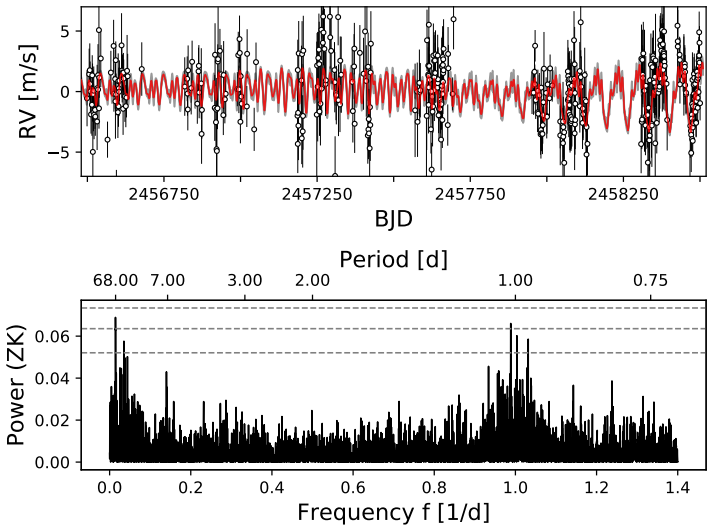


Fig. 5.10.: Median GP model and its GLS periodogram based on the stable posterior samples for YZ Ceti. In this plot the three-planet model is not included, and is subtracted from the RV data. We show only the densely sampled region between BJD 2456480 and BJD 2458520. The gray area indicates the interdecile range of the GP model.

between the planets. However, Pichierri et al. (2019) used the period of 1.97 days for YZ Ceti b, which is not favored by our analysis.

A full dynamical analysis using self-consistent *N*-body fits to the RV data of this compact three-planet system is beyond the scope of this paper and will be carried out in a separate study (Stock et al., in prep.), for which the results of this paper will serve as a basis. However, we tested an alternative approach where possible unstable parameter combinations are penalized during the Kepler fit in order to push the fit towards the stable solutions.

Several possibilities for such on-the-fly tests are possible. Since higher eccentricities tend to disturb the planetary system, a smooth cutoff for eccentricities could be implemented. If guided by dynamical simulations, reasonable cutoff values can be obtained. The mutual distances of the planets in units of their Hill radii are an alternative. Again, minimum Hill radii separations could be inferred from dynamical calculations, but on a more general level; however, both approaches are ad hoc, and the choice of cutoff values will restrict the parameter distribution.

The third approach is therefore to use the angular momentum deficit (AMD) and the Hill stability formulated using the AMD to assess dynamical stability. In a series of papers, Laskar (1997, 2000), Laskar & Petit (2017), and Petit et al. (2018) developed an easy-to-use formulation for AMD stability. In short, AMD is the sum of planetary eccentricities and mutual inclinations

Tab. 5.8.: Derived planetary parameters obtained for YZ Ceti b, c, and d.

Parameter[(a)]	YZ Ceti b	YZ Ceti c	YZ Ceti d
$M_p \sin i$ ($M_\oplus$)	$0.70^{+0.09}_{-0.08}$	$1.14^{+0.11}_{-0.10}$	$1.09^{+0.12}_{-0.12}$
a_p (10^{-2} au)	$1.634^{+0.035}_{-0.041}$	$2.156^{+0.046}_{-0.054}$	$2.851^{+0.061}_{-0.071}$
T_{eq} (K)[b]	$471.2^{+2.2}_{-2.1}$	$410.3^{+2.0}_{-1.9}$	$356.7^{+1.7}_{-1.6}$
S ($S_\oplus$)	$8.21^{+0.16}_{-0.15}$	$4.72^{+0.09}_{-0.09}$	$2.70^{+0.05}_{-0.05}$

[(a)] Error bars denote the 68% posterior credibility intervals. [(b)] Equilibrium temperatures estimated assuming zero Bond albedo.
Derivation using the stable posterior samples and taking the stellar parameter uncertainties (e.g., Gaussian uncertainty) into account.

weighted by planetary mass and orbital separation. Since this quantity is conserved it allows us to evaluate close possible encounters in the planetary system. In the last paper, Petit et al. (2018) derived a formulation of the Hill stability using AMD and compared it numerical N-body simulations. We implemented this AMD–Hill stability and used it to penalize unstable parameter combinations during an MCMC fitting procedure. As expected, the AMD–Hill stability criterion inhibits solutions with eccentricities that are too high. For YZ Ceti b and d, we find a flat distribution of eccentricities up to about 0.15 and 0.12, respectively, with a steep drop above these values. YZ Ceti c has a distribution that decreases continuously from 0 to 0.14. In Fig. 5.11 the eccentricities are selected from the full corner plot to show the posterior distributions for those parameters. Overall, the results from the AMD–Hill stability approach are consistent with our results from the stability analysis based on the posterior samples, indicating that the eccentricities of the planets must be lower than derived from a simple Keplerian three-planet fit to the data without modeling the activity.

5.6 Discussion and conclusions

Using additional 229 RV measurements of YZ Ceti compared to the discovery study (Astudillo-Defru et al. 2017), we constrained the true planetary configuration and resolved the aliases discussed in the literature (e.g., Robertson 2018). We achieved this by using the `AliasFinder` which uses a slightly modified version of the method suggested by Dawson & Fabrycky (2010)

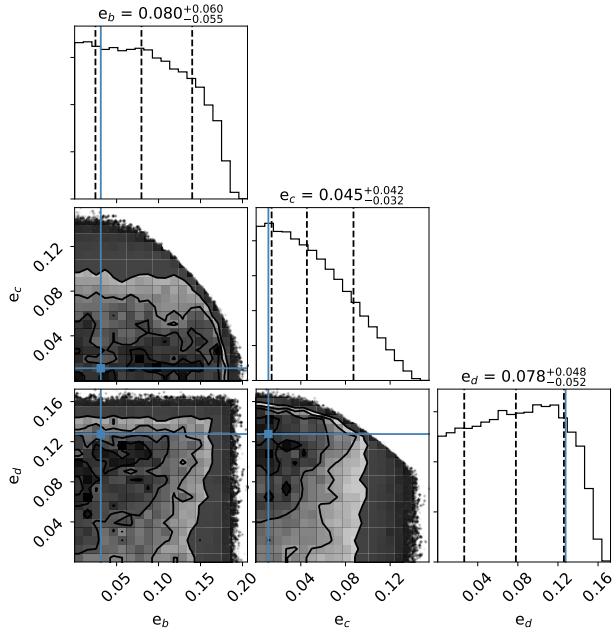


Fig. 5.11.: Selection from the corner plot showing the posterior distributions of the eccentricities from the AMD–Hill stability run. The blue line indicates the best fit. The vertical dashed lines denote the 68% posterior credibility intervals and the median.

to disentangle aliases. The results from the `AliasFinder` analysis were in agreement with an analysis regarding the comparison of the maximum log-likelihood within the posterior samples of different three-planet model realizations. The most likely planetary configuration determined from our data and both analyses was a system of three planets at periods of 2.02 d, 3.06 d, and 4.66 d, which differs from previously published configurations for this system. The new configuration results in an almost optimal 3:2 commensurability of the periods of neighboring planets. We found no statistically significant evidence for an additional fourth companion orbiting YZ Ceti even though we analyzed more than two times the number of RV measurements than did Astudillo-Defru et al. (2017). In particular, we found no sign of the tentative signal at 1.04 d, in contrast to the discovery study. However, we did observe variations in the RV data with a period around 68 d caused by the stellar rotation. In contrast to the discovery study, which adopted a stellar rotation period of 83 d, we found values of the rotation period of 68.4 ± 0.05 d and 68.5 ± 1.0 d based on combined *V*- and *R*-band photometric follow-up with a number of instruments, respectively.

YZ Ceti is an example of a relatively old star with a long rotational period quite distinct from the exoplanet periods, where the activity strongly influences the determination of the planetary

parameters from the RV model. Due to precise photometry, we were able to link an apparent period in the RV residuals of a circular three-planet Keplerian fit to the rotational period of the star. After modeling the stellar rotational signal with a quasi-periodic Gaussian process, we derived a lower eccentricity for the innermost planet than without modeling activity at all. This result is also more consistent with stability constraints that apply to this compact system. We found very good agreement between the photometric rotation period and the rotation period derived by the GP solely from the RV data. We observed only a small region where the quasi-periodic GP allowed low values for the inverse-lengthscale α, consistent with a rather stable periodic signal. This small region was consistent with the estimates of the stellar rotation period from photometry.

Interestingly, a harmonic of the orbital period of YZ Ceti b, which is related to the eccentricity, is very close to an alias of the rotation period. Thus, incorrectly modeled stellar activity RV modulations can cause deviations from a sinusoid in the reflex RV curve of YZ Ceti b. The Keplerian fit to YZ Ceti b accommodates this by fitting an eccentric orbit. This may explain the surprisingly strong influence of the modeling of the rotational variations on the derived eccentricity of YZ Ceti b.

We searched for transits using *TESS* light curves. From their non-detection we derived an upper limit to the inclination of the system of $i_{\mathrm{max}} = 87.43\,\mathrm{deg}$. Applying the criterion of long-term stability, we were able to reduce the uncertainties of the planetary parameters. We also determined a weak lower limit for the inclination of the planets, which is $i_{\mathrm{min}} = 0.9\,\mathrm{deg}$. Additionally, we noted that for 22% of the stable orbital integrations the three-body resonance angle librates, so it is possible that a resonant chain was established during the formation of the ultra-compact YZ Ceti system. Overall, the detailed analysis outlined within this work shows how different novel techniques can help to constrain the architecture of systems hosted by active stars.

6 Three temperate to warm super-Earths

> *Equipped with his five senses, man explores the universe around him and calls the adventure Science.*
>
> — **Edwin Hubble**
> (1889-1953)

Details of authorship: *The content and text passages of this chapter are almost entirely based on already published work in Stock et al. (2020c). The manuscript, as well as all major scientific work, calculations and conclusions contained therein, have been prepared by me. Before submission and during the review process I included suggestions and corrections by the co-authors and reviewer. The text has been slightly adjusted and extended at some parts to make this work more consistent with the rest of this thesis. Additionally, for this thesis I have slightly adjusted the format of figures and tables to better suit the one column style. The appendix of this work has been shifted to the appendix of this thesis.*

6.1 Motivation

More than 4200 exoplanets have been confirmed so far[1]. A significant fraction have been discovered with the radial velocity (RV) method. In the past decades, the development of new high-precision spectrographs allowed probing a large variety of planets with minimum masses of several Jupiter masses down to only 0.7 $M_\oplus$ for YZ Cet b, which is the least massive planet detected so far with the RV technique (Astudillo-Defru et al. 2017; Stock et al. 2020b). One such high-precision spectrograph is the CARMENES instrument (Quirrenbach et al. 2014, 2018), which is used to conduct a survey for detecting exoplanets around M dwarfs, which are the most abundant stars of our Galaxy (Kroupa 2001; Chabrier 2003; Henry et al. 2006). The detection of the large number of exoplanets has resulted in the discovery of exotic new types of planets that

[1] http://exoplanet.eu/catalog/ (25 May 2020)

have no counterpart in our own Solar System, such as super-Earths (M = 1.9–10 $M_\oplus$; Rivera et al. 2005; Valencia et al. 2007; Charbonneau et al. 2009). These super-Earths are abundant around M dwarfs (Dressing & Charbonneau 2015).

The detection of planets close to or inside the habitable zones (HZ, see Kasting et al. 1993; Kopparapu et al. 2013) of their parent stars is of particular interest. With the current technology, M dwarfs are ideal targets for detecting such temperate planets because the HZ of these stars corresponds to a relatively small orbital radius. The lower host star masses result in a higher Doppler amplitude (higher by a few $m\,s^{-1}$) than those of more massive stars, which can be measured by current techniques. However, M dwarfs tend to be very active (Johns-Krull & Valenti 1996; Delfosse et al. 1998; Mohanty & Basri 2003; Reiners et al. 2012). The activity can make the detection of small planets difficult by inducing distortions in the shape of the spectral line profiles; this mimicks a planetary signal (Queloz et al. 2001a; Desort et al. 2007; Barnes et al. 2011; Robertson et al. 2014, 2015).

Various methods can be used to distinguish stellar astrophysical signals from planet-induced signals. Photometric observations, ideally contemporaneous with the RV observations, as well as different spectral activity indicators can be used to derive more information on the stellar rotation period and activity-induced RV variations. In addition, many novel techniques have been developed to analyze the coherence of a signal, for example, Bayesian-stacked periodograms (Mortier et al. 2015; Mortier & Collier Cameron 2017), growth of the Lomb-Scargle power, or the evolution of the significance (Hatzes 2013; Ribas et al. 2018; Reichert et al. 2019). These tools can provide strong indications that a signal has a nonplanetary origin because an RV signal caused by Keplerian motion should be coherent and long-lived. When both planetary signals and activity contribute significantly to the RV variations, it can be necessary to simultaneously fit for these signals using Gaussian process (GP) regression (Rajpaul et al. 2015) or similar models, such as sinusoids (Boisse et al. 2011; Dumusque et al. 2012). Modeling the stellar activity simultaneously with the Keplerian fit is essential because this contamination can have a significant effect on the derived planetary parameters (see, e.g, Stock et al. 2020b).

In the following, we present a detailed analysis of photometric and spectroscopic data of GJ 251, HD 238090, and Lalande 21185. For GJ 251, Butler et al. (2017) reported a possible planet candidate at a period of 1.74 d, but with the more precise CARMENES data, we cannot confirm this claim. Lalande 21185 is the brightest M dwarf in the northern hemisphere, the fourth closest main-sequence star system after α Centauri, Barnard's star, and CN Leo, and the third closest planetary system. Lalande 21185 has a remarkable history regarding former planet claims. Those by van de Kamp & Lippincott (1951) and Gatewood (1996) were based on astrometric data, but have never been confirmed independently. Later, Butler et al. (2017) reported that Lalande 21185

Tab. 6.1.: Number and quality of the RV observations.

Instr.	$\mathrm{Obs_{start}}$ mm/yyyy	$\mathrm{Obs_{end}}$ mm/yyyy	$N_{\mathrm{obs.}}$	σ_{RV} [m s^{-1}]	rms [m s^{-1}]
		GJ 251			
CARM.	01/2016	01/2020	212	1.27	3.69
HIRES	10/1997	11/2013	75	2.13	4.63
		HD 238090			
CARM.	01/2016	04/2019	108	1.67	3.28
		Lalande 21185			
CARM.	01/2016	01/2020	321	1.40	4.38
HIRES	06/1997	07/2014	261	1.38	4.63
SOPHIE	10/2011	06/2018	155	1.32	2.54

has a planet candidate with an orbital period of 9.87 d. A recent study by Díaz et al. (2019) was unable to provide evidence for these previous planet claims. However, Díaz et al. (2019) announced the discovery of a super-Earth planet orbiting Lalande 21185 with a period of 12.93 d. The analysis of our CARMENES data agrees with the findings from Díaz et al. (2019) and confirms a single planet orbiting Lalande 21185. HD 238090 has no reported planet to date.

In Sec. 6.2 and Sec. 6.3 we describe the data, instruments, and methods we used within this study, while in Sec. 6.4 we compile the basic stellar properties of GJ 251, HD 238090, and Lalande 21185. We then analyze our photometric and RV data for the three stars in Sec. 6.5, Sec. 6.6, and Sec. 6.7, and provide a star-by-star discussion in Sec. 6.8 and a general summary in Sec. 6.9.

6.2 Data

6.2.1 High-resolution spectroscopy

CARMENES. GJ 251, HD 238090, and Lalande 21185 were observed as part of our CARMENES[2] guaranteed-time observation program (GTO) to search for exoplanets around M dwarfs (Reiners et al. 2018a). CARMENES is a double-channel échelle spectrograph installed at the 3.5 m telescope of the Calar Alto Observatory in Almería, Spain. Details regarding the instrument and its performance are given in Quirrenbach et al. (2014, 2018), Reiners et al. (2018a), and

[2] http://carmenes.caha.es

Trifonov et al. (2018). The data were processed with the standard pipelines and were reduced with `caracal` (Caballero et al. 2016b). The RVs obtained with `serval` (Zechmeister et al. 2018) were corrected for barycentric motion, secular perspective acceleration, instrumental drift, and nightly zero-point variations (Trifonov et al. 2018; Tal-Or et al. 2019; Trifonov et al. 2020). Table 6.1 shows a summary of the CARMENES visual arm (VIS) RVs and their overall quality. The median exposure times in the VIS channel were 509 s, 1000 s, and 95 s, resulting in a median signal-to-noise (S/N) of 116, 154, and 132 for GJ 251, HD 238090, and Lalande 21185, respectively.

In the CARMENES near-infrared (NIR) data, the scatter was not sufficiently small for the RV analysis of the planetary signals in this work; it was on the order of a few m s^{-1} (see Bauer et al. 2020, for a detailed analysis of the performance of CARMENES). The RV time series and their uncertainties for the CARMENES VIS data of GJ 251, HD 238090, and Lalande 21185 are listed in Tables D.1–D.3 together with some activity indicators[3].

HIRES. The High Resolution Echelle Spectrometer (HIRES; Vogt et al. 1994) is installed at the Keck I telescope in Hawai'i, USA. HIRES uses the iodine cell technique (Butler et al. 1996) to obtain RV measurements with a typical precision of a few m s^{-1}. We used archival HIRES data for GJ 251 and Lalande 21185 to confirm the planetary signals and to extend the time baseline, and to search for long-period signals. For our analysis, we used the HIRES data corrected by Tal-Or et al. (2019), which account for nightly zero-point offsets and an instrumental jump in 2004, which is an improvement over the original data reduction by Butler et al. (2017). Details on the quality of the data are given in Table 6.1. The median exposure times for GJ 251 and Lalande 21185 were 500 s and 135 s, respectively.

SOPHIE. We also used RV data for Lalande 21185 obtained with the SOPHIE instrument (Perruchot et al. 2008). These data were made public by Díaz et al. (2019), and further information on the acquisition and properties of these data is provided in their study. We show a summary of the quality of the RV data in Table 6.1.

[3]Tables D.1–D.3 are only available at the CDS via anonymous ftp to `cdsarc.u-strasbg.fr` (`130.79.128.5`) or via `http://cdsarc.u-strasbg.fr/viz-bin/cat/J/A+A/643/A112`

6.2.2 Photometry

We carried out a contemporaneous photometric follow-up of GJ 251 and HD 238090 during 2018 and 2019. We also compiled photometric data publicly available as described below.

T90. We monitored GJ 251 and HD 238090 in the Johnson V and R bands with the T90 telescope at the Observatorio de Sierra Nevada (OSN) in Granada, Spain. The T90 telescope is a 90 cm Ritchie-Chrétien telescope equipped with a $2k \times 2k$ pixel VersArray CCD camera, with a field of view of 13.2×13.2 arcmin^2 (Rodríguez et al. 2010). The observations of GJ 251 and HD 238090 were carried out on 42 nights from October 2018 to February 2019 and on 53 nights from February 2019 to July 2019, respectively. The typical number of exposures per night and target was around 35. We did not apply any binning, corrected each CCD frame in a standard way for bias and flat-fielding with IRAF, and selected the best aperture sizes and reference stars for the synthetic aperture photometry. In particular, we used the same aperture size as in Perger et al. (2019).

TJO. Observations of GJ 251 and HD 238090 with the 80 cm Telescopi Joan Oró (TJO) at Observatori Astronòmic del Montsec in Lleida, Spain, were conducted using a Johnson R filter and its main imaging camera LAIA, a $4k \times 4k$ back-illuminated CCD with a pixel scale of 0.4 arcsec and a field of view of 30×30 arcmin^2. The TJO data for GJ 251 were collected between February and November 2019 during 157 nights and for HD 238090 between February and November 2019 during 149 nights. We obtained several batches of five images per night. The images were calibrated with darks, bias, and flat fields with the `icat` pipeline (Colome & Ribas 2006). Differential photometry was extracted with `AstroImageJ` (Collins et al. 2017) using the aperture size and the set of comparison stars that minimized the root mean square (rms) of the photometry. Data with low S/N due to bad weather conditions or high airmass were removed. For GJ 251, we removed 392 low S/N measurements from the initial 2746 data points and for GJ458A, we removed 477 from the initial dataset of 6207 measurements. These correspond to the measurements for which the S/N of the target is below 30% of the best measurement. The resulting light curves were binned to one data point per hour.

LCO. We observed GJ 251 on 44 epochs using the 40 cm telescopes of Las Cumbres Observatory (LCO) in the V band at the Teide, Haleakalā, and McDonald observatories between 13 January and 3 March 2019. The telescopes are equipped with a $3k \times 2k$ SBIG CCD camera with a pixel scale of 0.571 arcsec, providing a field of view of 29.2×19.5 arcmin^2. We acquired 50 individual

exposures of 30 s per epoch. Weather conditions were mostly clear, and the average seeing varied from 1.5 arcsec to 3.0 arcsec. Raw data were processed using the `banzai` pipeline (McCully et al. 2018)[4], which includes bad pixel, bias, dark, and flat-field corrections for each individual night. We performed aperture photometry for GJ 251 and three reference stars in the field and obtained the relative differential photometry. We adopted an aperture of 13 pixels (7.4 arcsec), which minimized the dispersion of the differential light curve.

TESS. The Transiting Exoplanet Survey Satellite (*TESS*) is a space-borne instrument that searches for transiting planets around nearby stars (Ricker et al. 2015). The primary mission goal consists of observations of 26 sectors with 24×96 deg^2 in the northern and southern hemisphere, which are still ongoing. Each sector is observed for about 28 d. We obtained for all three targets of this work the pre-search data conditioning simple aperture photometry (PDCSAP) light curves. These are provided by the Science Processing Operations Center (SPOC; Jenkins et al. 2016) at the Mikulski Archive for Space Telescopes (MAST)[5].

MEarth. We used data of HD 238090 from the seventh data release (DR7[6]) of the MEarth project (Berta et al. 2012). The MEarth project is an all-sky transit survey that has been conducted since 2008. It consists of 16 robotic 40 cm telescopes, 8 located in the Northern Hemisphere at the Fred Lawrence Whipple Observatory in Arizona, USA, and the other 8 in the Southern Hemisphere located at Cerro Tololo Inter-American Observatory, Chile. The project monitors several thousand nearby mid- and late-M dwarfs over the whole sky. Each telescope is equipped with a 2k×2k CCD that provides a field of view of 26×26 arcmin^2. MEarth uses an *RG*715[7] long-pass filter, except for the 2010–2011 season, when an $I_{715-895}$ interference filter was chosen.

NSVS. The Northern Sky Variability Survey (Woźniak et al. 2004, NSVS) was a robotic survey that primarily targeted the northern sky with telephoto lenses located at the Los Álamos National Laboratory in New Mexico, USA. The survey provided data for 14 million objects in the magnitude range between 8 mag to 15.5 mag. For details on the instrumental setup and the conducted observations, we refer to the survey paper (Woźniak et al. 2004). We used public NSVS data for HD 238090, which we obtained from their public webpage[8].

[4] https://banzai.readthedocs.io/en/latest/
[5] https://mast.stsci.edu/portal/Mashup/Clients/Mast/Portal.html
[6] https://www.cfa.harvard.edu/MEarth/DataDR7.html
[7] https://www.pgo-online.com/intl/curves/optical_glassfilters/RG715_RG9_RG780_RG830_850.html
[8] https://skydot.lanl.gov/nsvs/nsvs.php

SuperWASP. For GJ 251 we used public data processed and collected by the Wide Angle Search for Planets (WASP) survey (Pollacco et al. 2006)[9], in particular SuperWASP-North at the Observatorio del Roque de los Muchachos in La Palma, Spain. SuperWASP-North consisted of one wide-field array of eight cameras, each with a 200 mm, f/1.8 lens, a broadband filter spanning the wavelength range between 400 nm and 700 nm, and a 2k × 2k CCD. The resulting plate scale was 13.7 arcsec pixel^{-1}.

6.3 Methods

6.3.1 Periodograms

We used generalized Lomb-Scargle (GLS) periodograms (Zechmeister & Kürster 2009) to assess significant periodicities in the photometric and spectroscopic data. We applied the normalization as given in Zechmeister & Kürster (2009), which is abbreviated as P_{ZK} throughout this work. For each periodogram, we computed false-alarm probabilities (FAPs) by applying bootstrapping with $n = 10\,000$ iterations. Our detection threshold for a signal deemed to be significant was at an FAP < 0.001. The uncertainties on the periods of significant GLS signals were estimated from the local χ^2 curvature by the GLS routine.

To assess the coherence of a periodic signal over the observation time, we used the stacked-Bayesian GLS periodogram (s-BGLS; Mortier et al. 2015; Mortier & Collier Cameron 2017). The Bayesian GLS periodogram allows the comparison of probabilities of periodic signals in the data, while the stacking examines the coherence of the signal with an increasing number of observations. As in Mortier & Collier Cameron (2017), we normalized all s-BGLS periodograms to their respective minimum values, which means that the probability of each signal and its growth or decrease over time is a relative measure compared to the lowest probability obtained within one calculated s-BGLS over a specific period range.

6.3.2 Modeling of RV and photometric data

For the modeling, we used `juliet` (Espinoza et al. 2019), which allows the fitting of photometric and RV data by searching for the global posterior maximum based on the evaluation of the Bayesian log-evidence ($\ln \mathcal{Z}$) within a provided prior volume of the fitting parameters. `juliet`

[9] https://wasp.cerit-sc.cz

Tab. 6.2.: Stellar parameters of HD 238090, GJ 251, and Lalande 21185.

Parameter	GJ 251	HD 238090	Lalande 21185	Ref.
		Identifiers		
Gliese-Jahreiß	GJ 251	GJ 458 A	GJ 411	Gli79
Karmn	J06548+332	J12123+544S	J11033+359	Cab16
		Coordinates and spectral type		
Epoch	J2015.5	J2015.5	J2000.0	GDR2 / GDR2 / vLe07
α	06 54 48.06	12 12 21.27	11 03 20.19	GDR2 / GDR2 / vLe07
δ	+33 15 59.3	+54 29 10.2	+35 58 11.6	GDR2 / GDR2 / vLe07
Sp. type	M3.0 V	M0.0 V	M1.5 V	Alo15 / PMSU / Alo15
G [mag]	8.8552 ± 0.0011	9.0379 ± 0.0005	...	GDR2
J [mag]	6.10 ± 0.02	6.88 ± 0.02	4.20 ± 0.24	2MASS
		Parallax and kinematics		
$\mu_\alpha \cos\delta$ [mas/yr]	−726.39 ± 0.13	+232.38 ± 0.04	−580.27 ± 0.62	GDR2 / GDR2 / vLe07
μ_δ [mas/yr]	−398.13 ± 0.12	+92.09 ± 0.04	−4765.85 ± 0.64	GDR2 / GDR2 / vLe07
π [mas]	179.16 ± 0.06	65.61 ± 0.03	392.64 ± 0.67	GDR2 / GDR2 / vLe07
d [pc]	5.581 ± 0.002	15.24 ± 0.01	2.547 ± 0.004	GDR2 / GDR2 / vLe07
γ [km/s]	22.654 ± 0.025	−17.668 ± 0.018	−85.016 ± 0.023	Laf19
U [km/s]	−27.41 ± 0.02	18.08 ± 0.01	46.29 ± 0.03	TW
V [km/s]	−3.67 ± 0.01	7.41 ± 0.01	−53.68 ± 0.09	TW
W [km/s]	−15.13 ± 0.01	−16.01 ± 0.02	−74.59 ± 0.02	TW
		Photospheric parameters		
$T_{\rm eff}$ [K]	3451 ± 51	3933 ± 51	3601 ± 51	Sch19
$\log g$ [dex]	4.96 ± 0.07	4.70 ± 0.07	4.87 ± 0.07	Sch19
[Fe/H] [dex]	−0.03 ± 0.16	−0.03 ± 0.16	−0.09 ± 0.16	Sch19
		Physical parameters		
L [$L_\odot$]	0.0169 ± 0.0003	0.0702 ± 0.0015	0.0195 ± 0.0013	Sch19
R [$R_\odot$]	0.364 ± 0.011	0.570 ± 0.016	0.392 ± 0.004	Sch19 / Sch19 / Boy12
M [$M_\odot$]	0.360 ± 0.015	0.578 ± 0.021	0.390 ± 0.011	Sch19 / Sch19 / TW
		Activity parameters		
pEW (Hα) [Å]	0.00 ± 0.01	+0.04 ± 0.01	−0.04 ± 0.01	Schf19
$v \sin i$ [km/s]	< 2	< 2	< 2	Rei18
$P_{\rm rot}$ [d]	$122.1^{+1.9}_{-2.2}$	$96.7^{+3.7}_{-3.2}$	56.15 ± 0.27	TW / TW / Dia19

TW: This work 2MASS: Skrutskie et al. (2006); Alo15: Alonso-Floriano et al. (2015); Cab16: Caballero et al. (2016a); Gli79: Gliese & Jahreiß (1979); GDR2: Gaia Collaboration et al. (2018); PMSU: Hawley et al. (1996); Sch19: Schweitzer et al. (2019); vLe07: van Leeuwen (2007); Boy12: Boyajian et al. (2012); Dia19: Díaz et al. (2019); Schf19: Schöfer et al. (2019); Laf19: Lafarga et al. (2020).

allows us to statistically compare models with different numbers of parameters within a Bayesian framework through the log-evidence, which includes the model complexity and the number of degrees of freedom within its assessment. Following Trotta (2008), a model is considered as a significant improvement if $\Delta \ln \mathcal{Z} > 5$. The `juliet` calculation of the log-evidence is conducted with nested sampling algorithms. In particular, we used the dynamic nested sampling algorithm `dynesty` (Speagle 2020).

We used `radvel` (Fulton et al. 2018) to model Keplerian RV signals, and `george` (Ambikasaran et al. 2015) for GP modeling of both photometric and RV data. In all cases, we used an exp-sin-squared kernel multiplied with a squared-exponential kernel, which is included as a default kernel within `juliet`. This kernel, also known as the quasi-periodic (QP) kernel, has the form

$$k(\tau) = \sigma_{\mathrm{GP}}^2 \exp\left(-\alpha_{\mathrm{GP}}\tau^2 - \Gamma \sin^2\left(\pi\tau/P_{\mathrm{rot}}\right)\right), \tag{6.1}$$

where σ_{GP} is the amplitude of the GP component given in parts per million (ppm) for photometric data or m s^{-1} for RV data, Γ is the amplitude of the GP sine-squared component and is dimensionless, α is the inverse length-scale of the GP exponential component given in d^{-2}, P_{rot} the period of the GP QP component given in d, and τ is the time lag. This choice of kernel represents one part of our prior knowledge, as it provides the framework of how an effective model of stellar activity should fit the data. The timescale P_{dec}[10] in days of the exponential decay can be approximated with

$$P_{\mathrm{dec}} = (2\alpha_{\mathrm{GP}})^{-1/2}. \tag{6.2}$$

The α_{GP} parameter is of particular interest with regard to the stability of a QP signal. A smaller α describes a more stable periodic signal in which data points are more strongly correlated with each other. For a review and a detailed description of each kernel hyperparameter and a possible physical interpretation, we refer to Angus et al. (2018).

The evaluation of the GP likelihood with `george` is computationally expensive and scales as $N \ln N$, where N is the number of data points (Ambikasaran et al. 2015). For the derivation of the stellar rotation, we searched for periods on timescales of days. To do this, it is reasonable to create nightly bins of the photometric data. This reduces the computation time of the GP log-likelihood evaluation and short-term variations based on the jitter of the star.

[10]The factor two is not included within `juliet`, see footnote 1 in Sec. 3.5.2. This circumstance has been confirmed via private communication with first author Nestor Espinoza. I have been unaware of this bug within the public code when this chapter has been produced. Fortunately, this does not significantly affect the results of this work. An error of $1/\sqrt{2}$ is introduced for transformation of the inverse length scale α to the decay timescale in days which has been done as an order of magnitude approximation of typical spot life times a few times within the text.

For the photometric analysis, we applied distinct GP hyperparameters for the amplitudes σ_{GP} and Γ, to account for the effect that stellar activity depends on wavelength, but we used global GP hyperparameters for the timescale of the amplitude modulation and the rotation period. In addition, we fit an offset and a jitter term (in quadrature to the diagonal of the resulting covariance matrix of the GP) for each data set. Table B.1 shows the priors of the photometric GP analysis.

For the final RV analysis, we applied global GP hyperparameters. A statistical comparison with models using distinct GP hyperparameters for each RV instrument did not show any significant improvement in log-evidence. For each data set, we fit an offset and a jitter term. Our priors for the RV GP analysis are provided in Table B.3.

6.3.3 De-aliasing

Aliases are spurious signals caused by the sampling of the data, which are often indistinguishable from the true signal. The significance of a signal or the goodness of a fit is not a sufficient criterion to differentiate between true signals and alias signals, especially in cases of non-optimal sampling, where the results of these metrics can be similar. For example, it is a common misconception that peaks close to one day are always alias frequencies, but a priori, it is not clear which of the peaks represents the true frequency of the signal and which represents the alias (Dawson & Fabrycky 2010). Alias frequencies can be calculated by $f_a = f_t \pm m f_s$, where f_t is the assumed true frequency, f_s the sampling frequency, and f_a the alias frequency. Because RV measurements are usually taken with a rather irregular sampling (Garcia-Piquer et al. 2017), more than one sampling frequency is often apparent in the window function of the data. This results in several peaks at alias frequencies related to the different sampling frequencies, and can make it even harder to distinguish the true underlying signal.

We used the `AliasFinder` (Stock & Kemmer 2020)[11] to confirm that the assumed planetary signal is the true signal and not an alias. The method on which the `AliasFinder` is based is described in Dawson & Fabrycky (2010), Stock & Kemmer (2020), and Stock et al. (2020b). For each frequency under consideration, `AliasFinder` simulates 1000 data sets based on the true sampling of the observed data and inserts one sinusoidal signal with one of the frequencies. `AliasFinder` also includes a noise contribution based on the RV jitter of the star, which we made use of for our analyses in this paper. We compared the resulting ensemble periodograms for each simulated frequency to the periodogram obtained from the observed data. Peak position, power, and phase are the parameters compared in this test. If the ensemble of the periodograms of one

[11] https://github.com/JonasKemmer/AliasFinder

simulated frequency reproduces the data periodogram significantly better than the periodograms of the other simulated frequencies, then the most probable planetary period has successfully been identified.

6.4 Stellar properties

Photospheric parameters, such as effective temperature, surface gravity, and metallicity, were determined by Schweitzer et al. (2019) by fitting an updated set of PHOENIX-ACES atmosphere models (Husser et al. 2013) to high-resolution CARMENES spectra. These updated PHOENIX models incorporated the latest solar abundances, molecular and atomic line lists, and a new equation of state (Meyer 2017), which were especially designed to treat low-temperature stellar atmospheres. The parameters were determined assuming a rotational velocity of $v \sin i = 2\,\mathrm{km\,s^{-1}}$ (Reiners et al. 2018c). To reduce degeneracies between the parameters, Schweitzer et al. (2019) constrained the surface gravity $\log g$ with the help of evolutionary models (PARSEC, Bressan et al. 2012; Chen et al. 2014, 2015; Tang et al. 2014) and stellar ages estimated by Passegger et al. (2019). The actual ages of the three investigated stars are probably older than tabulated, as derived from a new kinematics analysis (Cortés-Contreras et al., in prep.). The galactocentric space velocities in Table 6.2 were calculated from the latest *Hipparcos* and *Gaia* DR2 proper motions and parallaxes (van Leeuwen 2007; Gaia Collaboration et al. 2018) and absolute RVs of Lafarga et al. (2020), following the approach of Montes et al. (2001) and Cortés-Contreras (2016).

Physical parameters, such as luminosity, radius, and mass, were derived by Schweitzer et al. (2019). Cifuentes et al. (2020) exhaustively described the luminosity determination in M dwarfs. The radius (and hence mass) for Lalande 21185 was an outlier in Schweitzer et al. (2019) because the photometry for this star was of low quality, suggesting an uncertain and too low luminosity. They derived a stellar radius and mass of $0.3587 \pm 0.0157\,\mathrm{R_\odot}$ and $0.355 \pm 0.019\,\mathrm{M_\odot}$, respectively. We therefore used a slightly different approach to derive the mass and radius. We used its radius $0.3921 \pm 0.0037\,\mathrm{R_\odot}$, which was derived by Boyajian et al. (2012) using the interferometric angular diameter. Applying the same empirical mass-radius relationship as was used for the other two targets, we derived a stellar mass of $0.390 \pm 0.011\,\mathrm{M_\odot}$, which agrees better with the typical parameters of the ensemble. The detailed stellar parameters of all three stars and their references are given in Table 6.2.

The M0.0 V star HD 238090 is the primary component of a wide binary. The secondary component is the M3.0 V star GJ 458 B, with a stellar mass of $0.230 \pm 0.005\,\mathrm{M_\odot}$. The angular separation

of the two components of 14.68 ± 0.44 arcsec (Cortés-Contreras 2016) results in a projected separation of approximately 224 au. We computed the stellar mass of the secondary component using the mass-luminosity-metallicity relation of Mann et al. (2019). Based on the masses and projected minimum separation, we estimated the minimum orbital period of this binary to be longer than 3700 yr. This long binary period agrees with the 34 observations between 1955 and 2015 tabulated in the Washington Double Star Catalog (Mason et al. 2001), which do not indicate any change in the position angle.

6.5 GJ 251

6.5.1 Photometric monitoring

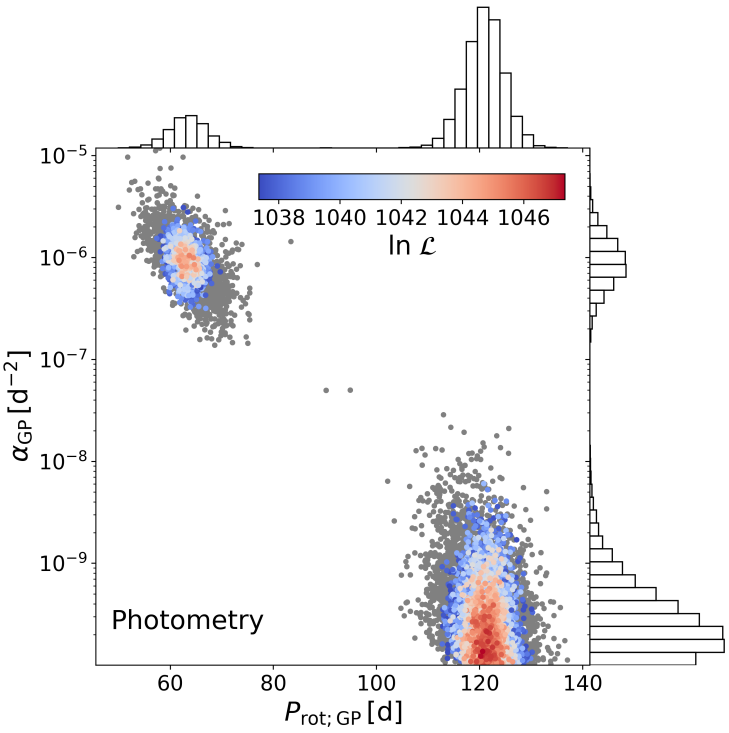


Fig. 6.1.: Posterior distribution in the α_{GP} vs. P_{rot} plane of the GP fit to the combined photometric data of T90, TJO, LCO, and SuperWASP for GJ 251. The color-coding shows the log-likelihood normalized to the highest achieved log-likelihood value within the posterior sample. Gray samples indicate solutions with $\Delta \ln L$ lower than 10.

For a significant fraction of the CARMENES RV observations of GJ 251, we obtained quasi-simultaneous photometry with the T90, TJO, and LCO telescopes. We combined these data with public data from SuperWASP. A joint GLS periodogram analysis, where we fitted for offsets and jitter of each data set, indicated significant signals at periods of 30 d, 70 d, and 120 d. However, a sinusoidal model, as used in the GLS analysis, is an imperfect description of stellar activity, which is often represented better by a QP signal. Therefore we fitted a more sophisticated model to the photometric data in the form of a QP GP to derive the stellar rotation period.

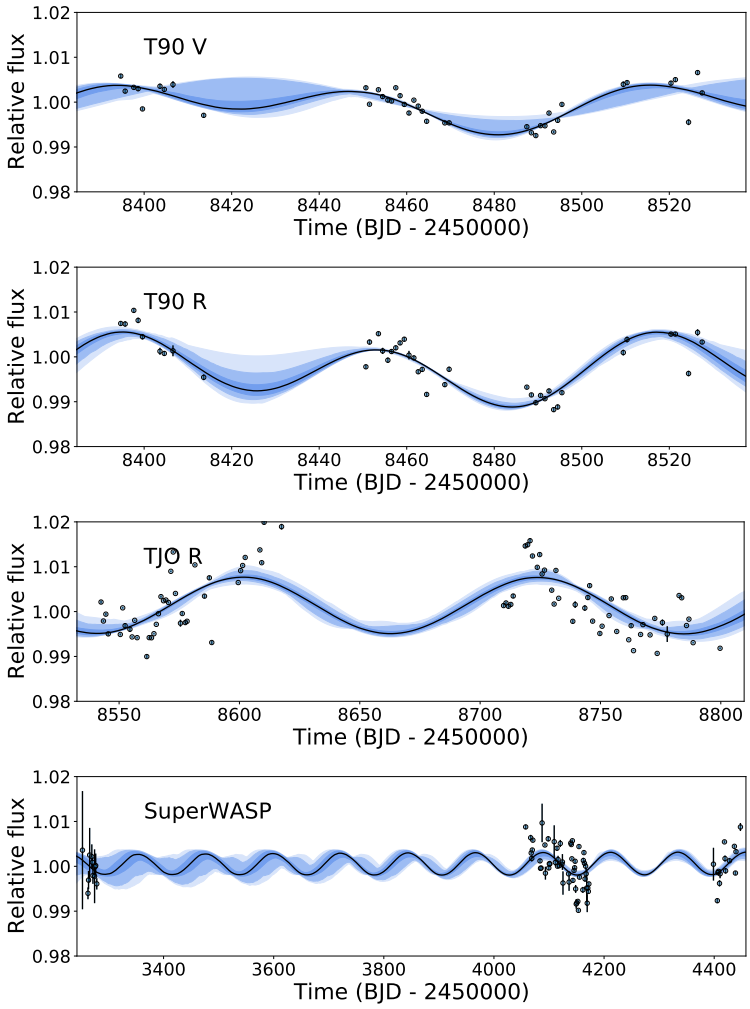


Fig. 6.2.: Joint GP model of the nightly binned photometric data of GJ 251. From top to bottom: T90 *V*, T90 *R*, TJO *R*, and SuperWASP.

Our GP analysis of the photometry of GJ 251 based on our T90, TJO, LCO, and SuperWASP data resulted in a bimodal distribution for the rotational period with posterior solutions around 120 d

and 60 d. We plot the informative GP α-period diagram ($\alpha_{\rm GP}$ versus $P_{\rm GP}$) in Fig. 6.1. This plane of parameters shows the decay-timescale over the rotation period, and it is useful for identifying whether stronger correlated noise (small α) favors a certain periodicity (see also Stock et al. 2020b for a more detailed explanation). Within this plane, we identified that the likelihood and number of posterior samples at 120 d is higher than that of the posterior samples around 60 d. Furthermore, the α values of the 120 d signal converge toward our prior boundary of $10^{-10}\,{\rm d}^{-2}$, representing a decay timescale longer than 70 000 d, which indicates a stable periodic signal over the entire time of observations. We determined the rotational period for each posterior solution and derived $63.5^{+3.7}_{-3.6}$ d and $P_{\rm rot,phot.} = 122.1^{+1.9}_{-2.2}$ d.

The latter we regard formally as the derived rotational period of GJ 251 because on average, its likelihood of posterior samples is higher than the former solution, because of the stronger coherence of the signal, and because the 60 d signal can be explained as the first harmonic of a signal with a fundamental period of about 120 d. A stronger coherence of signals related to stellar activity would be expected for M dwarfs because the spot lifetime increases with decreasing effective temperature (Giles et al. 2017; Shapiro et al. 2020). Additionally, if GJ 251 is a slowly rotating star, which means that it is relatively inactive, there is evidence that faculae, which are in general longer-lived then starspots, are dominant surface features (see Shapiro et al. 2020, and references therein). These long-lived faculae, in particular, affect the photometric variability of the star (Reinhold et al. 2019) and less so the RVs, which are typically spot-dominated. For this reason, among others, the same decay timescales $\alpha_{\rm GP}$ of the rotational signal between RV and photometric data should not be assumed. We show the binned photometric data overplotted with the median GP model and its uncertainties in Fig. 6.2.

Based on our estimate of the stellar rotation period, we used eqs. 1 and 2 from Suárez Mascareño et al. (2018) to estimate $\log(R'_{HK})$ and based on this, the expected RV semi-amplitude of the stellar rotational signal. By propagating all uncertainties of the parameters given by Suárez Mascareño et al. (2018) for M0-M3 stars and our measurement uncertainty of the rotation period (in the form of their actual distributions), we derived for the medians and 1σ uncertainties $\log(R'_{HK}) = -5.79^{+0.53}_{-0.61}$ (mean at -5.83) and $K_{\rm exp.} = 0.68^{+3.71}_{-0.58}\,{\rm m\,s^{-1}}$ (mean at $3.59\,{\rm m\,s^{-1}}$).

6.5.2 Spectroscopic activity indicators

We analyzed a number of spectral activity indicators for GJ 251 obtained from the CARMENES spectra using the indicators provided by `serval`, which includes the chromatic index and the differential line width (CRX and dLW, see Zechmeister et al. 2018). We also investigated the

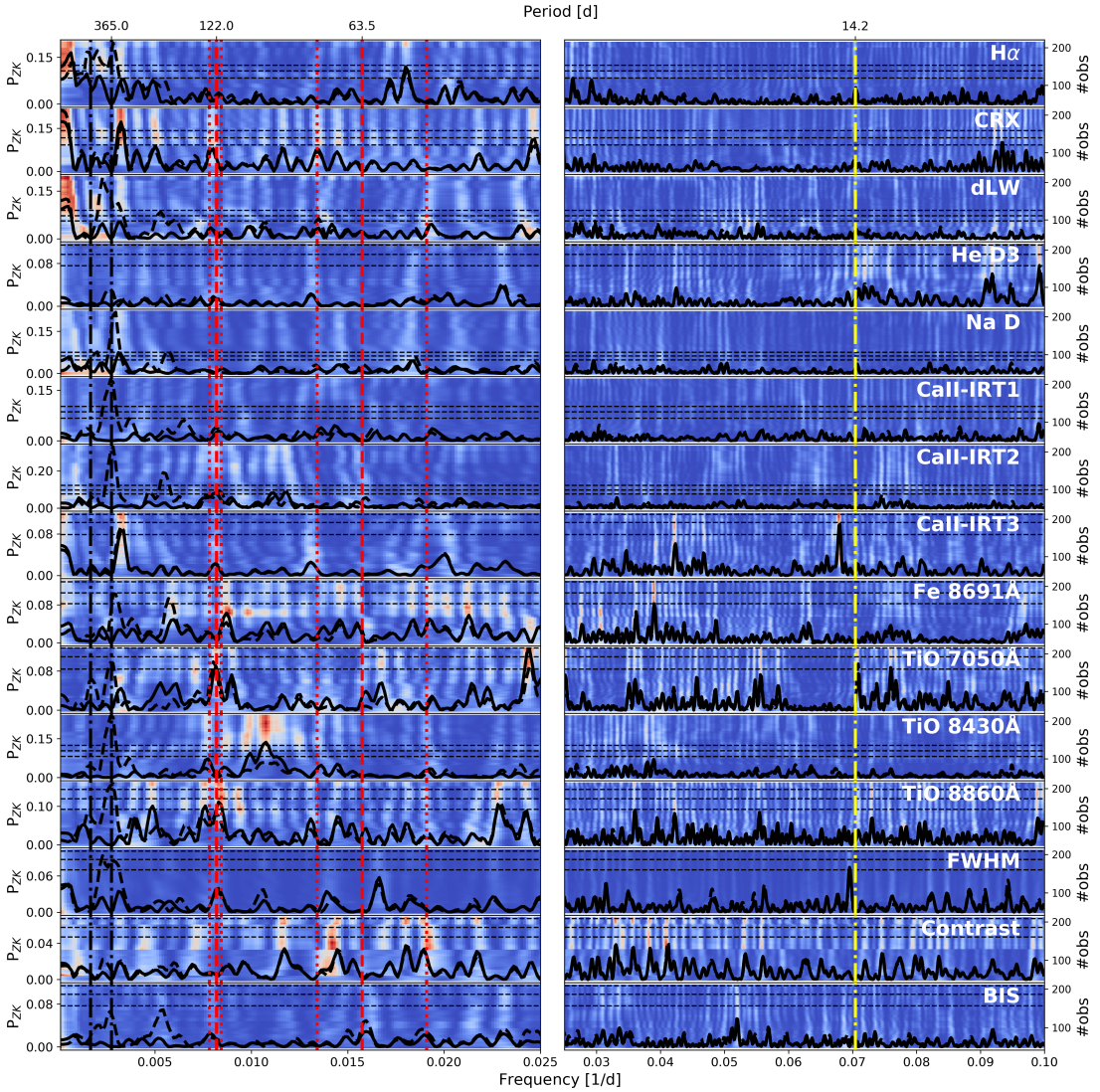


Fig. 6.3.: Generalized Lomb-Scargle periodograms of several activity indicators of GJ 251 from CARMENES spectroscopic data. The dashed black periodograms represent the GLS of the activity indicators, and the solid GLS periodogram represents the residuals after subtracting a 365 d signal. For the residuals from which the 365 d signal was subtracted, we also overplot the s-BGLS periodogram, where the probability increases from blue to white to red. The red dashed lines mark the rotation period and the first harmonic estimated from photometric data, while the dotted red lines show the 3σ uncertainties. The dashed black line marks a significant HIRES signal around 600 d, and the yearly period of 365 d. The dashed yellow line marks the period of the planetary signal published in this work.

cross-correlation function (CCF, see Lafarga et al. 2020; Reiners et al. 2018b) to derive the full width at half maximum (FWHM), contrast (CON), and bisector span (BIS), and we derived a

large number of additional indicators (see Schöfer et al. 2019). We searched for periodicities of all these indicators using the GLS periodogram. Many indicators show significant long-term signals around 365 d, and its 1 d aliases. The occurrence of this period in activity indicators of several other stars of our survey, in particular, of the other two targets discussed in this work, and the fact that it is compatible with one yearly cycle, makes it unlikely that stellar activity is the origin. This periodicity might be caused by small yearly environmental changes on the instrument or micro-tellurics that might affect the spectral line shapes to which the CCF and the measured pEW's are more sensitive than the actual RV measurements.

Because this yearly signal is not believed to be of stellar activity, and most importantly, because is far away from the planetary periods and derived stellar rotational period, we subtracted it so that we would be more sensitive to periods in the high-frequency regime. We show the residual GLS periodogram and its s-BGLS periodogram in Fig. 6.3. We found a signal at 121.0 d that is within the 1σ uncertainty of the photometric rotation period in TiO at 8430 Å with an FAP $< 10^{-2}$. Within the uncertainty of the first harmonic of the rotation period, we observed a peak in Hα with an FAP reaching almost 10^{-3}. From the s-BGLS, the star showed the strongest activity in most indicators at periods attributed to the stellar rotation, whether at 120 d or 60 d, between January 2019 and October 2019 (CARMENES observation numbers 130 to 180).

Recently, signals at approximately 90 d in TiO 8430 Å and around 45 d in TiO 7050 Å have become significant. It is not clear where these signals originate. Recent works, for example, Shapiro et al. (2020) and Nava et al. (2020), have shown that the interplay of activity signals that is due to the distribution and different lifetimes of starspots and faculae on the stellar surface, may result in signals that cannot be directly attributed to the stellar rotation. However, we find a good agreement between our photometric results and spectroscopic results (see further down). The measured median pEW of the Hα line is $+0.00 \pm 0.01$ Å, and indicates that GJ 215 is not a Hα active star (Jeffers et al. 2018; Schöfer et al. 2019), which is in line with the long rotational period derived for this star, as is the upper limit of $v \sin i < 2\,\mathrm{km\,s^{-1}}$ measured by Reiners et al. (2018a).

6.5.3 Periodogram analysis and RV modeling

We show the results of the periodogram analysis of the CARMENES RV data in Fig. 6.4. A significant peak with an FAP $< 10^{-7}$ is visible at 14.22 ± 0.01 d with an amplitude of $2.13 \pm 0.23\,\mathrm{m\,s^{-1}}$, as well as two additional peaks close to one day that we attributed to daily aliases of the 14 d period. Although the absolute GLS power and FAPs of the suspected aliases were

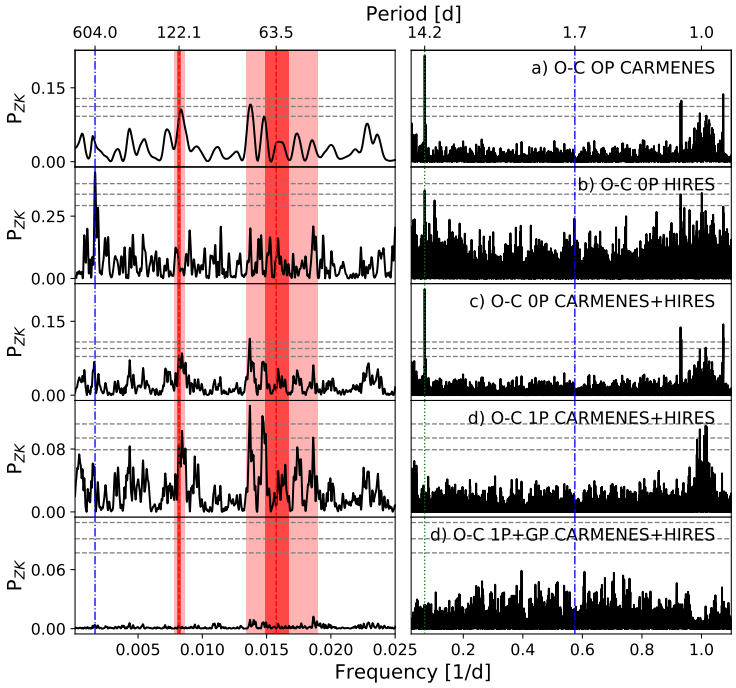


Fig. 6.4.: Generalized Lomb-Scargle periodograms of RV data for GJ 251 for CARMENES, HIRES, and a combination of both. The stellar rotational period derived by photometry is plotted as the dashed red line, and the 1σ and 3σ uncertainties are highlighted in red. We also indicate the harmonic of the rotational period and its uncertainty. The green line marks the suspected planetary signal. The blue lines mark the periods of the published planetary candidates by Butler et al. (2017) at 1.7 d, and the significant HIRES signal around 604 d.

smaller than the frequency of the 14.22 d signal, we used `AliasFinder` to verify that the 14.22 d signal represents the most probable true signal, which we confirmed. Additional strong secondary signals were identified at 73 d, and 119.5 d, each with an FAP of about 10^{-2}.

We also performed an independent periodogram analysis of the HIRES data. The strongest signal is at 604 d with an FAP of almost 10^{-5}, followed by one at 14.2 d with FAP $< 10^{-2}$ (see Fig. 6.4). The latter is consistent with our strongest signal in the CARMENES data.

We combined the CARMENES and HIRES spectroscopic RV data by fitting an offset and jitter term for each instrument. The combined periodogram showed the highest peak at 14.24 d with an FAP $< 10^{-11}$, and the daily aliases of this signal were the second and third highest signals. Within our activity indicators, we did not identify any significant GLS periodogram peak with an FAP $< 10^{-1}$ at the frequency of the 14.2 d RV signal. A signal at 14.731 ± 0.026 d in the Ca II IRT_3 line reaches almost 1 % FAP, but is still larger than and can be well separated from the

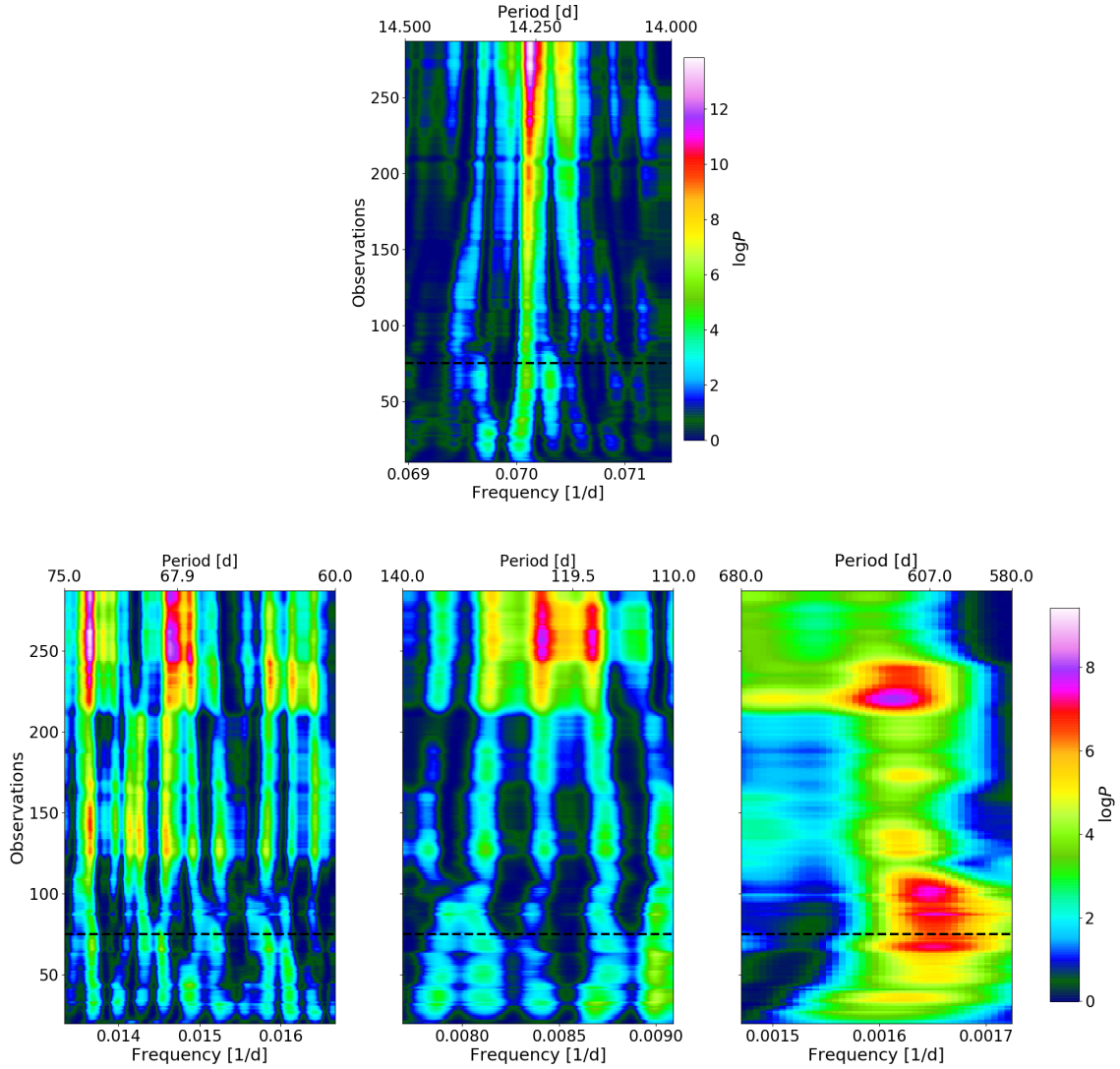


Fig. 6.5.: Stacked-Bayesian GLS periodogram of the planetary signal at 14.22 d (*top*) and on the zero-planet residuals (*bottom* and with its own normalization). The three s-BGLS on the bottom were calculated using the one-planet Keplerian RV residuals and show signals that we attributed to stellar activity: the forest of signals between 60 d and 75 d corresponding to roughly half of the rotation period (left), the RV signals around the photometrically derived rotation period at 119.5 d (middle), and the long period signal around 600 d. In all four plots, the dashed black line indicates the boundary between HIRES and CARMENES data, which were taken successively.

14.24 d signal within the resolution of the GLS periodogram over the observed time baseline. We fit a Keplerian model to the signal at 14.24 d. The log-evidence of the different model fits applied to the data sets is given in Table 6.3.

The residual periodogram of the one-planet Keplerian fit on the HIRES and CARMENES combined data shows several remaining significant peaks at periods of 73.02 d (FAP $< 10^{-5}$), 68.15 d (FAP $< 10^{-4}$), and 67.86 d (FAP $< 10^{-2}$). These periods are close to half of the derived rotational period of the star. We also observed a peak at 118.78 d with FAP $< 10^{-2}$, which is very close to the rotation period derived from photometry. As a simple test, we fit a sinusoid to the 118.78 d period. The signal at 67.86 d was then the most significant. It was necessary to fit an additional sinusoid for the 67.86 d signal to obtain a periodogram that did not show any signal with an FAP < 0.01, which showed that the other signals were connected through aliasing. The necessity of modeling two sinusoidal functions with periods close to the rotational period and its half suggests that these signals are caused by stellar activity, for instance, a multi-spot pattern, or amplitude variations caused by decreasing spot areas. To rule out the possibility of independent planet signals, we analyzed the coherence of these signals.

We used the s-BGLS periodogram to assess the coherence of the significant RV signals with increasing numbers of observations. We show the resulting s-BGLS diagrams in Fig. 6.5. We identified that neither the signals around 120 d nor the forest of signals between 50 d, and 73 d were stable over the observational time baseline. The 73 d signal lost about three orders of magnitude in signal probability after roughly observation 160 (May 2018), but reappeared in observation 210 (January 2019). All these mentioned signals showed a lack of coherence in the latest observations between observation 200 (January 2019) and 250 (October 2019). In contrast to these signals, the suspected planetary signal at 14.2 d never showed strong dips in its probability during the time of observations. These results together with the analysis of the activity indicators mean that this signal probably is of planetary origin. We refer to it as GJ 251 b.

6.5.4 A second planet in the system?

We found no evidence in the CARMENES and HIRES data for the planetary candidate claimed by Butler et al. (2017) at 1.74 d. Neither did we observe the 604 d signal in CARMENES data, which was highly significant in the HIRES data. We used the s-BGLS to verify whether these signals were more significant in the past but might have decayed over the time of observations. While we did not find any indication of the 1.74 d signal during the period of our observations, the 604 d signal showed variability in its signal probability (see Fig. 6.5). The 604 d signal already slightly lost coherence during the last HIRES observations. However, especially the CARMENES data show noncoherence of the signal. The fluctuation is a strong indication for a nonplanetary origin (Mortier & Collier Cameron 2017).

Tab. 6.3.: Bayesian log-evidence for GJ 251 for different models[a].

Model	P [d]	$\ln \mathcal{Z}$	$\Delta \ln \mathcal{Z}$
	CARMENES		
0p	...	-545.4 ± 0.1	0
1p	14.2	-525.8 ± 0.2	19.6
2p	14.2, 1.7	-528.7 ± 0.2	16.7
2p	14.2, 656.0	-524.5 ± 0.2	20.9
1p+GP	14.2	-492.2 ± 0.1	53.2
	HIRES		
0p	...	-227.3 ± 0.1	0
1p	14.2	-222.1 ± 0.1	5.2
2p	14.2, 1.7	-222.2 ± 0.2	5.1
2p	14.2, 601.9	-211.4 ± 0.2	15.9
1p+uGP	14.2	-213.3 ± 0.1	14.0
	CARMENES + HIRES		
0p	...	-772.0 ± 0.2	0
1p	14.2	-747.2 ± 0.2	24.8
1cp	14.2	-744.5 ± 0.2	27.5
2p	14.2, 1.7	-748.9 ± 0.2	23.1
2p	14.2, 629.2	-743.5 ± 0.2	28.5
GP	...	-743.3 ± 0.2	28.9
2p+GP	1.4, 14.2	-708.9 ± 0.4	63.1
2p+GP	14.2, 667.1	-707.1 ± 0.3	64.9
1p+uGP	14.2	-706.2 ± 0.1	65.8
1p+GP	14.2	-704.8 ± 0.2	67.2
1cp+GP	14.2	-703.8 ± 0.3	68.2

[(a)] Planetary models based on CARMENES, HIRES, and combined CARMENES+HIRES RV data. 0p: 0 planets, 1p: 1 planet, 1cp: 1 planet in circular orbit ($e = 0$), 2p: 2 planets. GP and uGP: additional constrained and unconstrained Gaussian processes, respectively. Orbital periods rounded to one decimal.

We performed a statistical test using model comparison in the framework of Bayesian evidence with `juliet`. We compared one-planet ($P = 14.24$ d) to two-planet models. Our results showed that the two-planet model with periods of 14.24 d and 1.74 d is not supported by the individual data sets or by their combination because its log-evidence is weaker than that of the simpler one-planet model. Fitting the 600 d signal as a second planet resulted in a significant model improvement compared to the one-planet model alone for the HIRES data. The same two-planet model (14.24 d, and 604 d) fit to the CARMENES data brought no significant improvement either compared to the one-planet model. Fitting the two-planet model to the combined CARMENES and HIRES data resulted in almost the same log-evidence as the one-planet model. Additionally, the derived planetary period at $629.2^{+20.2}_{-8.4}$ d deviates significantly from the $601.9^{+6.5}_{-5.2}$ d obtained from the fit on the HIRES data, even though we used a prior with an informative Gaussian distribution, hereafter referred to as normal prior, with mean of 604 d and $\sigma = 30$ d. These values were informed by the GLS periodogram peak in the HIRES data and its 3σ uncertainty.

We searched for any additional planetary signal hidden behind the stellar activity by once sampling a second Keplerian with a log-uniform prior between 15 d to 8000 d and then sampling with a log-uniform prior between 0.5 d to 14 d, while simultaneously modeling the stellar activity with a constrained GP model (see Sec. 6.5.5). We divided the two-planet model search into two runs for technical reasons: `juliet` needs a chronological order of the planetary periods. The two two-planet models combined with the GP showed no significant improvement compared to the one-planet and GP combined model, that is, the data suggest that all periodic variations except for the 14.2 d period are better or equally well described by a GP.

In the 600 d signal, we identified a periodicity with an FAP $< 10^{-2}$ in the Hα indicator at a period of 660 ± 21 d. The Na I doublet lines and the CRX showed a significant peak with an FAP $< 10^{-3}$ at 300 d. The s-BGLS of the dLW shows that a signal close to 600 d was more significant in past observations around observation 150, which corresponds to April 2018 (see Fig. 6.3 again). Comparing the activity s-BGLS of the dLW to the s-BGLS of the RV data showed that this is about the same time at which the 600 d signal was most significant in the RV data. These results, along with our photometric results, suggest that the signals at 73 d, 119 d, and 600 d are not caused by Keplerian motion.

6.5.5 Simultaneous Keplerian and GP modeling

We performed a simultaneous fit of a one-planet Keplerian model together with the QP GP (Equation 6.1) to account for activity-induced RV variations. For the first GP model we used

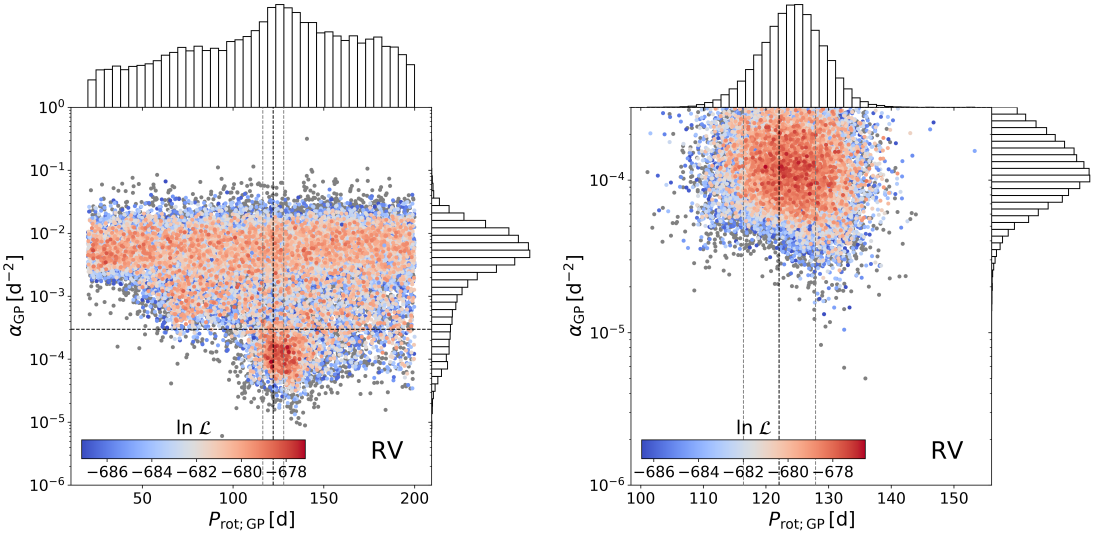


Fig. 6.6.: Posterior distribution of the GP fit to the RV data in the α_{GP} vs. P_{rot} plane for GJ 251. The color-coding shows the log-likelihood normalized to the highest value in the posterior sample. Gray samples indicate solutions with a $\Delta \ln L > 10$ compared to the best solution. *Left:* GP fit to the RV data with a wide uniform prior for the rotational period. *Right:* GP fit to the RV data with an informative normal prior based on the photometric GP results and additional constraints on the other hyperparameters. We overplot the derived rotational period of the photometric GP and its 3σ uncertainties with vertical lines. The horizontal line marks the cut in α_{GP} used to constrain the GP fit shown in the lower plot.

wide uninformative priors, which are shown in Table B.3, while we kept the same planetary and instrumental priors as for the one-planet fit (Table B.2). The posterior samples of this unconstrained GP can provide indications for the stellar rotational period given only the RV data (see also Angus et al. 2018; Stock et al. 2020b).

Including the GP as a model for activity significantly improved the log-evidence ($\Delta \log Z = 41$ on the combined CARMENES+HIRES data) compared to the one-planet fit alone. We show the α_{GP} versus period diagram of the unconstrained GP posterior samples in the top plot of Fig. 6.6. Around 125 d we identified a region of higher posterior density, higher likelihood, and lower values of α compared to the rest of the posterior solutions. This indicates a more strongly correlated periodic signal. The derived median GP rotational period based on the CARMENES and HIRES RV data is $P_{rot,RV} = 125^{+44}_{-59}$ d, which is consistent with the results from photometric data. For the final one-planet and GP simultaneous fit to the combined data, we applied several additional constrains on the GP to reduce the posterior volume of the model, which could lead to fitting incorrect residual signals (Angus et al. 2018). We applied a normal prior to the GP

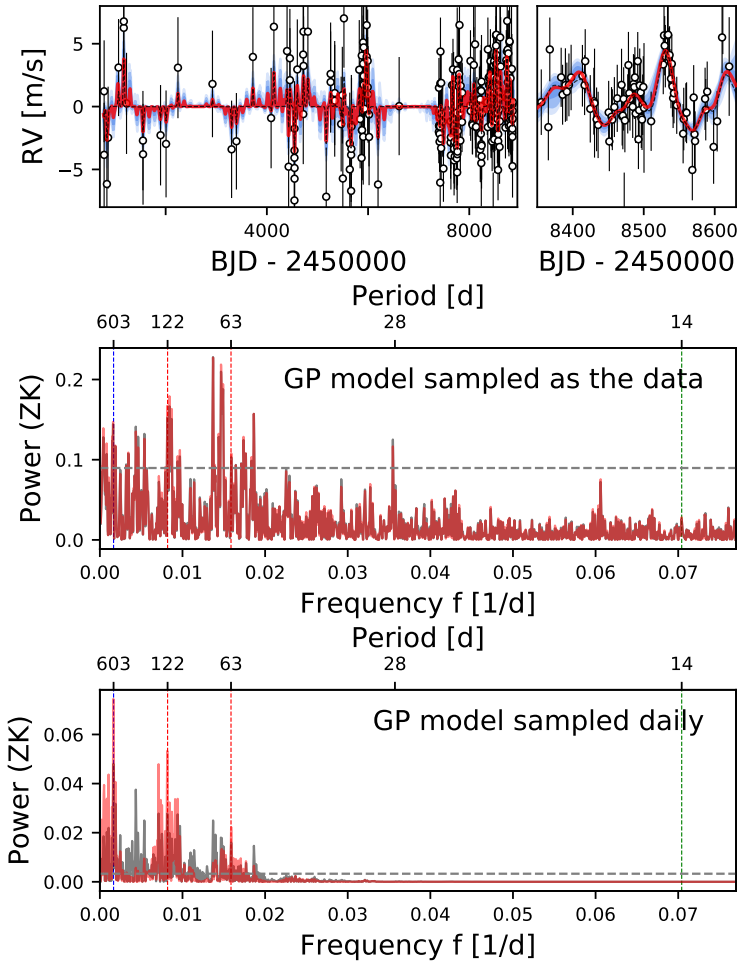


Fig. 6.7.: Gaussian process model for the RV data of GJ 251 without the planetary model, which is subtracted from the RV data. The constrained GP model is shown in red. The blue regions show 1σ, 2σ, and 3σ uncertainties. We show a zoom to some CARMENES observations (top right). The GLS is evaluated on the GP model at each observed data point (top GLS) and daily (bottom GLS). The dashed line in the GLS periodograms indicates an FAP level of 0.1 %. In addition, we show the unconstrained GP model as the dashed black line in the upper plots and as the gray periodograms in the lower plots.

rotational parameter based on the stellar rotation period derived from the photometry and its 3σ uncertainty.

For Γ, which can be interpreted as the overall number of inflection points per function period, we applied a log-uniform prior between 10^{-1} and 10^{1}. This prior is consistent with about one to three local maxima per rotation period. Jeffers & Keller (2009) showed that this assumption is to first approximation valid for any stellar surface, independent of the number of starspots and

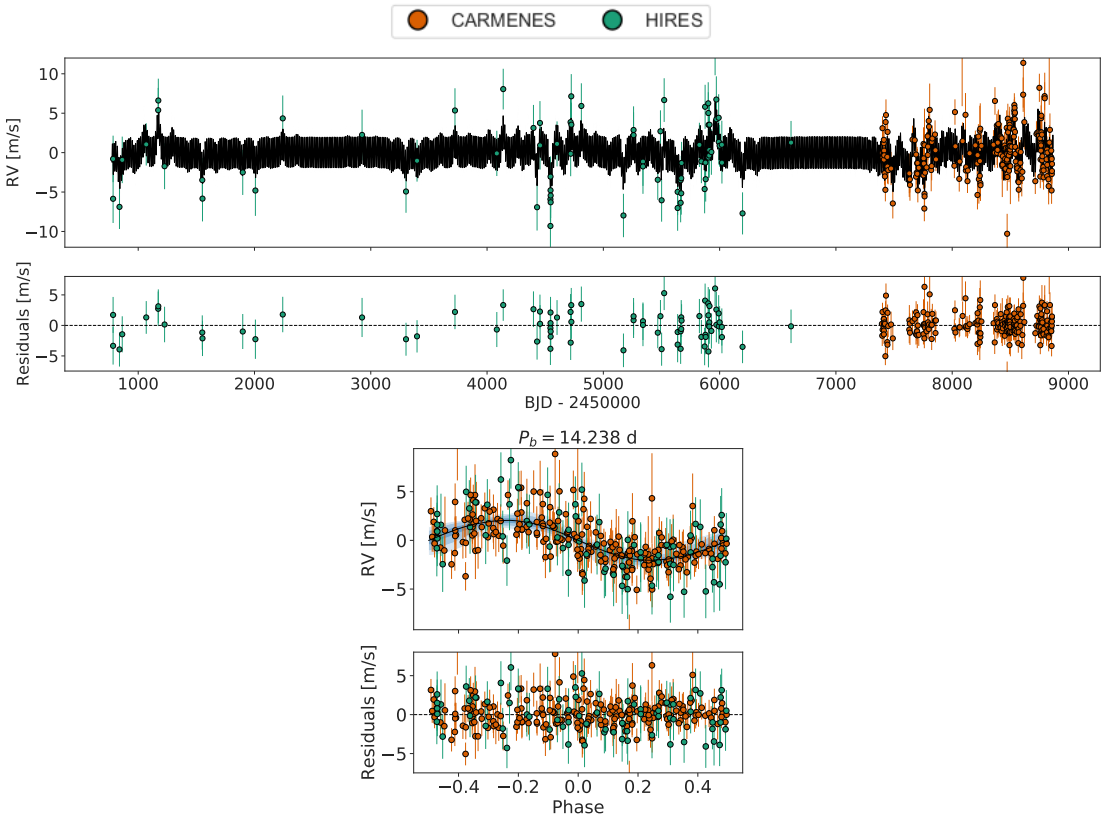


Fig. 6.8.: *Top:* Radial velocity data with a combined model of one-planet and stellar activity using a Keplerian model and a GP. *Bottom:* Plot phased to the orbital period of GJ 251 b without a GP component. The bottom plots show the residuals after the fit.

their distribution. Similar, but even more informative priors on Γ, have been applied in several studies that used the QP GP kernel (see Nava et al. 2020, and references therein). The timescale parameter of the QP GP kernel, $\alpha_{\rm GP}$, is crucial for modeling a meaningful rotational signal. For instance, if it is large, then the squared exponential term of the kernel dominates, which allows for good fits to the data without requiring any periodic covariance structure, even when the data show clear periodicities (see also Angus et al. 2018,). This effect is visible in the top plot of Fig. 6.6, where a plateau of posterior samples at high $\alpha_{\rm GP}$ values populates the entire prior volume of the GP rotation parameter. As discussed in Sec. 6.5.1, it should not be strictly assumed that photometric and RV GP timescales are similar. A prior on $\alpha_{\rm GP}$ based on photometry, as used for example for the stellar rotation, therefore needs future verification. For the moment, the upper boundary of the $\alpha_{\rm GP}$ prior needs to be assessed for each target individually. Angus et al. (2018) proposed that this hyperparameter should be larger than the observed stellar rotation period. In

Tab. 6.4.: Posterior parameters of the final fits obtained for GJ 251 b, HD 238090 b, and Lalande 21185 b using `juliet`.

Parameter[a]	GJ 251 b	HD 238090 b	Lalande 21185 b
	orbital parameters		
P (d)	$14.238^{+0.002}_{-0.002}$	$13.671^{+0.011}_{-0.010}$	$12.946^{+0.005}_{-0.005}$
$t_0 - 2450000$ (BJD)	$8626.69^{+0.34}_{-0.35}$	$8630.09^{+0.52}_{-0.55}$	$8622.23^{+0.48}_{-0.45}$
K (m s^{-1})	$2.11^{+0.21}_{-0.20}$	$2.85^{+0.38}_{-0.39}$	$1.39^{+0.14}_{-0.14}$
$\mathcal{S}_{1,b} = \sqrt{e_b}\sin\omega_b$	$0.20^{+0.16}_{-0.22}$	$0.44^{+0.16}_{-0.25}$	$0.07^{+0.19}_{-0.20}$
$\mathcal{S}_{2,b} = \sqrt{e_b}\cos\omega_b$	$0.05^{+0.21}_{-0.22}$	$-0.25^{+0.23}_{-0.18}$	$-0.27^{+0.25}_{-0.19}$
e	$0.10^{+0.09}_{-0.07}$	$0.30^{+0.16}_{-0.17}$	$0.12^{+0.12}_{-0.09}$
ω (deg)	$78.8^{+47.6}_{-44.7}$	$119.3^{+22.8}_{-24.8}$	$140.7^{+27.3}_{-53.0}$
	RV parameters		
$\gamma_{\rm CARMENES}$ (m s^{-1})	$-0.06^{+0.56}_{-0.56}$	$-0.03^{+26}_{-0.27}$	$-0.19^{+0.45}_{-0.45}$
$\sigma_{\rm CARMENES}$ (m s^{-1})	$1.05^{+0.17}_{0.16}$	$1.57^{+0.28}_{-0.25}$	$1.10^{+0.15}_{-0.14}$
$\gamma_{\rm HIRES}$ (m s^{-1})	$0.18^{0.58}_{-0.60}$	...	...
$\sigma_{\rm HIRES}$ (m s^{-1})	$1.85^{0.71}_{-0.77}$	...	...
$\gamma_{\rm SOPHIE}$ (m s^{-1})	...	...	$0.45^{+0.46}_{-0.45}$
$\sigma_{\rm SOPHIE}$ (m s^{-1})	...	...	$1.26^{+0.20}_{-0.19}$
	GP (constrained) hyper-parameters		
$\sigma_{\rm GP,RV}$ (m s^{-1})	$2.27^{+0.40}_{-0.34}$	$1.92^{+1.42}_{-0.82}$	$1.62^{+0.31}_{-0.25}$
$\alpha_{\rm GP,RV}$ (10^{-5} d^{-2})	$11.4^{+7.4}_{-4.5}$	10^{-20} (fixed)	$5.9^{+3.7}_{-1.9}$
$\Gamma_{\rm GP,RV}$	$4.6^{+2.7}_{-2.0}$	$1.1^{+2.5}_{-0.7}$	$1.3^{+1.1}_{-0.6}$
$P_{\rm rot;GP,RV}$ (d)	$124.2^{+4.8}_{-5.1}$	$105.9^{+1.07}_{-0.93}$	$56.2^{+0.7}_{-0.7}$
	derived planetary parameters		
$M_{\rm p}\sin i$ ($M_\oplus$)	$4.00^{+0.40}_{-0.40}$	$6.89^{+0.92}_{-0.95}$	$2.69^{+0.25}_{-0.25}$
$a_{\rm p}$ (10^{-2} au)	$8.18^{+0.11}_{-0.12}$	$9.32^{+0.11}_{-0.11}$	$7.890^{+0.068}_{-0.077}$
$T_{\rm eq}$ (K)[b]	$351.0^{+1.4}_{-1.3}$	$469.6^{+2.3}_{-2.6}$	$370.1^{+5.8}_{-6.8}$
S ($S_\oplus$)	$2.53^{+0.04}_{-0.04}$	$8.10^{+0.16}_{-0.18}$	$3.13^{+0.20}_{-0.22}$

[a] Error bars denote the 68% posterior credibility intervals. [b] Equilibrium temperatures estimated assuming zero Bond albedo.
Priors and descriptions for each parameter can be found in Table B.2 and Table B.3. Results of the derived parameters take also the stellar parameter uncertainties (as Gaussian uncertainty) into account.

the case of GJ 251, with a derived photometric rotation period of about 120 d, the suggested rule by Angus et al. (2018) would translate into $\alpha_{\rm GP} < 3.5\ 10^{-5}$[12].

However, it is not clear whether this general rule can be applied to slowly rotating stars like GJ 251 because Angus et al. (2018) did not discuss such stars. For example, because of active longitudes (Jeffers & Keller 2009), a meaningful QP signal might still be detected that would be caused by starspots that decay over approximately half of the stellar rotation every time the active region points toward the observer. More importantly, from the unconstrained GP posterior samples, we find that a constraint on $\alpha_{\rm GP}$ based on the rule by Angus et al. (2018) would mean that the overdensity of high-likelihood posterior samples detected at 120 d, given the data, would not be included in the final activity model. As expected, a GP model using the upper boundary of Angus et al. (2018) led to a log-evidence of −710.2, which is about four lower than the unconstrained GP. Finding the right mixture between physical priors and data-driven behavior is critical for modeling stellar activity with GPs.

We constrained the upper boundary to $\alpha_{\rm GP} < 3\ 10^{-4}\,{\rm d}^{-2}$. This constraint removed the plateau of posterior samples that fit noise on short timescales, which cannot be attributed directly to the stellar rotation and is captured by the instrument jitter parameter in our case. However, the observed high-likelihood posterior sample overdensity at the derived photometric rotation period is included in the GP model. We have applied similar constrains of $\alpha_{\rm GP}$ with success in Stock et al. (2020b). The priors of our constrained GP are summarized in Table B.3. The distribution of the posterior parameters of the constrained GP in the $\alpha_{\rm GP}$ versus $P_{\rm GP}$ diagram is shown in the bottom plot of Fig. 6.6. Corner plots of of all the fit parameters are provided in Figs. B.1 and B.2. The derived timescale parameter in our final GP model is $\alpha_{\rm GP} = 11.4^{+7.4}_{-4.5} \cdot 10^{-5}\,{\rm d}^{-2}$, which translates into a decay time of $P_{\rm dec} = 66^{+19}_{-15}\,{\rm d}$[13] and is close to half the stellar rotation. The GP semi-amplitude is consistent within 1σ with the expected RV semi-amplitude due to stellar rotation estimated based on the relations of Suárez Mascareño et al. (2018).

In Fig. 6.7 we show our final median GP model. We calculated the GLS periodogram of the GP model to assess its temporal behavior. To calculate the GLS periodogram we chose to sample the GP model in two different ways: first, sampling identical to that of the original data, and second, sampled daily over the entire observation time. The GP model sampled as the real observations includes the true window function of the data. A visual inspection of this GLS periodogram shows that the highest peak is at 73 d, followed by another peak at 68 d. These were the most significant signals in the residuals of the simple one-planet fit. A peak at 28 d, about twice the planetary period and close to the lunar cycle, is also visible. The GLS periodogram of the GP

[12] $\alpha_{\rm GP} < 6.95\ 10^{-5}$ due to the `juliet` bug (see footote 1 in Sec. 3.5.2).
[13] $P_{\rm dec} = 96.7^{+26.7}_{-20.8}$ d due to the `juliet` bug (see footote 1 in Sec. 3.5.2).

model, sampled once a day over the entire observation time, shows that the GP does not model the 28 d period. The peak can be explained by the convolution of the GP model with the window function of the observations.

From the daily sampled periodogram decomposition of the GP models, the tuned GP does not model any periods close to the planet (or twice the planetary period). It models primarily the activity related signals at 63 d, 122 d, and 600 d. The unconstrained GP modeled the 73 d signal more prominently than the signals at 120 d and 63 d, while the constrained GP modeled 120 d and 63 d more strongly. Nevertheless, the tuned GP was capable of producing the same strong peak at 73 d, given the data. This result shows in practice the conclusions and caveats given by Nava et al. (2020) that QP models can contain signals "unrelated to their true period". The 73 d signal can be explained by an alias based on a sampling frequency of $\sim 365^{-1}$ d^{-1} of the first harmonic at 63 d of the 120 d rotation period.

Finally, we show the combined Keplerian and tuned GP fit to the RV data, and a plot phased to the orbital period of GJ 251 b in Fig. 6.8. We display the final posterior solution of the planetary and GP parameters in Table 6.4. We derived a semi-amplitude of $K = 2.11^{+0.21}_{-0.20}$ m s^{-1}, a period of $P = 14.238 \pm 0.002$ d, and an eccentricity of $e = 0.10^{+0.09}_{-0.07}$. The eccentricity of the system is consistent with zero because fits without this parameter provided similar log-evidence with fewer parameters. Based on our posterior samples and the stellar parameters (see Table 6.2), we derived further planetary parameters, which we also show in Table 6.4. According to this analysis, GJ 251 b has a minimum mass of 4.00 ± 0.40 M$_\oplus$ and a semimajor axis of $0.0818^{+0.0011}_{-0.0012}$ au.

6.5.6 Transit search and analysis with *TESS*

GJ 251 was observed with the *TESS* satellite (Ricker et al. 2015) in sector 20, in the period from 24 December 2019 to 21 January 2020, with a total of 16556 data points, but was not marked as a *TESS* object of interest (TOI). We independently searched for a transit signal using the transit least-squares (TLS; Hippke & Heller 2019) algorithm on PDCSAP light curve. We did not identify any TLS signal that could be attributed to any possible transit for GJ 251. However, we identified a significant sinusoidal-like signal with a frequency $f \approx 6$ d^{-1} (period 0.165 d) and $(1.96 \pm 0.4)\ 10^{-4}$ relative flux amplitude variation, equivalent to about 0.2 mmag), as well as its harmonics $f/2$ and $2f$ with lower amplitudes. We show a phase plot of this signal in Fig. 6.9. This signal is not observed within the RV data of this target.

This 4 h signal was already present in the simple aperture photometry (SAP) light curve. We checked that it was not instrumental in origin by extracting and analyzing the light curves of the

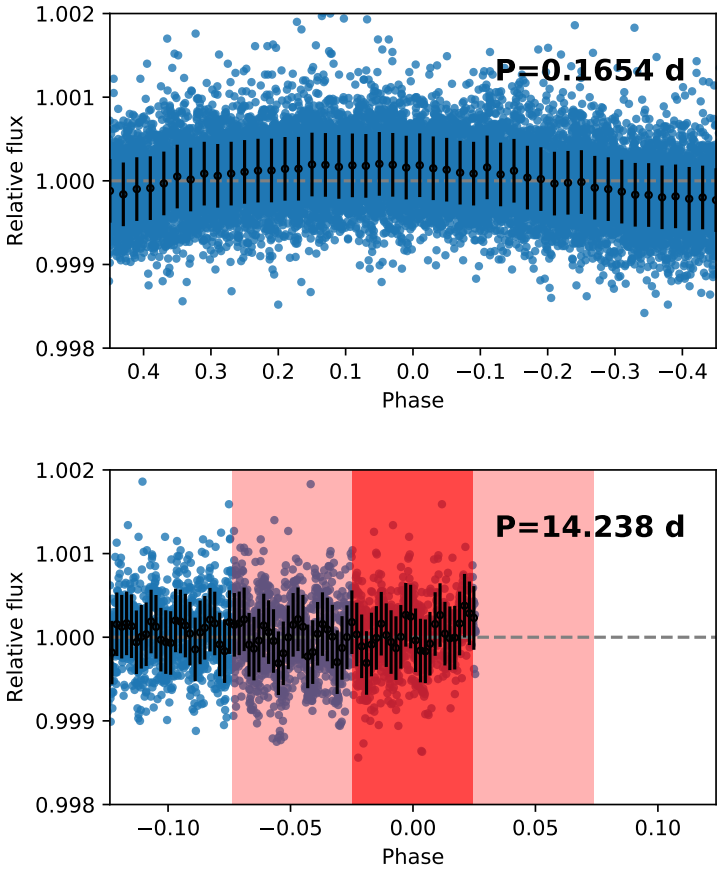


Fig. 6.9.: *Top: TESS* PDCSAP lightcurve of GJ 251 folded to the 0.165 d signal. *Bottom: TESS* PDCSAP lightcurve of GJ 251 folded to the time of transit center for GJ 251 b estimated by the RV fit. Red shaded areas indicate 1σ and 3σ uncertainties. The black dots and uncertainty bars represent binned TESS data. The estimated transit depth would be ~ 1.4 ppt. An observation gap is visible.

968 objects present in the same *TESS* S20 sector, Camera 1, and CCD 3 as GJ 251. No other star showed the same periodicity.

We considered the possibility that the signal originated from thermodynamical excitations of p- and g-modes, as theoretically predicted by Rodríguez-López et al. (2014). However, the pulsation hypothesis is unable to explain the presence of subharmonics of the main frequency in the periodogram. Moreover, solar-like pulsations or granulation, which have not yet been detected in M-dwarf stars, can also be discarded because they are predicted to be on the order of minutes.

Lucky-imaging observations with FastCam (Cortés-Contreras et al. 2017) and Robo AO images (Lamman et al. 2020) have not detected any resolved visual companion. The *TESS* aperture includes several objects. In particular, the two brightest stars in the aperture mask are only 4.87 mag and 5.95 mag fainter in the G band, corresponding to a flux contribution of 1.1 % and 0.4 %, respectively. A 18 mmag sinusoidal amplitude variation in the former or a 50 mmag amplitude variation in the latter could account for the detected 4 h signal. We chose different subapertures to extract the light curve from different regions of the *TESS* full-frame images. It did not affect the amplitude of the short-period signal, making it unlikely that the periodicity originated in background contamination. With our analysis, we cannot draw any final conclusion on the origin of the 4 h signal for GJ 251.

We estimated the radius of GJ 251 b with the mass-radius relation of Zeng et al. (2016) and assumed an Earth-like core-mass fraction of 0.26 to be approximately 1.48 $R_\oplus$, which translates into a transit depth of roughly 1.4 ppt for GJ 251 b. Such a signal should be detectable by *TESS* in case of a full transit. However, we were unable to detect any transit in the light curve, in particular given the estimated t_0 and the orbital period P of GJ 251 b by the RV fit and their uncertainties. In particular, we ruled out a transit event within 1σ of t_0, but not within 3σ, because of an observational gap in the *TESS* light curve. Unfortunately, GJ 251 will not be observed again by *TESS*. We show the 3σ window around t_0 in Fig 6.9.

6.6 HD 238090

6.6.1 Photometric monitoring

We took ground-based photometry for HD 238090. We combined our T90 and TJO data with public data from MEarth taken in 2009, 2010, and 2014, as well as data from NSVS taken between May 1999 and March 2000. A periodogram analysis of the combined data sets indicated periodicities around 100 d. Using `juliet`, we fit for an offset and jitter terms for each instrument and filter. We used the same GP kernel and priors as for the photometric analysis of GJ 251 and separated the amplitude hyperparameters for each instrument while keeping global hyperparameters for the timescale and rotation. The priors are given in Table B.1. From our GP analysis, we derived that HD 238090 has a rotation period of $96.7^{+3.7}_{-3.2}$ d. Figure 6.10 shows the distribution of the posterior samples in the α_{GP}-$P_{\mathrm{rot.}}$ space, and Fig. 6.11 shows the median GP model of each photometric data set together with the data and uncertainties. Following the same approach as for GJ 251 and applying the relations by Suárez Mascareño et al. (2018), we derived

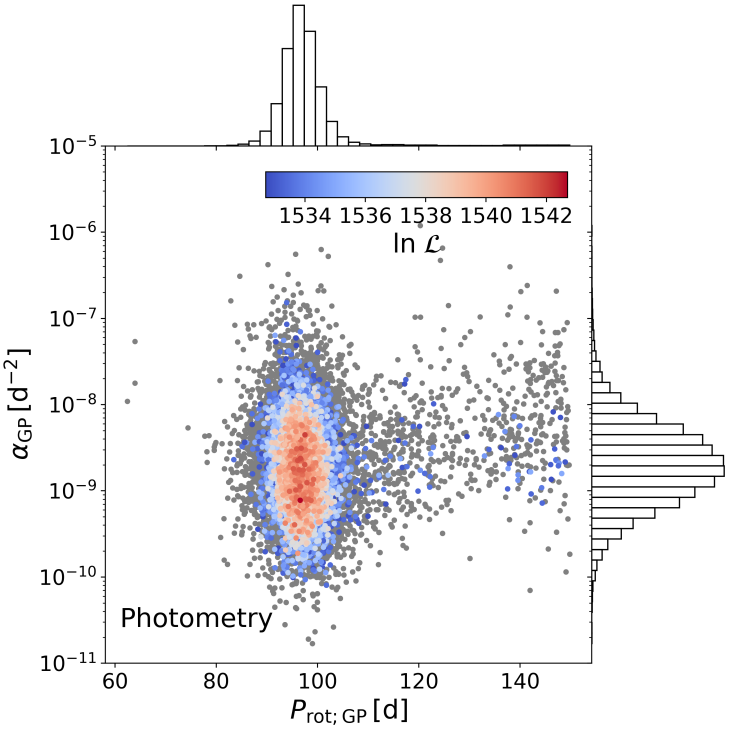


Fig. 6.10.: Posterior distribution of the GP fitted to the photometric data in the α_{GP} vs. P_{rot} plane for HD 238090. The color-coding shows the log-likelihood normalized to the highest value within the posterior sample. Gray samples indicate solutions with a $\Delta \ln L > 10$ compared to the best solution.

the median $\log(R'_{HK})$ and expected semi-amplitude to $\log(R'_{HK}) = -5.65^{+0.52}_{-0.58}$ (mean at −5.69) and $K_{exp.} = 0.83^{+4.40}_{-0.70}\,m\,s^{-1}$ (mean at $4.25\,m\,s^{-1}$).

6.6.2 Spectroscopic activity indicators

The periodogram analysis of our spectroscopic activity indicators is displayed in Fig. 6.12. We identified signals with an FAP $< 10^{-3}$ in some indices close to 1 d and 365 d (see Sec. 6.5.2 for a discussion of these signals). After subtracting the yearly signal, the GLS periodograms of the residuals of many indicators show a signal around 480 d with FAP $< 10^{-3}$ and a long-term trend. We also identified a signal in the FWHM CCF with an FAP $< 10^{-2}$ at 106.1 d, which is close to the derived stellar rotation period. Within the s-BGLS of the residual activity indicators of TiO, which we show in Fig. 6.12, we found various signals around 50 d, which is roughly half the photometrically derived stellar rotation period. These signals were more significant in

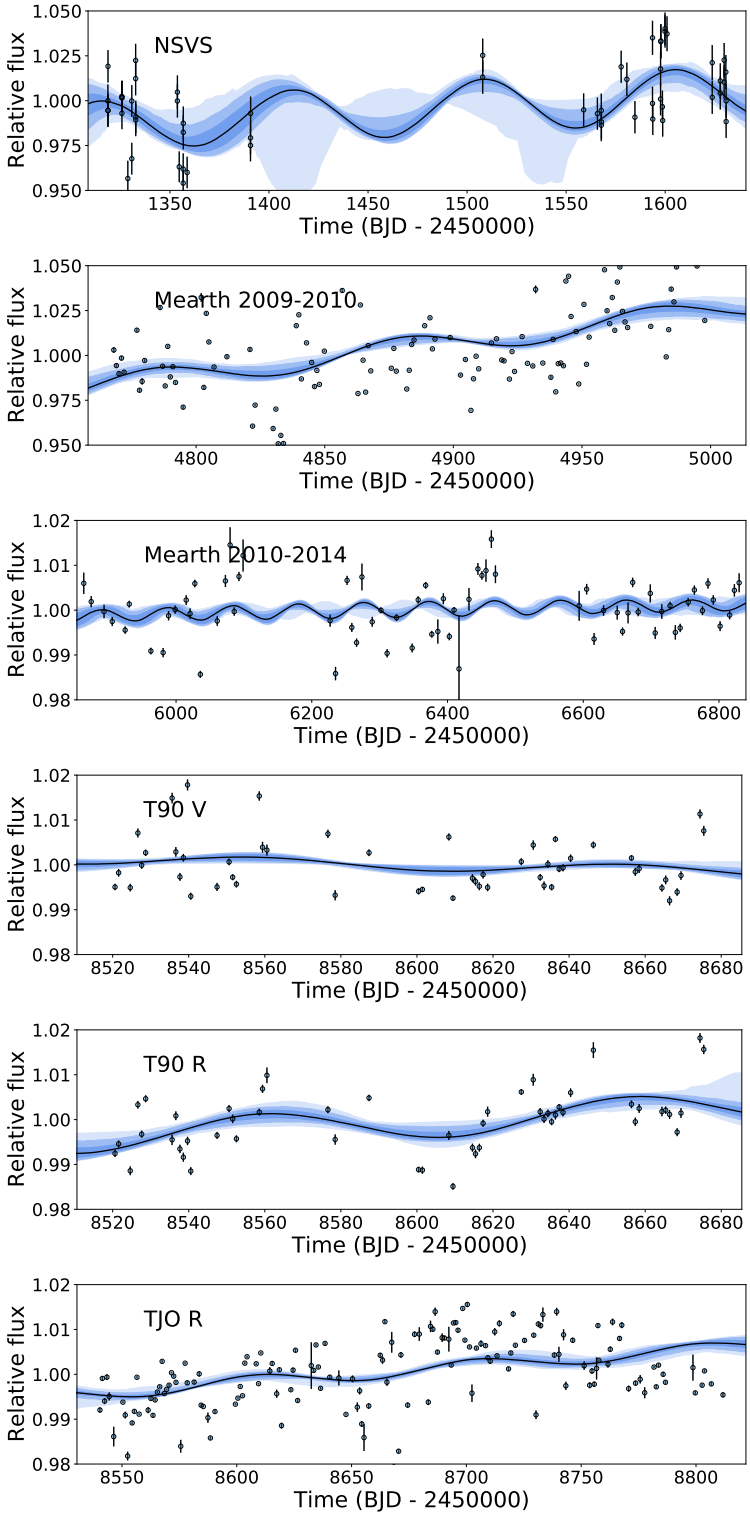


Fig. 6.11.: Gaussian-process model for each nightly binned photometric data set of HD 238090. From top to bottom: NSVS, MEarth 2009 to 2010, MEarth 2010 to 2014, SNO V, SNO R, and TJO. For each instrument, we fit individual GP hyperparameters for the amplitudes σ_{GP_i} and Γ_i, but we used global GP hyperparameters for the timescale of the amplitude modulation and the rotation period.

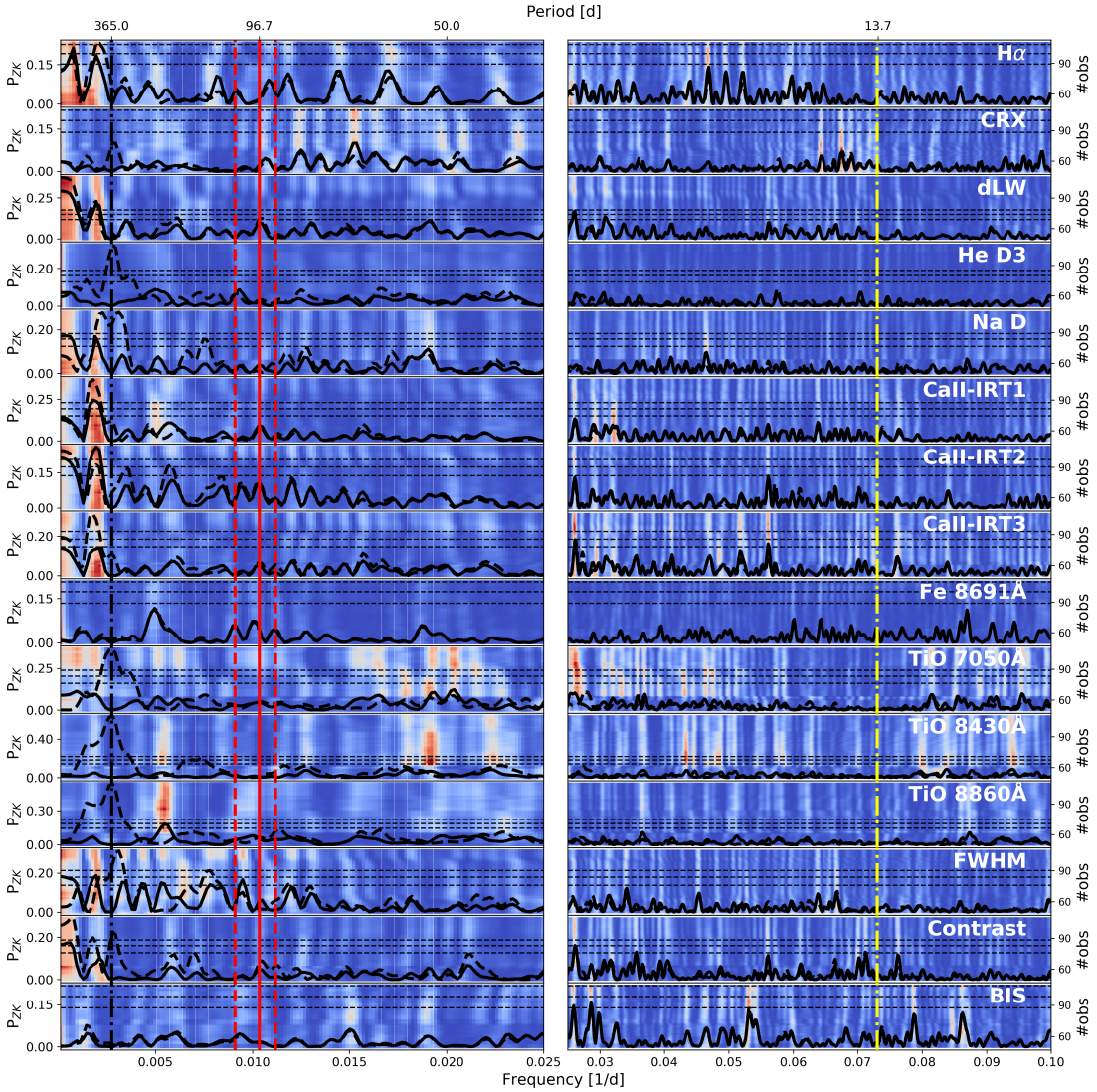


Fig. 6.12.: Generalized Lomb-Scargle periodograms of several activity indicators based on spectroscopic data obtained by CARMENES for HD 238090. The dashed black periodograms represent the GLS on the activity indicators, and the solid GLS periodogram represents the residuals from which a 365 d sinusoidal signal was subtracted. For the residuals from which the 365 d signal was subtracted, we also overplot the s-BGLS periodogram, where the probability increases from blue to white to red. The solid red lines mark the rotation period estimated by photometric data, and the dashed red lines show the 3σ uncertainties. The dashed black line marks a period of 365 d, and the dashed yellow line marks the period of the planetary signal published in this work.

previous observations between July 2018 and February 2019 (CARMENES observations 60 to

90). Overall, the activity indicators show that the star exhibits no significant level of activity at periods shorter than 20 d over the time of RV observations.

6.6.3 Periodogram analysis

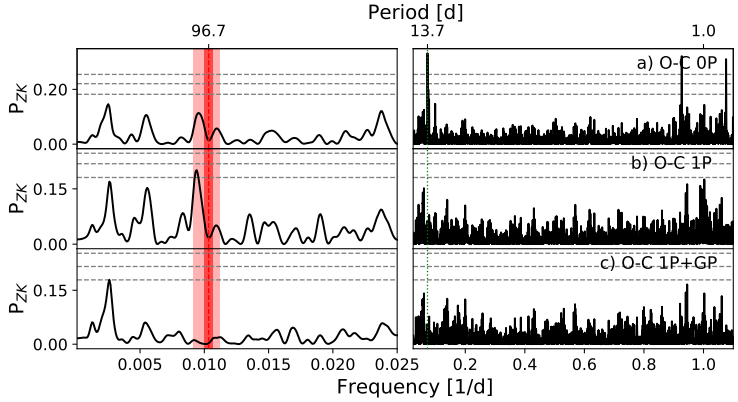


Fig. 6.13.: Generalized Lomb-Scargle periodogram of RV data of HD 238090 of the zero-planet fit, one-planet fit, and one-planet GP simultaneous fit. The stellar rotational period derived by photometry is plotted as the dashed red line, and 1σ and 3σ uncertainties are highlighted in red. The green line indicates the planet period at about 13.7 d.

The GLS periodogram of the RV data for HD 238090 is shown in Fig. 6.13. A significant peak with an FAP $< 10^{-5}$ is visible at 13.68 d. Two additional signals with almost the same GLS power accompany this signal at periods close to 0.93 d and 1.08 d. No additional signals were significant in the data. The investigation with `AliasFinder` led to the conclusion that the 13.68 d period is the most probable true period of the sampled signal because simulated periodograms based on this period fit the observed periodogram better than the periods close to one day. We show the corresponding plot obtained by `AliasFinder` in Fig. B.7.

An investigation of the 13.68 d signal with the s-BGLS showed that the signal was coherent and increased in probability over the observation time. We display the s-BGLS of the signal in Fig. 6.14.

6.6.4 RV modeling

Because the signal at 13.68 d showed long-term coherence and had no counterparts in the activity indicators, we fit a Keplerian model to the 13.68 d signal, hereafter referred to as HD 238090 b.

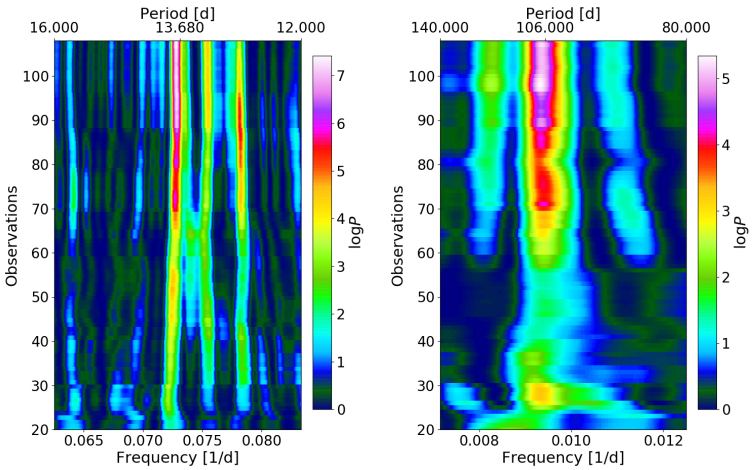


Fig. 6.14.: Stacked-Bayesian GLS of the planetary signal (left) and a signal close to the estimated stellar rotation (right).

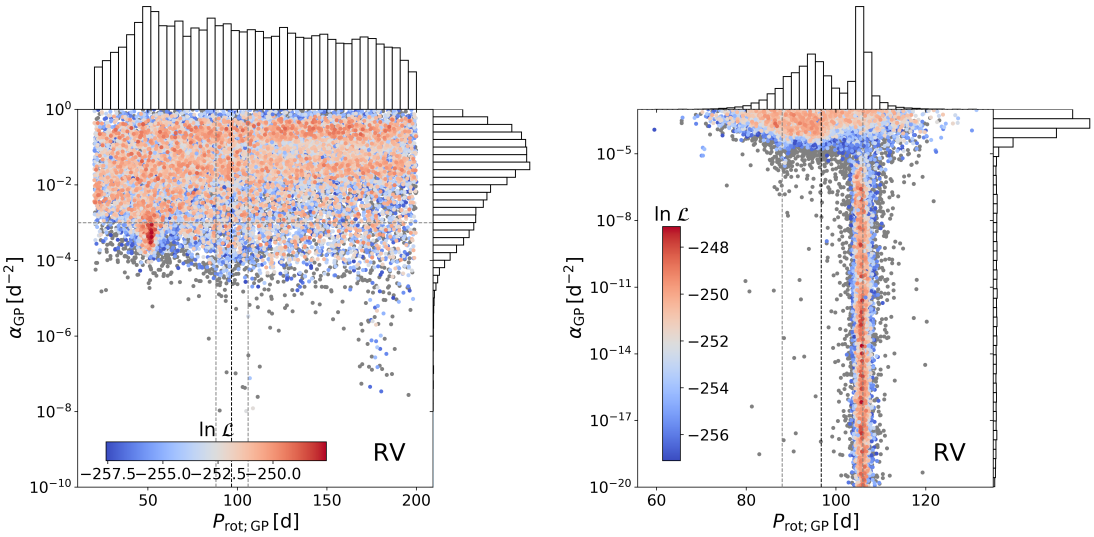


Fig. 6.15.: Posterior distribution of the GP fit to the RV data in the α_{GP} vs. P_{rot} plane for HD 238090. The color-coding shows the log-likelihood normalized to the highest value within the posterior sample. Gray samples indicate solutions with a $\Delta \ln L > 10$. *Left:* GP fit to the RV data with a wide uniform prior to the rotational period. *Right:* GP fit to the RV data with an informative normal prior based on the photometric GP results and an upper α_{GP} constraint.

Table 6.5 shows that a one-planet fit is significantly favored by the data compared to a flat model.

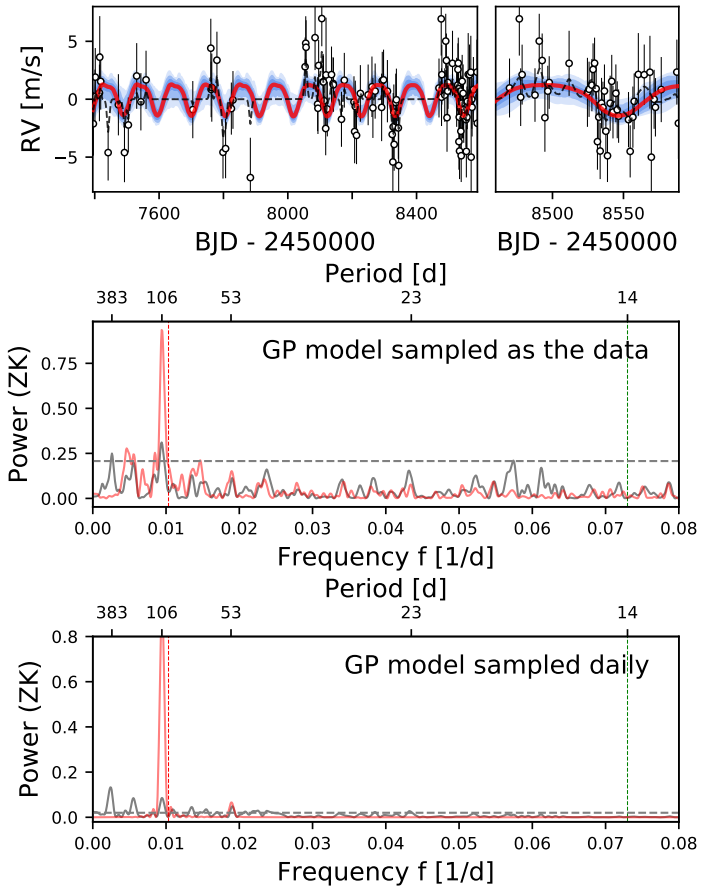


Fig. 6.16.: Gaussian-process model for the RV data of HD 238090. The planetary signal is not included in the model and subtracted from the RV data. The constrained GP model is shown in red. The blue regions shows the 1σ, 2σ, and 3σ uncertainties. We show a zoom into some CARMENES observations (top right). The GLS is evaluated on the GP model at each observed data point (top GLS) and daily (bottom GLS). The dashed line in the GLS periodograms indicates an FAP of 0.001. We also show the unconstrained GP model as the dashed black line in the upper plots and the gray periodograms in the lower plots.

The residual periodogram of a one-planet fit to the 13.68 d signal showed peaks with an FAP of almost 10^{-2} for 106.4 d. The signal at 106.4 d is below our optimal detection criterion by the GLS analysis, which is FAP $< 10^{-3}$. Additionally, it resides within the 3σ uncertainty of the derived rotation period of the star by photometry and has a counterpart in the FWHM CCF, as discussed before. An s-BGLS analysis of the 106 d signal indicated that the probability of

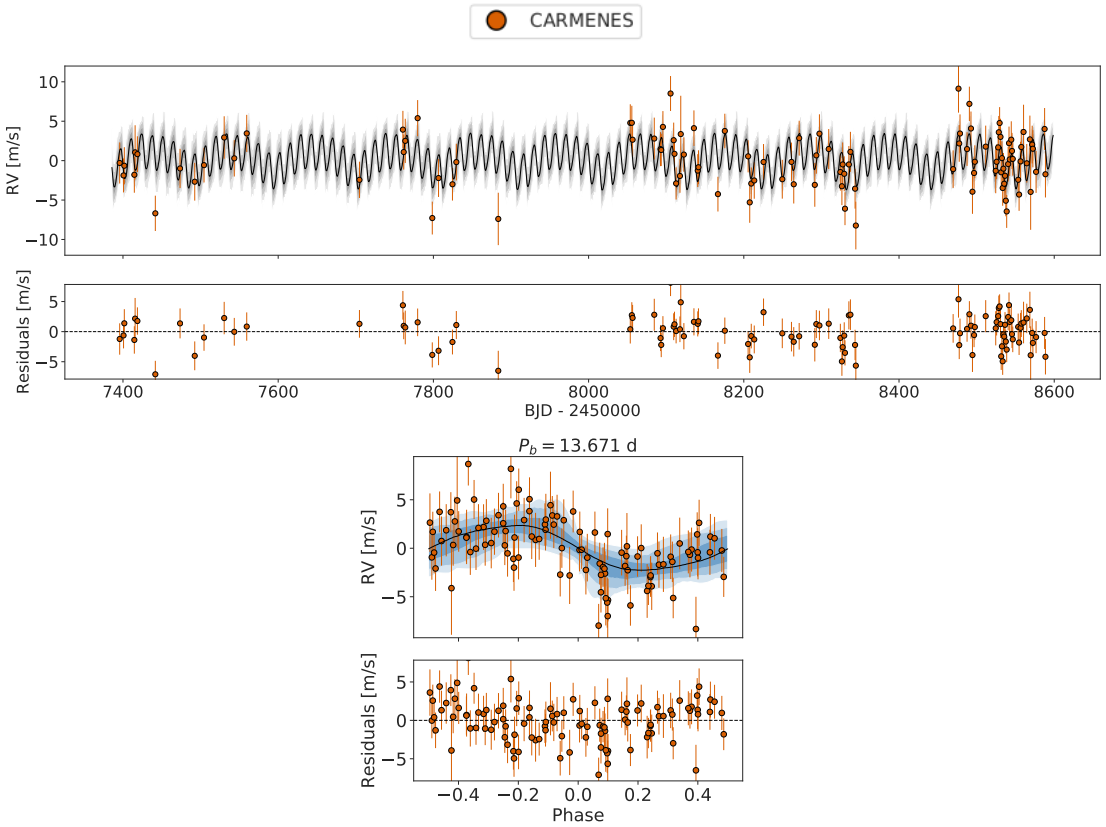


Fig. 6.17.: *Top:* Radial velocity data with a combined model for one planet and activity using a Keplerian model and a GP. *Bottom:* Plot phased to the orbital period of HD 238090 b without a GP component.

the signal decreased by almost two magnitudes after 30 observations before reappearing in later CARMENES epochs. We show the s-BGLS in Fig. 6.14.

These results indicate that the signal is probably of non-Keplerian origin. Nevertheless, we performed an additional statistical model comparison where we compared a second circular Keplerian to a GP for this signal. The two-planet fit resulted in a log-evidence improvement compared to a one-planet model of $\Delta \ln Z = 5.2$. A wide unconstrained GP to account for the 106 d signal performed equally well. Statistically, there is no clear tendency for a GP or Keplerian model. Future observations of HD 238090 might be warranted to completely exclude the possibility of a Keplerian signal with a period of 106 d, especially because such a planet would reside inside the optimal habitable zone described by Kopparapu et al. (2013). Based on the current data and our photometry, s-BGLS, and activity indicator analysis, we regard the 106 d signal as caused by stellar activity.

Tab. 6.5.: Bayesian log-evidence for HD 238090 and a number for different models based on CARMENES data.

Model[a]	Periods [d]	$\ln \mathcal{Z}$	$\Delta \ln \mathcal{Z}$
0p	...	-287.3 ± 0.1	0
GP	...	-284.9 ± 0.1	2.4
1p	13.7	-273.0 ± 0.2	14.3
1cp	13.7	-273.3 ± 0.2	14.3
1p+1cp	13.7,106.6	-267.8 ± 0.2	19.5
2p+GP	7.0, 13.7	-267.7 ± 0.2	19.4
1p+uGP	13.7	-267.0 ± 0.2	20.3
1p+GP	13.7	-267.1 ± 0.2	20.2
1cp+GP	13.7	-267.0 ± 0.2	20.3
2p+GP	13.7, 389.8	-265.1 ± 0.2	22.2

[(a)]Planetary models based on CARMENES RV data. 0p: 0 planets, 1p: 1 planet, 1cp: 1 planet in circular orbit ($e = 0$). GP and uGP: additional constrained and unconstrained Gaussian processes, respectively. Sin: additional sinusoidal model. Orbital periods rounded to one decimal.

As for GJ 251, we improved the GP modeling by constraining the prior volume (and therefore the posterior). The GP alpha-period diagram (α_{GP} versus P_{GP}) of the unconstrained GP is shown in the top plot of Fig. 6.10 and the priors are given in Table B.3. We found a posterior overdensity with a marginally higher likelihood around 50 d, which is close to half the derived photometric rotation period for the unconstrained GP. However, the distribution of posterior samples showed no peculiar structure overall and suggested that the RV data of HD 238090 are not significantly affected by a strong correlated quasi-periodic signal with decay-timescales of more than several days.

In the lower plot of Fig. 6.10 we show a GP for which we constrained the rotation parameter P_{GP} to be Gaussian distributed around the derived stellar rotation period and the timescale parameter α_{GP} to be between 10^{-3} and 10^{-20}. With the new priors, the dynamic nested sampling algorithm found posterior solutions around 106 d that reached a similar maximum likelihood as the unconstrained GP posterior samples. The log-evidence of this model was equal to the unconstrained GP. That the distribution of α_{GP} reached the prior boundary at 10^{-20} implies that this parameter converged to zero because this decay timescale is orders of magnitudes longer than the observation time.

These GP results motivated us to fix the α value to 10^{-20}, which is consistent with zero. This resulted in only three free hyperparameters to be fit by the GP. This simpler rotational GP performed similarly in terms of log-evidence as the two previously described QP-GPs. We applied this GP as the final activity model of the system, hereafter called constrained GP, and show the model in Fig. 6.16. For comparison, we plot the unconstrained quasi-periodic GP model, which included high $\alpha_{\rm GP}$ values within its posterior, in the same figure. The constrained GP model represents a more realistic fit of the data. The GP semi-amplitude is consistent within 1σ with the expected semi-amplitude that is due to the stellar rotation, estimated based on the relations of Suárez Mascareño et al. (2018), and the GP rotation period is within the 3σ uncertainty of the photometric estimate of the stellar rotation. The GLS periodogram decomposition of the constrained GP model sampled daily indicates that the GP only models the 106 d period and its first harmonic.

We performed a search for any additional planetary signal hidden behind the stellar activity with the tuned activity model. For this, we included a second Keplerian signal using a log-uniform prior between 0.5 d, and 13 d and then 14 d to 1000 d for its period, while simultaneously fitting for GJ 251 b and the stellar activity with the constrained GP. We found that the two two-planet models together with the GP did not perform significantly better than the one-planet plus GP model. We therefore preferred the one-planet model for its simplicity.

We show the final one-planet and activity model to the RV data in Fig. 6.17 and the posterior parameters in Table 6.4. We derived a nonsignificant eccentricity of $0.30^{+0.16}_{-0.17}$, as a circular model resulted in similar log-evidence. We derive the minimum mass of HD 238090 b to be $6.89^{+0.92}_{-0.95}\,M_\oplus$. We provide corner plots of all posterior samples in the appendix in Fig. B.3 and Fig. B.4, respectively.

6.6.5 Transit search with TESS

TESS observed HD 238090 (TIC 224289449) in sectors 15, 21, and 22. Based on the mass-radius relation by Zeng et al. (2016) and applying a core-mass fraction of 0.26, which corresponds to Earth-like composition, we estimated a planetary radius of $1.69\,R_\oplus$ for HD 238090 b. Given the stellar parameters of HD 238090, the transit depth was approximated to 0.72 ppt, which should be detectable in the *TESS* light curve. We investigated the *TESS* light curve around the estimated t_0 from the RV fit. We did not identify any transit event.

We calculated the TLS periodogram of the light curve and found three signals with a signal detection efficiency (SDE) > 7, which we regard as significant (Hippke & Heller 2019), at

periods of 30.00 d, 27.38 d, and 13.67 d. The first periods are close to the *TESS* sector length, while the 13.67 d period is about half the TESS sector length, but represents exactly the period of HD 238090 b. However, the time of transit center derived for the 13.67 d signal detected in the TLS is incompatible with the value obtained from the RV analysis ($t_{0,\mathrm{transit}} = 2458638.30 \pm 0.05$ BJD versus $t_{0,\mathrm{RV}} = 2458630.35 \pm 0.07$ BJD). Inspection of the *TESS* light curve showed that the presumed transits were fit at the edges or inside observational gaps of the light curves of the *TESS* sectors. We concluded that these TLS signals, although significant and close to the planetary period, represent false positives caused by the observational sampling and that no transits of HD 238090 b are detected.

6.7 Lalande 21185

Díaz et al. (2019) reported the discovery of a temperate super-Earth orbiting Lalande 21185 with a period of 12.95 d or, less likely, 1.08 d, but the period could not be determined unambiguously because of aliasing. Díaz et al. (2019) did not find evidence for a planetary candidate reported previously by Butler et al. (2017), which was supposed to orbit the star at 9.9 d. We reanalyzed the HIRES and SOPHIE data together with our CARMENES observations.

6.7.1 Photometry and spectroscopic activity indicators.

Díaz et al. (2019) took extensive photometric observations between 2011 and 2018 with the Tennessee State University T3 0.40 m automatic photoelectric telescope at Fairborn Observatory in southern Arizona. Based on their analysis, they reported a stellar rotation period of 56.15 ± 0.27 d for Lalande 21185. This rotation period is consistent with values previously obtained by Noyes et al. (1984, 48 d) and by Oláh et al. (2016, 54 d), although these studies did not provide uncertainties.

Based on the derived stellar rotation period by Díaz et al. (2019), we made use of the relations by Suárez Mascareño et al. (2018) and derived for the median $\log(R'_{HK})$ and median expected RV semi-amplitude $\log(R'_{HK}) = -5.34^{+0.53}_{-0.58}$ (mean at −5.37) and $K_{\mathrm{exp.}} = 1.50^{+7.50}_{-0.1.27}\,\mathrm{m\,s^{-1}}$ (mean at $7.27\,\mathrm{m\,s^{-1}}$), respectively.

The periodograms of the activity indicators are provided in Fig. 6.18. After subtracting the yearly signal (see Sec. 6.5.2 for discussion of this signal), we found several signals in the CARMENES activity indicators close to the reported stellar rotational period of Lalande 22185, e.g., TiO at

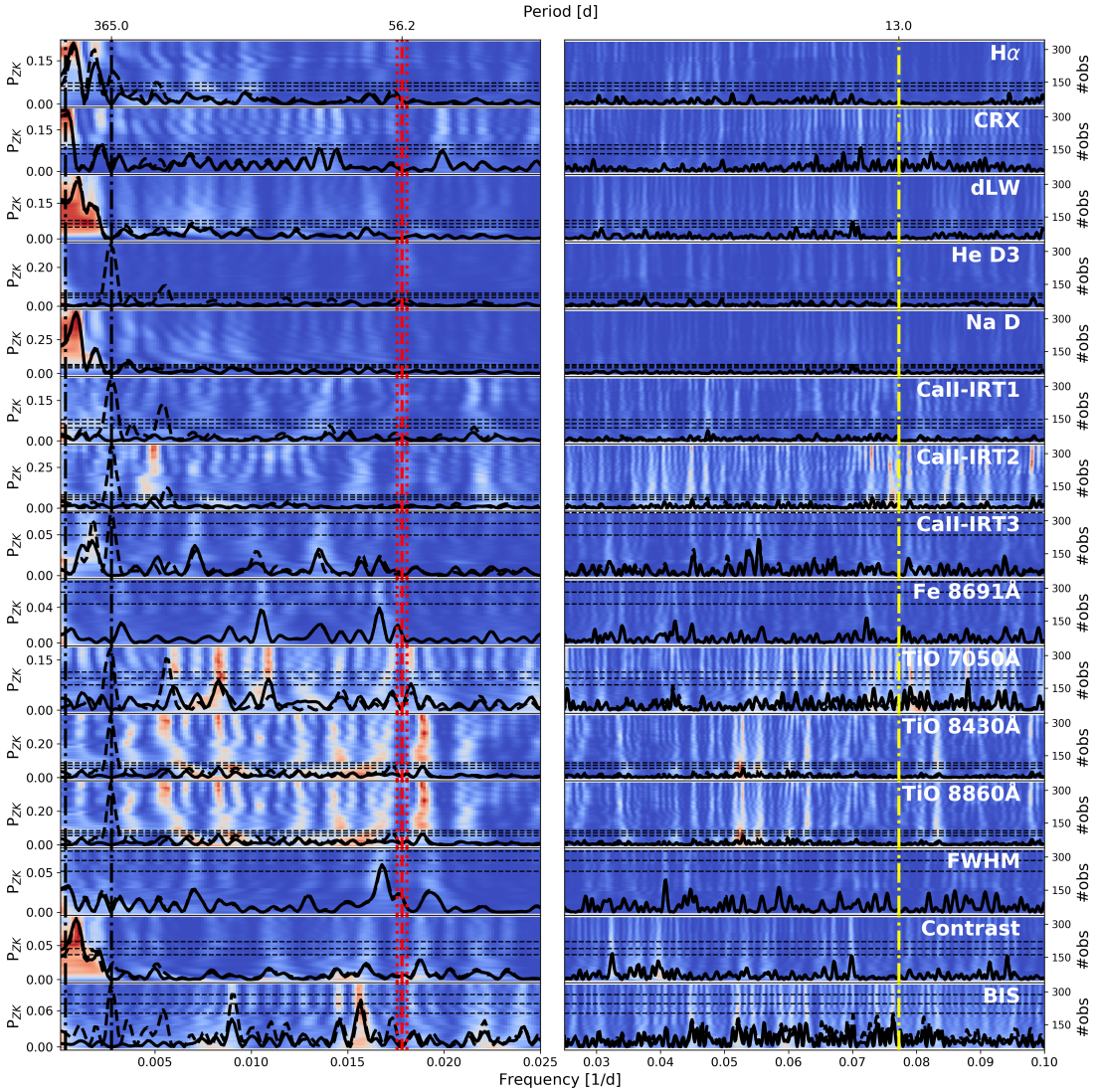


Fig. 6.18.: Generalized Lomb-Scargle periodograms of several activity indicators based on spectroscopic data obtained by CARMENES for Lalande 21185. The thinner dashed black periodograms represent the GLS on the activity indicators, and the solid GLS periodogram represents the residuals from which a 365 d sinusoidal signal was subtracted. For the residuals from which the 365 d signal was subtracted, we also overplot the s-BGLS periodogram, where the probability increases from blue to white to red. The dashed red lines mark the rotation period and the first harmonic estimated by photometric data, and the dotted red lines show the 3σ uncertainties. The dashed black lines mark a period of 365 d, 1400 d, and 2800 d, and the dashed yellow line marks the period of the planetary signal published in this work.

7050 Å with an FAP $< 10^{-1}$, TiO at 8430 Å and at 8860 Å with an FAP $< 10^{-2}$, in the FWHM with an FAP $< 10^{-1}$ and in BIS with an FAP $< 10^{-2}$. The s-BGLS of these signals show the

instability of these signals over the observation time. For the activity analysis of the SOPHIE data, we refer to Díaz et al. (2019).

In addition to these stellar rotation related signals, we observed two significant signals (FAP < 10^{-3}) in Hα at periods of 1313 d and 539 d, and around 1400 d in the dLW, the Na lines, and the contrast CCF. Additionally, we observed a linear trend in the CRX. In the CRX, dLW, and the Na lines, we identified signals at roughly 14 d (with FAPs of < 0.1, < 0.01, and ~ 0.1, respectively), which is about 1/4 of the stellar rotational period, but close to the claimed planetary signal by Díaz et al. (2019). Owing to the long CARMENES time baseline, the GLS periodogram resolution allows us to separate these peaks from the planetary signal at 12.95 d.

6.7.2 Periodogram analysis

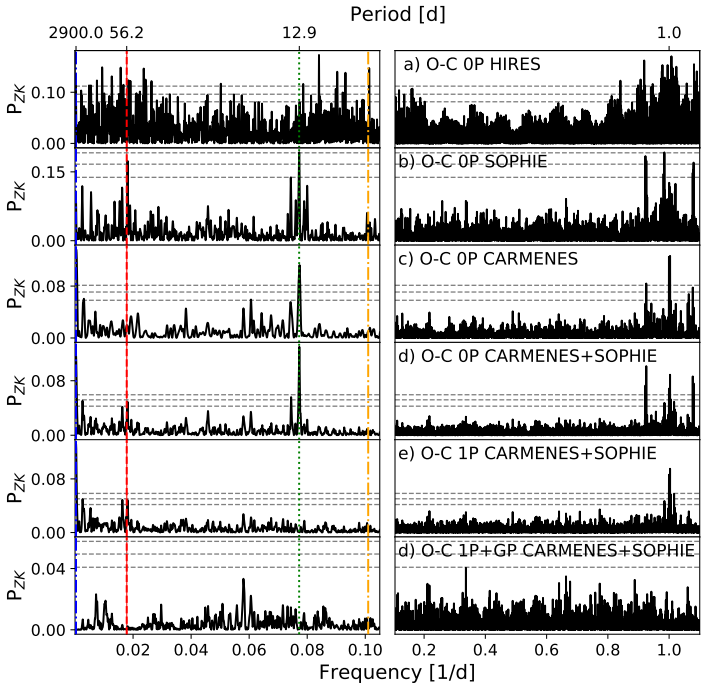
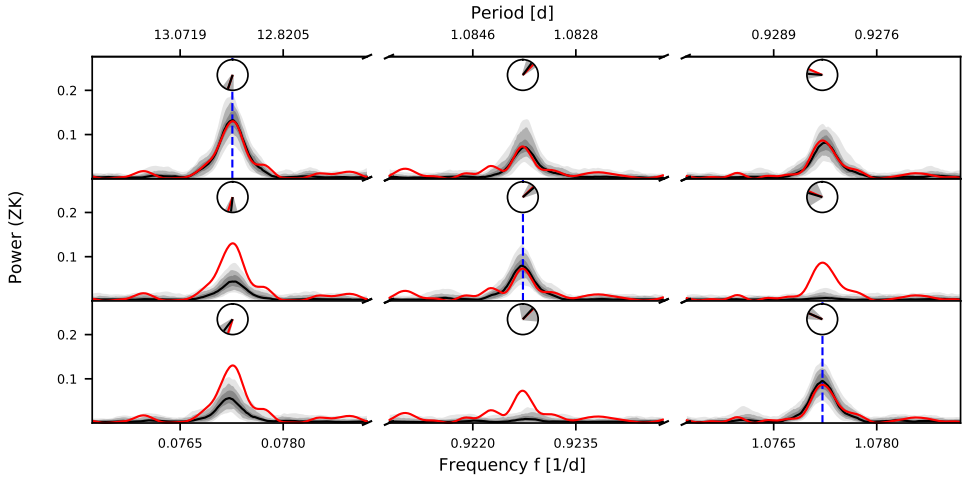


Fig. 6.19.: Generalized Lomb-Scargle periodograms of Lalande 21185 for the different data sets and the combined CARMENES and SOPHIE data. Residual periodogram of the one-planet fit and the one-planet GP simultaneous fit for the combined CARMENES and SOPHIE data are also shown. Marked frequencies represent the claimed planet at 12.95 d by Díaz et al. (2019) (green), photometric stellar rotational period (red), the claimed planet candidate by Butler et al. (2017) (orange), and the long-term period (blue).

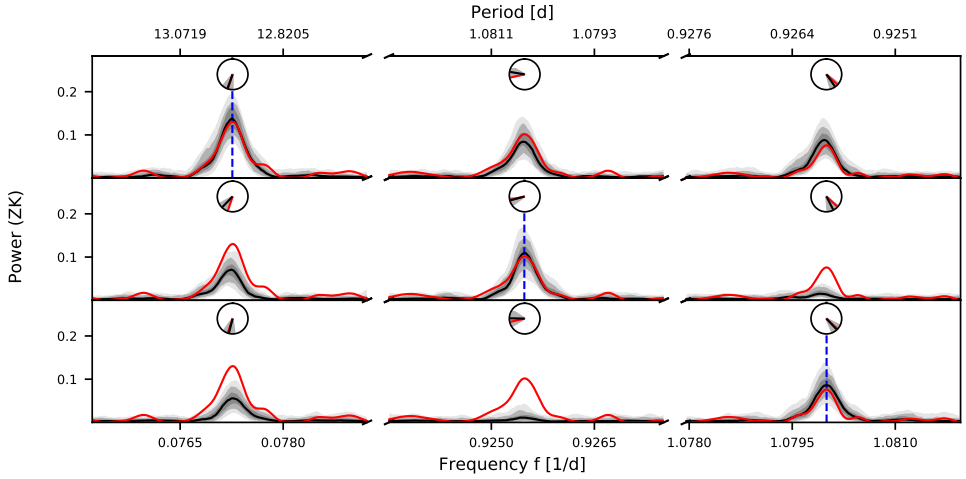
Fig. 6.19 displays our GLS periodograms for the CARMENES, SOPHIE, and HIRES data, as well as residual periodograms for different models fit to the combination of CARMENES and SOPHIE data. The CARMENES and the SOPHIE GLS periodograms show a significant peak at a period of 12.95 d, which is the period of the planetary signal published by Díaz et al. (2019). With our CARMENES data alone, we can confirm this signal. In addition to the 12.95 d signal, the SOPHIE data show a signal at 55 d, with an FAP $< 10^{-2}$, which is consistent with the stellar rotation period of 56.15±0.27 d. The CARMENES data also show a significant long-period signal at 2677 d. A linear trend has been reported by Díaz et al. (2019) from the SOPHIE data. With the addition of the CARMENES data, we now observed a long period.

Neither the CARMENES data nor SOPHIE data or their combination shows a significant signal at 9.9 d, where a signal was claimed by Butler et al. (2017) using HIRES data. This signal is visible with an FAP $< 10^{-3}$ in the periodogram of the HIRES data, but we find many more signals with similar or higher significance in the periodogram of the HIRES data, with amplitudes of a few m s^{-1}. All these signals are absent in the SOPHIE and CARMENES data, however. The time baseline of the combined CARMENES and SOPHIE observations is about 8.2 yr, and the precision of both instruments should be appropriate to identify these signals if they were still present in the RVs of Lalande 21185. The highly significant presumably planetary signal at 12.95 d, with an amplitude of roughly 1.4 m s^{-1} in the CARMENES and SOPHIE data, cannot be identified in the periodogram of the HIRES data. The amplitude of the signal might not be large enough for HIRES because it is at the limit of the long-term precision, which has been about 1–2 m s^{-1} since 2004 (Butler et al. 2017). The sampling of the HIRES data shows many nights with multiple observations. After applying a nightly binning scheme on the HIRES data, the GLS periodogram showed no peak with an FAP $< 10^{-2}$. Because the 12.95 d signal is absent in the HIRES data and the forest of significant but spurious signals at various frequencies, we restrict the RV analysis to the combined SOPHIE and CARMENES data sets and treat the HIRES data individually.

Díaz et al. (2019) reported that the SOPHIE data did not allow determining the orbital period of the planetary signal unambiguously because of aliasing. By adding our CARMENES data and using the `AliasFinder`, we can confirm that the sampled signal has a period of 12.95 d because the `AliasFinder` simulations were able to reproduce the properties of the observed periodogram only when this period was assumed to be the correct one. We show the relevant plots in Fig. 6.20.



(a)



(b)

Fig. 6.20.: Alias tests for Lalande 21185. The top plot (a) shows simulations motivated by a sampling frequency of $f_{s_1} = 1.0000\,d^{-1}$. The bottom plot (b) shows simulations motivated by a sampling frequency of $f_{s_2} = 1.0027\,d^{-1}$. Each row in these plots corresponds to one set of simulations for which the frequency of the injected signal is indicated by a vertical dashed blue line. The first row shows simulations with a period of 12.95 d, and the second and third row show the simulations in which the first-order aliases of 12.95 d, regarding the investigated sampling frequency, were injected. Each column shows informative ranges of the periodograms based on the assumed sampling frequency and can be used to compare data and simulations. From 1000 simulated data sets, we show the median of the obtained periodograms (solid black line), the interquartile range, and the ranges of 90% and 99% (gray shades). The periodogram of the observed data is plotted with a solid red line. The angular mean of the phase and the standard deviation is shown in the clock diagrams (black line and gray shades) and can be compared to the phase of the signals in the observed periodogram (red line).

Tab. 6.6.: Bayesian log-evidence for Lalande 21185 and a number of different models based on CARMENES, SOPHIE and combined data.

Model[a]	Periods	$\ln \mathcal{Z}$	$\Delta \ln \mathcal{Z}$
	CARMENES		
0p	...	-797.5 ± 0.1	0
1p	12.9	-783.7 ± 0.2	13.8
1p+uGP	12.9	-748.1 ± 0.2	49.4
	SOPHIE		
0p	...	-371.6 ± 0.1	0
1p	12.9	-362.4 ± 0.2	9.2
1p+uGP	12.9	-349.0 ± 0.2	22.6
	CARMENES + SOPHIE		
0p	...	-1169.5 ± 0.2	0
2p+GP	1.5,12.9	-1161.8 ± 0.3	7.7
1p	12.9	-1143.0 ± 0.2	26.5
1cp	12.9	-1142.2 ± 0.3	27.3
GP	...	-1125.4 ± 0.2	
1p+uGP	12.9	-1092.3 ± 0.3	77.2
2p+GP	12.9, 364.5	-1086.2 ± 0.3	83.3
1p+GP	12.9	-1085.7 ± 0.3	83.8
1cp+GP	12.9	-1085.3 ± 0.3	84.2
	HIRES		
0p	...	-777.7 ± 0.2	0
1p[b]	12.5	-761.5	16.2
1p[c]	12.9	-771.8	5.9

[a]Planetary models based on CARMENES, SOPHIE, HIRES and combined CARMENES and SOPHIE RV data. 0p: 0 planets, 1p: 1 planet, 1cp: 1 planet in circular orbit ($e = 0$). GP and uGP: additional constrained and unconstrained Gaussian processes, respectively. Orbital periods rounded to one decimal. [b]Priors as in Table B.2. [c]Gaussian priors for planetary parameters based on posterior solution from Table 6.4.

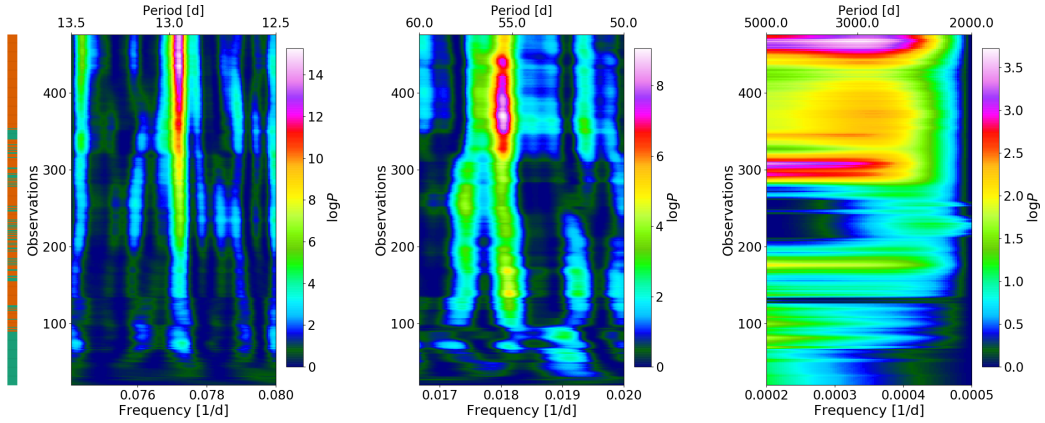


Fig. 6.21.: Stacked-Bayesian GLS periodogram of Lalande 21185. The color bar to the left color-codes each observation with the associated spectrograph (*orange*: CARMENES, and *teal: SOPHIE*). *Left:* s-BGLS of the zero-planet model at the period of the planetary signal. *Middle*: s-BGLS on the residuals of the one-planet fit with a period of 12.95 d shown around a period of 55 d, which is the rotational period determined by Díaz et al. (2019). *Right:* s-BGLS on the residuals of the one-planet fit around the observed long-period signal.

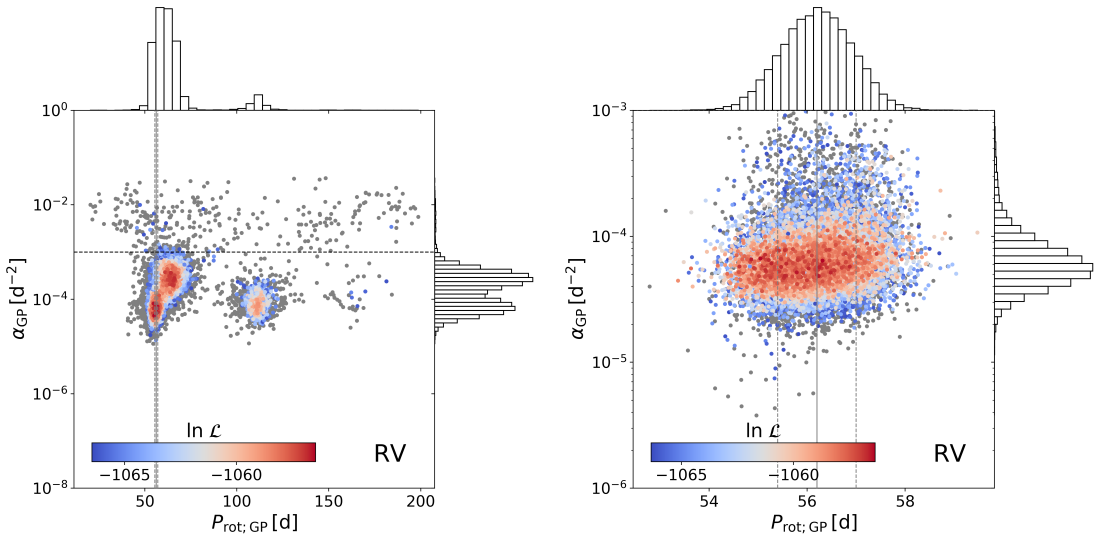


Fig. 6.22.: Posterior distribution in the GP_α vs. P_{rot} plane for Lalande 21185. The color-coding shows the log-likelihood normalized to the highest value within the posterior sample. Gray samples indicate solutions with a $\Delta \ln L > 10$. *Left:* GP fit to the RV data with a wide uniform prior to the rotational period. *Right:* GP fit to the RV data with an informative normal prior based on the photometric rotational period proposed by Díaz et al. (2019).

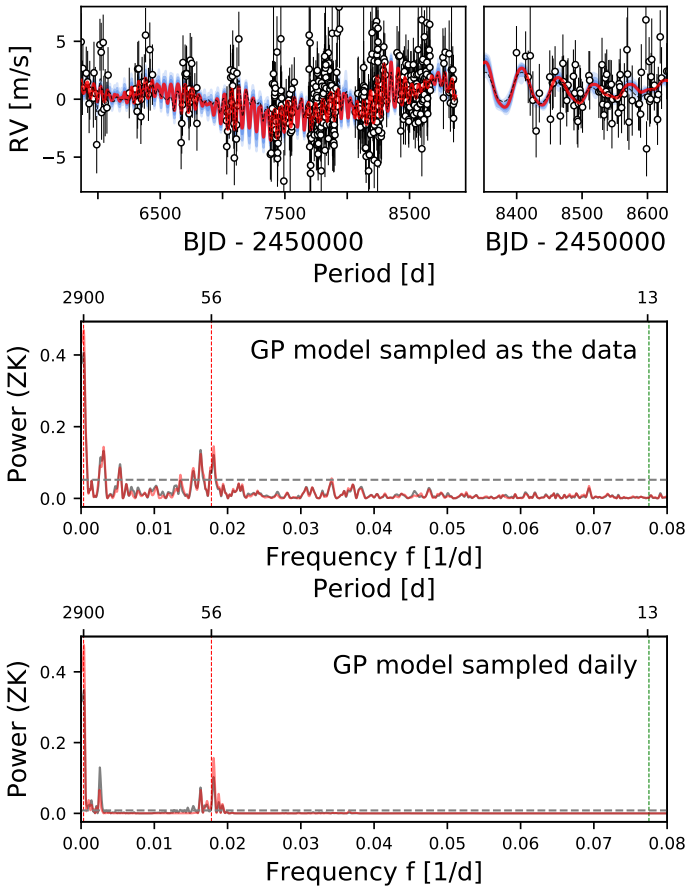


Fig. 6.23.: Gaussian process model for the RV data of Lalande 21185. The planetary signal is not included in the model and subtracted from the RV data. The constrained GP model is shown in red. The blue regions shows the 1σ, 2σ, and 3σ uncertainties. We show a zoom into some CARMENES observations (top right). The GLS is evaluated on the GP model at each observed data point (top GLS) and daily (bottom GLS). The dashed line in the GLS periodograms indicates an FAP of 10^{-3}. We also show the unconstrained GP model as the dashed black line in the upper plots and as the gray periodograms in the lower plots.

6.7.3 RV modeling with CARMENES and SOPHIE

We fit a Keplerian model to the 12.95 d signal (see Table 6.6 for the log-evidence). The GLS periodogram of the residuals of the combined data set reveals additional significant signals at periods of 2852 ± 568 d with an FAP $< 10^{-3}$ and at 55.3 ± 0.2 d, 61.3 ± 0.3 d and 383.8 ± 10.6 d

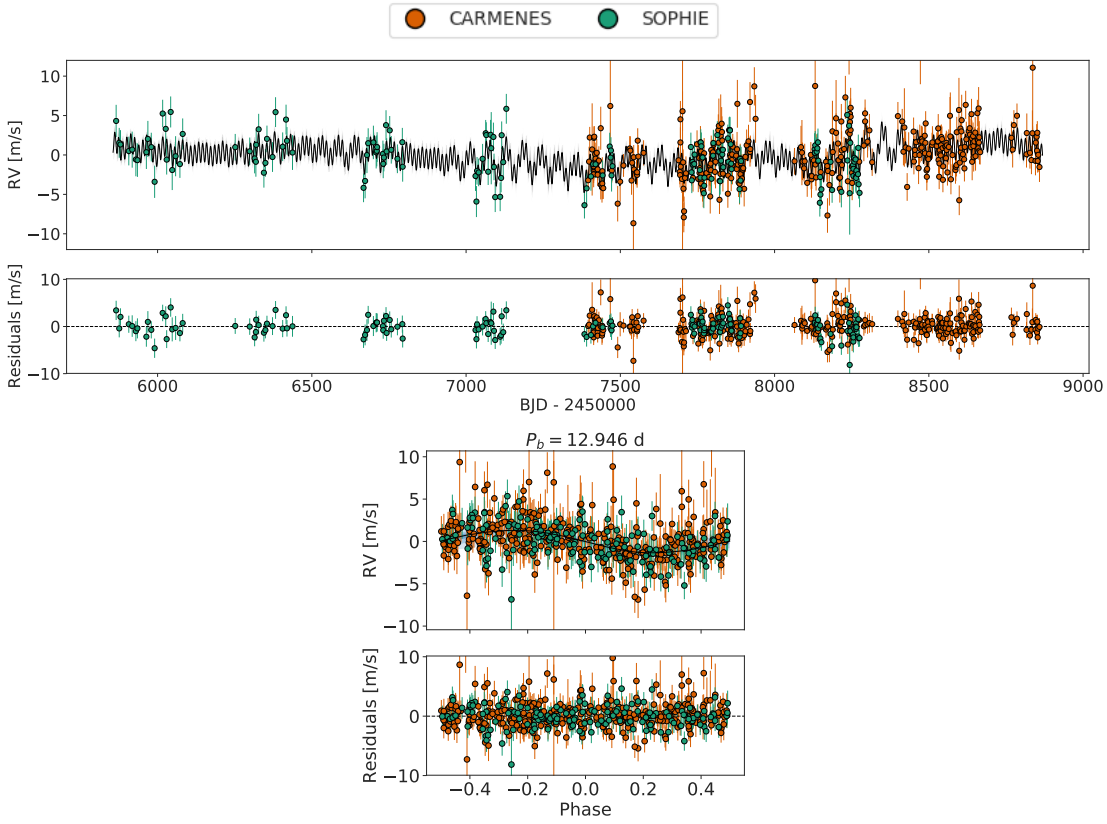


Fig. 6.24.: *Top:* Radial velocity data with a combined model for one planet and activity using a Keplerian model and a GP. *Bottom:* Plot phased to the orbital period of Lalande 21185 b without a GP component.

with an FAP < 0.01. The long-period signal is highly significant in the combined data set, but we find significant variations at similar periods or half this period in some of the activity indicators, mainly in CRX and Hα.

The s-BGLS was used to assess the coherence of all these signals. We show the s-BGLS of the combined data set around the orbital period of the planet signal at 12.95 d and the s-BGLS of the one-planet fit residuals around the long-periodic signal and the stellar rotational period in Fig. 6.21. The data are ordered chronologically. The signal probability of the suspected planetary signal at 12.95 d increases and shows coherence over the entire observation time. The signal at 55 d, which we related to the stellar rotational period, shows an increase in signal probability until roughly 360 observations and has decreased since then by about four orders of magnitude in probability. A similar pattern but anticorrelated to the rotational signal in terms of signal probability over time is visible for the long-period signal.

Based on the results on the activity indicators and the s-BGLS analysis, we find that the period around 2800 d can be best explained by a long-term activity cycle. We fit a simple sinusoid to this signal in order to search for additional signals. The residual periodogram of the one-planet + sinusoid fit has one remaining significant signal at 55.3 d. A fit of this signal, which represents the rotational period, with a second sinusoid, resulted in a flat periodogram; no peaks in the GLS periodogram reach an FAP < 0.1. Based on CARMENES and SOPHIE RV data, the Lalande 21185 system can be explained by one Keplerian model with an orbital period of 12.95 d, and two sinusoids that model the activity contribution.

We fit the system using a one-planet model simultaneously with a GP model, which accounts for these activity-related signals. In a first step, we fit a rather unconstrained GP to the data simultaneously with the one-planet Keplerian model. In the top plot of Fig. 6.22 we show the posterior sample distribution in the $\alpha_{\rm GP}$ versus $P_{\rm rot}$ plane for this fit to Lalande 21185. Most of the posterior samples peak with a bimodal distribution at a period of 55 d and 65 d and at rather low α-values representing a stable quasi-periodic signal. We also see fewer posterior samples around 100 d but with a lower likelihood. The 65 d signal was already visible in the residuals of a simple one-planet fit and belonged to an alias of the rotational period based on a yearly sampling frequency $f_s = 1/365.25\,d^{-1}$. In the next step, we fit a more constrained GP with a normal prior on the GP rotational period based on the photometric estimates and its 3σ uncertainty and additional constraints in Γ and α deduced from the posterior distribution of the unconstrained fit as before. The priors of the applied GP models are provided in Table B.3. This GP fit resulted in a significant improvement of the log-evidence compared to the unconstrained GP and represented the best model we derived for this system (see Table 6.6). This GP fit is compatible with the estimated RV semi-amplitude from the stellar rotation period given the relations by Suárez Mascareño et al. (2018).

We show the GP model and a GLS periodogram analysis to assess its temporal behavior in Fig. 6.23. We identify that in addition to the 56 d and long-term period, signals at about 380 d and 60 d are modeled. As for the other two targets, we searched for planetary signals hidden behind the stellar activity by sampling for a second Keplerian, using a log-uniform prior between 0.5 d, and 12 d and then a log-uniform prior from 13 d to 3000 d for the second Keplerian, while simultaneously fitting the stellar activity with our final GP model. The two two-planet models combined with the GP performed worse in log-evidence (see Table 6.6) than the one-planet model combined with the GP; this means that no additional Keplerian signal is statistically supported by the data. A plot of the final one-planet and GP model, the RV data, and a phase plot to the planetary period of Lalande 21185 b are provided in Fig. 6.24. The updated orbital parameters of Lalande 21185 b based on the posterior solutions of the fit to the combined CARMENES and

SOPHIE data are given in Table 6.4. Additionally, we list further derived planetary parameters, such as the planetary minimum mass, which is estimated to $2.69 \pm 0.25\,M_\oplus$.

6.7.4 HIRES RV data

We excluded the HIRES data from our final analysis of Lalande 21185 because of spurious frequencies, noisy data and the absence of an obvious planetary signal. We fit a one-planet model with the same priors as for the SOPHIE and CARMENES data to the HIRES data. For example, for the period, we used $\mathcal{U}(12.5, 13.5)$. While this improved the log-evidence significantly, it resulted in an inconsistent orbital period of $12.57^{+0.002}_{-0.001}$ d and an extremely high eccentricity of $0.9^{+0.04}_{-0.04}$.

We also tested more informed priors. For instance, we applied normal priors to every planetary parameter based on the solution of the fit to the CARMENES and SOPHIE data. This fit performed reasonably well because it was still significantly better than a flat model, which could indicate that the planetary signal is apparent in the HIRES data. However, the same model fit to the daily-binned HIRES data did not result in a log-evidence improvement compared to a zero-planet model. The noise level of the HIRES data compared to the other data sets and the small planetary amplitude, which is at the limit of the HIRES long-term precision, justifies the exclusion of this data set. Nevertheless, we used the extended HIRES time baseline to analyze the long-period signal. With HIRES, we have a total of 737 RV observations for Lalande 21185. We find that the long-period signal is also apparent in the HIRES data. However, the HIRES data between BJD 2452200 and 2453200 indicate a possible phase shift of that signal, consistent with our analysis that this signal is caused by a long-term activity cycle. We fit our simplistic model of one planet at 12.95 d, and two sinusoids, to the combined CARMENES, SOPHIE, and HIRES data. The residual GLS periodogram of this fit had no peaks with an FAP $< 10^{-3}$, indicating that the HIRES data do not indicate an additional coherent signal when combined with CARMENES and SOPHIE data.

6.7.5 Transit search with TESS

TESS observed Lalande 21185 in sector 22, but the star was not announced as a TOI. We ran our independent signal search with the TLS on the PDCSAP light curve. We find only one peak with SDE > 7 (Hippke & Heller 2019), which is at 13.0 d, very close to the planetary orbital period derived from the RV fit, just as for HD 238090. However, peaks in this period range are visible

in many light curves and are often caused by the observational gap of the *TESS* observations. Nevertheless, as for HD 238090, we performed a transit fit to this signal using `juliet` to evaluate how such a fit performs compared to a nontransit model. The log-evidence of a transit model was not significantly different ($\Delta \log Z \approx 0.5$), indicating that a simpler nontransit model is better than a transit model. The derived minimum mass of the planet was used to estimate the radius with the mass-radius relation of Zeng et al. (2016). With an approximated radius of 1.33 $R_\oplus$, the transit depth was approximated to 0.97 ppt for Lalande 21185 b. We were unable to identify any transit events around the RV estimated time of transit center for Lalande 21185 b.

6.8 Discussion

6.8.1 GJ 251

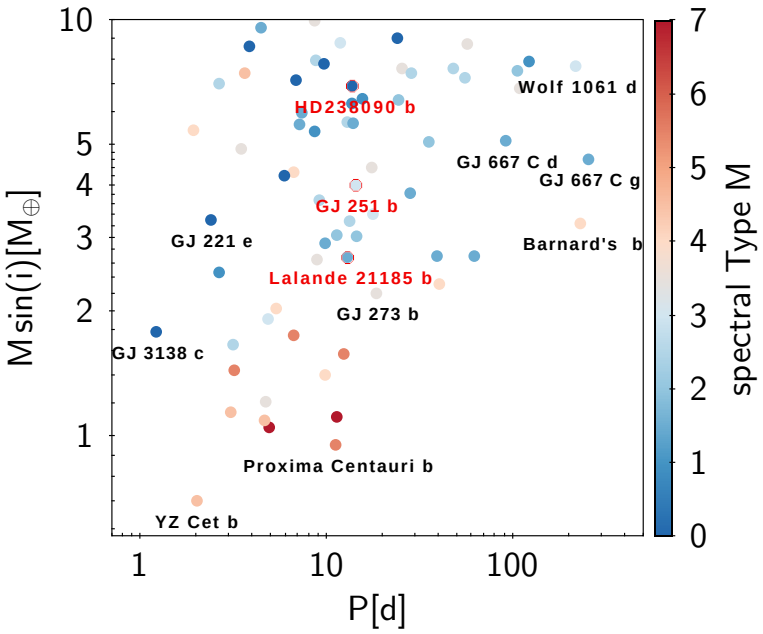


Fig. 6.25.: Confirmed exoplanets around M-dwarf host stars, detected with the RV method and with minimum masses below 10 $M_\oplus$ and orbital periods between 1 d and 400 d. The color-coding represents the spectral type. GJ 251 b, HD 238090 b, and Lalande 21185 b are marked in red. Data taken from `http://exoplanet.eu`.

Based on our analysis of CARMENES and HIRES RV data, we report the discovery of GJ 251 b, a planet that orbits its host star with a period of 14.24 d. The posterior sample median eccentricity is $0.10^{+0.09}_{-0.07}$, which is not significant and consistent with zero, as shown by a log-evidence

comparison with circular Keplerian models. In Fig. 6.25 we place GJ 251 into context with other confirmed exoplanets around M dwarfs detected with the RV method and the other two planets discussed in this work. The equilibrium temperature of GJ 251 b, assuming a zero Bond albedo, is $351.0^{+1.4}_{-1.3}$ K (see Table 6.4). Our minimum mass and temperature estimates add GJ 251 b to the family of temperate super-Earths. The planet receives about 2.5 times the flux of Earth. Of the three planets discussed in this work, GJ 251 b is the planet with the most moderate temperature. However, according to Kopparapu et al. (2013), the planet is too close to its host star to be in the habitable zone, that is, to allow liquid water on its surface.

Butler et al. (2017) previously claimed a planetary candidate for GJ 251 with an orbital period of 1.74 d. Our analysis of the CARMENES data and the combined data from CARMENES and HIRES did not confirm this claim. An independent analysis of the HIRES data does not identify any signal close to the 1.74 d period as significant. We note that Butler et al. (2017) used a different approach based on autocorrelation functions and a statistical model for the RVs, including a moving average to model correlated noise and information provided by the activity index based on Ca II lines.

The HIRES RV data show a significant second RV signal around 600 d. This signal was also visible during some epochs in the CARMENES data, but because the signal is incoherent and a significant Hα activity signal lies at the same period, we attribute this signal to nonplanetary origin. Any other additional significant signals can be best explained by the stellar rotation of GJ 251 or its harmonics. In the current RV data, we find no evidence for a second companion in the GJ 251 system. There is also no significant linear trend in the RV data over the entire time baseline of the combined HIRES and CARMENES observations, which is about 15.0 yr. However, the *Gaia* DR2 (Gaia Collaboration et al. 2018) catalog lists a significant astrometric excess noise for this star, which could be caused by a massive companion on a wide orbit.

6.8.2 HD 238090

Our analysis of CARMENES RV data shows that HD 238090 is orbited by a warm super-Earth, HD 238090 b, with an orbital period of 13.69 d. The posterior sample median eccentricity is $0.30^{+0.16}_{-0.17}$, which, as in the case of GJ 251, is not significant. HD 238090 b has a minimum mass of roughly 6.8 $M_\oplus$, and orbits its host star at a separation of approximately 0.093 au with an equilibrium temperature of 470 K (see Table 6.4). With total insolation about eight times that of Earth, the planet is too close to the host star to sustain liquid water on its surface. Figure 6.25 shows the position of the planet in the minimum mass-period plane.

6.8.3 Lalande 21185

Our analysis of the CARMENES and combined CARMENES and SOPHIE RV data for Lalande 21185 confirms the findings by Díaz et al. (2019) regarding Lalande 21185 b. With our data, we can break the degeneracy between the daily aliases and confirm that the planet orbits the star with a period of 12.95 d. With the additional CARMENES observations, we have reduced the uncertainties of most planetary parameters by a factor of two or more compared to the estimates by Díaz et al. (2019).

The CARMENES data of Lalande 21185 agree well with the SOPHIE data but cast doubt on the HIRES data for this system. With 476 precise high-precision RVs for the system by CARMENES and SOPHIE, we find no evidence for a second planet in the system. In particular, the planet candidate claimed by Butler et al. (2017) at a period of 9.9 d is absent in the CARMENES and SOPHIE RV data. In addition to the 12.95 d signal, there are two additional significant signals in the combined CARMENES and SOPHIE data set at 55.3 d and 2800 d, which can be attributed to the stellar rotation and possible long-term activity, respectively.

6.8.4 Formation scenario

The planetary systems presented in this work represent systems that share similar orbital properties (period, separation, insolation, and equilibrium temperature) and minimum masses that place them into the group of temperate or warm super-Earths. While the available data are insufficient to draw definite conclusions on the exact formation channel of these systems, the derived orbital and planetary parameters allow for some cautious conjectures. These planets are commonly thought to form by combined accretion of planetesimals and pebbles (e.g., Ormel & Klahr 2010; Lambrechts & Johansen 2012; Bitsch 2019).

Their final masses can be best explained if the supply of pebbles was cut off during their formation, preventing their evolution into gas giants. One way to stop the supply of solid material from the outer disk is the emergence of a massive companion that stops the pebble flux by opening a gap in the protoplanetary disk (Ormel 2017). However, we do not see evidence for additional planets in any of the three systems, even though the available long-baseline data allow for a strong sensitivity for the detection of such companions in the cases of GJ 251 and Lalande 21185.

Another proposed mechanism to terminate pebble accretion is self-isolation from the pebble flux by modulation of the gas pressure profile by the growing planet (Morbidelli & Nesvorny 2012; Lambrechts et al. 2014). For all three planets, their combination of mass and orbital separation

would be consistent with this possibility. In this case, the measured masses are simply their pebble isolation masses, regardless of other planets in the system. On the other hand, systems such as those presented here can also be explained by models that grow solid cores only by accretion of planetesimals. In this scenario, planetary core growth can reach a natural stall before entering runaway gas accretion because the accretion efficiency is lower than pebble accretion (Emsenhuber et al. 2020a,b). In a related study focusing on planet formation around low-mass stars, planets similar to our discoveries are among the most abundant in a synthetic planet population (Schlecker et al. 2020, ; Burn et al. in prep.). While the model by Burn et al. (in prep.) predicts an average multiplicity higher than one for super-Earths, the singular detection in GJ 251, HD 238090, and Lalande 21185 could be explained by planets with lower masses or wider orbits that do not reach the RV semi-amplitudes necessary for robust detection, especially in the case of strong activity.

6.9 Summary

We presented the discovery of two super-Earth planets around the low-mass stars GJ 251 and HD 238090 with orbital periods of 14.24 d, and 13.67 d, respectively, based on CARMENES VIS RV observations. For GJ 251, we additionally used RV data obtained by HIRES in order to increase the time baseline and to search for additional signals. We also confirmed the nearby temperate super-Earth Lalande 21185 b recently discovered by Díaz et al. (2019), and we can robustly determine its orbital period to be 12.95 d. No transits could be detected with *TESS* for any of the three systems. The RV data of GJ 251 and Lalande 21185 exhibit long-term periods, which we attribute to activity. Furthermore, all three systems show RV signals related to the stellar rotation period in the RV residuals of the planetary fits.

We modeled the stellar activity using GP models based on a quasi-periodic kernel simultaneously with the Keplerian signals. In particular, we carefully modeled the stellar activity by applying physically motivated constraints to the GP hyperparameters to ensure that the GP did not fit any signal unrelated to stellar activity. We advocate the use of classical periodograms to decompose the modeled frequencies by GPs. Such an analysis can be used as verification of the desired GP behavior on the data set. Nevertheless, the unconstrained GP posterior distribution can provide useful information on the stellar activity. In particular, we used the the GP timescale versus GP rotation plane to infer more information about possible rotation periods and lifetimes of stellar surface features. For the analysis of the RV data, we used various advanced tools, such as `juliet` together with a Bayesian approach based on the log-evidence, `AliasFinder` to further

distinguish samples signals and their aliases, and the s-BGLS to further constrain the planetary or stellar origin of the signals in addition to a classical periodogram analysis of an extensive number of activity indicators. We showed that with good statistical models, priors from auxiliary data, and elaborate simulations, planetary signals can be recovered and modeled that are on the order of the noise or even slightly weaker. The properties of all our detections are consistent with current formation scenarios regarding super-Earth planets.

7 Discussion and Conclusion

> *Life is like riding a bicycle. To keep your balance, you must keep moving.*
>
> — **Albert Einstein**
> (1879-1955)

This thesis' work has mainly addressed the detection and characterization of exoplanets around M-dwarf stars using radial velocity (RV) data, collected by the CARMENES survey. The RV measurements of M-dwarf stars, which rank among the most active stars in the Universe, typically contain signals related to the star's rotational activity. This makes it challenging to detect RV signals of low-mass planets orbiting these stars in the temperate zone since such planetary RV signals have similar amplitudes and periods as the activity signals. Additionally, the applied observational cadence in search of these planets, coupled with a low signal-to-noise ratio of the data, can lead to aliasing, complicating the planetary periods' determination. The results I have obtained and presented in this thesis demonstrate that it is possible to detect and precisely model planetary RV signals at the limit of the stellar astrophysical noise, in particular, if statistical models in a Bayesian framework, Gaussian process (GP) models, prior information from auxiliary data, simulations, and modern tools like `AliasFinder` (Stock & Kemmer 2020) or the Bayesian GLS periodogram (Mortier et al. 2015; Mortier & Collier Cameron 2017) are combined for the analysis of the data. By using these methods for RV data, primarily obtained by the CARMENES survey, two new planets have been discovered and four already known planets have been characterized more precisely. The results and applied methodologies within this thesis have contributed to a better understanding of aliasing and of modeling correlated noise within RV data of active M-dwarf host stars.

Although GPs were applied to RV data for the first time almost a decade ago (Aigrain et al. 2012), the widespread usage and acceptance of this method within the RV and transit community has only begun to gain momentum in recent years. In particular, the community has just recently started to deeply analyze the exact behavior of different GP models for real and simulated data (see, for example, Rajpaul et al. 2015; Angus et al. 2018; Nava et al. 2020; Gilbertson et al. 2020; Cabot et al. 2021; Perger et al. 2021). This recent spike of interest for GPs is motivated

by the fact that these types of models are highly required when it comes to the modeling of data collected by current and future high-resolution RV surveys that search for Earth analogs and that reach instrumental precisions below the level of the stellar astrophysical noise. Investigations on GP kernel functions for simulated data sets are crucial in assessing parameter degeneracies, physical parameter interpretation, and possible absorption of planetary signals by the GP model. Nevertheless, despite the recent rise in interest, there are still not enough investigations on GP behavior and their performance on simulated data sets.

To investigate the properties of GP models, I simulated RV data and performed numerical experiments. In particular, the RV signal of an active M-dwarf star has been simulated using the tool `StarSim` (Herrero et al. 2016). These numerical experiments allowed investigating several controversial aspects of GP models. The modeling of the stellar astrophysical noise within this thesis has been carried out with the quasi-periodic (QP) GP kernel provided within the package `george` (Ambikasaran et al. 2015). The results show that the QP-GP kernel is a robust tool to derive stellar rotation periods and model RV variations due to stellar activity. Fitting GP models to simulated RV data proved that the GP is capable to accurately and precisely reproduce the simulated rotation period in the vast majority of cases. Additionally, it was also possible to derive an estimate of the simulated typical starspot lifetime for many simulated data sets.

However, a constant offset between the GP length-scale hyperparameter, which is the quantity connected to the typical lifetime of active regions, and the spot lifetime simulated in `StarSim` has been observed. Within the small number of simulated cases, the correction factor between the QP-GP length-scale parameter l and the simulated spot lifetime P_{life} by `StarSim` has been found to be $2\,l \approx P_{\mathrm{life}}$. This estimate is consistent with a value of $1.7\,l \approx P_{\mathrm{life}}$ found in Perger et al. (2021). However, this result should be viewed with some caution. It is a priori not clear how well the squared-exponential kernel can model the lifetime of a single starspot or even an ensemble of spots. For example, the decay of the starspot in the `StarSim` model is assumed to be linear while the kernel follows a Gaussian shape. Additionally, in the case of a positional correlation of spots, e.g., active longitudes, it can happen that recurring spots will increase the estimated spot lifetime as they are able to produce a coherent long-lived signal. The length-scale hyperparamter can, therefore, not directly be connected to the stellar physics of the star and it should be more regarded as an effective model parameter. Nevertheless, the numerical experiment of fitting these QP-GP models to the simulated data demonstrated that the QP-GP kernel, although computationally demanding, represents an adequate noise model of stellar activity superior to sinusoidal models. However, the correct application of the GP to the data, especially, the prior settings of the hyperparameters, is crucial for an efficient and correct determination of planetary parameters.

The GP estimates of the rotation period have also been compared to estimates determined by utilization of the GLS periodogram (Zechmeister & Kürster 2009), a common method used in the literature. It has been found that the QP-GP is more robust in determining the right rotation period for several different spot distributions compared to the GLS periodogram, for which more than half of the rotation estimates corresponded to the first harmonic of the signal. Additionally, the uncertainty of the parameters derived by the QP-GP is probabilistically motivated. As a result, the QP-GP rotation period's uncertainty has been realistic in most cases, while the uncertainties provided by the GLS periodogram have been underestimated in many cases.

While the QP-GP is a flexible model capable of fitting various types of variabilities within the RV data, including potential planetary signals, the results of Chapter 3 indicate that a model comparison in the framework of the Bayesian evidence will, in most of the cases, lead to a correct conclusion regarding the origin of the signal, even without any prior information on the nature of these signals. This is a crucial observation, as it approaches one of the main concerns regarding the usage of GPs. Many scientific discussions I participated in the last years were dominated by reservations regarding the application of GP models since they "apparently may fit everything" and "work like a filter". While a GP is undoubtedly a powerful model, incorrect conclusions can often be caused by the incorrect application of the model, rather than by an incorrect model itself. Unfortunately, these models are sometimes used without proper investigations of their behavior on the fitted data set, leading to erroneous conclusions. In this thesis, I have adopted several ways to improve the GP behavior's transparency on the data.

I showed that it is essential to test various model combinations for the observed periodic variations in the RV data. Apart from using periodograms on the RV data to identify these periodicities, it has been demonstrated that it can be beneficial to use periodograms to decompose the GP model itself. This will, in general, reveal any periodic components fitted by the GP model. While in many cases the GP model's periodogram is similar to the periodogram of the RV data, sometimes the periodicities are more discernible. Although the numerical experiments in Chapter 3 indicate that the GP can absorb a Keplerian signal, it is shown that the Keplerian can be identified within the GP fit residuals when the GP model has been well constrained to the activity signal. This works best when the Keplerian signal has a period shorter than the GP length-scale hyperparameter.

Although the results of Chapter 3 are encouraging, there are a few caveats and limitations that must be mentioned. The simulations and results have been based on only a few varying parameters. These were the spot distribution, the spot lifetime, and the average number of spots. However, several other parameters can have a notable effect on the activity signal and, therefore, may also impact the performance of the QP-GP. The simulated star's inclination has always been assumed to be equator-on ($i = 90°$). However, the RV signal of stars is sensitive to the inclination. For

example, a star that is pole-on ($i = 0°$) will not show variation within one rotation period other than due to the spot evolution. Furthermore, the inclination can effect whether spots or faculae are more pronounced features on the stellar surface. As a result the inclination may affect the derived spot lifetime as well as the rotation period if the star is rotating differentially. Additional complicating factors that could impact the GP's performance but were simplified or neglected are differential rotation, the occurrence of faculae, and variations in the spot lifetime, since the spot lifetime has been assumed to be constant for all spots.

Further parameters that may have played a role regarding the investigations on the simultaneous modeling of Keplerian and GP signals, but which were not further investigated, are the period and amplitude ratios of the different signals. Only two different Keplerian signals with different planetary periods, one at approximately one-quarter of the rotation period and one twice the rotation period's value, have been injected in the simulated data and investigated. It might prove interesting to test signals with orbital periods that are several magnitudes larger than the rotation period, e.g., signals on the timescales of years, to test whether these very long-period signals are stronger absorbed by the flexible GP model. The amplitude ratio between the planetary and activity signal varies between the different configurations and individual simulations due to the generation of spots at different longitudes and at different times. However, in general, the value of the investigated planetary amplitude ($K = 3\,\mathrm{m\,s^{-1}}$) has been chosen in such a way that its amplitude is similar or smaller than the activity signal, which represents a conservative scenario.

While a rigorous statistical analysis of all these different degrees of freedom would certainly be informative, it involves significant computational efforts, and such a systematic analysis has not been the primary goal of this thesis but is planned for the near future. Despite the few mentioned shortcomings, the goal of the investigations on the QP-GP carried out in Chapter 3 has been to provide a proof of concept and to show the general reliability of the Bayesian framework coupled with GP models on a few simulated examples under known conditions and with know properties. Given the simple cases that were investigated, the method and models proved to be reliable. In particular, given how the Bayesian framework is built and how uncertainties are estimated within this framework, there is no strong reason to believe that the results based on this statistical approach will break down for more complicated real cases. Additionally, the investigations presented in Chapter 3 provide the reader with a basic intuition regarding these noise models and justify the approaches taken for the analysis and modeling of the planetary systems. For the planetary systems analyzed in this thesis, the usage of GP models was a necessity, especially for the YZ Ceti multiplanetary system.

As of February 2021, YZ Ceti b is the planet with the smallest minimum mass detected so far using the RV method. Its minimum mass is only $0.70 \pm 0.09\,M_\oplus$ while its RV semi-amplitude is about $1.3 \pm 0.15\,\mathrm{m\,s^{-1}}$. In this thesis, a GP has been used to model the stellar activity signal of its host star, and the activity signal shows a mean amplitude of about $1.5^{+0.3}_{-0.2}\,\mathrm{m\,s^{-1}}$, which is, within uncertainties, slightly larger as the RV semi-amplitude of YZ Ceti b ($K_\mathrm{b}/(\sqrt{2}\sigma_\mathrm{GP}) \sim 0.61$). The RV planet signal of YZ Ceti b was severely affected by correlated noise caused by its host star's stellar rotation, resulting in uncertain and wrong estimates of some of the planetary parameters, most notably, the eccentricity. With the results in Chapter 3 it seems reasonable to assume that the eccentricity parameter of Keplerian models is excited and that it absorbs stellar activity contributions within the RV data if these are not appropriately modeled.

A coincidence within the YZ Ceti system that seems to have severely affected the results on the eccentricity of YZ Ceti b is that an alias of the stellar rotational signal is close to one of the harmonics of the planetary signal. The information on the eccentricity of an RV signal is, however, contained in the harmonics of the orbital frequency (see Anglada-Escudé et al. 2010), which is why it seems plausible that the alias of the correlated stellar noise signal might have severely affected the derived eccentricity of YZ Ceti b in this particular case. Simulations of synthetic RV data with similar activity-to-planet period ratios have been made in Chapter 3 and were able to reproduce the observed behavior of an overestimated eccentricity if such a configuration is only modeled with a Keplerian component.

The YZ Ceti multiplanetary system has been particularly interesting as the dynamical stability considerations allowed to verify that the Keplerian fit estimates without any simultaneous activity model were unphysical. Most posterior solutions were dynamically unstable on short timescales in the absence of an activity model. The host star's activity signal was not visible in the residual periodogram of a fit with free eccentricity parameters, as the eccentricity parameter completely absorbed the activity signal. For a single detected planet on a wider orbit, so that one would not expect circularized orbits due to tides, and with a similar ratio of orbital period and activity related signal, a less precise analysis could result in a significant eccentricity that is not existing. The observed effect has also been confirmed and investigated in Sec. 3.5.5. While the effect of too high derived eccentricities for planets in 2:1 period commensurabilities has been investigated by Anglada-Escudé et al. (2010), such an effect has never been observed before in combination with an activity signal or its alias.

Although it has not been included in the work presented in Chapter 5 (Stock et al. 2020b), it is worth noting that the problem of the excited eccentricity of YZ Ceti b has been more severe within a former dataset with 100 RV measurements less than the final analysis. In that former dataset, the median value of YZ Ceti b's eccentricity derived by a fit without a GP component

has been $e \sim 0.7$, and none of the `juliet` posterior solutions without a simultaneous activity model showed long-term stability of the multiplanetary system when analyzed by an N-body integrator.

The GP models fitted to the RV data of YZ Ceti have shown that it can be extremely beneficial to constrain the GP hyperparameters by imposing physical priors. Such constraints helped to improve the estimates of the simultaneously modeled Keplerian planetary parameters and their uncertainties. The consistency with the stability considerations confirm that such an approach is valid. The effect of the prior volume's reduction has also been investigated on a few simulated examples in Chapter 3, and the results are consistent with what has been observed for the YZ Ceti system. The reduction of the GP prior volume helps increase the detection efficiency of planetary signals and better constrain the planetary parameters. This thesis' results point towards the direction that it is recommendable to constrain the GP hyperparameters by priors based on theoretical assessments or based on auxiliary data results, e.g., photometric observations. This is well in line with a recent statement by Gilbertson et al. (2020): "*An overly flexible model is likely to result in unnecessarily broad posterior distributions and reduced marginal likelihood. In the context of EPRV exoplanet surveys, this would correspond to reduced statistical power for detecting planets and reduced precision of planet masses and orbital parameters*".

If no prior knowledge for the QP-GP hyperparameters is available, it has been demonstrated that it is possible to empirically constrain the prior volume in some cases by using several iterations of GP fits. By fitting GPs with wide priors using efficient nested sampling algorithms that sample the posteriors of the hyperparameters within reasonable set boundaries, one can investigate the derived posterior distributions. The results of Chapter 3 and of the planetary systems analyses within this thesis point towards the fact that the host star's rotational signal produces a characteristic structure within the two-dimensional posterior distribution of the GP length-scale-vs.-GP rotation hyperparameter ($\alpha_{\rm GP}$-vs.-$P_{\rm GP}$ diagram). The analysis within this diagram seems to be informative, and it represents something novel that has, to the best of my knowledge, not been used in such a way before. Nevertheless, results in Chapter 3 indicate that the application of this diagram is to some extent limited. Characteristic structures can also occur at half of the rotation period or at periods related to the amplitude variations within the data. In particular, any Keplerian signal within RV data that is absorbed by the GP will also produce these structure. Therefore, it is recommendable to derive the stellar rotation period by applying the GP to photometric data and to combine the information obtained by the $\alpha_{\rm GP}$-vs.-$P_{\rm GP}$ diagram with other indicative information, e.g., activity indicators.

Constraining the QP-GP prior on the length-scale seems particularly important. In some of the simulated cases, mainly those with short spot lifetimes with respect to the rotation period or with

random spot distributions, and in the case of the real RV data of YZ Ceti, GJ 251, and HD 238090, the QP-GP has primarily modeled noise at short time scales. This type of noise can be observed in the $\alpha_{\rm GP}$-vs.-$P_{\rm GP}$ diagram as a plateau of posterior solutions of small length-scales l (large inverse length-scales $\alpha_{\rm GP}$ in the `juliet` parametrization) that are consistent with the complete prior volume of possible rotation periods. While this clearly indicates that there is some significant variability at these short time scales that needs to be modeled, it seems as if the flexibility of QP-GP is limited to properly account for the combination of small and long time scale correlated noise. The QP-GP is a multiplication of two kernels. Therefore, the length-scale and the period hyperparameter are not independent of each other. If the time scale of the correlated noise is significantly smaller than the rotation period of the star, the signal is strictly speaking not quasi-periodic. As a result, the length-scale hyperparameter renders the period hyperparameter meaningless, allowing all possible values for the period. As a result, the QP-GP is performing as an squared-exponential GP.

The results based on the simulated RV data, as well as in the case of YZ Ceti show that the QP-GP performance can be significantly affected by this type of noise on short time scales. For cases with a pronounced plateau of posterior samples in the $\alpha_{\rm GP}$-vs.-$P_{\rm GP}$ plane, the estimated rotation period by the QP-GP was less precise and accurate. Additionally, for combined fits of QP-GPs and Keplerians in these cases it has been found that the planetary parameters derived by the Keplerian model are slightly less precise if the QP-GP modeled primarily this short-term noise than when the QP-GP is stronger constrained to model correlated noise on longer time scales. This may indicate that for the simulated cases, the also apparent QP correlations on longer time scales affects the derivation of the planetary parameters stronger than the noise on short time scales. This seems to have been also the case for the YZ Ceti system. In particular, it has been shown in numerical experiments that the inclusion of an additional periodic component in the form of a sinusoidal model is strongly favored by the log-evidence for these cases where both long-term and short-term noise are apparent. This is caused by the fact that only a few posterior solutions account for the still apparent periodic reappearance of surface features in the case of active longitudes. The QP-GP has been particularly designed to model QP signals; therefore, it should be constrained in such a way that its period hyperparameter stays relevant. As demonstrated by the numerical experiments, even for short spot lifetimes relative to the rotation period, or for random spot distributions, a QP signal at the rotation period can be identified in many cases.

Within the literature it has been proposed to constrain the length-scale of the QP-GP to values larger than the rotation period ($l > P_{\rm rot}$; see, for example, Angus et al. 2018). In this thesis, the length-scale hyperparameter for the final GP fit has been constrained empirically based on the

observed plateau within the $\alpha_{\rm GP}$-vs.-$P_{\rm GP}$ plane of a previously less constrained GP fit. This is a valid approach that also seems less restrictive than implying $l > P_{\rm rot.}$ for the length-scale as its connection to the spot lifetime is not straightforward. However, this leaves the short-term correlations unmodeled. It is not completely clear how this might effect the estimates, although results indicated it is more important to constrain the GP to model the correlated noise on long time scales. For some simulated cases with strong plateaus in the $\alpha_{\rm GP}$-vs.-$P_{\rm GP}$ plane a white noise model performed as good as the QP-GP model in terms of log-evidence. Therefore, the approach within this thesis has been to absorb these short-time-scale correlations with the extra jitter term that is added to the diagonal of the GP covariance matrix. This assumes a white-noise model, which depending on the sampling of the data can be appropriate. A more elegant solution for the future would be to extend the QP-GP model with an additional additive kernel component designed specifically for such short-term variations. This would allow the fitting of these short-term correlated noise together with any QP signal on longer time scales. However, any parameter degeneracies of such a potential QP-and-squared-exponential kernel would need to be carefully investigated by empirically testing the kernel properties similar as for the QP-GP in Chapter 3. Alternatively, one may use and test one of the other many different GP kernels that are already available or in development.

Several studies are currently testing or analyzing new forms of GP kernel functions and their applications to RV data (Foreman-Mackey et al. 2017; Gilbertson et al. 2020; Perger et al. 2021; Luger et al. 2021). These kernels may provide better fitting of astrophysical noise (Perger et al. 2021) than the QP-GP or a better detection efficiency of additional planetary candidates within the RV data than the QP-GP (Gilbertson et al. 2020), or they are considerably faster than the `george` QP-GP (see, for example, `celerite`, Foreman-Mackey et al. 2017), or they allow for better derivation of physical activity parameters (Luger et al. 2021). In all real cases analyzed within this thesis, the `george`'s QP-GP has performed significantly better in terms of log-evidence than the faster `celerite` simple-harmonic oscillator (SHO) and the approximated QP-GP kernel by `celerite`. Both these kernels are also incorporated within `juliet`. The better performance of the `george` QP-GP kernel for stellar activity has also been found and discussed within Cabot et al. (2021). Nevertheless, in the future, it will be required to find kernel functions that are faster than the `george` QP kernel. In particular, for high-cadence photometric data, the `george` kernel is not well suited since the time for the calculations increases rapidly with any additional data point.

A promising new form of GP kernel for stellar activity modeling is the additive combination of several SHO kernels (see, for example, Gillen et al. 2020). Such double or triple SHO kernels are able to model the main rotation period and its first harmonic, as well as any short

term variations which the QP-GP struggled to model simultaneously with the quasi-periodic component. Additionally, the computation time of the multiple SHO kernel is extremely fast in comparison to the QP-GP kernel of `george`. Furthermore, the hyperparameters of the multiple SHO kernel also have the potential to allow, to a certain degree, a physical interpretation similar as for the QP-GP. For the near future, it would be beneficial to perform a more extensive study similar to Chapter 3 for the QP-GP, but also for the new double and triple SHO kernels, for which there is currently a lack of studies available in the literature. The multiple SHO kernel is particularly useful for data sets with a high number of measurements, e.g., photometric observations, as it is much faster than the QP-GP.

I would like to make one final comment on the prior settings that were used for the GPs within the RV data fits. For all real systems within this work, the rotation period could have been determined by fitting a GP to the photometric data. This estimate of the rotation period has, in general, been used for the prior of the GP fit to the RV data. In general, the estimate based on photometric data agreed well with the observed posterior distributions of an unconstrained GP fit to the RV data. However, the derived inverse length-scale parameter α_{GP} between photometry and RV data differed significantly in all cases where both types of data have been available. Additionally, while in many RV data sets a plateau could be observed in the α_{GP}-vs.-P_{GP} plane, the posterior solutions of the GP fitted to the photometric data never showed such a plateau. As already discussed, the connection of the length-scale parameter to the lifetime of active regions is not straightforward. Photometric observations of stars can be more dominated by faculae and plages (Meunier & Lagrange 2019b), while RV observations are generally more spot dominated (Meunier & Lagrange 2019a; Bauer et al. 2018). Additionally, faculaes have been observed to be more persistent than starspots (Collier Cameron et al. 2019; Shapiro et al. 2020), and they have been found to be the dominant surface features for less active Sun-like stars with $\log(R'_{HK}) \leq -4.75$ (Reinhold et al. 2019). Although the stars presented in this thesis are M dwarfs, they have a $\log(R'_{HK})$ which is below that value, and, therefore, they might have similar properties. As a result, one should not expect to observe the same typical lifetime of active regions between photometry and RVs, as one might observe different types of active regions with different properties. Therefore, one should not apply a prior on the GP length-scale hyperparameter based on any previous photometrically derived estimate.

The derived physical properties of planets detected by the RV method rely on the correct assessment of the orbital period. In addition to correlated noise, the determination of the orbital period can be hampered by aliasing. The examples of YZ Ceti, HD 238090, and Lalande 21185 have demonstrated that the correct determination of the orbital period can be challenging. The problem of aliasing has always existed within the RV exoplanet community, but it is often not

given proper attention. Wrong understanding and misconceptions about aliasing (see chapter 2.6 of Dawson & Fabrycky 2010, for a discussion) have led to the fact that this effect is sometimes underestimated.

The discovery paper of the YZ Ceti multiplanetary system (Astudillo-Defru et al. 2017) is an example. In this paper, the periodogram has only been plotted up to a frequency of 1 d^{-1}, and despite the strong aliasing in the data and the implications that follow by this, the possibility of aliasing has not been mentioned or discussed transparently within the study. It has been assumed that the highest peaks in the periodograms automatically correspond to the planetary orbits' periods. The follow-up study by Robertson (2018) has shown that the planetary orbital periods of all three planets cannot be determined unambiguously with the data of Astudillo-Defru et al. (2017). Robertson (2018) has particularly favored a period of 0.75 d for planet c instead of 3.06 d as published by Astudillo-Defru et al. (2017). It is a coincidence that the configuration, which has been derived in this thesis and which bases on twice the number of RV measurements as well as improved methods for alias analysis, resulted in an orbital configuration that is similar to that of Astudillo-Defru et al. (2017). Only the period of planet b has been falsely determined by Astudillo-Defru et al. (2017), and the difference to the original configurations is not affecting the physical parameters as much, as the orbital period has only slightly changed due to the proximity of the alias signal to the true signal in the case of YZ Ceti b.

Fortunately, it seems that the awareness of the aliasing problem has improved recently within the community. The RV community has developed methods to disentangle aliases (Dawson & Fabrycky 2010; Baluev 2012). However, a code using the method of Dawson & Fabrycky (2010) has not been publicly available yet. The self-developed tool `AliasFinder`, which has been introduced in this thesis and which is based on an improved version of the method of Dawson & Fabrycky (2010), has been published on GitHub and in the journal JOSS (Stock & Kemmer 2020). Hopefully, this will enhance alias testing of RV signals within the exoplanet community. The code, which is freely available via "pip" and hence easy to install, might reduce the number of falsely published orbital periods in the future.

The major improvement of `AliasFinder` over the original method by Dawson & Fabrycky (2010) is the incorporation of noise and uncertainty. However, one general drawback of the method by Dawson & Fabrycky (2010) is that the assessment of the nature of the signals (alias or true signal) is currently made by visual inspection rather than by a statistical metric. This is cumbersome and, although it is recalling a time when isochrones were fitted by eye to clusters, there is certainly some room for further improvements. The code `AliasFinder` has recently been improved by myself to provide a basic statistical metric, the root-mean-square difference between the simulated periodograms and the original periodogram for signal's power and phase around

the tested frequencies. However, the reliability of this simple metric has not been tested yet with synthetic data. For the future, it is planned to include and test more sophisticated metrics to compare the periodogram simulations to the true data periodogram. This will help to statistically assess the probability of the signal to be an alias. Additionally, while `AliasFinder` includes noise, it is currently assumed to be uncorrelated white noise (jitter). An investigation on the effect of correlated noise on aliasing and how `AliasFinder` performs under these conditions would be an additional beneficial task for the future, in particular, because `AliasFinder` will be most-likely used for signals that have similar amplitudes as the noise. For example, it might be possible to replace the random white noise in the periodogram simulations by including GPs models trained on the observed correlated noise in the data when performing the periodogram simulations.

As shown in the case of the ultra-compact multiplanetary system YZ Ceti, it is important to correctly resolve the aliases before analyzing the dynamical state of a system. The follow-up observations of the YZ Ceti system by CARMENES and HARPS subsequent to the first discovery by Astudillo-Defru et al. (2017) were aimed at further characterizing the system, in particular its dynamical state. While it was possible to further characterize and constrain the system's orbital parameters, it proved difficult to perform a full dynamical N-body fit to the YZ Ceti system. The requirement to fit the system with a GP in order to obtain realistic planetary parameters made it computationally expensive to combine this with an N-body component, particularly because the small orbital periods of the three planets required very small time steps for the self-consistent N-body fit. All dynamical fits without a GP component resulted in smaller log-likelihood and log-evidence than the Keplerian and GP simultanous fits. Therefore, the question, whether the YZ Ceti system is in any three-body resonance or double two-body resonance could not be finally resolved, and it remains an open question. Nevertheless, N-body integrations of the Keplerian fit's posterior solutions have been used to further constrain the planetary parameters. Within the stable posterior solutions, a fraction of 22% showed clear libration of the three-body Laplace resonance angle. Currently, only very few systems are known to be in three-body resonance. Therefore, it could be worth the effort to further investigate the possibility of a proper full-dynamical analysis of the YZ Ceti system by using the much faster double or triple SHO GP kernels mentioned before.

In addition to the YZ Ceti system, `AliasFinder` proved also to be useful for the unambiguous determination of the orbital periods of HD 238090 b ($\sim$ 13.7 d) and Lalande 21185 b ($\sim$ 12.9 d) as both systems showed strong aliasing in the RV data. HD 238090 b is a warm super-Earth that has been detected within the work presented in this thesis. It orbits an M0.0V star whose stellar activity seems to have been reduced at the time of the RV observations, as the rotational signal of

the star, although present in the data, was not very strong. Given the ratio of the planetary RV amplitude to the activity signal's amplitude ($K/(\sqrt{2}\sigma_{\mathrm{GP}}) \sim 1.05$) this system has been the most straightforward detection presented in this thesis, although, the evidence difference between a Keplerian model or a GP model for the presumed rotational signal at ~ 106 d did not favor one over the other. However, as shown in Chapter 3, this can be the case even if the signal is only based on stellar activity, particularly if a strong plateau in the α_{GP}-vs.-P_{GP} plane is observed, which has been the case for the RV data of HD 238090. Nevertheless, based on the photometric estimate of the rotation period and based on one activity indicator, the 106 d signal's origin has been attributed to be rather caused by activity.

The second planet detected and presented within this thesis is GJ 251 b, a super-Earth orbiting an M3.0V star in the temperate zone. The planet's RV-amplitude-to-activity ratio has been less favorable for this system ($K/(\sqrt{2}\sigma_{\mathrm{GP}}) \sim 0.66$), and the system showed several additional signals (~ 60 d, ~ 73 d, ~ 120 d, and ~ 600 d) in the data for which the origin needed to be carefully analyzed. However a large number of RV observations and a detailed analysis was able to confirm the planet at 14.2 d and to show that the origin of the other observed signals is related to the stellar rotation, its aliases, as well as a presumed magnetic cycle. To classify the long-term signals as a magnetic cycle, the signals's coherence over the time of observations has played an important role, as the signal diminished over the time of the CARMENES observations. This resulted in the fact that, in the final combined data set consisting of CARMENES and HIRES observations, an additional Keplerian fit for the 600 d signal was not justified in terms of the log-evidence.

Last but not least, the temperate super-Earth Lalande 21185 b could be independently confirmed using CARMENES data, and most of its planetary parameters could be improved by a factor of more than two. It is worth noting that Lalande 21185, for which more than 470 RV measurements were taken over several years, has been the only real system for which no significant plateau of posterior solutions was observed in the α_{GP}-vs.-P_{GP} plane of a GP fitted to the RV data. This might indicate that the active surface features of this star have significantly longer typical lifetimes than the rotation period or that the star has active longitudes.

The methods I used within this thesis have been at the forefront of the current field of RV exoplanetary research and RV data modeling. The results obtained by the application of these methods have contributed to their better understanding and allowed to assess their reliability and properties. In particular, the effects of noise caused by stellar activity and its modeling by GP regression models, as well as data sampling and the effect of aliasing within RV data, have been investigated throughout this thesis on simulated and multiple real world examples. The different approaches presented in this thesis, their combination, as well as the self-developed tools and improvements, e.g., `AliasFinder`, periodogram decomposition of GP models, investigations in

the $\alpha_{\rm GP}$-vs.-$P_{\rm GP}$ plane, allowed to precisely characterize planetary systems with difficult noise and sampling properties. This dissertation may serve as a guide or handbook for researchers who are new or interested in the topic of RV modeling of planetary signals close to the stellar noise limit.

The results of the real planetary systems in this thesis have revealed interesting planetary properties and dynamics, e.g., the possibility of a three-body resonance within the YZ Ceti system or the temperate super-Earth planets orbiting GJ 251 and Lalande 21185. The methods used within this thesis can be extended and applied to other systems in the future that are even more complicated than the ones presented in this work. Several of these systems are on the waiting list within the CARMENES survey. Furthermore, there are several additional areas where the Bayesian framework in general, and GPs, in particular, could probably be applied with great success. The Lick survey in search of exoplanets around K giants, that has been partially carried out by people from our research group, has several complicated systems with planetary candidates on the waiting list. For these systems, it is not clear whether the observed periodicities in the RV data are related to stellar oscillations or planets orbiting these stars. Although the noise of K giants is not dominated by rotational modulation but rather by stellar p-mode oscillations, GPs coupled with nested sampling might be a powerful tool to investigate these systems that are not as straightforward to model. However, it has to be investigated whether the sparse sampling of those systems, as well as the different time scales of noise and planet candidates represent an obstacle for the training of the GP model.

I want to conclude this thesis by rephrasing a sentence that I heard several times during the course of my work: *"it is dangerous to fit a GP to RV data"*. After some experience with these types of noise models, I have learned that this is a subject that consists of many facets and, as is so often the case in science, is rich in complexity. Indeed, GPs can be a risky tool if they are not applied correctly. One has to chose the correct approach, the correct priors, and investigate the obtained results carefully. However, the results within this thesis seem to indicate that GPs can also be an extremely useful tool, and that it can be also dangerous to not fit for a GP, particularly, if significant residual noise remains in the data after fitting for the planets.

Bibliography of own publications

This chapter lists, according to the rules of the HGSFP, all publications where I am either author or co-author, and it comments on which of these have been used in this thesis.

Bibliography of first-author papers used in this thesis

- **Stock, S.**, Nagel, E., Kemmer, J., et al.: The CARMENES search for exoplanets around M dwarfs. Three temperate-to-warm super-Earths. – *A& A, 643, A112*, November 2020
- **Stock, S.** & Kemmer, J.: `AliasFinder`: A Python script to search for the true planetary frequency within radial velocity data. – *JOSS, vol. 5, issue 45, id 1771*, January 2020
- **Stock, S.**, Kemmer, J., Reffert, S., et al.: The CARMENES search for exoplanets around M dwarfs. Characterization of the nearby ultra-compact multiplanetary system YZ Ceti. – *A& A, 636, A119*, April 2020

Bibliography of first-author papers not used in this thesis

- **Stock, S.**, Reffert, S., Quirrenbach, A.: Precise radial velocities of giant stars. X. Bayesian stellar parameters and evolutionary stages for 372 giant stars from the Lick planet search. – *A& A, 616, A33*, August 2018

Bibliography of co-author papers not used in this thesis

- Kemmer, J., **Stock, S.**, Kossakowski, D., et al.: Discovery of a hot, transiting, Earth-sized planet and a second temperate, non-transiting planet around the M4 dwarf GJ 3473 (TOI-488). – *A& A, 642, A236*, October 2020
- Trifonov, T., **Stock, S.**, Henning, Th., et al.: Two Jovian Planets around the Giant Star HD 202696: A Growing Population of Packed Massive Planetary Pairs around Massive Stars? – *ApJ., 157, 93*, March 2019

- Reichert, K., Reffert, S., **Stock, S.**, et al.: Precise radial velocities of giant stars. XII. Evidence against the proposed planet Aldebaran b. – *A& A, 625, A22*, May 2019
- Tala Pinto, M., Reffert, S., Quirrenbach, A., et al. (inc. **Stock, S.**): Precise radial velocities of giant stars. XIV. Evidence of planetary companions around HD 25723, 17 Sco, 3 Cnc, and 44 UMa. – *A& A, 644, A1*, December 2020
- Quirrenbach, A., CARMENES Consortium, Amado, P.J., et al. (inc. **Stock, S.**): The CARMENES M-dwarf planet survey – *Proceedings of the SPIE, Volume 11447, id. 114473C*, December 2020
- Nowak, G., Luque, R., Parviainen, H., et al. (inc. **Stock, S.**): The CARMENES search for exoplanets around M dwarfs. Two planets on opposite sides of the radius gap transiting the nearby M dwarf LTT 3780. – *A& A, 642, A173*, October 2020
- Bluhm, P., Luque, R., Espinoza, N., et al. (inc. **Stock, S.**): Precise mass and radius of a transiting super-Earth planet orbiting the M dwarf TOI-1235: a planet in the radius gap? – *A& A, 639, A132*, July 2020
- Trifonov, T., Lee, M.H., Kürster, M., et al. (inc. **Stock, S.**): The CARMENES search for exoplanets around M dwarfs. Dynamical characterization of the multiple planet system GJ 1148 and prospects of habitable exomoons around GJ 1148 b. – *A& A, 638, A16*, June 2020
- Campante, T. L., Corsaro, E., Lund, M. N.., et al. (inc. **Stock, S.**): TESS Asteroseismology of the Known Red-giant Host Stars HD 212771 and HD 203949. – *ApJ., 885, 31*, November 2019
- Morales, J. C., Mustill, A. J., Ribas, I., et al. (inc. **Stock, S.**): A giant exoplanet orbiting a very-low-mass star challenges planet formation models . – *Science, 365, 1441*, September 2019
- Luque, R., Pallé, E., Kossakowski, D., et al. (inc. **Stock, S.**): Planetary system around the nearby M dwarf GJ 357 including a transiting, hot, Earth-sized planet optimal for atmospheric characterization. – *A& A, 628, A39*, August 2019
- Zechmeister, M., Dreizler, S., Ribas, I., et al. (inc. **Stock, S.**): The CARMENES search for exoplanets around M dwarfs. Two temperate Earth-mass planet candidates around Teegarden's Star. – *A& A, 627, A49*, July 2019
- Trifonov, T., Kürster, M., Reffert, S., et al. (inc. **Stock, S.**): New HARPS and FEROS Observations of GJ 1046. – *RNAAS, 2, 180*, July 2019

Bibliography

Aigrain, S., Pont, F., & Zucker, S. 2012, MNRAS, 419, 3147

Alonso-Floriano, F. J., Morales, J. C., Caballero, J. A., et al. 2015, A&A, 577, A128

Ambikasaran, S., Foreman-Mackey, D., Greengard, L., Hogg, D. W., & O'Neil, M. 2015, IEEE Transactions on Pattern Analysis and Machine Intelligence, 38, 252

Andersen, J. M. & Korhonen, H. 2015, MNRAS, 448, 3053

Anderson, D. R., Collier Cameron, A., Hellier, C., et al. 2011, ApJ, 726, L19

Andrae, R. 2010, arXiv e-prints, arXiv:1009.2755

Andrae, R., Schulze-Hartung, T., & Melchior, P. 2010, arXiv e-prints, arXiv:1012.3754

Anglada-Escudé, G., Amado, P. J., Barnes, J., et al. 2016, Nature, 536, 437

Anglada-Escudé, G. & Butler, R. P. 2012, ApJS, 200, 15

Anglada-Escudé, G., López-Morales, M., & Chambers, J. E. 2010, ApJ, 709, 168

Anglada-Escudé, G. & Tuomi, M. 2015, Science, 347, 1080

Angus, R., Morton, T., Aigrain, S., Foreman-Mackey, D., & Rajpaul, V. 2018, MNRAS, 474, 2094

Arens, T., Hettlich, F., Karpfinger, C., et al. 2010, Mathematik, ed. M. Radke (Spektrum Akademischer Verlag)

Astropy Collaboration, Price-Whelan, A. M., Sipocz, B. M., et al. 2018, AJ, 156, 123

Astropy Collaboration, Robitaille, T. P., Tollerud, E. J., et al. 2013, A&A, 558, A33

Astudillo-Defru, N., Díaz, R. F., Bonfils, X., et al. 2017, A&A, 605, L11

Bahng, J. & Schwarzschild, M. 1961, ApJ, 134, 337

Baliunas, S. L. & Vaughan, A. H. 1985, ARA&A, 23, 379

Baluev, R. V. 2009, MNRAS, 393, 969

Baluev, R. V. 2012, MNRAS, 422, 2372

Baranne, A., Queloz, D., Mayor, M., et al. 1996, A&AS, 119, 373

Barnes, J. R., Jeffers, S. V., & Jones, H. R. A. 2011, MNRAS, 412, 1599

Barnes, R. & Greenberg, R. 2007, ApJ, 665, L67

Barnes, R. & Raymond, S. N. 2004, ApJ, 617, 569

Basri, G. & Shah, R. 2020, ApJ, 901, 14

Batista, V. 2018, Finding Planets via Gravitational Microlensing, ed. H. J. Deeg & J. A. Belmonte, 120

Batygin, K. 2015, MNRAS, 451, 2589

Bauer, F. F., Reiners, A., Beeck, B., & Jeffers, S. V. 2018, A&A, 610, A52

Bauer, F. F., Zechmeister, M., Kaminski, A., et al. 2020, A&A, 640, A50

Bauer, F. F., Zechmeister, M., & Reiners, A. 2015, A&A, 581, A117

Bean, J. L. & Seifahrt, A. 2009, A&A, 496, 249

Beck, J. G. 2000, Sol. Phys., 191, 47

Berdyugina, S. V. 2005, Living Reviews in Solar Physics, 2, 8

Berdyugina, S. V. & Usoskin, I. G. 2003, A&A, 405, 1121

Berta, Z. K., Irwin, J., Charbonneau, D., Burke, C. J., & Falco, E. E. 2012, AJ, 144, 145

Bitsch, B. 2019, Astronomy & Astrophysics, 630, A51

Boisse, I., Bouchy, F., Hébrard, G., et al. 2011, A&A, 528, A4

Bond, I. A., Udalski, A., Jaroszyński, M., et al. 2004, ApJ, 606, L155

Borucki, W. J., Koch, D., Basri, G., et al. 2010, Science, 327, 977

Borucki, W. J. & Summers, A. L. 1984, Icarus, 58, 121

Boss, A. P. 1997, Science, 276, 1836

Boss, A. P. 2006, ApJ, 643, 501

Boss, A. P., Butler, R. P., Hubbard, W. B., et al. 2007, Transactions of the International Astronomical Union, Series A, 26A, 183

Bouchy, F. & Carrier, F. 2001, A&A, 374, L5

Bouchy, F., Pepe, F., & Queloz, D. 2001, A&A, 374, 733

Boyajian, T. S., von Braun, K., van Belle, G., et al. 2012, ApJ, 757, 112

Brems, S. S., Kürster, M., Trifonov, T., Reffert, S., & Quirrenbach, A. 2019, A&A, 632, A37

Bressan, A., Marigo, P., Girardi, L., et al. 2012, MNRAS, 427, 127

Brown, T. M. 1990, in Astronomical Society of the Pacific Conference Series, Vol. 8, CCDs in astronomy, ed. G. H. Jacoby, 335–344

Buchner, J., Georgakakis, A., Nandra, K., et al. 2014, A&A, 564, A125

Butler, R. P., Marcy, G. W., Fischer, D. A., et al. 1999, ApJ, 526, 916

Butler, R. P., Marcy, G. W., Williams, E., Hauser, H., & Shirts, P. 1997, ApJ, 474, L115

Butler, R. P., Marcy, G. W., Williams, E., et al. 1996, PASP, 108, 500

Butler, R. P., Vogt, S. S., Laughlin, G., et al. 2017, AJ, 153, 208

Caballero, J. A., Cortés-Contreras, M., Alonso-Floriano, F. J., et al. 2016a, in 19th Cambridge Workshop on Cool Stars, Stellar Systems, and the Sun, 148

Caballero, J. A., Guàrdia, J., López del Fresno, M., et al. 2016b, in Proc. SPIE, Vol. 9910, Observatory Operations: Strategies, Processes, and Systems VI, 99100E

Cabot, S. H. C., Roettenbacher, R. M., Henry, G. W., et al. 2021, AJ, 161, 26

Campbell, B. & Walker, G. A. H. 1979, PASP, 91, 540

Carroll, B. W. & Ostlie, D. A. 2007, An Introduction to Modern Astrophysics, 2nd edn., ed. A. R. S. Black (Pearson Education, Addison Wesley)

Cassan, A., Kubas, D., Beaulieu, J. P., et al. 2012, Nature, 481, 167

Chabrier, G. 2003, PASP, 115, 763

Chambers, J. E. 1999, MNRAS, 304, 793

Chaplin, W. J., Cegla, H. M., Watson, C. A., Davies, G. R., & Ball, W. H. 2019, AJ, 157, 163

Chaplin, W. J. & Miglio, A. 2013, ARA&A, 51, 353

Charbonneau, D., Berta, Z. K., Irwin, J., et al. 2009, Nature, 462, 891

Charbonneau, D., Brown, T. M., Latham, D. W., & Mayor, M. 2000, ApJ, 529, L45

Charbonneau, D., Brown, T. M., Noyes, R. W., & Gilliland, R. L. 2002, ApJ, 568, 377

Charbonneau, P. 2020, Living Reviews in Solar Physics, 17, 4

Chen, Y., Bressan, A., Girardi, L., et al. 2015, MNRAS, 452, 1068

Chen, Y., Girardi, L., Bressan, A., et al. 2014, MNRAS, 444, 2525

Christensen-Dalsgaard, J. 2004, Sol. Phys., 220, 137

Christie, W. H. & Wilson, O. C. 1938, ApJ, 88, 34

Chubak, C., Marcy, G., Fischer, D. A., et al. 2012, arXiv e-prints, arXiv:1207.6212

Chugainov, P. F. 1971, Information Bulletin on Variable Stars, 520, 1

Cifuentes, C., Caballero, J. A., Cortés-Contreras, M., et al. 2020, A&A, 642, A115

Cincotta, P. M. & Simó, C. 2000, A&AS, 147, 205

Cochran, W. D., Hatzes, A. P., Endl, M., Paulson, D. B., & Wittenmyer, R. A. 2008, in Precision Spectroscopy in Astrophysics, ed. N. C. Santos, L. Pasquini, A. C. M. Correia, & M. Romaniello, 175–180

Coleman, G. A. L., Leleu, A., Alibert, Y., & Benz, W. 2019, A&A, 631, A7

Collier Cameron, A., Mortier, A., Phillips, D., et al. 2019, MNRAS, 487, 1082

Collins, K. A., Kielkopf, J. F., Stassun, K. G., & Hessman, F. V. 2017, AJ, 153, 77

Colome, J. & Ribas, I. 2006, IAU Special Session, 6, 11

Correia, A. C. M., Couetdic, J., Laskar, J., et al. 2010, A&A, 511, A21

Correia, A. C. M., Delisle, J.-B., & Laskar, J. 2018, Planets in Mean-Motion Resonances and the System Around HD45364, ed. H. J. Deeg & J. A. Belmonte, 12

Cortés-Contreras, M. 2016, PhD thesis, Universidad Complutense de Madrid

Cortés-Contreras, M., Béjar, V. J. S., Caballero, J. A., et al. 2017, A&A, 597, A47

Cumming, A. 2010, Statistical Distribution of Exoplanets, ed. S. Seager, 191–214

Curiel, S., Ortiz-León, G. N., Mioduszewski, A. J., & Torres, R. M. 2020, AJ, 160, 97

da Costa-Luis, C. 2019, The Journal of Open Source Software, 4, 1277

Davies, M. B., Adams, F. C., Armitage, P., et al. 2014, in Protostars and Planets VI, ed. H. Beuther, R. S. Klessen, C. P. Dullemond, & T. Henning, 787

Dawson, R. I. 2018, Tightly Packed Planetary Systems, ed. H. J. Deeg & J. A. Belmonte, 114

Dawson, R. I. & Fabrycky, D. C. 2010, ApJ, 722, 937

Dawson, R. I. & Johnson, J. A. 2018, ARA&A, 56, 175

Deeming, T. J. 1975, Ap&SS, 36, 137

Delfosse, X., Forveille, T., Mayor, M., et al. 1998, A&A, 338, L67

Desort, M., Lagrange, A. M., Galland, F., Udry, S., & Mayor, M. 2007, A&A, 473, 983

Díaz, R. F. 2018, in Asteroseismology and Exoplanets: Listening to the Stars and Searching for New Worlds, ed. T. L. Campante, N. C. Santos, & M. J. P. F. G. Monteiro, Vol. 49, 199

Díaz, R. F., Delfosse, X., Hobson, M. J., et al. 2019, A&A, 625, A17

Díez Alonso, E., Caballero, J. A., Montes, D., et al. 2019, A&A, 621, A126

Dirac, P. 1958, The Principles of Quantum Mechanics, fourth edition edn. (Clarendon Press, Oxford)

Dreizler, S., Jeffers, S. V., Rodríguez, E., et al. 2020, MNRAS, 493, 536

Dressing, C. D. & Charbonneau, D. 2015, ApJ, 807, 45

Dumusque, X. 2016, A&A, 593, A5

Dumusque, X., Lovis, C., Ségransan, D., et al. 2011a, A&A, 535, A55

Dumusque, X., Pepe, F., Lovis, C., et al. 2012, Nature, 491, 207

Dumusque, X., Santos, N. C., Udry, S., Lovis, C., & Bonfils, X. 2011b, A&A, 527, A82

Dumusque, X., Udry, S., Lovis, C., Santos, N. C., & Monteiro, M. J. P. F. G. 2011c, A&A, 525, A140

Duncan, M. J., Levison, H. F., & Lee, M. H. 1998, AJ, 116, 2067

Dvorak, R. 2007, Extrasolar Planets. Formation, Detection and Dynamics

Einstein, A. 1911, Annalen der Physik, 340, 898

Einstein, A. 1916, Annalen der Physik, 354, 769

Einstein, A. 1936, Science, 84, 506

Emsenhuber, A., Mordasini, C., Burn, R., et al. 2020a, arXiv e-prints, arXiv:2007.05561

Emsenhuber, A., Mordasini, C., Burn, R., et al. 2020b, arXiv e-prints, arXiv:2007.05562

Engle, S. G. & Guinan, E. F. 2017, The Astronomer's Telegram, 10678

Espinoza, N., Kossakowski, D., & Brahm, R. 2019, MNRAS, 490, 2262

Eyer, L. & Bartholdi, P. 1999, A&AS, 135, 1

Fabrycky, D. C. 2010, Non-Keplerian Dynamics of Exoplanets, ed. S. Seager, 217–238

Fang, J. & Margot, J.-L. 2013, ApJ, 767, 115

Feroz, F., Hobson, M. P., & Bridges, M. 2009, MNRAS, 398, 1601

Feroz, F. & Skilling, J. 2013, in American Institute of Physics Conference Series, Vol. 1553, Bayesian Inference and Maximum Entropy Methods in Science and Engineering: 32nd International Workshop on Bayesian Inference and Maximum Entropy Methods in Science and Engineering, ed. U. von Toussaint, 106–113

Fischer, D. A., Marcy, G. W., Butler, R. P., et al. 2008, ApJ, 675, 790

Ford, E. B. 2005, AJ, 129, 1706

Ford, E. B. & Rasio, F. A. 2008, ApJ, 686, 621

Foreman-Mackey, D., Agol, E., Angus, R., & Ambikasaran, S. 2017, AJ, 154, 220

Frink, S., Mitchell, D. S., Quirrenbach, A., et al. 2002, ApJ, 576, 478

Frink, S., Quirrenbach, A., Fischer, D., Röser, S., & Schilbach, E. 2001, PASP, 113, 173

Froeschlé, C., Gonczi, R., & Lega, E. 1997, Planet. Space Sci., 45, 881

Fulton, B. J., Petigura, E. A., Blunt, S., & Sinukoff, E. 2018, PASP, 130, 044504

Gaia Collaboration, Brown, A. G. A., Vallenari, A., et al. 2018, A&A, 616, A1

Garcia-Piquer, A., Morales, J. C., Ribas, I., et al. 2017, A&A, 604, A87

Gaspar, A. & Rieke, G. 2020, Proceedings of the National Academy of Science, 117, 9712

Gatewood, G. 1996, in American Astronomical Society Meeting Abstracts, Vol. 188, American Astronomical Society Meeting Abstracts #188, 40.11

Gaudi, B. S. 2010, Microlensing by Exoplanets, ed. S. Seager, 79–110

Gelman, A. & Rubin, D. B. 1992, Statistical Science, 7, 457

Getling, A. V. & Brandt, P. N. 2002, A&A, 382, L5

Gilbertson, C., Ford, E. B., Jones, D. E., & Stenning, D. C. 2020, ApJ, 905, 155

Giles, H. A. C., Collier Cameron, A., & Haywood, R. D. 2017, Monthly Notices of the Royal Astronomical Society, 472, 1618

Gillen, E., Briegal, J. T., Hodgkin, S. T., et al. 2020, MNRAS, 492, 1008

Gladman, B. 1993, Icarus, 106, 247

Gliese, W. & Jahreiß, H. 1979, A&AS, 38, 423

Goldreich, P. & Sari, R. 2003, ApJ, 585, 1024

Groth, E. J. 1975, ApJS, 29, 285

Haffert, S. Y., Bohn, A. J., de Boer, J., et al. 2019, Nature Astronomy, 3, 749

Hale, G. E. 1908, ApJ, 28, 315

Hall, D. S. & Henry, G. W. 1994, International Amateur-Professional Photoelectric Photometry Communications, 55, 51

Han, C. 2006, ApJ, 638, 1080

Hastings, W. K. 1970, Biometrika, 57, 97

Hatzes, A. P. 1996, PASP, 108, 839

Hatzes, A. P. 2013, Astronomische Nachrichten, 334, 616

Hatzes, A. P., Cochran, W. D., Endl, M., et al. 2015, A&A, 580, A31

Hatzes, A. P., Endl, M., Cochran, W. D., et al. 2018, AJ, 155, 120

Hawley, S. L., Gizis, J. E., & Reid, I. N. 1996, AJ, 112, 2799

Haywood, R. D., Collier Cameron, A., Queloz, D., et al. 2014, MNRAS, 443, 2517

Henry, G. W., Marcy, G. W., Butler, R. P., & Vogt, S. S. 2000, ApJ, 529, L41

Henry, T. J., Jao, W., Subasavage, J. P., et al. 2006, AJ, 132, 2360

Herrero, E., Ribas, I., Jordi, C., et al. 2016, A&A, 586, A131

Higson, E., Handley, W., Hobson, M., & Lasenby, A. 2019, Statistics and Computing, 29, 891

Hill, G. 1993, in Astronomical Society of the Pacific Conference Series, Vol. 38, New Frontiers in Binary Star Research, ed. K.-C. Leung & I.-S. Nha, 127

Hippke, M. & Heller, R. 2019, A&A, 623, A39

Howard, R. 2000, Sunspot Evolution, ed. P. Murdin, 2297

Huggins, W. 1868, Philosophical Transactions of the Royal Society of London Series I, 158, 529

Hunter, J. D. 2007, Computing in Science & Engineering, 9, 90

Husser, T.-O., Wende-von Berg, S., Dreizler, S., et al. 2013, A&A, 553, A6

Ida, S. & Lin, D. N. C. 2004, ApJ, 604, 388

Inselberg, A. 1997, in Proceedings of VIZ '97: Visualization Conference, Information Visualization Symposium and Parallel Rendering Symposium, 100–107

Irwin, J., Berta, Z. K., Burke, C. J., et al. 2011, ApJ, 727, 56

Jacob, W. S. 1855, MNRAS, 15, 228

Järvinen, S. P., Berdyugina, S. V., & Strassmeier, K. G. 2005a, A&A, 440, 735

Järvinen, S. P., Berdyugina, S. V., Tuominen, I., Cutispoto, G., & Bos, M. 2005b, A&A, 432, 657

Jayasinghe, T., Stanek, K. Z., Kochanek, C. S., et al. 2017, The Astronomer's Telegram, 10643

Jeffers, S. V. & Keller, C. U. 2009, in American Institute of Physics Conference Series, Vol. 1094, 15th Cambridge Workshop on Cool Stars, Stellar Systems, and the Sun, ed. E. Stempels, 664–667

Jeffers, S. V., Schöfer, P., Lamert, A., et al. 2018, A&A, 614, A76

Jeffreys, H. 1946, Proceedings of the Royal Society of London Series A, 186, 453

Jeffreys, H. 1961, Theory of probability, 3rd edn. (Oxford, England: Oxford University Press)

Jenkins, J. M., Twicken, J. D., McCauliff, S., et al. 2016, in Society of Photo-Optical Instrumentation Engineers (SPIE) Conference Series, Vol. 9913, Proc. SPIE, 99133E

Johns-Krull, C. M. & Valenti, J. A. 1996, ApJ, 459, L95

Johnson, J. A., Fischer, D. A., Marcy, G. W., et al. 2007, ApJ, 665, 785

Jurgenson, C., Fischer, D., McCracken, T., et al. 2016, in Society of Photo-Optical Instrumentation Engineers (SPIE) Conference Series, Vol. 9908, Ground-based and Airborne Instrumentation for Astronomy VI, ed. C. J. Evans, L. Simard, & H. Takami, 99086T

Kalas, P., Graham, J. R., Chiang, E., et al. 2008, Science, 322, 1345

Kasting, J. F., Whitmire, D. P., & Reynolds, R. T. 1993, Icarus, 101, 108

Kay, C., Opher, M., & Kornbleuth, M. 2016, ApJ, 826, 195

Keller, C. U., Schüssler, M., Vögler, A., & Zakharov, V. 2004, ApJ, 607, L59

Kemmer, J., Stock, S., Kossakowski, D., et al. 2020, A&A, 642, A236

Kennedy, G. M. & Kenyon, S. J. 2008, ApJ, 673, 502

Keppler, M., Benisty, M., Müller, A., et al. 2018, A&A, 617, A44

Khodachenko, M. L., Ribas, I., Lammer, H., et al. 2007, Astrobiology, 7, 167

Kiefer, F. 2019, A&A, 632, L9

Kjeldsen, H., Bedding, T. R., Butler, R. P., et al. 2005, ApJ, 635, 1281

Kley, W., Lee, M. H., Murray, N., & Peale, S. J. 2005, A&A, 437, 727

Kochanek, C. S., Shappee, B. J., Stanek, K. Z., et al. 2017, PASP, 129, 104502

Koen, C. 2006, MNRAS, 371, 1390

Kopparapu, R. K., Ramirez, R., Kasting, J. F., et al. 2013, ApJ, 765, 131

Kreidberg, L. 2015, Publications of the Astronomical Society of the Pacific, 127, 1161

Kroupa, P. 2001, MNRAS, 322, 231

Kunkel, W. E. 1970, Information Bulletin on Variable Stars, 442, 1

Lafarga, M., Ribas, I., Lovis, C., et al. 2020, A&A, 636, A36

Lambrechts, M. & Johansen, A. 2012, Astronomy and Astrophysics, 544, 1

Lambrechts, M., Johansen, A., & Morbidelli, A. 2014, Astronomy and Astrophysics, 572, 1

Lamman, C., Baranec, C., Berta-Thompson, Z. K., et al. 2020, AJ, 159, 139

Lampón, M., López-Puertas, M., Lara, L. M., et al. 2020, A&A, 636, A13

Lanza, A. F., Pagano, I., Leto, G., et al. 2009, A&A, 493, 193

Laskar, J. 1997, A&A, 317, L75

Laskar, J. 2000, Phys. Rev. Lett., 84, 3240

Laskar, J. & Petit, A. C. 2017, A&A, 605, A72

Latham, D. W., Mazeh, T., Stefanik, R. P., Mayor, M., & Burki, G. 1989, Nature, 339, 38

Laughlin, G. & Chambers, J. 2006, ISSI Scientific Reports Series, 6, 233

Laughlin, G. & Chambers, J. E. 2001, ApJ, 551, L109

Lee, M. H. & Peale, S. J. 2002, ApJ, 567, 596

Lee, M. H. & Peale, S. J. 2003, ApJ, 592, 1201

Liu, M. C., Delorme, P., Dupuy, T. J., et al. 2011, ApJ, 740, 108

Lo Curto, G., Pepe, F., Avila, G., et al. 2015, The Messenger, 162, 9

Lomb, N. R. 1976, Ap&SS, 39, 447

Loredo, T. J. 2012, arXiv e-prints, arXiv:1208.3035

Lovis, C. & Fischer, D. 2010, Radial Velocity Techniques for Exoplanets, ed. S. Seager, 27–53

Ludwig, H. G., Allard, F., & Hauschildt, P. H. 2002, A&A, 395, 99

Luger, R., Agol, E., Foreman-Mackey, D., et al. 2019, AJ, 157, 64

Luger, R., Foreman-Mackey, D., & Hedges, C. 2021, arXiv e-prints, arXiv:2102.01697

Luque, R., Pallé, E., Kossakowski, D., et al. 2019, A&A, 628, A39

Malbet, F. & Sozzetti, A. 2018, Astrometry as an Exoplanet Discovery Method, ed. H. J. Deeg & J. A. Belmonte, 196

Malla, S. P., Stello, D., Huber, D., et al. 2020, MNRAS, 496, 5423

Mann, A. W., Dupuy, T., Kraus, A. L., et al. 2019, ApJ, 871, 63

Marcy, G. W., Butler, R. P., Fischer, D., et al. 2001, ApJ, 556, 296

Marcy, G. W., Butler, R. P., Vogt, S. S., Fischer, D., & Liu, M. C. 1999, ApJ, 520, 239

Marois, C., Macintosh, B., Barman, T., et al. 2008, Science, 322, 1348

Martinez Pillet, V., Moreno-Insertis, F., & Vazquez, M. 1993, A&A, 274, 521

Mason, B. D., Wycoff, G. L., Hartkopf, W. I., Douglass, G. G., & Worley, C. E. 2001, AJ, 122, 3466

Maunder, E. W. 1904, Popular Astronomy, 12, 616

Mayor, M., Pepe, F., Queloz, D., et al. 2003, The Messenger, 114, 20

Mayor, M. & Queloz, D. 1995, Nature, 378, 355

McArthur, B. E., Endl, M., Cochran, W. D., et al. 2004, ApJ, 614, L81

McCully, C., Turner, M., Volgenau, N., et al. 2018, Lcogt/Banzai: Initial Release

Metropolis, N., Rosenbluth, A. W., Rosenbluth, M. N., Teller, A. H., & Teller, E. 1953, J. Chem. Phys., 21, 1087

Meunier, N. & Lagrange, A. M. 2019a, A&A, 628, A125

Meunier, N. & Lagrange, A. M. 2019b, A&A, 629, A42

Meyer, M. 2017, PhD thesis, Universität Hamburg, Germany

Mohanty, S. & Basri, G. 2003, ApJ, 583, 451

Montes, D., López-Santiago, J., Gálvez, M. C., et al. 2001, MNRAS, 328, 45

Morales, J. C., Mustill, A. J., Ribas, I., et al. 2019, Science, 365, 1441

Morbidelli, A. & Nesvorny, D. 2012, Astronomy and Astrophysics, 546, 1

Mordasini, C., Alibert, Y., Benz, W., & Naef, D. 2009, A&A, 501, 1161

Morin, J., Donati, J. F., Petit, P., et al. 2010, MNRAS, 407, 2269

Mortier, A. & Collier Cameron, A. 2017, A&A, 601, A110

Mortier, A., Faria, J. P., Correia, C. M., Santerne, A., & Santos, N. C. 2015, A&A, 573, A101

Moss, D. 2004, MNRAS, 352, L17

Mróz, P., Poleski, R., Gould, A., et al. 2020, ApJ, 903, L11

Murray, C. D. & Dermott, S. F. 2000, Solar System Dynamics

Nava, C., López-Morales, M., Haywood, R. D., & Giles, H. A. C. 2020, AJ, 159, 23

Nielsen, M. B., Gizon, L., Cameron, R. H., & Miesch, M. 2019, A&A, 622, A85

Noyes, R. W., Hartmann, L. W., Baliunas, S. L., Duncan, D. K., & Vaughan, A. H. 1984, ApJ, 279, 763

Oláh, K., Kővári, Z., Petrovay, K., et al. 2016, A&A, 590, A133

O'Leary, B. T. 1966, Icarus, 5, 419

Oliphant, T. E. 2006, A guide to NumPy, Vol. 1 (Trelgol Publishing USA)

Ormel, C. W. 2017, The Emerging Paradigm of Pebble Accretion (Springer International Publishing), 197–228

Ormel, C. W. & Klahr, H. H. 2010, Astronomy and Astrophysics, 520, A43

Palle, E., Nortmann, L., Casasayas-Barris, N., et al. 2020, A&A, 638, A61

Palle, P. L., Jimenez, A., Perez Hernandez, F., et al. 1995, ApJ, 441, 952

Parker, E. N. 1979, ApJ, 230, 905

Parviainen, H. 2018, Bayesian Methods for Exoplanet Science, ed. H. J. Deeg & J. A. Belmonte, 149

Passegger, V. M., Reiners, A., Jeffers, S. V., et al. 2018, A&A, 615, A6

Passegger, V. M., Schweitzer, A., Shulyak, D., et al. 2019, A&A, 627, A161

Pepe, F., Mayor, M., Galland, F., et al. 2002, A&A, 388, 632

Pepe, F. A., Cristiani, S., Rebolo Lopez, R., et al. 2010, in Society of Photo-Optical Instrumentation Engineers (SPIE) Conference Series, Vol. 7735, Ground-based and Airborne Instrumentation for Astronomy III, ed. I. S. McLean, S. K. Ramsay, & H. Takami, 77350F

Perger, M., Anglada-Escudé, G., Ribas, I., et al. 2021, A&A, 645, A58

Perger, M., Scandariato, G., Ribas, I., et al. 2019, A&A, 624, A123

Perruchot, S., Kohler, D., Bouchy, F., et al. 2008, in Society of Photo-Optical Instrumentation Engineers (SPIE) Conference Series, Vol. 7014, Proc. SPIE, 70140J

Perryman, M. 2011, The Exoplanet Handbook

Perryman, M., Hartman, J., Bakos, G. Á., & Lindegren, L. 2014, ApJ, 797, 14

Petit, A. C., Laskar, J., & Boué, G. 2018, A&A, 617, A93

Pichierri, G., Batygin, K., & Morbidelli, A. r. 2019, A&A, 625, A7

Pinto, M. S. 2019, PhD thesis, University of Heidelberg

Pojmanski, G. 1997, Acta Astron., 47, 467

Pollacco, D. L., Skillen, I., Collier Cameron, A., et al. 2006, PASP, 118, 1407

Press, W. H., Teukolsky, S. A., Vetterling, W. T., & Flannery, B. P. 1992, Numerical recipes in FORTRAN. The art of scientific computing

Queloz, D. 1995, in New Developments in Array Technology and Applications, ed. A. G. D. Philip, K. Janes, & A. R. Upgren, Vol. 167, 221

Queloz, D., Henry, G. W., Sivan, J. P., et al. 2001a, A&A, 379, 279

Queloz, D., Mayor, M., Udry, S., et al. 2001b, The Messenger, 105, 1

Quirrenbach, A. 2010, Astrometric Detection and Characterization of Exoplanets, ed. S. Seager, 157–174

Quirrenbach, A., Amado, P. J., Caballero, J. A., et al. 2014, in Proc. SPIE, Vol. 9147, Ground-based and Airborne Instrumentation for Astronomy V, 91471F

Quirrenbach, A., Amado, P. J., Mandel, H., et al. 2010, in Society of Photo-Optical Instrumentation Engineers (SPIE) Conference Series, Vol. 7735, Proc. SPIE, 773513

Quirrenbach, A., Amado, P. J., Ribas, I., et al. 2018, in Society of Photo-Optical Instrumentation Engineers (SPIE) Conference Series, Vol. 10702, Proc. SPIE, 107020W

Rajpaul, V., Aigrain, S., Osborne, M. A., Reece, S., & Roberts, S. 2015, MNRAS, 452, 2269

Rajpurohit, A. S., Reylé, C., Allard, F., et al. 2013, A&A, 556, A15

Ramírez, I., Allende Prieto, C., Koesterke, L., Lambert, D. L., & Asplund, M. 2009, A&A, 501, 1087

Rasmussen, C. & Williams, C. 2006, Gaussian Processes for Machine Learning, Adaptive Computation and Machine Learning (Cambridge, MA, USA: MIT Press), 248

Rauer, H., Catala, C., Aerts, C., et al. 2014, Experimental Astronomy, 38, 249

Reffert, S., Bergmann, C., Quirrenbach, A., Trifonov, T., & Künstler, A. 2015, A&A, 574, A116

Reichert, K., Reffert, S., Stock, S., Trifonov, T., & Quirrenbach, A. 2019, A&A, 625, A22

Reiners, A. & Basri, G. 2007, ApJ, 656, 1121

Reiners, A., Joshi, N., & Goldman, B. 2012, AJ, 143, 93

Reiners, A., Ribas, I., Zechmeister, M., et al. 2018a, A&A, 609, L5

Reiners, A., Ribas, I., Zechmeister, M., et al. 2018b, A&A, 609, L5

Reiners, A., Zechmeister, M., Caballero, J. A., et al. 2018c, A&A, 612, A49

Reinhold, T., Bell, K. J., Kuszlewicz, J., Hekker, S., & Shapiro, A. I. 2019, A&A, 621, A21

Ribas, I., Tuomi, M., Reiners, A., et al. 2018, Nature, 563, 365

Ricker, G. R., Winn, J. N., Vanderspek, R., et al. 2015, Journal of Astronomical Telescopes, Instruments, and Systems, 1, 014003

Rieutord, M. & Rincon, F. 2010, Living Reviews in Solar Physics, 7, 2

Rivera, E. J., Laughlin, G., Butler, R. P., et al. 2010, ApJ, 719, 890

Rivera, E. J., Lissauer, J. J., Butler, R. P., et al. 2005, ApJ, 634, 625

Roberts, D. H., Lehar, J., & Dreher, J. W. 1987, AJ, 93, 968

Robertson, P. 2018, ApJ, 864, L28

Robertson, P., Endl, M., Cochran, W. D., & Dodson-Robinson, S. E. 2013, ApJ, 764, 3

Robertson, P., Mahadevan, S., Endl, M., & Roy, A. 2014, Science, 345, 440

Robertson, P., Roy, A., & Mahadevan, S. 2015, ApJ, 805, L22

Robertson, P., Stefansson, G., Mahadevan, S., et al. 2020, ApJ, 897, 125

Rodríguez, E., García, J. M., Costa, V., et al. 2010, MNRAS, 408, 2149

Rodríguez-López, C. 2019, Frontiers in Astronomy and Space Sciences, 6, 76

Rodríguez-López, C., MacDonald, J., Amado, P. J., Moya, A., & Mullan, D. 2014, MNRAS, 438, 2371

Saar, S. H. & Donahue, R. A. 1997, ApJ, 485, 319

Sahlmann, J., Lazorenko, P. F., Ségransan, D., et al. 2013, A&A, 556, A133

Sánchez-López, A., Alonso-Floriano, F. J., López-Puertas, M., et al. 2019, A&A, 630, A53

Santerne, A., Moutou, C., Tsantaki, M., et al. 2016, A&A, 587, A64

Savanov, I. S. 2012, Astronomy Reports, 56, 716

Savanov, I. S. 2014, Astronomy Reports, 58, 478

Scargle, J. D. 1982, ApJ, 263, 835

Schäfer, S., Guenther, E. W., Reiners, A., et al. 2018, in Society of Photo-Optical Instrumentation Engineers (SPIE) Conference Series, Vol. 10702, Ground-based and Airborne Instrumentation for Astronomy VII, ed. C. J. Evans, L. Simard, & H. Takami, 1070276

Schlecker, M., Mordasini, C., Emsenhuber, A., et al. 2020, arXiv e-prints, arXiv:2007.05563

Schöfer, P., Jeffers, S. V., Reiners, A., et al. 2019, A&A, 623, A44

Schrijver, C. J. 2002, Astronomische Nachrichten, 323, 157

Schulze-Makuch, D., Méndez, A., Fairén, A. G., et al. 2011, Astrobiology, 11, 1041

Schuster, A. 1898, Terrestrial Magnetism (Journal of Geophysical Research), 3, 13

Schwabe, M. 1843, Astronomische Nachrichten, 20, 283

Schweitzer, A., Passegger, V. M., Cifuentes, C., et al. 2019, A&A, 625, A68

Seager, S. 2010, Exoplanets

See, T. J. J. 1896, AJ, 16, 17

Semel, M. 1989, A&A, 225, 456

Shakhovskaya, N. I. 1995, VizieR Online Data Catalog, 2055

Shannon, C. 1949, Proceedings of the IRE, 37, 10

Shapiro, A. I., Amazo-Gómez, E. M., Krivova, N. A., & Solanki, S. K. 2020, A&A, 633, A32

Shapiro, A. I., Solanki, S. K., Krivova, N. A., Yeo, K. L., & Schmutz, W. K. 2016, A&A, 589, A46

Shappee, B. J., Prieto, J. L., Grupe, D., et al. 2014, ApJ, 788, 48

Shvartzvald, Y., Yee, J. C., Calchi Novati, S., et al. 2017, ApJ, 840, L3

Skilling, J. 2004, in American Institute of Physics Conference Series, Vol. 735, Bayesian Inference and Maximum Entropy Methods in Science and Engineering: 24th International Workshop on Bayesian Inference and Maximum Entropy Methods in Science and Engineering, ed. R. Fischer, R. Preuss, & U. V. Toussaint, 395–405

Skilling, J. 2006, Bayesian Anal., 1, 833

Skrutskie, M. F., Cutri, R. M., Stiening, R., et al. 2006, AJ, 131, 1163

Skumanich, A. 1972, ApJ, 171, 565

Solanki, S. K. 1999, in Astronomical Society of the Pacific Conference Series, Vol. 158, Solar and Stellar Activity: Similarities and Differences, ed. C. J. Butler & J. G. Doyle, 109

Solanki, S. K. 2003, A&A Rev., 11, 153

Speagle, J. S. 2020, MNRAS, 493, 3132

Stahler, S. W. & Palla, F. 2005, The Formation of Stars, 1st edn. (Wiley-VCH), 865

Steffen, J. H. & Hwang, J. A. 2015, MNRAS, 448, 1956

Stock, K., Cai, M. X., Spurzem, R., Kouwenhoven, M. B. N., & Portegies Zwart, S. 2020a, MNRAS, 497, 1807

Stock, S. & Kemmer, J. 2020, Journal of Open Source Software, 5, 1771

Stock, S., Kemmer, J., Reffert, S., et al. 2020b, A&A, 636, A119

Stock, S., Nagel, E., Kemmer, J., et al. 2020c, A&A, 643, A112

Stock, S., Reffert, S., & Quirrenbach, A. 2018, A&A, 616, A33

Struve, O. 1952, The Observatory, 72, 199

Suárez Mascareño, A., Faria, J. P., Figueira, P., et al. 2020, A&A, 639, A77

Suárez Mascareño, A., Rebolo, R., & González Hernández, J. I. 2016, A&A, 595, A12

Suárez Mascareño, A., Rebolo, R., González Hernández, J. I., & Esposito, M. 2015, MNRAS, 452, 2745

Suárez Mascareño, A., Rebolo, R., González Hernández, J. I., et al. 2018, A&A, 612, A89

Tal-Or, L., Trifonov, T., Zucker, S., Mazeh, T., & Zechmeister, M. 2019, MNRAS, 484, L8

Tal-Or, L., Zechmeister, M., Reiners, A., et al. 2018, A&A, 614, A122

Tan, X., Payne, M. J., Lee, M. H., et al. 2013, ApJ, 777, 101

Tang, J., Bressan, A., Rosenfield, P., et al. 2014, MNRAS, 445, 4287

Topka, K. P., Tarbell, T. D., & Title, A. M. 1997, ApJ, 484, 479

Traub, W. A. & Oppenheimer, B. R. 2010, Direct Imaging of Exoplanets, ed. S. Seager, 111–156

Trifonov, T., Kürster, M., Zechmeister, M., et al. 2018, A&A, 609, A117

Trifonov, T., Tal-Or, L., Zechmeister, M., et al. 2020, A&A, 636, A74

Trotta, R. 2008, Contemporary Physics, 49, 71

Tuomi, M., Jones, H. R. A., Anglada-Escudé, G., et al. 2019, arXiv e-prints, arXiv:1906.04644

Udry, S., Mayor, M., & Santos, N. C. 2003, A&A, 407, 369

Valencia, D., Sasselov, D. D., & O'Connell, R. J. 2007, ApJ, 656, 545

van de Kamp, P. 1963, AJ, 68, 515

van de Kamp, P. & Lippincott, S. L. 1951, AJ, 56, 49

van Driel-Gesztelyi, L. & Green, L. M. 2015, Living Reviews in Solar Physics, 12, 1

van Leeuwen, F. 2007, A&A, 474, 653

VanderPlas, J. T. 2018, ApJS, 236, 16

Vida, K., Oláh, K., Kovári, Z., et al. 2010, Astronomische Nachrichten, 331, 250

Vilhu, O. 1984, A&A, 133, 117

Virtanen, P., Gommers, R., Oliphant Travis E., et al. 2020, Nature Methods, 17, 261

Vogt, S. S., Allen, S. L., Bigelow, B. C., et al. 1994, in Society of Photo-Optical Instrumentation Engineers (SPIE) Conference Series, Vol. 2198, Proc. SPIE, ed. D. L. Crawford & E. R. Craine, 362

Vogt, S. S., Butler, R. P., Rivera, E. J., et al. 2010, ApJ, 723, 954

Wang, J. J., Ginzburg, S., Ren, B., et al. 2020, AJ, 159, 263

Weiss, L. M., Marcy, G. W., Petigura, E. A., et al. 2018, AJ, 155, 48

West, A. A., Weisenburger, K. L., Irwin, J., et al. 2015, ApJ, 812, 3

Wolszczan, A. & Frail, D. A. 1992, Nature, 355, 145

Woźniak, P. R., Vestrand, W. T., Akerlof, C. W., et al. 2004, AJ, 127, 2436

Wright, J. T. 2018, Radial Velocities as an Exoplanet Discovery Method, 4

Wright, J. T., Marcy, G. W., Howard, A. W., et al. 2012, ApJ, 753, 160

Wright, N. J., Newton, E. R., Williams, P. K. G., Drake, J. J., & Yadav, R. K. 2018, MNRAS, 479, 2351

Xu, W. & Seifert, W. 2012, CARMENES VIS Channel Optics, Tech. rep., Landessternwarte Heidelberg

Yan, F., Casasayas-Barris, N., Molaverdikhani, K., et al. 2019, A&A, 632, A69

Zechmeister, M. 2011, PhD thesis, Ruperto-Carola-University of Heidelberg

Zechmeister, M., Dreizler, S., Ribas, I., et al. 2019, A&A, 627, A49

Zechmeister, M. & Kürster, M. 2009, A&A, 496, 577

Zechmeister, M., Reiners, A., Amado, P. J., et al. 2018, A&A, 609, A12

Zeng, L., Sasselov, D. D., & Jacobsen, S. B. 2016, ApJ, 819, 127

List of Abbreviations

A
AFOE Advanced Fiber-Optic Echelle spectrometer
AMD angular momentum deficit
API Application Programming Interface
ASAS All-Sky Automated Survey
ASAS-SN All-Sky Automated Survey for Supernovae
ASH2 Astrograph for Southern Hemisphere

B
BIS bisector span
BJD Barycentric Julian Date

C
CARMENES Calar Alto high-Resolution search for M dwarfs with Exoearths with Near-infrared and optical Échelle Spectrographs
CCF cross-correlation function
CNO cycle carbon-nitrogen-oxygen cycle
CON contrast
CRX chromatic index

D
dLW differential line width
DR data release

F
FAP false-alarm probability
FOV field of view
FP interferometer Fabry-Pérot interferometer
FWHM full width at half maximum

G
GLS periodogram generalized Lomb-Scargle periodogram
GP Gaussian Process

GTO Guaranteed Time Observation

H
HARPS High Accuracy Radial velocity Planet Searcher
HCL hollow-cathode lamp
HF hydrogen fluoride
HIRES High Resolution Echelle Spectrometer
HZ habitable zone

I
IAU International Astronomical Union
IQR interquartile range

J
JOSS Journal of Open Source Software

L
LCO Las Cumbres Observatory
LM least-squared method Levenberg-Marquardt least-squares method
LS periodogram Lomb-Scargle periodogram

M
MAST Mikulski Archive for Space Telescopes
MCMC Markov chain Monte Carlo
MEGNO Mean Exponential Growth factor of Nearby Orbit
MIR mid-infrared wavelength range
MMR mean-motion resonance

N
NIR near-infrared wavelength range
NSVS Northern Sky Variability Survey
NZP nightly-zero point

O
OSN Observatorio de Sierra Nevada

P
PDCSAP Pre-search Data Conditioning Simple Aperture Photometry

PDF probability density function
ppm parts per million
PRV precise radial velocity
PSF point spread function

Q
QP quasi-periodic
QP-GP quasi-periodic Gaussian Process

R
RMS, rms root mean square
RV radial velocity

S
s-BGLS stacked-Bayesian generalized Lomb-Scargle periodogram
SAP Simple Aperture Photometry
SDE signal detection efficiency
SHO Simple Harmonic Oscillator
S/N ratio signal-to-noise ratio
SNO Sierra Nevada Observatory
SPACEOBS San Pedro de Atacama Celestial Explorations Observatory
SPOC Science Processing Operations Center
SRT simultaneous reference technique

T
TESS Transiting Exoplanet Survey Satellite
Th-Ar lamp thorium-argon lamp
Th-Ne lamp thorium-neon lamp
TiO titanium oxide
TJO Telescopi Joan Oró
TLS transit least-squares
TOI TESS object of interest

U
U-Ar lamp uranium-argon lamp
U-Ne lamp uranium-neon lamp
UV ultraviolet wavelength range

V

VIS visual wavelength range

W

WASP Wide Angle Search for Planets

Appendix for Chapter 5

A

A.1 RV data

Table B.1 is available at the CDS.

A.2 Cornerplot of stable solutions

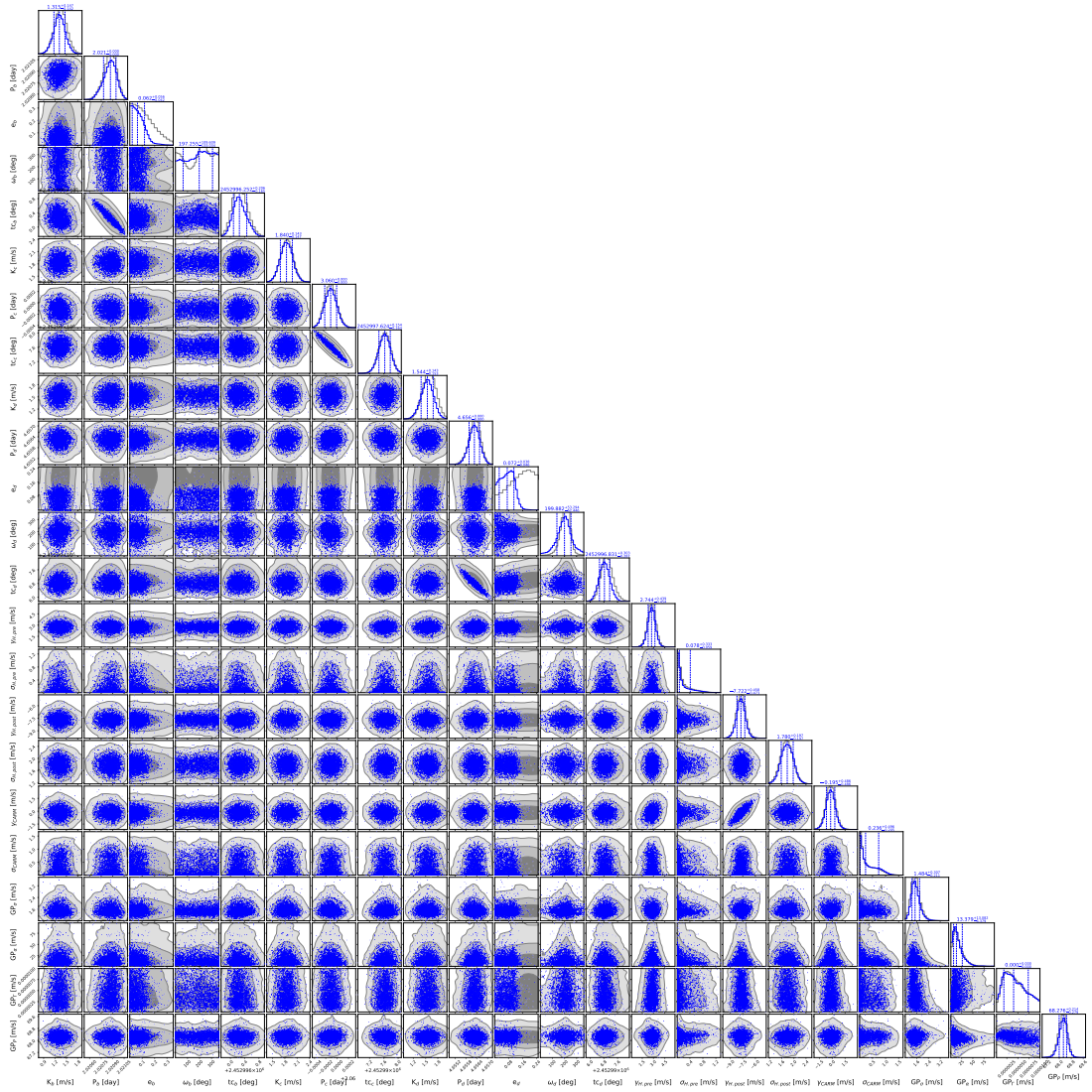


Fig. A.1.: Corner plot of the planetary parameters. The gray areas indicate the different sigma levels of the `juliet` samples with the GP model (run c in Table 5.6). The blue points show the distribution of samples stable over 1 million orbits of the innermost planet (approximately 5557 years). Error bars denote the 68% posterior credibility intervals.

A.3 Additional table

Tab. A.1.: Priors used within `juliet` to model the YZ Ceti multiplanetary system.

Parameter name	Prior	Units	Description
		Planet b	
P_b	$\mathcal{U}(2, 2.1)$	d	Period
$t_{0,b} - 2450000$	$\mathcal{U}(2995, 2997)$	d	Time of transit-center
K_b	$\mathcal{U}(0, 5)$	$\mathrm{m\,s^{-1}}$	Radial-velocity semi-amplitude
e_b	$\mathcal{U}(0, 1)$	...	Eccentricity of the orbit
ω_b	$\mathcal{U}(0, 360)$	deg	Argument of periastron passage of the orbit
		Planet c	
P_c	$\mathcal{U}(3, 3.1)$	d	Period
$t_{0,c} - 2450000$	$\mathcal{U}(2995, 2997.5)$	d	Time of transit-center
K_c	$\mathcal{U}(0, 5)$	$\mathrm{m\,s^{-1}}$	Radial-velocity semi-amplitude
e_c	$\mathcal{U}(0, 1)$	...	Eccentricity of the orbit
ω_c	$\mathcal{U}(0, 360)$	deg	Argument of periastron passage of the orbit
		Planet d	
P_d	$\mathcal{U}(4.6, 4.7)$	d	Period
$t_{0,d} - 2450000$	$\mathcal{U}(2995, 2999)$	d	Time of transit-center
K_d	$\mathcal{U}(0, 5)$	$\mathrm{m\,s^{-1}}$	Radial-velocity semi-amplitude
e_d	$\mathcal{U}(0, 1)$	...	Eccentricity of the orbit
ω_d	$\mathcal{U}(0, 360)$	deg	Argument of periastron passage of the orbit
		RV parameters	
$\gamma_{\mathrm{HARPS\text{-}PRE}}$	$\mathcal{U}(-10, 10)$	$\mathrm{m\,s^{-1}}$	Systemic velocity for HARPS before fiber upgrade
$\sigma_{\mathrm{HARPS\text{-}PRE}}$	$\mathcal{J}(0.01, 100)$	$\mathrm{m\,s^{-1}}$	Extra jitter term for HARPS before fiber upgrade
$\gamma_{\mathrm{HARPS\text{-}POST}}$	$\mathcal{U}(-10, 10)$	$\mathrm{m\,s^{-1}}$	Systemic velocity for HARPS after fiber upgrade
$\sigma_{\mathrm{HARPS\text{-}POST}}$	$\mathcal{J}(0.01, 100)$	$\mathrm{m\,s^{-1}}$	Extra jitter term for HARPS after fiber upgrade
$\gamma_{\mathrm{CARMENES}}$	$\mathcal{U}(-10, 10)$	$\mathrm{m\,s^{-1}}$	Systemic velocity for CARMENES
$\sigma_{\mathrm{CARMENES}}$	$\mathcal{J}(0.01, 100)$	$\mathrm{m\,s^{-1}}$	Extra jitter term for CARMENES

The prior labels $\mathcal{U}$ and $\mathcal{J}$ represent uniform and Jeffrey's distributions (Jeffreys 1946). The planetary and RV priors were not changed between models with different numbers of planets. The GP hyperparameter priors for four different runs are shown in Table 5.6.

A.4 α_{GP}-vs.-P_{GP} diagram of the photometry

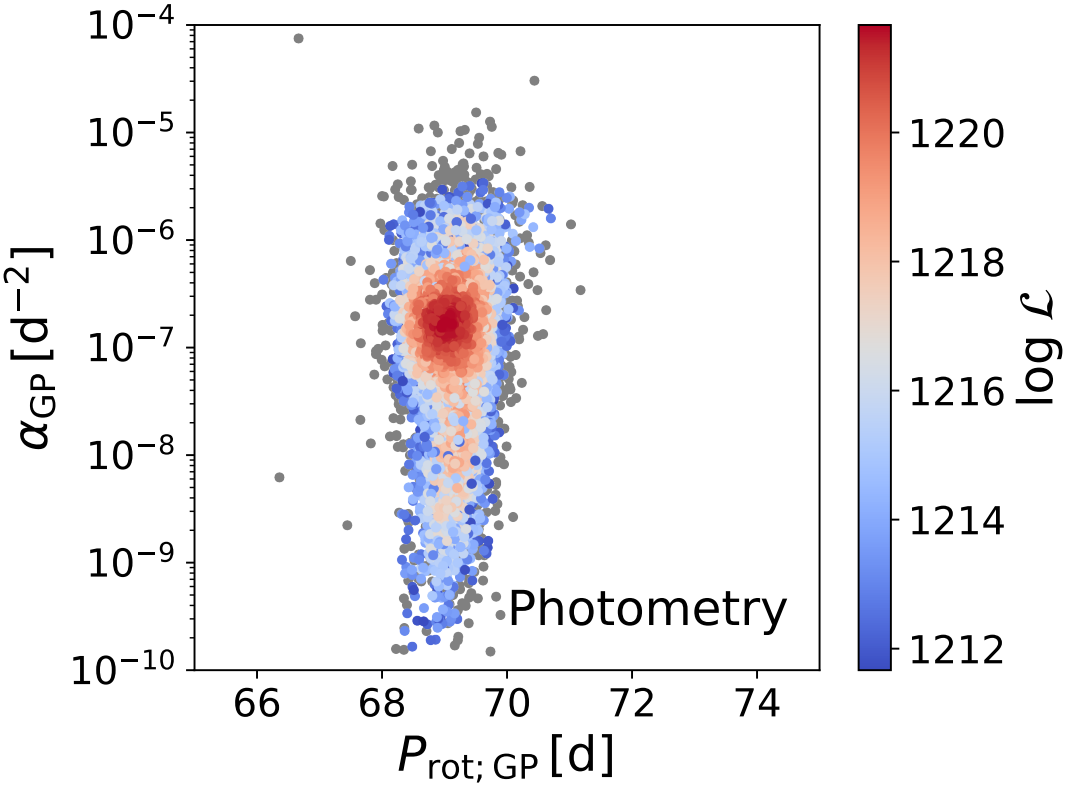


Fig. A.2.: α_{GP}-vs.-P_{GP} diagram of the QP-GP fitted to the photometry of YZ Ceti.

Appendix for Chapter 6

B

B.1 Priors for `juliet`

Tab. B.1.: Priors used within `juliet` to model the photometric data.

Parameter name	Prior	Units	Description
		GP parameters	
$\sigma_{\mathrm{GP,\,instrument}}$	$\mathcal{J}(10^{-8}, 10^{8})$	ppm	Amplitude of GP component of instrument
$\Gamma_{\mathrm{GP,\,instrument}}$	$\mathcal{J}(10^{-6}, 10^{6})$	...	Amplitude of GP sine-squared component of instrument
$\alpha_{\mathrm{GP,\,global}}$	$\mathcal{J}(10^{-10}, 10^{0})$	d^{-2}	Global inverse length-scale of GP exp. component of instruments
$P_{\mathrm{rot,\,GP,\,global}}$	$\mathcal{U}(1, 200)$	d	Global period of the GP QP component of instruments
		instrumental parameters	
$D_{\mathrm{instrument}}$	1 (fixed)	...	Dilution factor of instrument
$M_{\mathrm{Instrument}}$	$\mathcal{N}(0, 10^{5})$	ppm	Relative flux offset of instrument
$\sigma_{w,\mathrm{instrument}}$	$\mathcal{J}(10^{-5}, 10^{5})$	ppm	Extra jitter term of instrument

The prior labels $\mathcal{U}$, $\mathcal{N}$, and $\mathcal{J}$ represent uniform, normal, and Jeffrey's distributions (Jeffreys 1946).

Tab. B.2.: Planetary and instrumental parameter priors used within `juliet`.

Parameter name	Prior	Units	Description
		GJ 251 b	
P_b	$\mathcal{U}(14, 15)$	d	Period
$t_{0,b} - 2450000$	$\mathcal{U}(8620, 8635)$	d	Time of transit center
K_b	$\mathcal{U}(0, 5)$	$\mathrm{m\,s^{-1}}$	RV semiamplitude
$\mathcal{S}_{1,b} = \sqrt{e_b}\sin\omega_b$	$\mathcal{U}(-1, 1)$	...	Parameterization for e and ω.
$\mathcal{S}_{2,b} = \sqrt{e_b}\cos\omega_b$	$\mathcal{U}(-1, 1)$	...	Parameterization for e and ω.
		HD 238090 b	
P_b	$\mathcal{U}(13, 14)$	d	Period
$t_{0,b} - 2450000$	$\mathcal{U}(8620, 8634)$	d	Time of transit center
K_b	$\mathcal{U}(0, 5)$	$\mathrm{m\,s^{-1}}$	RV semiamplitude
$\mathcal{S}_{1,b} = \sqrt{e_b}\sin\omega_b$	$\mathcal{U}(-1, 1)$	...	Parameterization for e and ω.
$\mathcal{S}_{2,b} = \sqrt{e_b}\cos\omega_b$	$\mathcal{U}(-1, 1)$	...	Parameterization for e and ω.
		Lalande 21185 b	
P_b	$\mathcal{U}(12.5, 13.5)$	d	Period
$t_{0,b} - 2450000$	$\mathcal{U}(5865, 5878)$	d	Time of transit center
K_b	$\mathcal{U}(0, 5)$	$\mathrm{m\,s^{-1}}$	RV semiamplitude
$\mathcal{S}_{1,b} = \sqrt{e_b}\sin\omega_b$	$\mathcal{U}(-1, 1)$	...	Parameterization for e and ω.
$\mathcal{S}_{2,b} = \sqrt{e_b}\cos\omega_b$	$\mathcal{U}(-1, 1)$	...	Parameterization for e and ω.
		RV parameters	
$\gamma_{\mathrm{CARMENES}}$	$\mathcal{U}(-10, 10)$	$\mathrm{m\,s^{-1}}$	Velocity zero-point for CARMENES
$\sigma_{\mathrm{CARMENES}}$	$\mathcal{J}(0.01, 100)$	$\mathrm{m\,s^{-1}}$	Extra jitter term for CARMENES
γ_{HIRES}	$\mathcal{U}(-10, 10)$	$\mathrm{m\,s^{-1}}$	Velocity zero-point for HIRES
σ_{HIRES}	$\mathcal{J}(0.01, 100)$	$\mathrm{m\,s^{-1}}$	Extra jitter term for HIRES
γ_{SOPHIE}	$\mathcal{U}(-10, 10)$	$\mathrm{m\,s^{-1}}$	Velocity zero-point for SOPHIE
σ_{SOPHIE}	$\mathcal{J}(0.01, 100)$	$\mathrm{m\,s^{-1}}$	Extra jitter term for SOPHIE

The prior labels $\mathcal{U}$ and $\mathcal{J}$ represent uniform, and Jeffrey's distributions (Jeffreys 1946).

Tab. B.3.: Gaussian process priors used within `juliet` for the RV data of GJ 251, HD 238090, and Lalande 21185.

Parameter name	Prior	Units	Description
	uGP (wide priors) for GJ 251, HD 238090, Lalande 21185		
$\sigma_{\mathrm{GP,\,RV}}$	$\mathcal{U}(0,5)$	$\mathrm{m\,s^{-1}}$	Amplitude of GP component for RVs
$\Gamma_{\mathrm{GP,\,RV}}$	$\mathcal{J}(10^{-2},10^{2})$	...	Amplitude of GP sine-squared component for RVs
$\alpha_{\mathrm{GP,\,RV}}$	$\mathcal{J}(10^{-8},10^{0})$	$\mathrm{d^{-2}}$	Inverse length-scale of GP exponential component for RVs
$P_{\mathrm{rot,\,GP,RV}}$	$\mathcal{U}(20,200)$	d	Period of the GP quasi-periodic component for RVs
	GP (constrained) for GJ 251		
$\sigma_{\mathrm{GP,\,RV}}$	$\mathcal{U}(0,5)$	$\mathrm{m\,s^{-1}}$	Amplitude of GP component for RVs
$\Gamma_{\mathrm{GP,\,RV}}$	$\mathcal{J}(10^{-1},10^{1})$	...	Amplitude of GP sine-squared component for RVs
$\alpha_{\mathrm{GP,\,RV}}$	$\mathcal{J}(10^{-8},3\cdot10^{-4})$	$\mathrm{d^{-2}}$	Inverse length-scale of GP exponential component for RVs
$P_{\mathrm{rot,\,GP,RV}}$	$\mathcal{N}(122.1,6.6)$	d	Period of the GP quasi-periodic component for RVs
	GP (constrained) for HD 238090		
$\sigma_{\mathrm{GP,\,RV}}$	$\mathcal{U}(0,5)$	$\mathrm{m\,s^{-1}}$	Amplitude of GP component for RVs
$\Gamma_{\mathrm{GP,\,RV}}$	$\mathcal{J}(10^{-1},10^{1})$	...	Amplitude of GP sine-squared component for RVs
$\alpha_{\mathrm{GP,\,RV}}$	10^{-20} (fixed)	$\mathrm{d^{-2}}$	Inverse length-scale of GP exponential component for RVs
$P_{\mathrm{rot,\,GP,RV}}$	$\mathcal{N}(96.7,9.3)$	d	Period of the GP quasi-periodic component for RVs
	GP (constrained) for Lalande 21185		
$\sigma_{\mathrm{GP,\,RV}}$	$\mathcal{U}(0,5)$	$\mathrm{m\,s^{-1}}$	Amplitude of GP component for RVs
$\Gamma_{\mathrm{GP,\,RV}}$	$\mathcal{J}(10^{-1},10^{1})$	...	Amplitude of GP sine-squared component for RVs
$\alpha_{\mathrm{GP,\,RV}}$	$\mathcal{J}(10^{-8},10^{-3})$	$\mathrm{d^{-2}}$	Inverse length-scale of GP exponential component for RVs
$P_{\mathrm{rot,\,GP,RV}}$	$\mathcal{N}(56.2,0.81)$	d	Period of the GP quasi-periodic component for RVs

The prior labels $\mathcal{U}$, $\mathcal{N}$, and $\mathcal{J}$ represent uniform, Normal and Jeffrey's distributions (Jeffreys 1946).

B.2 Corner plots

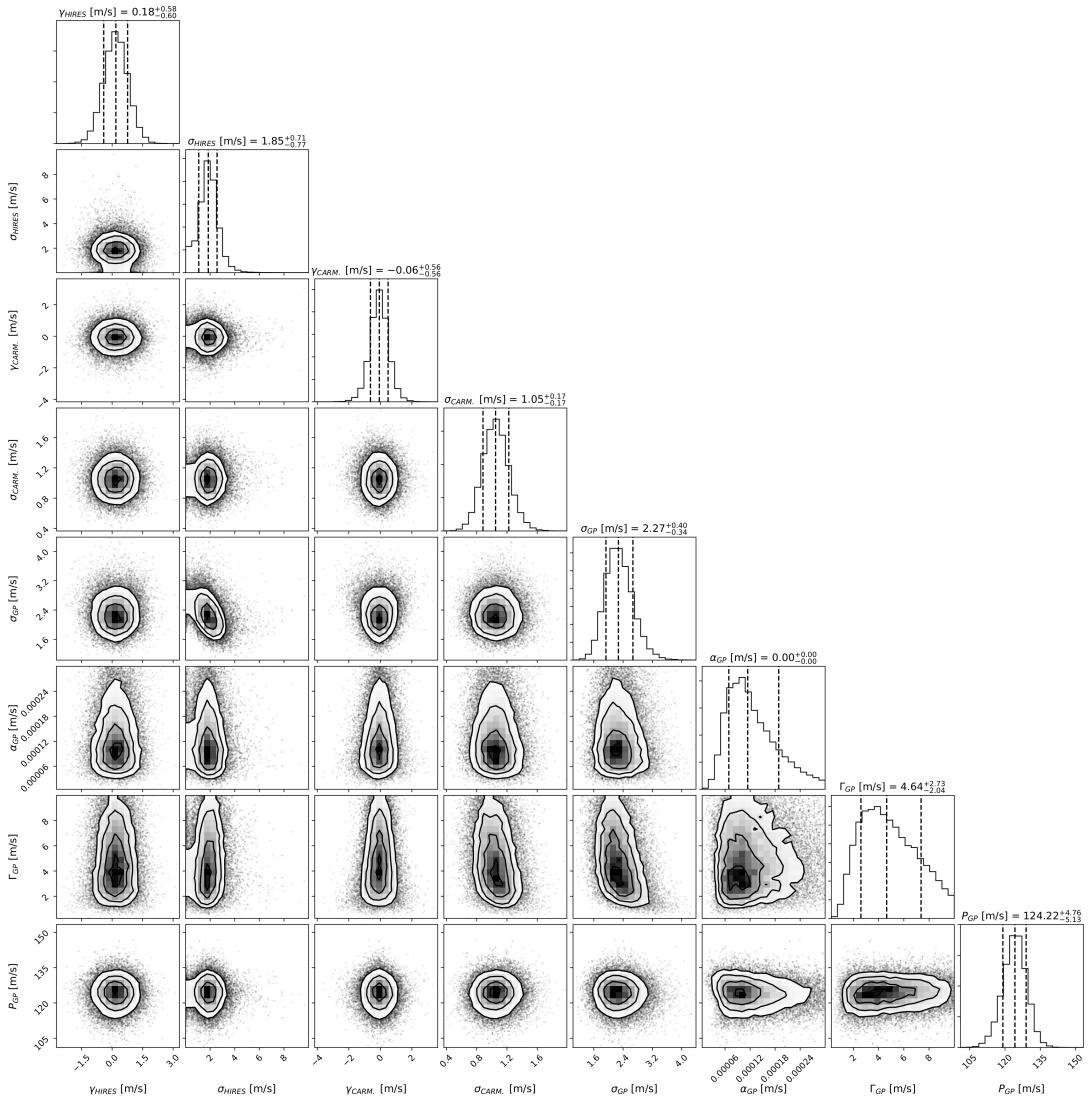


Fig. B.1.: Corner plot of the instrumental and GP parameters for GJ 251. Error bars denote the 68% posterior credibility intervals.

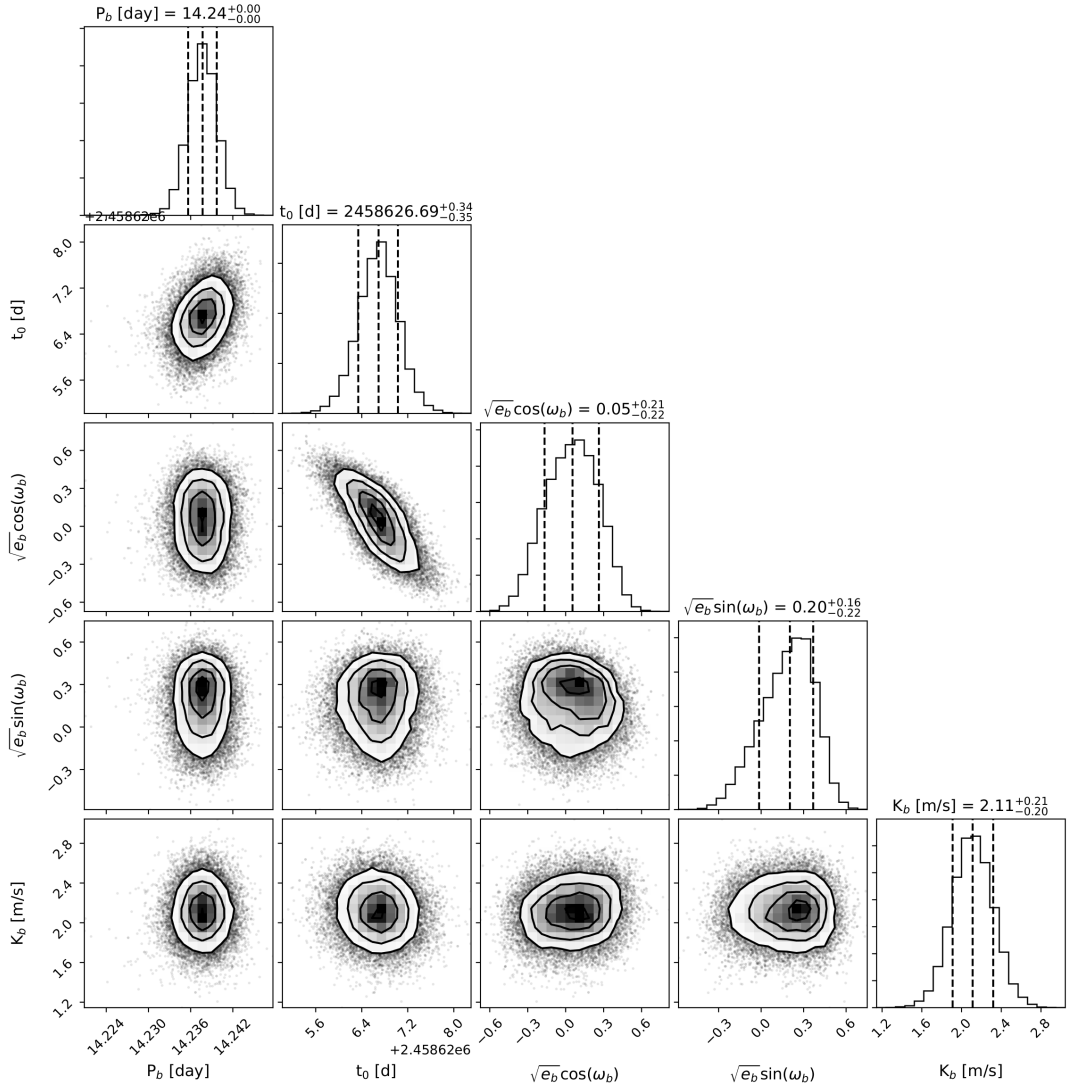


Fig. B.2.: Corner plot of the planetary parameters for GJ 251. Error bars denote the 68% posterior credibility intervals.

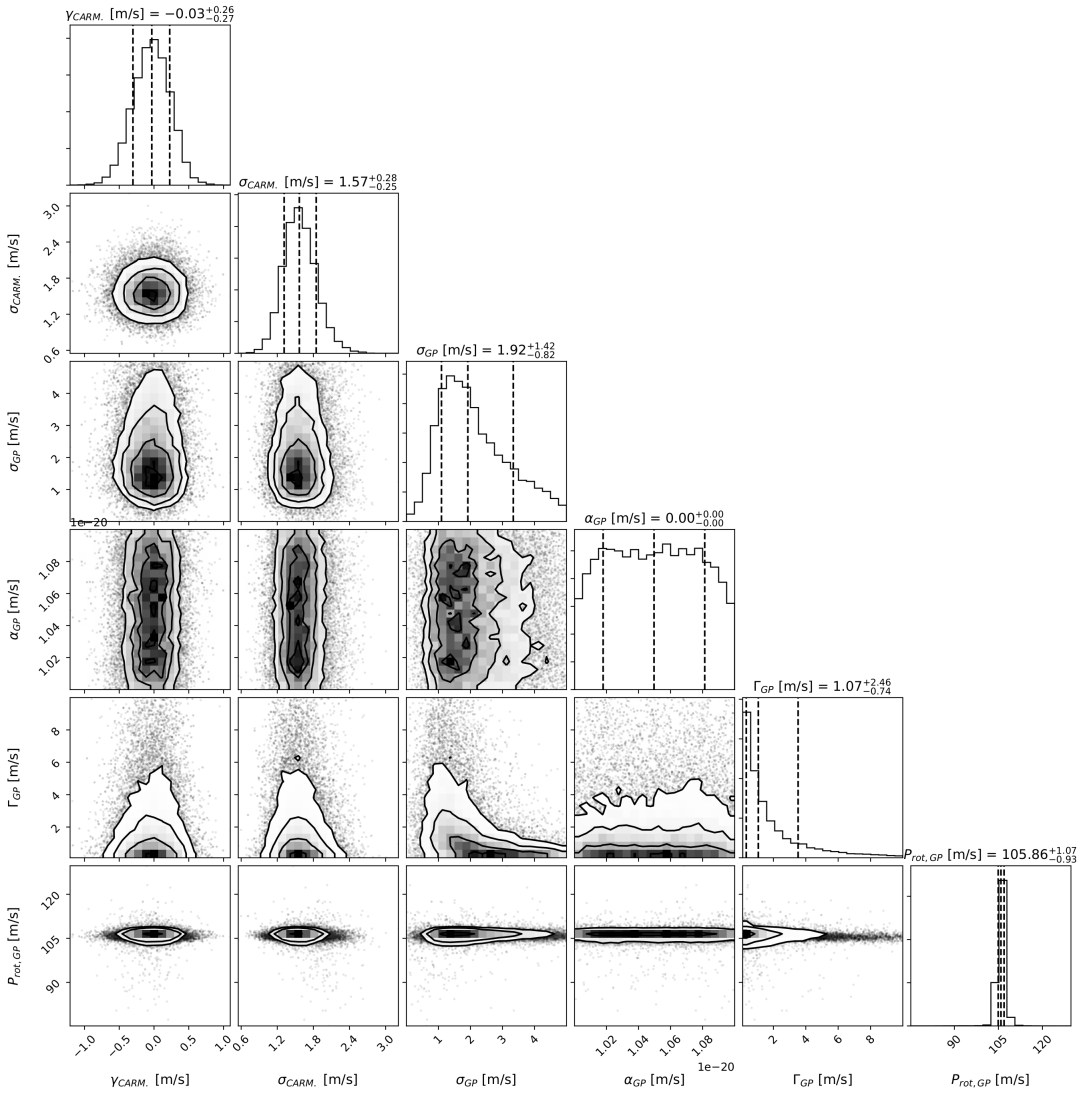


Fig. B.3.: Corner plot of the instrumental and GP parameters for HD 238090. Error bars denote the 68% posterior credibility intervals.

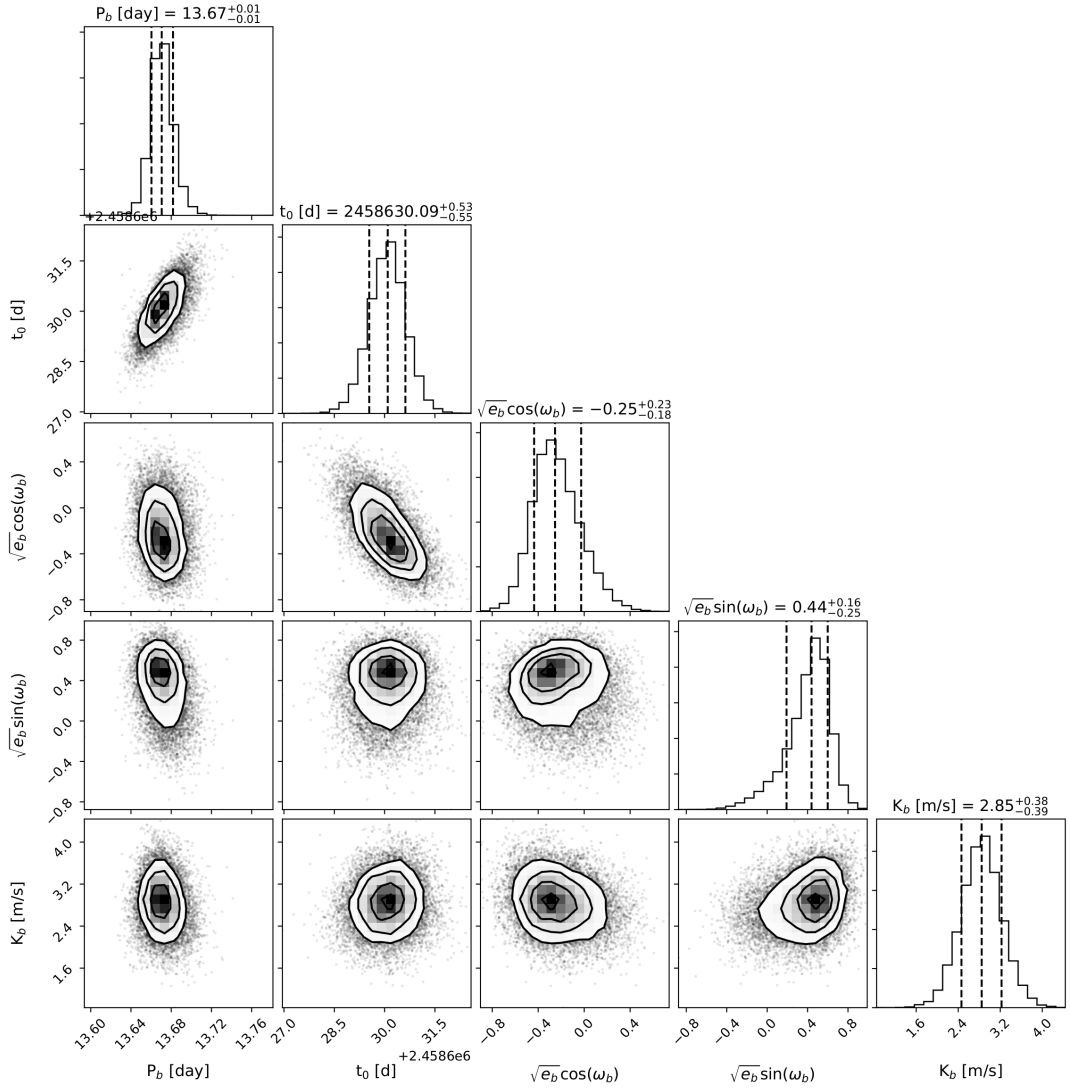


Fig. B.4.: Corner plot of the planetary parameters for HD 238090. Error bars denote the 68% posterior credibility intervals.

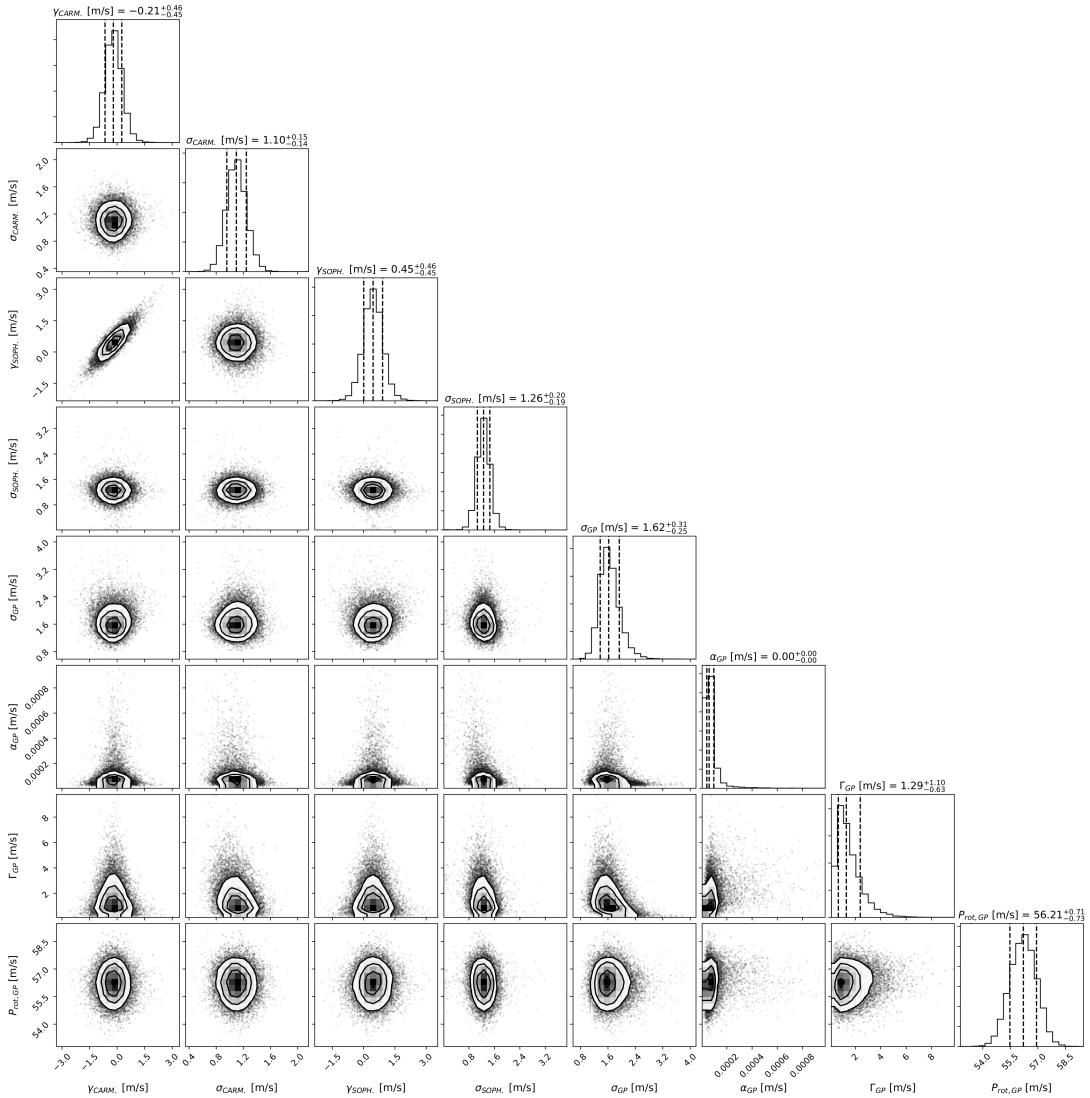


Fig. B.5.: Corner plot of the instrumental and GP parameters for Lalande 21185. Error bars denote the 68% posterior credibility intervals.

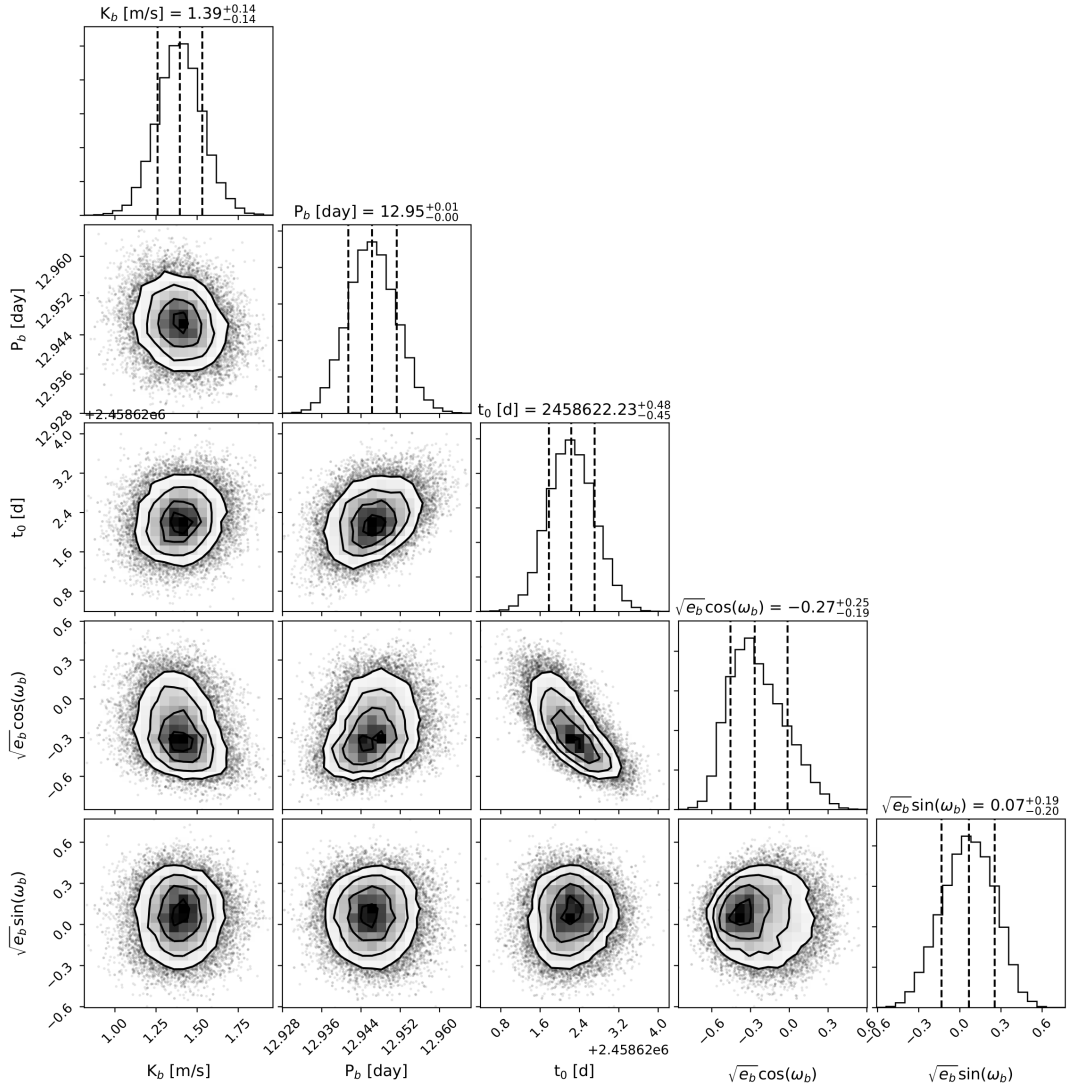
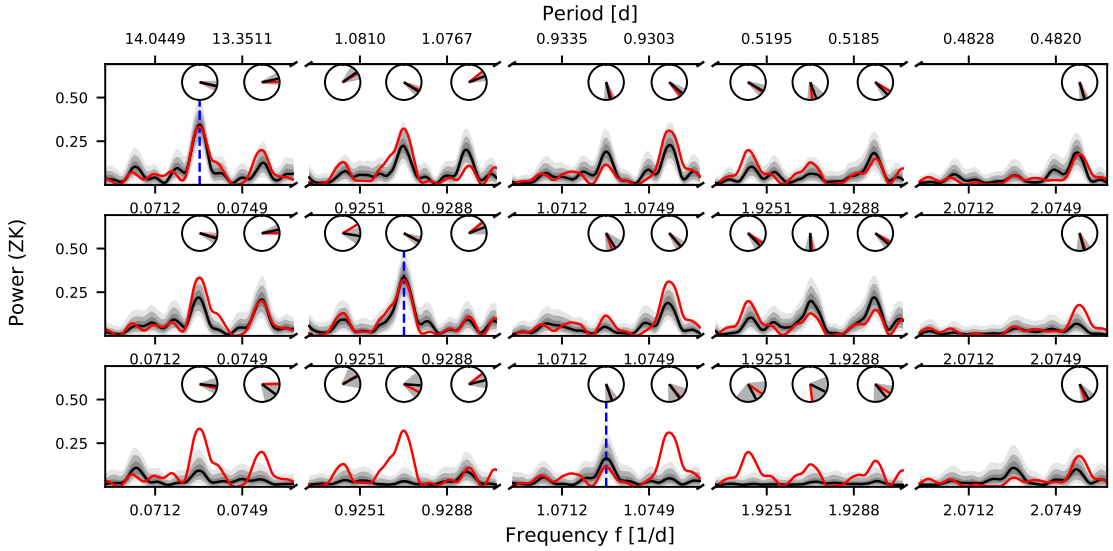
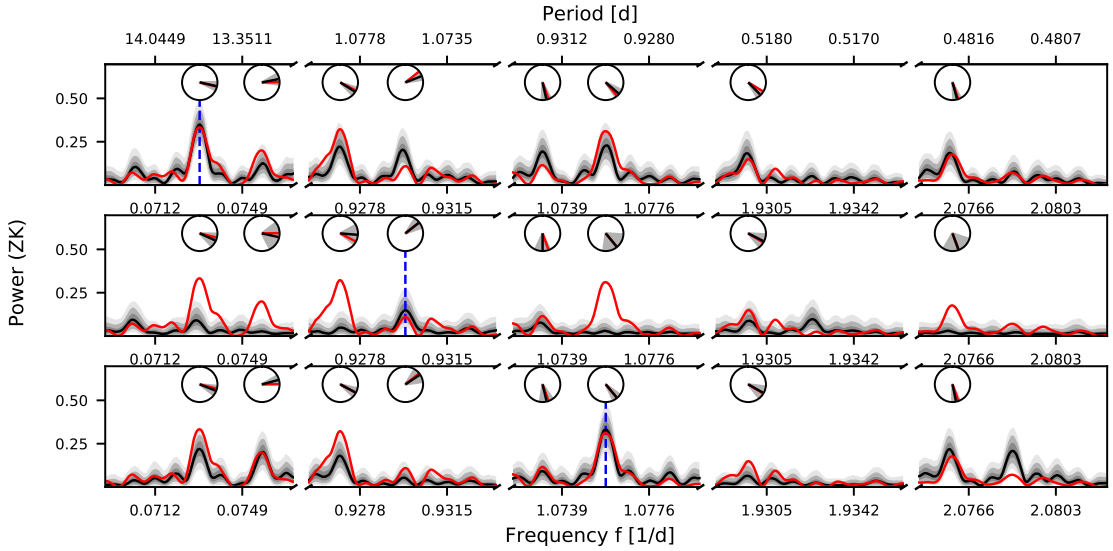


Fig. B.6.: Corner plot of the planetary parameters for Lalande 21185. Error bars denote the 68% posterior credibility intervals.

B.3 `AliasFinder` plot of HD 238090



(a)



(b)

Fig. B.7.: Alias tests for HD 238090. The top plot (a) shows simulations motivated by a sampling frequency of $f_{s_1} = 1.0000\,d^{-1}$. The bottom plot (b) shows simulations motivated by a sampling frequency of $f_{s_2} = 1.0027\,d^{-1}$. Each row in these plots corresponds to one set of simulations for which the frequency of the injected signal is indicated by a vertical dashed blue line. The first row shows simulations with a period of 13.6838 d, and the second and third row show the simulations where the first-order aliases of 13.68 d, regarding the investigated sampling frequency, were injected. Each column shows informative ranges of the periodograms, which are based on the assumed sampling frequency, and can be used for the comparison of data and simulations. From 1000 simulated data sets each, the median of the obtained periodograms (solid black line), the inter-quartile range, and the ranges of 90% and 99% (gray shades) are shown. For comparison, the periodogram of the observed true data is plotted with a solid red line. The angular mean of the phase of some peaks and their standard deviation are shown in the clock diagrams (black line and gray shades) and can be compared to the phase of these peaks in the observed periodogram (red line).

Colophon

This thesis was typeset with LaTeX 2_ε. It uses the *Clean Thesis* style developed by Ricardo Langner. The design of the *Clean Thesis* style is inspired by user guide documents from Apple Inc.

Download the *Clean Thesis* style at http://cleanthesis.der-ric.de/.

Declaration

I hereby declare that this thesis is my own work and that I have used no other than the stated sources and aids.

Ich versichere, dass ich diese Arbeit selbstständig verfasst habe und keine anderen als die angegebenen Quellen und Hilfsmittel benutzt habe.

Heidelberg, February 15, 2021

Stephan Amir Stock